UNIVERSITÄT HAMBURG
Department PHYSIK

Exclusive Search for Supersymmetry with Same-Flavour Di-Lepton Final States with the ATLAS Detector

Dissertation
zur Erlangung des Doktorgrads
des Departments Physik
der Universität Hamburg

vorgelegt von
Michael Böhler
aus Konstanz

Hamburg
2012

Gutachter der Dissertation	:	Dr. Philip Bechtle Prof. Dr. Johannes Haller Prof. Dr. Rainer Wallny
Gutachter der Disputation	:	Dr. Philip Bechtle Prof. Dr. Peter Schleper
Datum der Disputation	:	08. März 2012
Vorsitzender des Prüfungsausschusses	:	Dr. Georg Steinbrück
Vorsitzender des Promotionsausschusses	:	Prof. Dr. Peter H. Hauschildt
Leiter des Departments Physik	:	Prof. Dr. Daniela Pfannkuche
Dekan der MIN-Fakultät	:	Prof. Dr. Heinrich Graener

Abstract

Supersymmetry (SUSY) is one of the most promising extensions of the Standard Model of particle physics. It introduces a new symmetry between fermions and bosons by adding a bosonic superpartner to each SM fermion and a fermionic one to a each SM boson. If an excess of SUSY like signal is observed, SUSY particle properties (e.g. masses or mass differences) must be measured in order to determine the underlying SUSY parameters. Therefore, exclusive SUSY decay cascades with two leptons in the final state are isolated by the flavour subtraction method, in order to fit the endpoint of the invariant mass distribution of these leptons and determine SUSY particle mass differences.

This analysis uses a data sample collected during the first half of 2011, corresponding to an integrated luminosity of $1\,\mathrm{fb}^{-1}$ of $\sqrt{s} = 7\,\mathrm{TeV}$ proton-proton collisions recorded with the ATLAS detector at the Large Hadron Collider. Since no significant same flavour excess is observed, the variable $\mathcal{S}$, which is the measure of a same-flavour excess, is used to determine model-independent and model-dependent limits for different SUSY scenarios. The tightest limits can be set for models expecting exactly two opposite-sign same-flavour leptons and missing transverse momentum larger than 250 GeV. Assuming no combinatorial SUSY background events from different decay chains ($\ell\ell'$), models with di-lepton decays ($\ell\ell$) with SUSY same-flavour excess $\mathcal{S}_s \geq 4.5$ can be excluded at 95% CL. Considering a combinatorial SUSY background contribution with a ratio $BR(\ell\ell')/BR(\ell\ell) = 50\%\,(100\%)$ models with $\mathcal{S}_s \geq 5.5$ (6.7) can be excluded at 95% CL. For the GMSB model with a slepton NLSP, this translates into a limit of the GMSB parameter $\Lambda = 40\,\mathrm{TeV}$ exceeding the current LEP limits.

Zusammenfassung

Supersymmetrie (SUSY) ist eine der vielversprechendsten Erweiterungen des Standardmodells der Teilchenphysik. Es führt eine neue Symmetrie zwischen Fermionen und Bosonen ein, indem jedem SM-Fermion ein bosonischer Superpartner und jedem SM-Boson ein fermionischer zugeordnet wird. Sollte ein Signalüberschuss in Übereinstimmung mit SUSY-Vorhersagen beobachtet werden, müssen Eigenschaften der SUSY-Teilchen (wie z.B. Massen oder Massenunterschiede) gemessen werden, um die zugrundeliegenden SUSY-Parameter zu bestimmen. Dafür könnten exklusive SUSY-Zerfallskaskaden mit zwei Leptonen im Endzustand durch das *Flavour Subtraction*-Verfahren isoliert werden, um den Endpunkt der invarianten Massenverteilung dieser Leptonen zu fitten und die Massenunterschiede der SUSY-Teilchen bestimmen zu können.

Diese Analyse wertet Daten aus, die während der ersten Hälfte des Jahres 2011 in $\sqrt{s} = 7\,\text{TeV}$ Proton-Proton-Kollisionen mit dem ATLAS-Detektor am Large Hadron Collider aufgezeichnet wurden, welche einer integrierten Luminosität von $1\,\text{fb}^{-1}$ entsprechen. Da kein offensichtlicher same-flavour Überschuss gemessen werden konnte, wird die Variable $\mathcal{S}$ verwendet, die den same-flavour Überschusses quantifiziert, um Modell-unabhängige und Modell-abhängige Grenzwerte für verschiedene SUSY Szenarien zu bestimmen. Die besten Grenzen können für Modelle bestimmt werden, die genau zwei unterschiedlich geladene same-flavour Leptonen und fehlenden transversalen Impuls größer als 250 GeV vorhersagen. Unter der Annahme, dass keine kombinatorischen SUSY-Hintergrund-Ereignisse aus verschiedenen Zerfallsketten ($\ell\ell'$) vorhanden sind, können Modelle mit Di-Lepton Zerfällen ($\ell\ell$) mit SUSY same-flavour Überschuss $\mathcal{S}_s \geq 4.5$ mit 95 % CL ausgeschlossen werden. Unter Berücksichtigung kombinatorischer SUSY-Hintergrund-Beiträge mit einem Verhältnis $BR(\ell\ell')/BR(\ell\ell) = 50\%\,(100\%)$, können Modelle mit $\mathcal{S}_s \geq 5.5$ (6.7) mit 95 % CL ausgeschlossen werden. Dies ergibt ein Limit auf den GMSB parameter $\Lambda = 40\,\text{TeV}$ für GMSB Modelle mit slepton NLSP, welche die gegenwärtigen LEP Limits verbessern.

Science and art belong to the whole world,
and before them vanish the barriers of nationality.

Wissenschaft und Kunst gehören der Welt an,
und vor ihnen verschwinden die Schranken der Nationalität.

Johann Wolfgang von Goethe 1813

Contents

Introduction

The Standard Model (SM) of elementary particle physics describes the fundamental constituents of matter and their interactions. In the past decades it has been tested by many experiments and measured to a high precision. The only particle that is still missing is the Higgs boson, that is therefore the main focus of searches currently. The first hints of a Higgs boson with a mass of 126 GeV have been seen at the Large Hadron Collider (LHC), but up to now the statistical significance of the observed signal events is not sufficient to claim an observation. Although the SM has stood up to rigorous testing by various experiments, there are some observed phenomena which remain unexplained and cannot be incorporated into the existing SM.

Supersymmetry (SUSY) is one of the most attractive extension of the SM being able to solve some of its weak points. It provides a natural explanation of the hierarchy problem of the Higgs mass and gives a good candidate for the dark matter of the universe. SUSY introduces a new symmetry between fermions and bosons by adding a bosonic superpartner to each SM fermion and a fermionic superpartner to each SM boson. In this framework a new quantum number can be introduced: the R-parity. If R-parity conservation is assumed SUSY particles are produced in pairs and decay to the lightest supersymmetric particle (LSP), a neutral only weakly interacting particle that is a very good candidate for dark matter. Since SUSY particles have not been observed yet, the symmetry must be broken at the electroweak scale. Different breaking mechanism have been proposed in the literature.

The searches for both, the Higgs boson and new physics beyond the SM were two of the main reasons for the construction of the LHC and its experiments, located at CERN near Geneva. The ATLAS experiment is the largest of these experiments. Designed as multi-purpose experiment, the goal of the ATLAS detector is the discovery of the Higgs boson and new physics.

The aim of this thesis is the measurement of SUSY masses or more specifically: mass differences, through an exclusive search for SUSY with same flavour lepton pairs and missing transverse momentum in the final state, using data recorded by the ATLAS experiment in LHC proton-proton collisions at a centre-of-mass energy of $\sqrt{s} = 7\,\text{TeV}$. The analysis evaluates the data set recorded from March 13th to June 28th 2011, corresponding to an integrated luminosity of $1.04\,\text{fb}^{-1}$. In total, the ATLAS experiment recorded $5.21\,\text{fb}^{-1}$ in the year 2011 and the analyses on the full data set are still ongoing.

The analysis is based on the so-called flavour subtraction (FS) method that is very powerful to suppress SM background processes and to isolate the signal contribution of specific SUSY signals and decay chains: the opposite-sign different-flavour lepton pairs are subtracted from the opposite-sign same-flavour lepton pairs. By applying the FS all flavour symmetric SM backgrounds, such as top-anti-top di-leptonic decays, as well as combinatorial background from SUSY processes cancel out. Exploiting this analysis strategy it would be possible to measure SUSY mass differences of R-parity conserving SUSY models by fitting the endpoint of the invariant mass distribution of two SM leptons produced in sequence in decay chains like $\tilde{\chi}_2^0 \to \tilde{\ell}^+\ell^- \to \ell^+\ell^-\tilde{\chi}_1^0$.

The amount of the same-flavour di-leptons excess is measured with the variable $\mathcal{S}$.

Since no signal of new physics was observed exclusion limits on SUSY scenarios are determined using $\mathcal{S}$. Both model-independent limits on $\mathcal{S}_s$ (same flavour excess of a given signal hypothesis) and model-dependent interpretations in hyperplanes for a given SUSY parameter space are evaluated and compared to other SUSY searches.

The thesis is organised as follows: after an introduction of the Standard Model of elementary particle physics and Supersymmetry in Chapter 1, the experimental setup, specifically the LHC and the ATLAS experiment, is described in Chapter 2. The data taking and prompt data reconstruction are described in the first sections of Chapter 3 including the data-driven auto-configuration tool used for reconstruction of data and simulated Monte Carlo (MC) samples. Chapter 3 concludes with a brief overview of MC generation and detector simulation. The reconstruction and identification algorithms as well as several performance studies for electron, muon, jet and missing transverse momentum identification are presented in Chapter 4. The analysis is described in Chapters 5-7. After introducing the concept of the flavour subtraction analysis and explaining the search strategy through the example of a preliminary Monte Carlo based study in Chapter 5, the analysis is described in detail in Chapter 6. The results are interpreted using model-independent and model-dependent limit procedures based on the variable $\mathcal{S}$ and compared to results of inclusive SUSY searches in Chapter 7. Summary and outlook are given in Chapter 8.

1 The Standard Model and its supersymmetric extensions

The theoretical concepts of elementary particle physics are summarized in the so-call Standard Model [1–3]. It describes the fundamental constituents of matter and their interactions. Since many years the Standard Model predictions are tested successfully to very high precision. The theory predicted for example the existence of gluons, the charm quark and the top quark before their observation. One last particle is not yet discovered, even though its mass range has been predicted within a certain range; the Higgs boson [4–7].

The following section gives a brief overview of the ingredients of the Standard Model (SM) of elementary particles physics, namely the particles, fermions and bosons, the interactions and their underlying symmetry groups and the Higgs mechanism. The SM section is closed with an overview of the open issues which are not covered by the existing SM (Sec. 1.1.2).

The second part of this chapter discusses one possible extension of the SM, the so-called supersymmetry (SUSY). The general description of SUSY generates too many free parameters, such that from an experimental point of view, SUSY has to be constrained, in order to provide predictions which can be tested in particle experiments like proton-proton collisions in ATLAS. After summarising the general idea of SUSY, the Minimal Supersymmetric Standard Model (MSSM) is introduced (cf. Sec. 1.2.2). Different breaking mechanisms are discussed in Sec. 1.2.3. The chapter concludes with experimental results of SUSY searches and the expected signatures in the ATLAS experiment at LHC (Sec. 1.2.5).

1.1 The Standard Model of Elementary Particle Physics

The Standard Model is based on quantum field theory. The matter is described by fermion fields and the interactions are mediated via vector bosons. The particle masses are introduced by the Higgs mechanism. From experimental point of view, the objects, which can be measured directly and indirectly are the entry points, for the measurement of elementary particle physics. Those are the vector bosons (spin one particles) and the fermions (spin one-half particles), both type of particles are listed with some fundamental properties in Tab. 1.1.

The fermions are subdivided into leptons and quarks. There are two different types of leptons, charged leptons (e, μ and τ) carrying electromagnetic charge (-1) and neutral neutrinos (ν_e, ν_μ and ν_τ). The quarks have electromagnetic charge ($^2/_3$ and $-^1/_3$), and so-called colour charge (explained in Sec. 1.1.1). Quarks couple to electroweak and strong gauge bosons, leptons are colour singlets ('colourless') and couple only to electroweak bosons. The fermions are arranged in 3 families consisting of a charged-neutral lepton doublet, e.g (e, ν_e) and an up- and down-type quark doublet (u,d) (cf. Tab. 1.1). The masses of the leptons are differ over several orders of magnitude (sub. eV - GeV) from

neutrinos to the top-quark.

Table 1.1: Some fundamental properties of Standard Model fermions (leptons and quarks) and bosons are listed. All numbers taken from [8].

Fermions					
Leptons			Quarks		
	el. charge	Mass		el. charge	Mass
ν_e	0	$< 0.002\,\mathrm{MeV}$	u	$2/3$	$1.7 - 3.1\,\mathrm{MeV}$
e	-1	$0.511 \pm 1.3 \cdot 10^{-8}\,\mathrm{MeV}$	d	$-1/3$	$4.1 - 5.7\,\mathrm{MeV}$
ν_μ	0	$< 0.19\,\mathrm{MeV}$	c	$2/3$	$1.29^{+0.05}_{-0.11}\,\mathrm{GeV}$
μ	-1	$105.67 \pm 4.0 \cdot 10^{-6}\,\mathrm{MeV}$	s	$-1/3$	$100^{+30}_{-20}\,\mathrm{GeV}$
ν_τ	0	$< 18.2\,\mathrm{MeV}$	t	$2/3$	$172.0 \pm 0.9 \pm 1.3\ \mathrm{GeV}$ [1]
τ	-1	$1776.82 \pm 0.16\,\mathrm{MeV}$	b	$-1/3$	$4.19^{+0.18}_{-0.06}\,\mathrm{GeV}$

[1] Based on published top mass measurements using data from Tevatron Run-I and Run-II. Including also the most recent unpublished results from Run-II, the Tevatron Electroweak Working Group reports a top mass of $173.1 \pm 0.6 \pm 1.1\,\mathrm{GeV}$ [9].

Bosons		
	el. charge	Mass
γ	0	$< 1 \cdot 10{-}18\,\mathrm{eV}$
$W^\pm$	± 1	$80.399 \pm 0.023\,\mathrm{GeV}$
Z^0	0	$91.1876 \pm 0.0021\,\mathrm{GeV}$
g	0	massless [2]

[2] Theoretical value. A mass as large as a few MeV may not be precluded [10].

The bosons are the particles mediating the different type of interactions: the electromagnetic, the weak (unified in the electroweak) and the strong interactions. Different theoretical concepts explain the coexistence of massless (γ,g) and heavy vector bosons ($W^\pm$,Z^0).

1.1.1 The Standard Model in a Nutshell

The Standard Model (SM) is based on a relativistic quantum field theory formulated within a Lagrangian formalism. The fundamental concepts of the SM are the consideration of symmetries and the requirement of the invariance of the Lagrangian under local gauge transformations. The invariance under local transformations can be ensured by including gauge fields into the Lagrangian. The quanta of the gauge fields are the gauge bosons. In total, the SM has 12 gauge bosons. The symmetry group is:

$$U(1)_Y \times SU(2)_L \times SU(3)_C. \tag{1.1}$$

The symmetry group $U(1)_Y$ describes the quantum electrodynamics (QED) [11, 12]. It has one gauge field, the electromagnetic field. The weak interaction is described by a $SU(2)_L$ symmetry group [13, 14], providing three weak bosons. The unification of the electromagnetic and the weak interaction is combined in the so-called electroweak theory explained in more detail in the following section. Finally, the $SU(3)_C$ group describes the quantum chromodynamics (QCD) [15], with eight gauge bosons, the gluons.

Electroweak Theory

The symmetry group of the electroweak theory is the $SU(2)_L \times U(1)$ symmetry. The invariance of the Lagrangian under local gauge transformations can be achieved by adding a triplet for $SU(2)_L$ and a singlet for $U(1)$. The weak isospin currents couple with strength g to the weak isotriplet $W_\mu^{(1,2,3)}$, whereas the weak hypercharge current couples with g' to the isosinglet B_μ. The electroweak eigenstates of the bosons are denoted $W_\mu^{1,2,3}$ and B_μ. In order to consider gauge boson masses without spoiling the renormalizability of the theory, the so-called *spontanous symmetry breaking* has been adopted. After the electroweak symmetry breaking the mass eigenstates can be expressed as rotations of the weak eigenstates:

$$\begin{pmatrix} W_\mu^+ \\ W_\mu^- \end{pmatrix} = \frac{1}{\sqrt{2}} \begin{pmatrix} 1 & -1 \\ 1 & 1 \end{pmatrix} \begin{pmatrix} W_\mu^1 \\ W_\mu^2 \end{pmatrix} \tag{1.2}$$

$$\begin{pmatrix} Z_\mu^0 \\ A_\mu^0 \end{pmatrix} = \begin{pmatrix} \cos\theta_W & -\sin\theta_W \\ \sin\theta_W & \cos\theta_W \end{pmatrix} \begin{pmatrix} W_3^\mu \\ B^\mu \end{pmatrix} \tag{1.3}$$

with θ_W the weak mixing angle (or Weinberg angle) which is defined by the following connection:

$$\cos\theta_W = \frac{g}{\sqrt{g^2 + g'^2}}, \quad \sin\theta_W = \frac{g'}{\sqrt{g^2 + g'^2}}. \tag{1.4}$$

The Weinberg angle [3] is a free parameter of the SM and has to be determined experimentally, its measured value is $\sin^2\theta_W(M_Z) \approx 0.23116(13)$ [8]. A_μ^0 represents the massless photon field. W_μ^+, W_μ^- and Z^0 couple to the Higgs field, such that those bosons are massive. The corresponding gauge bosons are denoted γ, $W^\pm$ and Z^0.

As in the case of the electroweak gauge bosons, the mass eigenstates of the quarks are not identical to the weak eigenstate. Usually, the down type quarks are defined as mixing states, which can be calculated with couplings given by the Cabbibo-Kobayashi-Maskawa (CKM) matrix [16]:

$$\begin{pmatrix} d' \\ s' \\ b' \end{pmatrix} = \begin{pmatrix} V_{ud} & V_{us} & V_{ub} \\ V_{cd} & V_{cs} & V_{cb} \\ V_{td} & V_{ts} & V_{tb} \end{pmatrix} \begin{pmatrix} d \\ s \\ b \end{pmatrix} \tag{1.5}$$

The generation mixing allows flavour changing currents ($W^\pm$), whereas flavour changing neutral currents are suppressed. The CKM matrix is unitary and can be parametrized by three mixing angles and one complex phase, which is the only source of CP-violation in the SM [17]. The same generation mixing can be expressed for the lepton sector, described in the neutrino mixing matrix, the so-called Maki-Nakagawa-Sakata (MNS)-matrix [18]. The neutrino mixing was an important discovery [19], because only massive particles can mix. Even though the neutrino masses have been experimentally established by now, the common formulation of the SM still treats neutrinos as approximately massless particles.

Quantum Chromodynamics (QCD)

The strong interactions are described by a $SU(3)$ symmetry group. There are eight quanta of the gauge fields called gluons. The theory describing the interactions of quarks and gluons is called quantum chromodynamics [15], according to the charge of the strong interactions, which is denoted as *colour charge*. The $SU(3)_C$ is a non-abelian gauge group. This introduces several characteristics. The gauge bosons themselves are carry-

ing colour charge, which yield gluon self-coupling. The range of the strong interaction is limited, even though the gluons are massless. The coupling constant of the strong interaction (α_s) is a function of the momentum transfer Q^2 (cf. Fig. 1.1(a)), as the coupling constants of $SU(2)_L$ and $U(1)_y$. Due to the non-abelian gauge group gluons couple to each other and α_s is large at low values of Q^2 where α_s is not small compared to one and perturbation calculation cannot be applied, for increasing Q^2 α_s falls exponentially (for $Q^2 \to \infty$ α_s goes to zero). In experiments with larger momentum transfer (Q^2) the quarks within hadrons behave like free particles. This behaviour for low and high Q^2 is called confinement and asymptotic freedom [20, 21] respectively. Due to the confinement, no free quark can be observed. The quarks are bound to colourless objects either as quark-anti-quark pairs (mesons) with colour and anti-colour or as three quark state with complementary colour (e.g. q_r,q_g, and q_b) (baryons).

The proton is a baryon of three quarks following the most simplified description. The three valence quarks *uud* characterise the proton properties, for example the electromagnetic charge $((+2/3)+(+2/3)+(-1/3) = +1)$. It has been found, that the proton consists, in addition to the three valence quarks, of so-called sea quarks and gluons.

The substructure of the proton has been studied at the HERA electron-proton collider at DESY by deep inelastic scattering [22, 23]. The parton density function (pdf) is studied as function of the momentum transfer (Q^2) from the electron to the interacting proton and the parton momentum fraction x of the total proton momentum. Figure 1.1(b) shows the parton distribution functions (pdf) as a function of the momentum fraction x for $Q^2 = 10\,\mathrm{GeV}^2$ measured by the HERA experiments ZEUS and H1 [24]. The momentum fraction of the valence quarks are shown as xu_v and xd_v, the contribution from the gluons as xg and the contribution from the sea quarks is plotted as xS.

The LHC is a proton-proton collider, therefore it is crucial to know the proton pdf as precisely as possible. The Monte Carlo simulation of each process produced in a proton-proton collision has to consider the proton substructure in the initial interaction. In searches for non-SM particles, which might be rather heavy, it has to be considered that not the full energy of the colliding protons of 7 TeV (14 TeV at design energy) is available for the production process, but only the fraction of the colliding partons of the proton.

The Higgs Mechanism

One of the fundamental concepts of the SM would be broken by adding simple mass terms to the Lagrangian, namely the local gauge invariance. The short range of the weak interaction can only be explained by massive gauge bosons. Also the masses of the fermions and gauge bosons have been measured in experiments with high precision. The Higgs mechanism [4–7] allows the description of particle masses also in the presence of local gauge invariance, as discussed briefly in this section.

The simplest way is to add a weakly-coupling spin-zero particle with a potential that is minimized at a non-zero field value. This scalar field can additionally be used to give mass to the fermions, after it develops a vacuum expectation value (VEV). Therefore it should have Yukawa couplings with the fermions. The fermions are arranged in singlets and doublets, such that the scalar field must be a doublet or a triplet. It turns out that a triplet cannot couple to itself and generate a mass for all known fermions, as needed. So the simplest solution is to add a single complex scalar doublet:

$$\phi = \begin{pmatrix} \phi^\dagger \\ \phi^0 \end{pmatrix} = \frac{1}{\sqrt{2}} \begin{pmatrix} \phi_1 + i\phi_2 \\ \phi_3 + i\phi_4 \end{pmatrix}, \quad |\phi^2| = v^2. \tag{1.6}$$

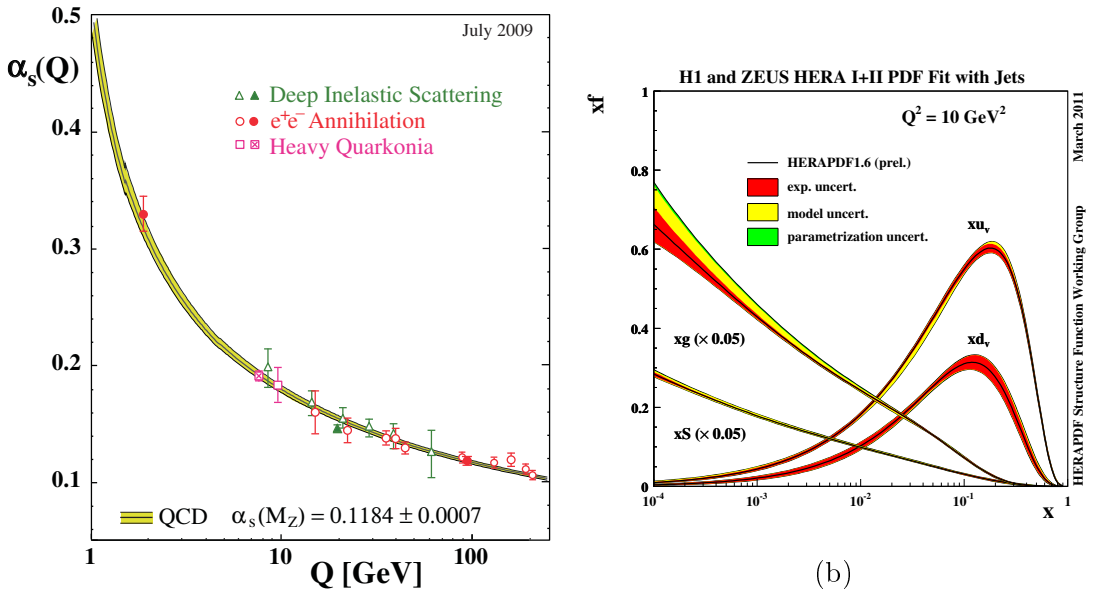

(a) (b)

Figure 1.1: Summary of measurements of α_s as a function of the respective energy scale Q. The curves are QCD predictions for the combined world average value of $\alpha_s(M_{Z_0}$ [25] (a).Parton distribution functions from combined HERA experiments as a function of x for $Q^2 = 10\,\mathrm{GeV}^2$. The central value (solid line) is shown together with the experimental, model and parametrization uncertainties represented by the red, yellow and green shaded bands, respectively [24] (b).

This scalar field is called Higgs field and the mechanism of generating mass due to the coupling to the scalar field is called *Higgs mechanism*. The following potential can be defined:

$$V(\phi^\dagger\phi) = \mu^2\phi^\dagger\phi + \lambda(\phi^\dagger\phi)^2 \tag{1.7}$$

with the mass term μ and the self-coupling term λ. The parameter λ has to be positive to ensure that $V \to \infty$ for $\phi \to \pm\infty$. By choosing $\mu^2 > 0$ and $\lambda > 0$, the minimum of the potential would be in $\phi = 0$. This would not induce the needed symmetry breaking, which would allow to generate the mass terms. Instead, choosing $\mu^2 < 0$, shifts the minimum to a value

$$\phi_0 = \sqrt{-\frac{\mu^2}{\lambda}} = v. \tag{1.8}$$

Choosing these parameters, allows the construction of a potential V which is $SU(2)_L$ symmetric, but every possible ground state breaks the $SU(2)_L$ symmetry. By choosing a specific ground state: $\phi_1 = \phi_2 = \phi_4 = 0$ and $\phi_3 = v$ the field can be expanded around the minimum and one obtains:

$$\phi = \frac{1}{\sqrt{2}} = \begin{pmatrix} 0 \\ v + H(x) \end{pmatrix}. \tag{1.9}$$

In the resulting Lagrangian density a mass term for h appears: $m_h = \sqrt{-2\mu^2}$. Then the mass terms of the gauge fields can be derived as:

$$m_W = \frac{gv}{2}, \tag{1.10}$$

$$m_Z = \frac{v}{2}\sqrt{g^2 + g'^2} = \frac{m_W}{\cos\theta_W}, \tag{1.11}$$

$$m_\gamma = 0. \tag{1.12}$$

with the coupling constants g, g', the mixing angle θ_W and the vacuum expectation value v. The Higgs mechanism allows to introduce all gauge boson masses based on the gauge interactions only. No additional free parameters are needed to calculate the rather different but precisely measured boson masses. Replacing the coupling in Eq. (1.10), by the Fermi constant, which has be measured precisely and can be expressed as [8]:

$$G_F = \sqrt{2}\frac{g^2}{8M_W^2} = 1.16637(1) \cdot 10^{-5}\,\mathrm{GeV}^{-2}, \tag{1.13}$$

the vacuum expectation value can be calculated as:

$$v = \frac{1}{\sqrt[4]{2} \cdot \sqrt{G_F}} \approx 246\,\mathrm{GeV}. \tag{1.14}$$

Additionally to the vital task of giving masses to the gauge bosons, the Higgs mechanism allows to add mass terms for all fermions. They are given by the Yukawa coupling terms in the Lagrangian such that the masses are depending on the Higgs VEV v and the coupling constants λ_i, which are free parameters of the Standard Model:

$$m_f = \lambda_f \frac{v}{\sqrt{2}}. \tag{1.15}$$

The quadratic potential energy in the Lagrangian is the Higgs mass term. The quantum of the Higgs field is a bosonic scalar particle with mass:

$$m_H = \sqrt{-2\mu^2} = \sqrt{2\lambda v^2}. \tag{1.16}$$

The VEV v has been measured indirectly and calculated above. But both μ and the coupling λ have not been measured so far, such that the Higgs mass has not been determined and the Higgs particle has not been discovered yet. This is the last missing part(icle) of the Standard Model of elementary particle physics.

The Higgs mass can be constrained indirectly by exploiting the electroweak precision data. The *GFitter* [26, 27] program uses several observables measured in different experiments as input parameters (e.g the top quark mass, the W-boson mass and width, etc.) and performs an electroweak fit. The $\Delta\chi^2$ of the fit is determined as a function of the Higgs mass. The best fit value (the minimum of $\Delta\chi^2$) can be interpreted as predicted the Higgs mass. *GFitter* [27] is predicting the Higgs boson mass to be $96^{+31}_{-24}\,\mathrm{GeV}$ and $120^{+12}_{-5}\,\mathrm{GeV}$ when not including and including the direct Higgs searches from LEP, TeVatron and the LHC (2010 Higgs search results), respectively. Figure 1.2 shows the $\Delta\chi^2$ function of the M_H fit for the predictions without and with included direct searches.

In addition to the indirect predictions, several particle experiments are working on direct searches for the Higgs boson at three different particle colliders. The first results of direct Higgs searches are the combined results of the LEP experiments [28], which

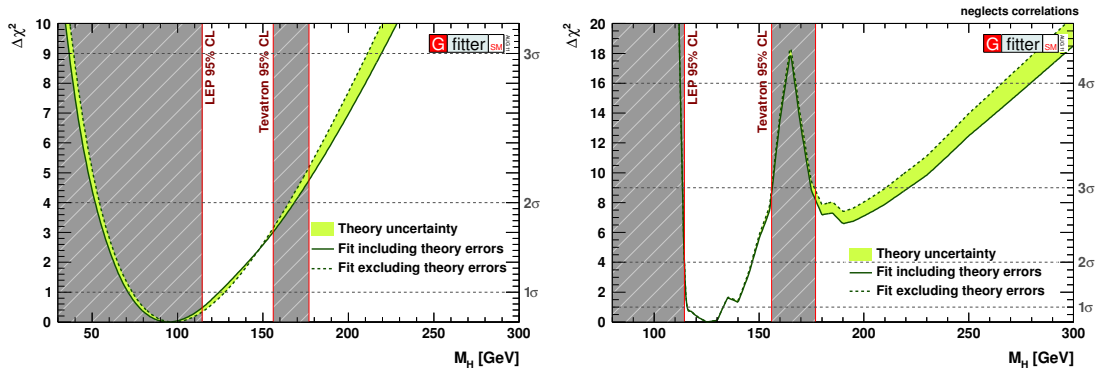

(a) (b)

Figure 1.2: Indirect determination of the Higgs boson mass: $\Delta\chi^2$ as a function of M_H for the *standard fit*(a) without considering direct Higgs search results and the *complete fit*(b) taking into account the direct Higgs searches results from LEP, TeVatrom and LHC 2010 data. The solid (dashed) lines give the results when including (ignoring) theoretical errors [27].

were shut down in November 2000 and replaced by the LHC. LEP was an electron-positron collider operating finally at centre-of-mass energies between 189 and 209 GeV. These searches could establish a lower bound of the Higgs mass. TeVatron is a proton-anti-proton collider operating at centre of mass energy $\sqrt{s} = 1.96\,\text{TeV}$. The integrated luminosity, which has been analysed for the limits quoted below is $L = 8.2\,\text{fb}^{-1}$. Since 2009 LHC has tarted its operation at $\sqrt{s} = 7\,\text{TeV}$, the analysed ATLAS data set used for the limit settings below correspond to an integrated luminosity per decay channel ranging from $1.0 - 4.9\,\text{fb}^{-1}$ of pp collisions.

- **LEP** A lower bound the mass of the Standard Model Higgs boson at 114.4 GeV is established first by the combined LEP results [28], at a 95% confidence level (C.L.).
- **TeVatron** The SM Higgs boson is excluded at 95% C.L., at mass between $100 < m_H < 108\,\text{GeV}$ and between $156 < m_H < 177]GeV$ [29] (cf. Fig. 1.3(a)).
- **LHC** The SM Higgs boson is excluded at 95% C.L. or higher in the mass range $112.7 - 115.5\,\text{GeV}$, $131 - 237\,\text{GeV}$ and $251 - 468\,\text{GeV}$ (cf. Fig. 1.3(b)). An excess of events is observed for Higgs boson mass hypothesis close to $m_H = 126\,\text{GeV}$ [30].

The direct searches at the LEP and the latest results from the ATLAS experiment narrow the low Higgs mass region lying in a range between $115.45 - 131\,\text{GeV}$.

1.1.2 The Standard Model Status and Open Issues

The Standard Model of the elementary particle physics introduced above is describing the interactions of fermions, leptons (ν_e, e, ν_μ, μ, ν_τ, and τ) and quarks (u, d, c, s, t, and b) via gauge bosons (γ, $W^\pm$, Z^0 and g). The underlying theory is a quantum field theory combining the electroweak theory and the quantum chromodynamics. It is mathematically described by a $SU(3)_C \times SU(2)_L \times U(1)$ symmetry group. The particle masses are generated by the scalar Higgs field. The Higgs boson is the only missing particle predicted by the SM which has not yet been discovered. However, its mass has

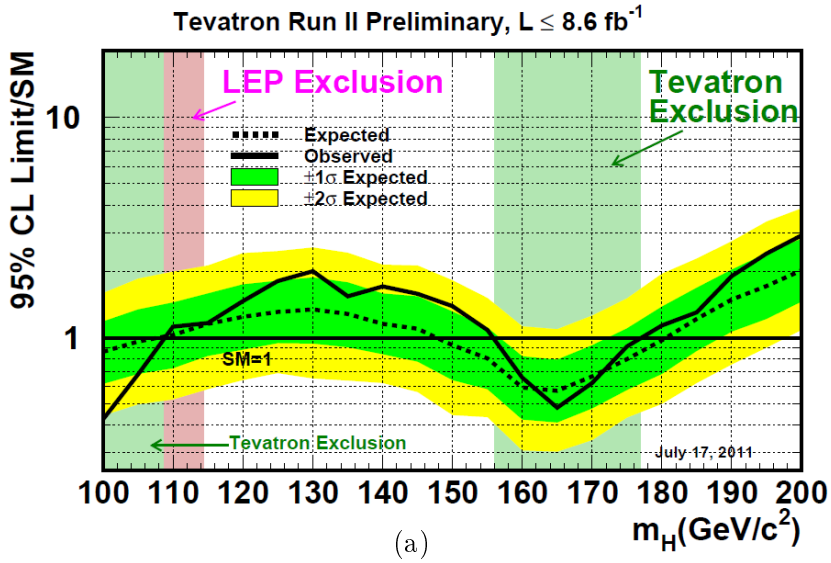

(a)

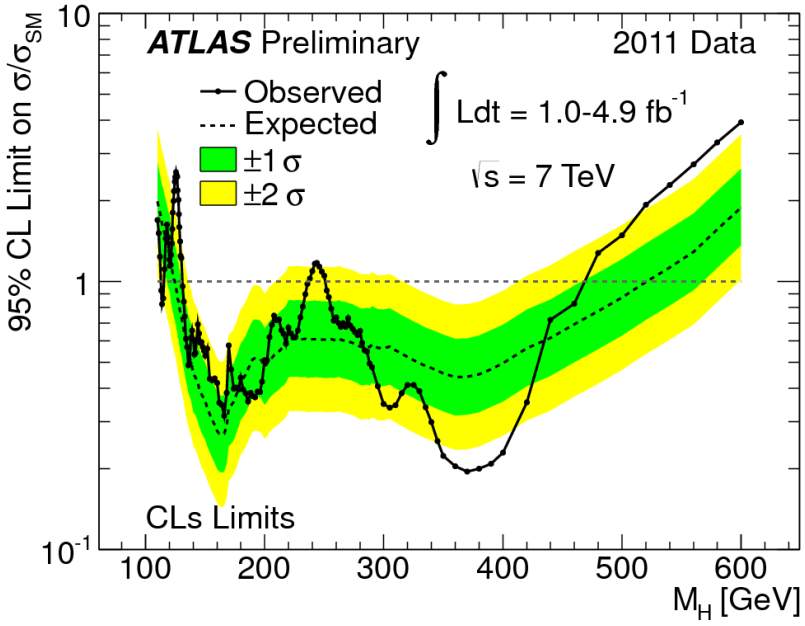

(b)

Figure 1.3: Observed and expected (median, for the background-only hypothesis) 95% C.L. upper limits on the ratios to the SM cross section, as functions of the Higgs boson mass for the combined CDF and D0 analyses The bands indicate the 68% and 95% probability regions where the limits can fluctuate, in the absence of signal [29] (a).
The ATLAS combined upper limit on the Standard Model Higgs boson production cross section divided by the Standard Model expectation as a function of m_H is indicated by the solid line. This is a 95% C.L. limit using the CL_s method in the entire mass range. The dotted line shows the median expected limit in the absence of a signal and the green and yellow bands reflect the corresponding 68% and 95% expected regions [30].

been constrained indirectly by high precision measurement fits and directly by the Higgs boson searches at LEP, TeVatron, and LHC.

The theory is renormalisable, which means that finite results are obtained for all higher-order corrections. The theory is well-defined and calculable. Remarkable predictions with high precision have been made and perfect agreement with measurements has been found. Although the SM has been tested and verified in several experiments with high precision, there are some open issues, which cannot be explained or incorporated by the existing SM. Before introducing a possible extension of the SM some theoretical shortcomings and phenomena that cannot be described by the SM are discussed in the following.

Many Free Parameters

Many free parameters, which have to be determined by experiments and added to the theory raise the question if there is a more fundamental theory, which describes the measured quantities without adjusting almost 20 free parameters. The free parameters of the SM are the three gauge couplings (e, g, g'), the nine coupling constants of the heavy fermions to the Higgs field (λ_i), two additional couplings from the Higgs sector (the Higgs quadratic coupling, and the self-coupling strength) and four free parameters of the CKM matrix (three mixing angles and one complex phase) [31].

The Hierarchy Problem

The Higgs mechanism introduced above causes new problems. Namely, the Higgs mass m_H^2 receives enormous quantum corrections from virtual effects of every particle which is coupling directly or indirectly to the Higgs field [32]. For example, a fermion (f) coupling to the Higgs field (cf. Fig. 1.4 a)) yields a correction to the Higgs mass:

$$\Delta m_H^2 = -\frac{|\lambda_f|^2}{8\pi^2}\Lambda_{UV}^2 + ... \tag{1.17}$$

with the ultraviolet momentum cutoff (Λ_{UV}), which is needed to regulate the loop integral. It can be interpreted as the energy scale where new physics enters and changes the behaviour of the theory at high energies. Assuming that Λ_{UV} is of the order of the Planck scale ($O(M_P) \sim 10^{18}\,\mathrm{GeV}$), the energy scale where quantum gravitational effects become important and thus the theory has to be adopted in order to describe those effects as well the resulting quantum corrections to m_H^2 from Λ_{UV} is some 30 orders of magnitude larger than the predicted Higgs mass ($O(m_H^2) \sim (100\,\mathrm{GeV})^2$). This problem is known as the *hierarchy problem*.

A possible solution for the hierarchy problem could be the existence of a heavy complex scalar particle S (cf. Fig. 1.4 b)) with mass m_S, which is coupling to the Higgs field with a Lagrangian term $-\lambda_s|H|^2|S|^2$. This yields a correction to the Higgs mass:

$$\Delta m_H^2 = \frac{|\lambda_S|^2}{12\pi^2}\left[\Lambda_{UV}^2 - 2m_S^2\ln(\Lambda_{UV}/m_S) + ...\right] \tag{1.18}$$

which cancel the fermion contribution due to the negative sign. The contributions from Λ_{UV} cancel completely, if each lepton and quark is accompanied by two complex scalars of the same mass with $\lambda_S = |\lambda_f|^2$. Supersymmetric models, which assume that there exists a symmetry relating fermions to bosons, introduce the needed heavy scalar particles by construction, such that each quantum loop correction of a SM fermion is cancelled due to the supersymmetric partner boson.

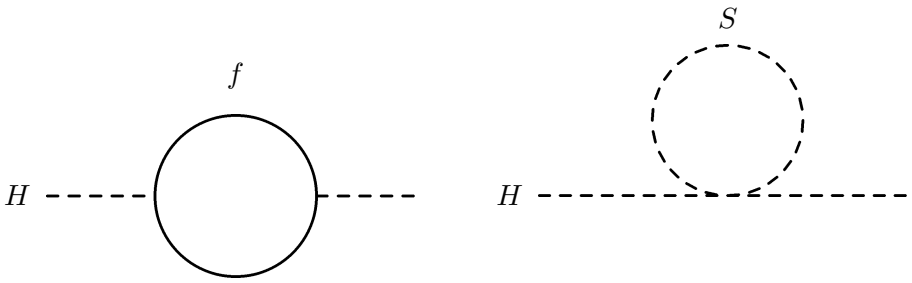

Figure 1.4: One-loop quantum corrections to the Higgs squared mass parameter m_H^2, due to (a) a Dirac fermion f, and (b) a scalar S [32].

Dark Matter and Dark Energy

Astrophysical measurements [33] are in good agreement with the cosmological model, which predicts a flat universe composed of 4.4% baryons, 22% dark matter and 73% dark energy. The SM of elementary particle physics can only describe the baryonic fraction of the universe. Dark matter does not interact electromagnetically, but gravitationally such that the existance of dark matter can be observed indirectly, by its gravitational effects in the universe. Dark energy is a theoretical concept, which has been introduced to the cosmological model, in order to explain the accelerated expansion of the universe.

By considering R-parity (cf. Sec 1.2.2) conserving supersymmetry as an extension of the SM, additional SUSY particles are introduced. The lightest-supersymmetric particle (LSP) is neutral, only weakly interacting and not decaying into SM particles. Therefore it is a good candidate for dark matter.

Matter - Anti-matter Asymmetry

The observed predominance of matter over anti-matter [34] in the universe cannot be explained by the SM. This asymmetry can be expressed by the baryon-to-photon ratio β. Two independent observations, the Big Bang Nucleosynthesis (BBN) [8] and the Cosmic Microwave Background Radiation (CMBR) [35] are in good agreement with [36]:

$$\beta = \frac{n_B - n_{\bar{B}}}{n_\gamma} \approx 6 \cdot 10^{-10}, \tag{1.19}$$

where $n_B \gg n_{\bar{B}}$, whereas the freeze-out abundances in a homogeneous baryon-symmetric universe would be $n_B/n_\gamma = n_{\bar{B}}/n_\gamma \sim 10^{-18}$ [34]. Even though the complex phase of the CKM matrix is a source of CP-violation in SM physics, it is by far not big enough, to explain a baryon-to-photon ratio neither of order $O(10^{-10})$ nor $O(10^{-18})$ as found in different astrophysical experiments.

Unification

The symmetry group of the SM has been discussed above as well as the necessity of fixing the values of many free parameters according to experimental results. Grand Unified Theories (GUT)s have been designed which should supersede the $SU(3)_C \times SU(2)_L \times U(1)$ symmetry group by symmetries like $SU(N)$ or $SO(N)$ and thereby reducing the number of coupling constants to on single gauge coupling.

The simplest group into which $SU(3)_C \times SU(2)_L \times U(1)_Y$ can be embedded, is the $SU(5)$ symmetry group. Comparable to the electroweak symmetry breaking, there should

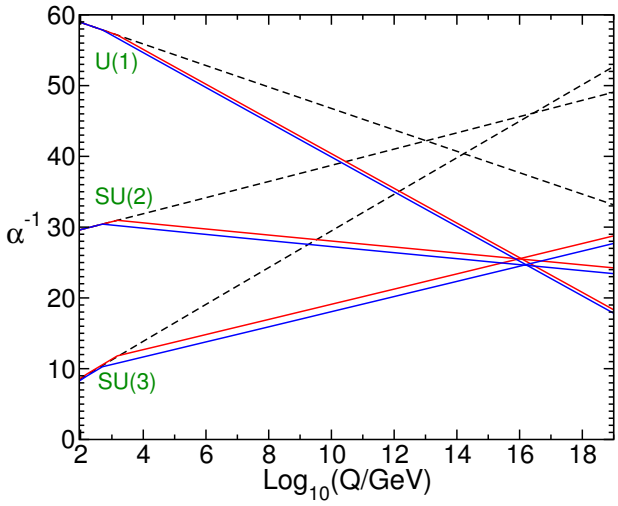

Figure 1.5: Two-loop renormalization group evolution of the inverse gauge couplings $\alpha_a^{-1}(Q)$ in the Standard Model (dashed lines) and the MSSM (solid lines). In the MSSM case, the sparticle masses are treated as a common threshold varied between 500 GeV and 1.500 TeV, and $\alpha_3(m_Z)$ is varied between 0.117 and 0.121 [32].

exist a energy scale M, at which the $SU(5)$ symmetry is broken. Below this energy scale, the different couplings as described in the SM are valid, above all couplings can be replaced by the $SU(5)$ gauge coupling. Therefore the gauge couplings have to be unified at a certain energy scale. Figure 1.5 shows the inverse running coupling constants of the SM model (dashed black lines). The coupling constants cross, but they fail to cross all together at the same energy scale.

This problem can be solved by assuming a (minimal) supersymmetric extension of the standard model (MSSM) which govern the running of the gauge couplings around 1TeV [32].

Gravity

The Standard Model of elementary particle physics does not include a theory of gravity. The natural phenomena of gravitation is described in Newton's theory of gravitation, but not included into the SM. In order to formulate a fundamental theory which considers all known particles and interactions it is absolutely necessary to include gravity into the model.

Since some of the shortcomings of the SM can be covered by supersymmetry, it is a very attractive extension to the SM. The following section will give a brief introduction to supersymmetry and discuss in more detail some constrained models which are considered in the SUSY search in this thesis.

1.2 Supersymmetry

1.2.1 Supersymmetry in a Nutshell

The basic concept of supersymmetric models [37] is the assumption, that there exists a symmetry relating fermions to bosons. Therefore, a transformation is needed which turns a bosonic state into a fermionic state and vice versa:

$$Q|\text{fermion}\rangle = |\text{boson}\rangle, \quad Q|\text{boson}\rangle = |\text{fermion}\rangle. \tag{1.20}$$

The fermions and bosons, which can be transferred into each other by the generator Q, are called *superpartners*. The single-particle states of supersymmetric models can be arranged in multiplets as in the electroweak theory. The presentation of the supersymmetric multiplets are call supermultiplets. Each supermultiplet contains fermion and boson states of both superpartners. According to the supersymmetry algebra, the particles in one supermultiplet have to have the same mass, the same electric charge, weak isospin and colour degrees of freedom. In addition, the number of fermion and boson degrees of freedom within one supermultiplet has to be equal:

$$n_F = n_B. \tag{1.21}$$

This can be achieved by combining a single Weyl fermion (with two helicity states, $n_F = 2$) with two real scalars (each with $n_B = 1$) within one supermultiplet. Gravity can be included by combining the spin-2 graviton (two helicity states, $n_B = 2$) with a spin-3/2 superpartner, called gravitino, which would be massless in case of unbroken supersymmetry and therefore having two helicity states ($n_F = 2$).

If SUSY has an exact symmetry, the additional SUSY particles would have been discovered by now. Due to the fact that there is no evidence of supersymmetric particles with the same masses as the SM particles, SUSY has to be broken. The complete cancellation of the quantum loop corrections to the Higgs mass only works, if the SUSY particles and the SM particles have exactly the same mass. By considering a *soft* symmetry breaking, the effective Lagrangian can by written as:

$$\mathcal{L} = \mathcal{L}_{SUSY} + \mathcal{L}_{soft} \tag{1.22}$$

with $\mathcal{L}_{SUSY}$ containing all gauge and Yukawa couplings and preserving supersymmetry invariance and $\mathcal{L}_{soft}$ violating supersymmetry, but containing only terms with positive mass dimension. In order to break SUSY, inducing the mass splitting between SM and SUSY partners, but preserving the cancellation of the quantum loop correction, the superpartner masses cannot be too huge. Typical masses for the few lightest superpartners of about 1 TeV are expected.

The content of the supermultiplet in the Minimal Supersymmetric Standard Model (MSSM), its mass eigenstates, the concept of R-parity and different SUSY breaking mechanisms are discussed in the following.

1.2.2 The MSSM

The first step is to determine how the known particles fit into the supermultiplets and which undiscovered particles are predicted by the model. If the left-handed part transforms differently under the gauge group than the right-handed, as it is the case for all

Standard Model fermions (quarks and leptons), they have to be arranged in chiral supermultiplets. The superpartners of the quarks and leptons are called *squarks* and *sleptons* ('scalar' quarks and 'scalar' leptons), respectively. The left-handed and the right-handed component of the fermions have different gauge transformations, thus each has to have a separate superpartner. For example, the left- and right-handed electron is transformed into a left and right-handed selectron, denoted as $\tilde{e}_L$ and $\tilde{e}_R$. The handedness denoted L and R of the $\tilde{e}$, does not indicated the helicity of the selectron, but the one of its superpartner. There is no specific handedness denoted for sneutrinos, because their superpartners, the neutrino, are always left-handed. The complete list of the superpartners of the SM particles and their arrangement in supermultiplets can be found in Tab. 1.2. The gauge interactions of the sparticles are identical to the corresponding SM particles, for example only the left-handed sparticles couple to the W-boson, the right-handed do not.

The Higgs scalar boson has to be resided into two Higgs supermultiplets to avoid that the electroweak gauge symmetry suffers a gauge anomaly. The structure of the supersymmetric theory implies, that only a $Y = 1/2$ (Y is the electroweak hypercharge) Higgs chiral supermultiplet can have the Yukawa couplings needed for giving the masses to up-type quarks and only a $Y = -1/2$ Higgs chiral supermultiplet can have the Yukawa couplings needed for giving the masses to down-type quarks and to charged leptons. The corresponding $SU(2)_L$-doublet complex scalar fields are called H_u and H_d, respectively. The weak isospin components of H_u have electric charge +1, 0 and the components of H_d 0 and -1 (cf. Tab. 1.2). By introducing two Higgs doublets, both the VEV of H_u^0 and the VEV of H_d^0 have to be consistent with the observed phenomenology of the electroweak symmetry breaking. The VEVs can be written as:

$$v_u = \langle H_u^0 \rangle, \qquad v_d = \langle H_d^0 \rangle. \tag{1.23}$$

The ratio of the VEVs is written as:

$$\tan\beta \equiv v_u/v_d, \tag{1.24}$$

which is not fixed by the present experimental results, but it can be constrained by additional assumptions of the MSSM masses. Several constrained MSSM models do not fix the ratio of the vacuum expectation values $\tan\beta$ to a given value, but determine scenarios as function of $\tan\beta$ (cf. Sec. 1.2.3 and Sec. 1.2.3).

Assuming that non of the MSSM sparicles is heavier than of order of 1 TeV and all couplings of the theory remain perturbative up to the unification scale the upper bound of the lightest neutral MSSM Higgs boson must be:

$$m_{h^0} < 135\,\text{GeV}. \tag{1.25}$$

The superpartners of the SM gauge bosons are arranged in gauge supermultiplets given in Tab. 1.3. The superpartners of the spin-1 gauge bosons (W^+, W^0, W^- and B^0) are spin-1/2 superpartners ($\tilde{W}^+$, $\tilde{W}^0$, $\tilde{W}^-$and $\tilde{B}^0$). The chiral and the gauge supermultiplets listed in Tab. 1.2 and Tab. 1.3 are the particle content of the MSSM.

Another important feature of the MSSM is the fact, that the superpartners listed in Tab. 1.2 and Tab. 1.3 are not necessarily the mass eigenstates of the theory. Considering effects of the electroweak and the supersymmetry breaking, there can be mixing of the electroweak gauginos and the higgsinos, within squarks, and within sleptons.

Table 1.2: Chiral supermultiplets in the Minimal Supersymmetric Standard Model. The spin-0 fields are complex scalars, and the spin-1/2 fields are left-handed two-component Weyl fermions [32].

Names		spin 0	spin 1/2	$SU(3)_C, SU(2)_L, U(1)_Y$
squarks, quarks	Q	$(\tilde{u}_L, \tilde{d}_L)$	(u_L, d_L)	$(3, 2, \frac{1}{6})$
($\times$ 3 families)	$\bar{u}$	$\tilde{u}_R^*$	$\tilde{u}_R^\dagger$	$(\bar{3}, 1, -\frac{2}{3})$
	$\bar{d}$	$\tilde{d}_L^*$	$\tilde{d}_R^\dagger$	$(\bar{3}, 1, \frac{1}{3})$
sleptons, leptons	L	$(\tilde{\nu}_e, \tilde{e}_L)$	$(\nu, \bar{e}_L)$	$(1, 2, -\frac{1}{2})$
($\times$ 3 families)	$\bar{e}$	$\tilde{e}_L^*$	$\tilde{e}_R^\dagger$	$(1, 1, 1)$
Higgs, Higgsinos	H_u	(H_u^+, H_u^0)	$(\tilde{H}_u^+, \tilde{H}_u^0)$	$(1, 2, +\frac{1}{2})$
	H_d	(H_d^0, H_d^-)	$(\tilde{H}_d^0, \tilde{H}_d^-)$	$(1, 2, -\frac{1}{2})$

Table 1.3: Gauge supermultiplets in the Minimal Supersymmetric Standard Model [32].

Names	spin 1/2	spin 1	$SU(3)_C, SU(2)_L, U(1)_Y$
gluinos, gluons	$\tilde{g}$	g	$(8, 1, 0)$
winos, W bosons	$\tilde{W}^{(1,2,3)}$	$W^{(1,2,3)}$	$(1, 3, 0)$
bino, B boson	$\tilde{B}$	B	$(1, 1, 0)$

R-Parity

The most general gauge-invariant renormalizable superpotential include terms which violate either the baryon number (B) or the lepton number (L). In case of the SM, there does not exist a renormalizable term in the Lagrangian, which would violate B or L. If the additional B and L violating terms were present and unsuppressed, the lifetime of the proton would be extremely short. The experimentally measured proton life time is $> 10^{31}$ to 10^{33} years[1] [8]. Since there have not been observed any B- and L- violating processes in nature so far, another mechanism should be introduced to get rid of those terms. A new symmetry, the so-called *R-parity*, is added to the MSSM for the elimination of B and L violating terms. The *R-parity* is defined for each particle as:

$$P_R = (-1)^{3B+L+2s} \tag{1.26}$$

with the baryon number B, the lepton number L and the spin s. It is defined as a multiplicatively conserved quantum number. The definition of P_R gives even *R-parity* values to Standard Model particles and the Higgs bosons ($P_R = +1$) and odd *R-parity* values to gauginos, higgsinos, squarks and sleptons ($P_R = -1$). Thus the SM particles differ from the SUSY particles by the *R-parity*. With an exact *R-parity* conservation no mixing between SM and SUSY particles is allowed and only even numbers of sparticles with $P_R = -1$ are allowed to interact at one vertex. The second requirement leads to very important phenomenological consequences:

- The lightest supersymmetric particle (LSP) with $P_R = -1$ must be stable. Since the LSP is expected to interact only weakly with ordinary matter, it is a good candidate for dark matter, and it cannot be detected directly by particle experiments,

[1] The first limit is for $p \to$ anything or disappearance modes of a bound proton. The second entry, a rough range of limits combined in [8].

such that the only LSP signature is missing transverse energy.

- Every other sparticle with $P_R = -1$ must decay into another sparticle with $P_R = -1$ until the LSP is produced. Usually a SM particle is produced at each decay vertex, such that in case of long decay chains, many SM particles are expected to be measured in SUSY events.
- Sparticles can be produced in collider experiments only in pairs. Following the decay rules above, exactly two LSPs are expected to escape the detector.

In the following the conservation of *R-parity* is assumed.

Mass-Eigenstates

The MSSM superpotential is:

$$W_{MSSM} = \bar{u}\mathbf{y_u}QH_u - \bar{d}\mathbf{y_d}QH_d - \bar{e}\mathbf{y_e}LH_d + \mu H_u H_d \tag{1.27}$$

with the chiral supermultiplets from Tab. 1.2. The Yukawa coupling parameters ($mathbfy_u$, $mathbfy_d$, and $mathbfy_e$) are 3 × 3 matrices in family space. Both Higgs supermultiplets (H_u and H_d) are needed to generate the masses of all MSSM particles. After the neutral scalars (H_u and H_d) got VEVs, the current masses and the CKM mixing of the ordinary quarks and leptons are determined by the Yukawa couplings. The big mass differences of the third family leptons and quarks in comparison to the first and the second family, allow the approximation, that only the (3, 3) family component of each Yukawa matrix is important:

$$\mathbf{y_u} \approx \begin{pmatrix} 0 & 0 & 0 \\ 0 & 0 & 0 \\ 0 & 0 & y_t \end{pmatrix}, \quad \mathbf{y_d} \approx \begin{pmatrix} 0 & 0 & 0 \\ 0 & 0 & 0 \\ 0 & 0 & y_b \end{pmatrix}, \mathbf{y_e} \approx \begin{pmatrix} 0 & 0 & 0 \\ 0 & 0 & 0 \\ 0 & 0 & y_\tau \end{pmatrix}. \tag{1.28}$$

Any scalar with same electric charge, colour, and R-parity can mix. The mass eigenstates can be calculated by diagonalizing the three 6 × 6 squark ($\tilde{u}_L$, $\tilde{c}_L$, $\tilde{t}_L$, $\tilde{u}_R$, $\tilde{c}_R$, $\tilde{t}_R$), ($\tilde{d}_L$, $\tilde{s}_L$, $\tilde{b}_L$, $\tilde{d}_R$, $\tilde{s}_R$, $\tilde{b}_R$), the slepton ($\tilde{e}_L$, $\tilde{\mu}_L$, $\tilde{\tau}_L$, $\tilde{e}_R$, $\tilde{\mu}_R$, $\tilde{\tau}_R$) and the 3 × 3 sneutrino($\tilde{\nu_e}$, $\tilde{\nu_\mu}$, $\tilde{\nu_\tau}$) squared mass matrices. According to the renormalization group (RG) equations, only the contributions to the (3, 3) family component of each Yukawa matrix is significant and the assumptions in Eq. (1.28) are allowed. The mixing angles in the first and second family are very small such that they are degenerated unmixed pairs, like ($\tilde{e}_R$, $\tilde{\mu}_R$). The masses of the third family are rather different to those of the first families and show substantial mixing. The top squark mass eigenstates have a significant mixing of the gauge eigenstates $\tilde{t}_\mathrm{L}$ and $\tilde{t}_\mathrm{R}$, which is caused by the non-negligible off-diagonal entries of the mixing matrix. Several models predict that the $\tilde{t}_1$ is the lightest squark with a bigger $\tilde{t}_\mathrm{R}$ contribution.The off-diagonal entries of the squared mass matrices $\mathbf{m}^2_{\tilde{t}}$, $\mathbf{m}^2_{\tilde{b}}$, and $\mathbf{m}^2_{\tilde{\tau}}$ depend on the Yukawa coupling and the $\tan\beta$-value. Due to the relation y_b, $y_\tau \ll y_t$, the mixing of the stau and the bottom squarks are driven by the $\tan\beta$-value. If $\tan\beta$ is small (about less than 10) the mixing is small and the mass eigenstates are nearly the same as the gauge eigenstate. For large values of $\tan\beta$ the mixing can be quite significant. In this case the lighter stop, the lighter sbottom and the lighter stau can be significantly lighter than the first and second family squarks and sleptons.

The mass eigenstates of the neutralinos can be expressed in terms of the following parameters: bino mass term M_1, wino mass term M_2, μ, the ratio of the VEVs $\tan\beta$,the

Table 1.4: The undiscovered particles in the Minimal Supersymmetric Standard Model (with sfermion mixing for the first two families assumed to be negligible) [32].

Names	Spin	P_R	Gauge eigenstates	Mass eigenstates
Higgs bosons	0	+1	$H_u^0, H_d^0, H_u^+, H_d^-$	$h^0, H^0, A^0, H^\pm$
Squarks	0	-1	$\tilde{u}_L, \tilde{u}_R, \tilde{d}_L, \tilde{d}_R$ $\tilde{s}_L, \tilde{s}_R, \tilde{c}_L, \tilde{c}_R$ $\tilde{t}_L, \tilde{t}_R, \tilde{b}_L, \tilde{b}_R$	(same) (same) $\tilde{t}_1, \tilde{t}_2, \tilde{b}_1, \tilde{b}_2$
Sleptons	0	-1	$\tilde{e}_L, \tilde{e}_R, \tilde{\nu}_e$ $\tilde{\mu}_L, \tilde{\mu}_R, \tilde{\nu}_\mu$ $\tilde{\tau}_L, \tilde{t}_R, \tilde{\tau}_L, \tilde{\tau}_\tau$	(same) (same) $\tilde{\tau}_1, \tilde{\tau}_2, \tilde{\nu}_\tau$
Neutralinos	1/2	-1	$\tilde{B}^0, \tilde{W}^0, \tilde{H}_u^0, \tilde{H}_d^0$	$\tilde{\chi}_1^0, \tilde{\chi}_2^0, \tilde{\chi}_3^0, \tilde{\chi}_4^0$
Charginos	1/2	-1	$\tilde{W}^\pm, \tilde{H}_u^+, \tilde{H}_d^-$	$\tilde{\chi}_1^\pm, \tilde{\chi}_2^\pm$
Gluino	1/2	-1	$\tilde{g}$	(same)
Goldstino (Gravitino)	1/2 (3/2)	-1	$\tilde{G}$	(same)

Weinberg angle θ_W and Z-boson mass m_Z. Under the assumption, that the gaugino masses unify at the same mass scale as the gauge couplings ($Q = M_U = 2 \times 10^{16}\,\mathrm{GeV}$) with a unified mass $m_{1/2}$ all gaugino masses are connected by:

$$\frac{M_1}{g_1^2} = \frac{M_2}{g_2^2} = \frac{M_3}{g_3^2} = \frac{m_{1/2}}{g_U^2} \tag{1.29}$$

with the unified coupling constant g_U^2. If a given model satisfies Eq. (1.29), the bino and wino mass terms are constrained as:

$$M_1 \approx \frac{5}{3} \tan^2 \theta_W M_2 \approx 0.5 M_2 \tag{1.30}$$

at the electroweak scale and the neutralino masses and mixing angles depend only on three unknown parameters. If the model is constrained further by the relation $m_Z \ll |\mu \pm M_1|, |\mu \pm M_2|$ the neutralino eigenstates yield a *bino-like* $\tilde{\chi}_1^\pm$, a *wino-like* $\tilde{\chi}_2^\pm$, and a *higgsino-like* $\tilde{\chi}_3^0$, $\tilde{\chi}_4^0$.

The chargino mass eigenstates can be expressed by M_2, μ, $\tan\beta$, and m_W. $\tilde{\chi}_1^\pm$is nearly degenerated in mass with $\tilde{\chi}_1^0$, whereas $\tilde{\chi}_2^\pm$ and $\tilde{\chi}_3^0$ and $\tilde{\chi}_4^0$ have masses of order $|\mu|$.

Finally, the gluino cannot mix with any other particle in the MSSM spectrum. If Eq. (1.29) is satisfied by the given model, the gluino mass parameter M_3 is connected to the bino and wino mass parameters by:

$$M_3 = \frac{\alpha_s}{\alpha} \sin\theta_W M_2 = \frac{3\alpha_s}{5\alpha} \cos^2\theta_W M_1 \tag{1.31}$$

This leads to the following rough estimate at the TeV scale:

$$M_3 : M_2 : M_1 \approx 6 : 2 : 1. \tag{1.32}$$

A summary of all MSSM sparticles, with the spin, R-parity, gauge- and mass eigenstates is given in Tab. 1.4. In conclusion, the MSSM extension to the SM of particle physics introduces 32 masses corresponding to undiscovered new particles. In order to

make any specific estimates for particle physics experiments additional boundaries have to be considered. Two possible supersymmetry breaking models are discussed in the following. In case of minimal supergravity models, the number of free parameters can be reduced to five, in case of gauge mediated supersymmetry breaking to six unknown values. The remaining free parameters have to be fixed, such that the SUSY masses and branching ratios can be calculated and expected detector signatures can be simulated.

1.2.3 SUSY Breaking

As mentioned above, there must be a supersymmetry breaking mechanism, otherwise SUSY particles would have the same masses as the SM particles and they would have been discovered already. The full Lagrangian density for a renormalizable supersymmetric theory contains auxiliary fields which can be purely expressed as scalar fields. Two types of terms are distinguished, the so-called *D-terms* and the *F-terms*. The *D-terms* are fixed by gauge-couplings, the *F-terms* by Yukawa couplings and fermion mass terms. If the vacuum expectation value of the *D-term* or the *F-term* auxiliary field does not vanish, symmetry would be broken spontaneously.

SUSY breaking with non-zero *D-terms* VEV is described in the so-called Fayet-Iliopoulos mechanism [38]. However, a *D-term* VEV for $U(1)_Y$ would not lead to an acceptable spectrum. The *F-term* symmetry breaking is described in the O'Raifeartaigh models [39]. The MSSM does not have a gauge singlet candidate, which would develop a *F-term* VEV. Thus, spontaneous symmetry breaking requires the extension of the MSSM, because the supersymmetry parameters cannot belong to any of the MSSM supermultiplets.

Adding new supermultiplets including gauge singlets would not induce the needed masses to the sparticles only with renormalizable interactions at tree-level. There are no scalar-gaugino-gaugino couplings that would allow to give masses to the gauginos. In addition some of the squark and sleptons would be too light. Therefore, the MSSM soft breaking terms must arise indirectly or radiative. The breaking must happen in a hidden sector of particles, which does not have direct couplings to the visible sector chiral supermultiplets of the MSSM. The two sectors have to share some interactions, which mediate the symmetry breaking from the hidden sector to the MSSM (visible) sector. Amongst others, there are two proposals for the mediation of the interactions. The first is the *gravitational mediation*. Supersymmetry is broken in a hidden sector by a VEV $\langle F \rangle$. A rough estimate following a dimensional analysis gives:

$$m_{soft} \sim \langle F \rangle / M_P. \tag{1.33}$$

The second proposal is that the flavour blind mediation interactions are the ordinary electroweak and QCD gauge interactions. This approach is called *gauge-mediated-supersymmetry* breaking. The MSSM soft terms come from loop diagrams of so-called *messenger* particles. The messenger particles couple to a supersymmetry breaking VEV $\langle F \rangle$, and have electroweak and QCD gauge interactions. Thus they provide the necessary connection between the hidden sector and the MSSM. The messengers build N_5 additional chiral supermultiplet. The MSSM soft breaking mass term can be estimates as:

$$m_{soft} \sim \frac{\alpha_a}{4\pi} \frac{\langle F \rangle}{M_{mes}}. \tag{1.34}$$

However, both breaking scenarios require the existence of a massless Weyl fermion, the golstino whose auxiliary field obtains a VEV. This fermion is called goldstino. By considering the conservation of the supercurrent an effective Lagrangian containing goldstino-scalar-chiral fermion and goldstino-gaugino-gauge boson vertices can be imposed.

So far, gravity was not considered by the SM and the MSSM, respectively. If gravity is taken into account, which is known as supergravity [40–42], the spin-2 graviton gets a superpartner with spin-3/2 called gravitino. Analogously to the Higgs mechanism, a *super-Higgs mechanism* can be formulated:

Both the graviton and the gravitino are massless, each with two spin helicity states, as long as SUSY is not broken. After spontaneous supersymmetry breaking the gravitino acquires mass by absorbing the goldstino (inducing longitudinal helicity states). The gravitino mass $m_{3/2}$ can be estimated for *F-term* symmetry breaking models from its VEV (cf. Eq (1.33) and Eq (1.34)). The different prediction of $\langle F \rangle$ for gravity-mediated and gauge-mediated supersymmetry breaking models lead to very different predictions of the gravitino mass.

In case of gravity-mediated SUSY breaking models the gravitino mass is comparable to the MSSM sparticle masses and its interactions will be of gravitational strength. Thus it would not play an important role in collider physics [32].

In case of gauge-mediated SUSY breaking models the gravitino is much lighter (cf. Eq. (1.34) and Eq. (1.33)) than the MSSM sparticles if $M_{mes} \ll M_P$ (more phenomenological properties of GMSB are discussed in Sec. 1.2.3).

Minimal Supergravity - MSUGRA

In the gravitationally mediated SUSY models the sector where supersymmetry is broken spontaneously is connected to the MSSM sector through gravitational interactions only [43]. Assuming a soft breaking at $m_{soft} \sim$ a few hundred GeV, in order to solve the hierarchy problem the VEV has to be set to $\sqrt{\langle F \rangle} \sim 10^{10} - 10^{11}\,\mathrm{GeV}$. The SUSY model has still many free parameters. This can be simplified, by assuming a minimal form of normalization of kinetic terms and gauge interactions in the full non-renormalizable supergravity Lagrangian. This simplification reduces the three couplings of the gauginos to a common coupling constant f, whereas k can be introduced as a coupling constant for all scalars. The other couplings are all proportional to the superpotential parameters. All parameters of the soft breaking Lagrangian can be expressed by only five free parameters:

the common gaugino mass at the unification scale $m_{1/2}$, the common scalar mass at the unification scale m_0, the common trilinear scalar coupling A_0, the ratio of the vacuum expectation value of the Higgs field $\tan\beta$ and the sign of the Higgsino mass term $sgn(\mu)$.

Models which are based on the assumption described above are the so-called *minimal supergravity* (MSUGRA) models or constrained MSSM (CMSSM). After this simplification, the model is highly predictive, because the entire MSSM spectrum can be determined based on only five parameters: $m_{1/2}$, m_0, A_0, $\tan\beta$, and $sgn(\mu)$ by the RG evolution of the soft parameters down to the electroweak scale.

Figure 1.6 shows an example of the expectation of the running of scalar and gaugino masses in a typical model based on the MSUGRA boundary conditions imposed at $Q = 2 \times 10^{16}\,\mathrm{GeV}$. By fixing the five free MSUGRA parameters to $m_0 = 200\,\mathrm{GeV}$, $m_{1/2} = -A_0 = 600\,\mathrm{GeV}$, $\tan\beta = 10$ and $sgn(\mu) = +$ the evolution of the bino, wino and gluino mass parameters (M_1, M_2, and M_3), the running values of the quantities $(\mu^2 + m_{H_u}^2)^{1/2}$ and $(\mu^2 + m_{H_d}^2)^{1/2}$, and the running squark and slepton masses are plotted over Q.

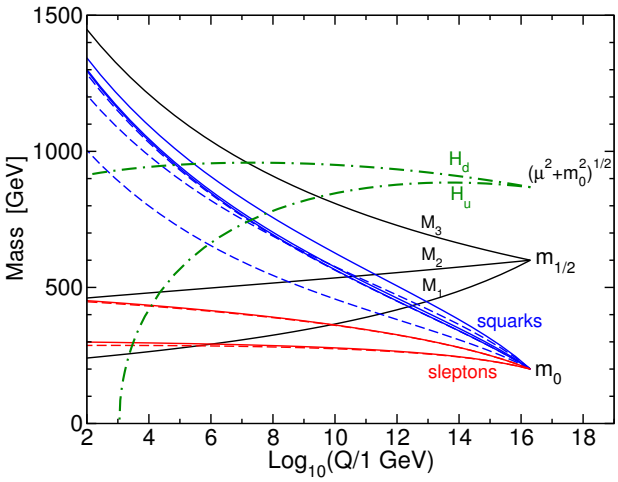

Figure 1.6: RG evolution of scalar and gaugino mass parameters in the MSSM with MSUGRA boundary conditions imposed at $Q_0 = 2 \times 10^{16}\,\text{GeV}$. The parameter $\mu^2 + m_{Hu}^2$ runs negative, provoking electroweak symmetry breaking. [32].

Phenomenological Models

The phenomenological models [44] studied in this analysis are *supergravity-inspired* in case of couplings, particle content and R-parity conservation. As the final states of SUSY decays are predominantly driven by the sparticle masses, the phenomenological models are constructed in a way that the free parameters are squark, slepton, and gaugino masses and no longer the SUSY parameters at the unification scale.

The squark mass parameters are set identically for the two first generations to $m_{\tilde{q}}$ while the third generation is set to a high mass (3 TeV). The neutralino-chargino sector is constrained by the relation $M_1 < M_2 < \mu$ such that the masses of the lightest neutralino ($\tilde{\chi}_1^0$), the next-to-lightest neutralino ($\tilde{\chi}_2^0$), and the sleptons ($\tilde{\ell}$) are defined by the squark and gluino masses and the equations Eq. (1.35) or Eq. (1.38) only.

The SUSY parameters of the phenomenological models are tuned, such that the $\tilde{\chi}_1^0$ is a bino and the $\tilde{\chi}_2^0$ and $\tilde{\chi}_1^\pm$ have pure wino eigenstates. The heavier neutralinos and charginos have Higgsino-like eigenstates. They are not relevant for the phenomenology of this specific model, because they would be produced dominantly by third squark generation decays, but the production of the third squark generation is suppressed by choosing a mass at 3 TeV. The slepton mass of the first and second generation is defined as $(m_{\tilde{\chi}_2^0} - m_{\tilde{\chi}_1^0})/2$.

The phenomenology is studied in two different hyperplanes of the SUSY parameter space (Grid). In the first one, the light neutralino mass is defined as the minimum of the squark and gluino mass minus 150 GeV. This yields a compressed spectrum, because the masses of the sparticles are close to each other (cf. Eq. (1.35)). This phenomenological grip is called *compressed spectrum* (*PG CS*). The event topology expected for this grid is leptons with small transverse momentum and modest missing transverse energy.

The second grid fixes the $\tilde{\chi}_1^0$ mass to 100 GeV. As the other sparticle masses depend on the squark and gluino masses only (cf. Eq. (1.38)) high missing transverse energy and high lepton transverse momenta are expected for higher squark and gluino masses. This phenomenological grid is called light neutralino (*PG LN*).

In summary, the SUSY parameters are fixed to $m_A = 1000\,\text{GeV}$, $\mu = 1.5 \cdot min(m_{\tilde{g}}, m_{\tilde{q}})$,

$\tan\beta = 4$, $A_t = \mu/\tan\beta$, $A_b = \mu \cdot \tan\beta$ and $A_l = \mu \cdot \tan\beta$ in both phenomenological grids. The masses $m_{\tilde{\chi}_2^0}$, $m_{\tilde{\ell}}$, and $m_{\tilde{\chi}_1^0}$ are expressed as function of $m_{\tilde{g}}$ and $m_{\tilde{q}}$ for the *PG CS*:

$$\begin{aligned} m_{\tilde{\chi}_2^0} &= min(m_{\tilde{g}},\, m_{\tilde{q}}) - 50\,\text{GeV} && (1.35)\\ m_{\tilde{\ell}} &= (m_{\tilde{\chi}_2^0} + m_{\tilde{\chi}_1^0})/2 && (1.36)\\ m_{\tilde{\chi}_1^0} &= min(m_{\tilde{g}}, m_{\tilde{q}}) - 150\,\text{GeV}, && (1.37) \end{aligned}$$

and for the *PG LN*:

$$\begin{aligned} m_{\tilde{\chi}_2^0} &= min(m_{\tilde{g}},\, m_{\tilde{q}}) - 100\,\text{GeV} && (1.38)\\ m_{\tilde{\ell}} &= (m_{\tilde{\chi}_2^0} + m_{\tilde{\chi}_1^0})/2 && (1.39)\\ m_{\tilde{\chi}_1^0} &= 100\,\text{GeV}. && (1.40) \end{aligned}$$

The only difference between the *PG CS* and *PG LN* is the different $\tilde{\chi}_1^0$ mass. In the compressed spectrum grid the mass difference between the $\tilde{\chi}_2^0$ and $\tilde{\chi}_1^0$ is always 150 GeV with the $\tilde{\ell}$ mass in between, in the light neutralino grid $\tilde{\chi}_1^0$ mass is fixed to 100 GeV. The remaining free parameters, which are varied in order to study a given hyperplane are: $m_{\tilde{g}}$ and $m_{\tilde{q}}$.

Gauge-mediated supersymmetry breaking - GMSB

The gauge-mediated supersymmetry breaking (GMSB) models introduce messenger particles, which couple to the source of the supersymmetry breaking. Those messenger particles couple indirectly to the (s)quarks, (s)leptons and the Higgs(inos) of the MSSM through the ordinary gauge interactions. The mediation between the source of the supersymmetry breaking and the MSSM (s)particles can also be communicated by gravitation. But the gravitational effect is much smaller than the effect of the other gauge interactions.

In contrast to the *supergravity* models, the GMSB models can be described in terms of loop effects only. The messenger fields can be arranged in left-handed chiral supermultiplets containing messenger quarks and scalar quarks, messenger leptons, as well as scalar leptons. The gauge mediation provides that the quark messenger loops give masses to the gluino and bino and the lepton messenger loops give masses to the bino and wino.

The messengers, which can be arranged in complete multiplets of $SU(5)$ symmetry similar masses, allow the unification of the gauge couplings as shown in Fig. 1.5. The gaugino masses scale linearly with N_5, the scalar masses scale with $\sqrt{N_5}$. The squarks and sleptons tend to be lighter than the gauginos in non-minimal models ($N_5 > 1$). The messenger mass should not be too large, because otherwise the gauge couplings would diverge before unifying. The number of N_5 fields needs to be smaller than four for messenger masses of order 10^6 GeV or smaller.

The strongly interacting sparticles should be heavier than the weakly interacting sparticles because of the relation of the couplings $\alpha_3 > \alpha_2 > \alpha_1$. The most important phenomenological feature of the GMSB models is the fact that the gravitino is expected to be much lighter than every other MSSM sparticle. Depending on the exact GMSB parameters, the gravitino mass is expected to be of order $\sim$ 1 keV. This yields the gravitino being the LSP. The big mass difference to the other MSSM sparticles leads to the relation that only the next-to-lightest (NLSP) supersymmetric particle can decay into the LSP. The final states of the specific GMSB scenario are dominated by the SM

partners of the NLSP.

The minimal set of free parameters which describes the GMSB mass spectrum completely are the SUSY breaking scale Λ (typically between $10 - 100\,\text{TeV}$), the messenger mass M_{mes}, the number of messenger fields in $SU(5)$ supermultiplets N_5, the ratio of the vacuum expectation values $\tan\beta$, the sign of the Higgsino mass term $sgn(\mu)$ appearing in the neutralino and chargino mass matrix, and the scale factor of the Goldstino coupling C_{grav} which determines the NLSP lifetime.

1.2.4 SUSY Signatures at Proton-Proton Colliders

This section summarises the expected SUSY signatures in proton-proton collider experiments with R-parity conserving SUSY models.

Sparticle Production

Supersymmetric particles can be produced in hadron colliders either in parton interactions of QCD strength:

$$gg \rightarrow \tilde{g}\tilde{g},\ \tilde{q}_i\tilde{q}_j^*, \tag{1.41}$$
$$gq \rightarrow \tilde{g}\tilde{q}_i, \tag{1.42}$$
$$q\bar{q} \rightarrow \tilde{g}\tilde{g},\ \tilde{q}_i\tilde{q}_j^*, \tag{1.43}$$
$$qq \rightarrow \tilde{q}_i\tilde{q}_j, \tag{1.44}$$

the appropriate Feynman diagrams are shown in Fig. 1.8 and Fig. 1.7. Also, parton interactions of electroweak strength can occur:

$$q\bar{q} \rightarrow \tilde{\chi}_i^+\tilde{\chi}_j^-,\ \tilde{\chi}_i^0\tilde{\chi}_j^0, \quad u\bar{d} \rightarrow \tilde{\chi}_i^+\tilde{\chi}_j^0, \quad d\bar{u} \rightarrow \tilde{\chi}_i^-\tilde{\chi}_j^0, \tag{1.45}$$
$$q\bar{q} \rightarrow \tilde{\ell}_i^+\tilde{\ell}_j^-,\ \tilde{\nu}_\ell\tilde{\nu}_\ell^*, \quad u\bar{d} \rightarrow \tilde{\ell}_L^+\tilde{\nu}_\ell, \quad d\bar{u} \rightarrow \tilde{\ell}_L^-\tilde{\nu}_\ell^* \tag{1.46}$$

as shown in Fig. 1.9. The processes in Eq. (1.41) - Eq. (1.43) get contributions from both t- and s-channel exchange of gluinos and squarks (cf. Fig. 1.8 and Fig. 1.7), whereas the processes in Eq. (1.44) only get t-channel contributions. The electroweak production processes in Eq. (1.45) - Eq. (1.46) both have contributions from electroweak bosons in the s-channel, whereas Eq. (1.45) also has contributions from t-channel squark exchange (cf Fig. 1.9), which are less important in most models.

The gluino and squark production processes are expected to have the highest SUSY production cross sections at the LHC. They are dominated by gluon-gluon and quark-gluon fusion, if the squark and gluino masses are roughly below 1 TeV.

Sparticle Decay

As discussed in Sec. 1.2.2, the neutralinos and charginos contain mixings from the electroweak gauginos ($\tilde{B}^0$, $\tilde{W}^0$ and $\tilde{W}^\pm$), thus they couple of weak interaction strength. If sleptons or squarks are sufficiently light, the neutralinos and charginos decay into a squark+quark or slepton+lepton pair (cf. Fig. 1.10(a) ,(d)). They can also decay into lighter neutralinos or charginos and an electroweak gauge boson (cf. Fig. 1.10(b), (e)) or a Higgs scalar (cf. Fig. 1.10(c), (f)). If all decay modes are kinematically forbidden for a given chargino or neutralino the same decays as described above will take place

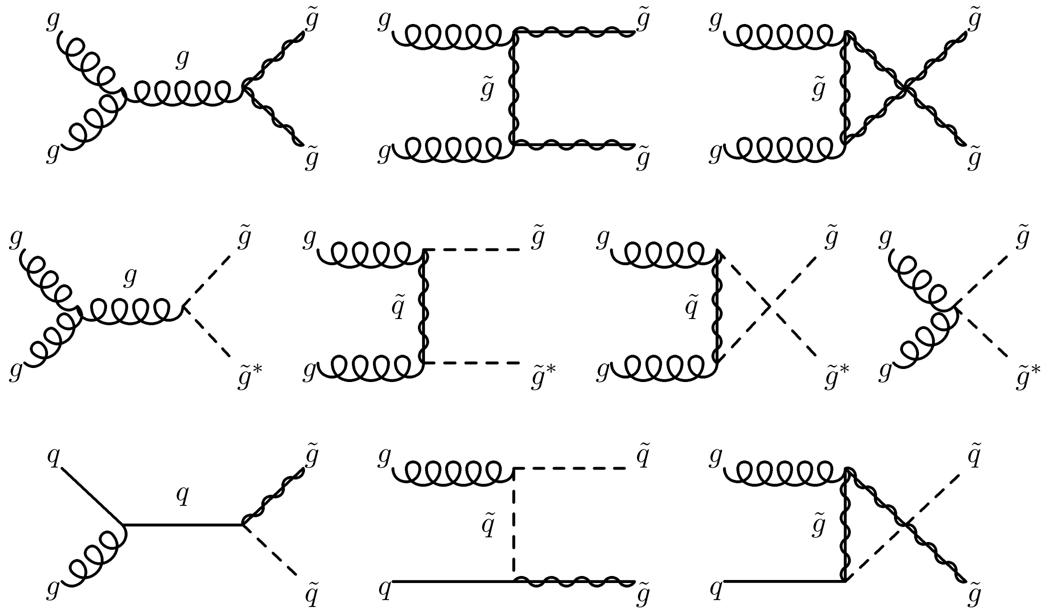

Figure 1.7: Feynman diagrams for gluino and squark production at hadron colliders from gluon-gluon and gluon-quark fusion [32].

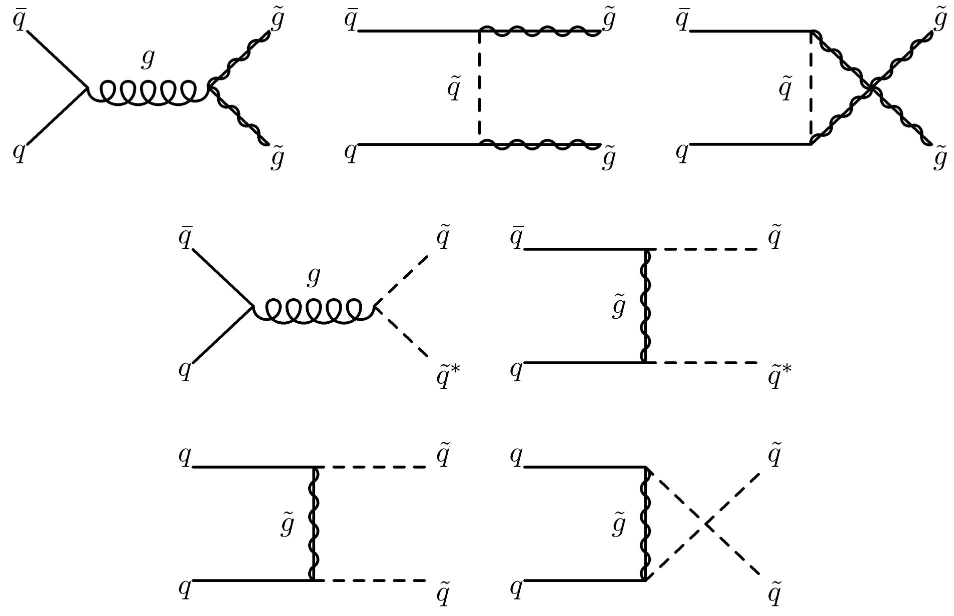

Figure 1.8: Feynman diagrams for gluino and squark production at hadron colliders from strong quark-antiquark annihilation and quark-quark scattering [32].

via a three body decay (same Feynman diagrams) with an intermediate particle which is off-shell. Sleptons decay into a lepton and a chargino or a neutralino conserving the lepton flavour. This thesis is searching for same flavour di-lepton pairs produced in one SUSY decay chain directly in a row, like:

$$\tilde{\chi}_2^0 \to \ell^+\ell^-\tilde{\chi}_1^0. \tag{1.47}$$

The enhanced mixing of staus often results in larger branching fractions into final states with tau-leptons than electron or muon final states.

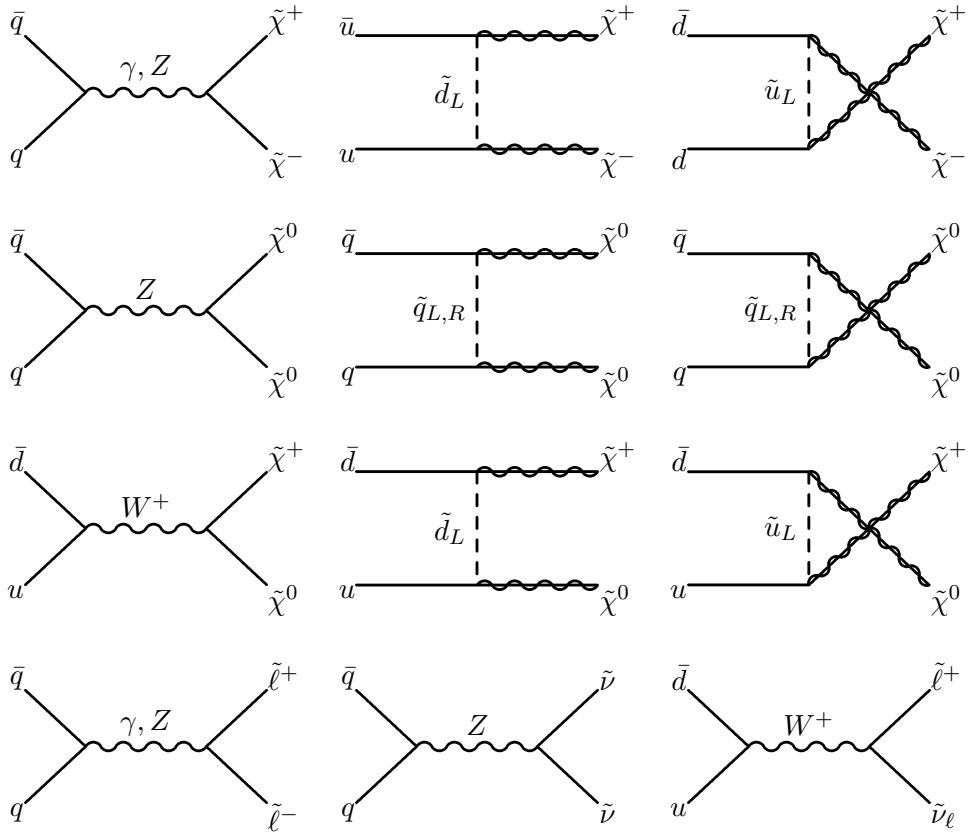

Figure 1.9: Feynman diagrams for electroweak production of sparticles at hadron colliders from quark-anti-quark annihilation. The charginos and neutralinos in the t-channel diagrams only couple because of their gaugino content, for massless initial-state quarks, and so are drawn as wavy lines superimposed on solid [32].

The squark decays are dominated by decaying into gluino-quark pairs, if the process is kinematically allowed. Otherwise the squark can decay into a quark and a neutralino or a chargino. Those particles will decay further as described above. The direct decay into the lightest neutralino is kinematically favoured, but the branching ratio also depends on the mixing. The right-handed squark decays are dominated by direct $\tilde{\chi}_1^0$ production, because of the bino-like character of the $\tilde{\chi}_1^0$. The left-handed squarks strongly prefer to decay into heavier charginos and neutralinos because of their wino-like properties and the enhanced squark-quark-wino coupling.

The gluino can only decay into a squark either on-shell, if the process is kinematically allowed, otherwise it decays off-shell via a three body decay (cf. Fig. 1.11). The gluino decay product decays further until the lightest neutralino is produced. Numerous decay chains are possible. Figure 1.11 just shows a small extract of all possible decay cascades. The simplest gluino cascades can produce several leptons in the final state.

Mass Edges

If SUSY is realized in nature, sparticle masses have to be measured by exploiting the kinematics of the decays. Due to the escaping LSP the masses cannot be determined directly by measuring an invariant mass peak as for the Z-boson. However, mass differences can be measured by determining the endpoint of the invariant mass spectrum [45–47].

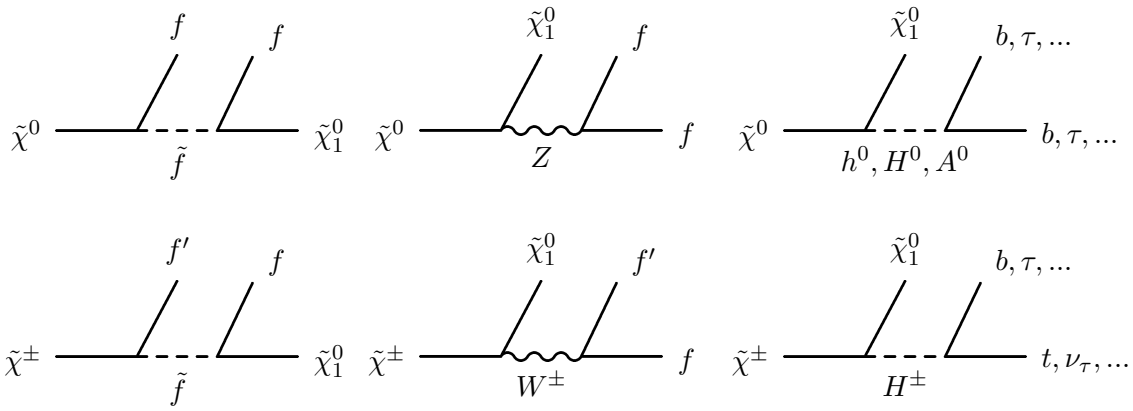

Figure 1.10: Feynman diagrams for neutralino and chargino decays with $\tilde{\chi}^0_1$ in the final state. The intermediate scalar or vector boson in each case can be either on-shell (so that actually there is a sequence of two-body decays) or off-shell, depending on the sparticle mass spectrum. The neutralinos are denoted as $\tilde{\chi}^0_i$, the charginos as $\tilde{\chi}^\pm_i$ and the (s)leptons and (s)quarks as f and $\tilde{f}$, respectively [32].

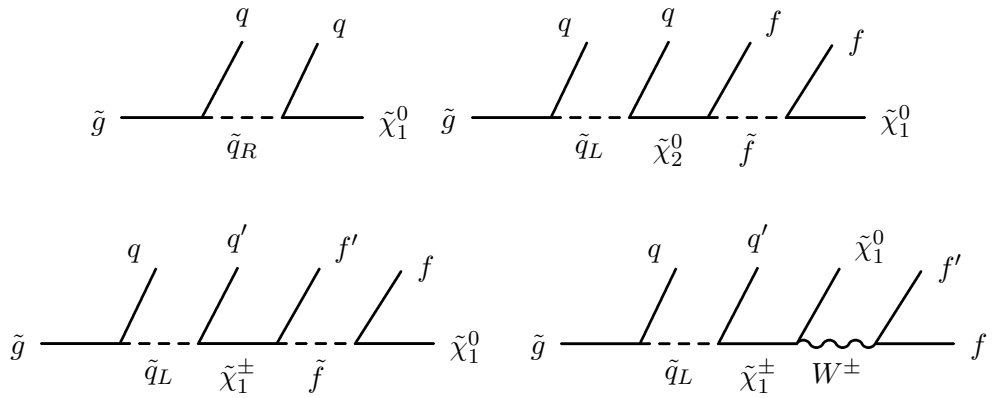

Figure 1.11: Some of the many possible examples of gluino cascade decays ending with a neutralino LSP in the final state. The squarks appearing in these diagrams may be either on-shell or off-shell, depending on the mass spectrum of the model. The neutralinos are denoted as $\tilde{\chi}^0_i$, the charginos as $\tilde{\chi}^\pm_i$ and the (s)leptons and (s)quarks as f and $\tilde{f}$, respectively [32].

Models with SUSY decay cascades with di-lepton final states caused by successive two-body decays such as $\tilde{\chi}^0_2 \to \ell\tilde{\ell}$ followed by a slepton decay $\tilde{\ell} \to \ell\tilde{\chi}^0_1$ (Fig. 1.12(a)) have a sharp edge at the endpoint of the di-lepton invariant mass distribution. The invariant mass can be calculated by Eq. (1.48) with the masses m_ℓ, the Energy E_ℓ, the absolute value of the momentum $|\mathbf{p}_\ell|$ and the angle between the SM leptons. The corresponding kinematics are drawn in Fig. 1.12(b) in the rest frame of the slepton.

$$\begin{aligned} m^2_{\ell_1,\ell_2} &= (p_{\ell_1}, p_{\ell_2})^2 \\ &= m^2_{\ell_1} + m^2_{\ell_2} + 2(E_{\ell_1} \cdot E_{\ell_2} - |\mathbf{p_{\ell_1}}| \cdot |\mathbf{p_{\ell_2}}| \cdot \cos\theta) \end{aligned} \tag{1.48}$$

The maximum of the invariant mass distribution is obtained in the rest frame of the

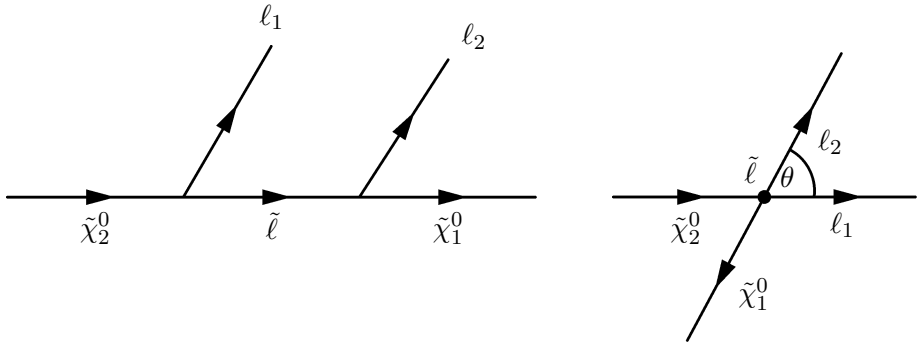

Figure 1.12: Two successive SUSY two-body decays in a chain (a) with the kinematics of the drawn in the rest frame of the $\tilde{\ell}$ in (b). The arrows indicate the direction of motion. θ denotes the angle between the leptons.

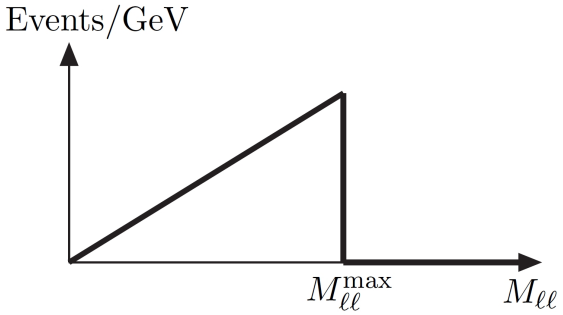

Figure 1.13: Shape of the di-lepton invariant mass distribution from events with $\tilde{\chi}_2^0 \to \ell^+\ell^-\tilde{\chi}_1^0$. No cuts or detector effects are considered [32].

slepton, if the lepton momenta are back-to-back, the minimum if they are collinear (cf. Eq. (1.49)).

$$(m_{\ell_1,\ell_2}^{max})^2 = m_{\ell_1}^2 + m_{\ell_2}^2 + 2(E_{\ell_1} \cdot E_{\ell_2} + |\mathbf{p_{\ell_1}}| \cdot |\mathbf{p_{\ell_2}}|) \quad (1.49)$$

$$(m_{\ell_1,\ell_2}^{min})^2 = m_{\ell_1}^2 + m_{\ell_2}^2 + 2(E_{\ell_1} \cdot E_{\ell_2} - |\mathbf{p_{\ell_1}}| \cdot |\mathbf{p_{\ell_2}}|) \quad (1.50)$$

In events with an invariant mass below the maximum, the only free kinematic variable of interest is the polar angle $\cos\theta$ defined as the angle between the first and the second lepton, which is uniformly distributed. The shape of the $m_{\ell\ell}$-distribution is linear from 0 to $m_{ll,max}^2$ with a sudden drop at the upper end (cf. Fig 1.13). The measured endpoint of the $m_{\ell\ell}$-distribution can be fitted and the result compared to calculated endpoints. The expected sparticles involved in the studied decays are much heavier than the SM particles. Therefore, the SM lepton masses can be neglected in Eq (1.51) and the formula for calculating the maximum of the invariant mass distribution can be simplified (cf. Eq. (1.52)).

$$\begin{aligned}(m_{\ell_1,\ell_2}^{max})^2 &= \underbrace{m_{\ell_1}^2 + m_{\ell_2}^2}_{m_\ell \ll E_\ell} + 2(E_{\ell_1} \cdot E_{\ell_2} + |\mathbf{p_{\ell_1}}| \cdot |\mathbf{p_{\ell_2}}|) \\ &\sim 2(E_{\ell_1} \cdot E_{\ell_2} + E_{\ell_1} \cdot E_{\ell_2}) \end{aligned} \quad (1.51)$$

with $E_{\ell_1} = (m_{\tilde{\chi}_2^0}^2 - m_{\tilde{\ell}}^2)/(2 \cdot m_{\tilde{\ell}}^2)$, $E_{\ell_2} = (m_{\tilde{\ell}}^2 - m_{\tilde{\chi}_1^0}^2)/(2 \cdot m_{\tilde{\ell}}^2)$ the endpoint can be calculated

based on the sparticle masses only:

$$(m_{\ell\ell}^{max})^2 = \frac{(m^2_{\tilde{\chi}_2^0} - m^2_{\tilde{\ell}})(m^2_{\tilde{\ell}} - m^2_{\tilde{\chi}_1^0})}{m^2_{\tilde{\ell}}}. \tag{1.52}$$

Heavier sparticle mass combinations can be determined, for example, by analysing invariant mass distributions of lepton-lepton-quark combinations.

1.2.5 Experimental Results

Electroweak precision data and direct SUSY searches are analysed and interpreted separately and combined for several collider experiments as well as results from astrophysics. No SUSY signal has been discovered in any particle experiment so far. Thus the available data is used either directly to determine exclusion limits or indirectly in fit programs or in order to test predictions of new physics models.

The electroweak mixing angle for example is studied in [48] by comparing predictions of ordinary and supersymmetric grand unified theory models with the precision data from the LEP experiments. The authors obtained a predicted mixing angle of $sin^{2\hat{}}\theta_W(M_Z) = 0.2333 \pm 0.0008$ within minimal supersymmetric models, which is in perfect agreement with the experimental results ($sin^{2\hat{}}\theta(M_Z)(\bar{M}S) = 0.23116(13)$) [8].

Programs like *Fittino* [49] use experimental results of low energy observables (LEO) as input and fit the free parameters of a given model. This can be done for minimal SUSY models like MSUGRA and GMSB. *Fittino* determines the free parameters directly from the LEO without any a priori knowledge of the free SUSY parameters. The following LEO are considered: the rare decays of B- and K-mesons, the anomalous magnetic moment of the muon, a_μ, the electroweak precision measurements from LEP, SLC and the TeVatron, the Higgs boson mass limit from LEP, and the relic density of cold dark matter in the universe Ω_χ. Figure 1.14 shows the best fit value in the $m_0 - m_{1/2}$-plane of the MSUGRA parameter space for fits with LEO only (dashed lines) and including first results (2010 analysis with L = 35 pb^{-1}) of SUSY searches with 4 jet and zero lepton final states with the ATLAS experiment (solid lines). The ATLAS results are simulated by the *Fittino* group and found to be in good agreement with the published ATLAS results. Based on the same data set, *Fittino* performs mass predictions for the SUSY sparticles shown in Fig. 1.14 b).

The results of the direct searches for supersymmetry in the MSUGRA model is summarized in Fig. 1.15 for the ATLAS [51, 52], the LEP [53] and the TeVatron [54–56] experiments. The plots show the status of the results from the 2010 analyses before the analysis performed in this thesis has been started. Figure 1.15 a) shows the combined result of the 0-lepton and the 1-lepton search for the data taken in 2010, whereas Fig. 1.15 b) are the results of the di-lepton searches for the same integrated luminosity. Both the 0- and the 1-lepton limits can exclude a much bigger parameter space than the di-lepton limits of the same sign (SS) and the opposite sign (OS) analyses, because the production cross section of strong processes is much larger than the electroweak production in the MSUGRA parameter space.

The results of the di-lepton searches with missing transverse energy at $\sqrt{s} = 7$ TeV at the ATLAS experiment [52] interpreted in the phenomenological grids (*PG LN* and *PG CS*), which are described in Sec. 1.2.3, are shown in Fig. 1.16 for SS in (a) and for OS in (b). The hashed areas are the observed exclusions limits of the compressed spectrum model and the blue coloured areas are the observed exclusion in the light neutralino

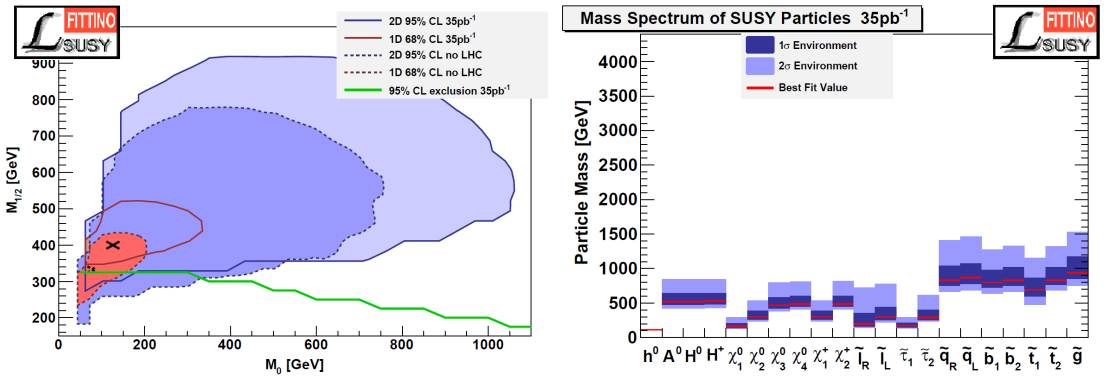

(a) (b)

Figure 1.14: The allowed parameter range for the fits without LHC and for the fit with *LHC-like Fittino implementation* of 4 jets and no lepton searches(a). Comparison of the allowed mass ranges of all sparticles and Higgs bosons for the fits with $L = 35\text{pb}^{-1}$ (b) [50].

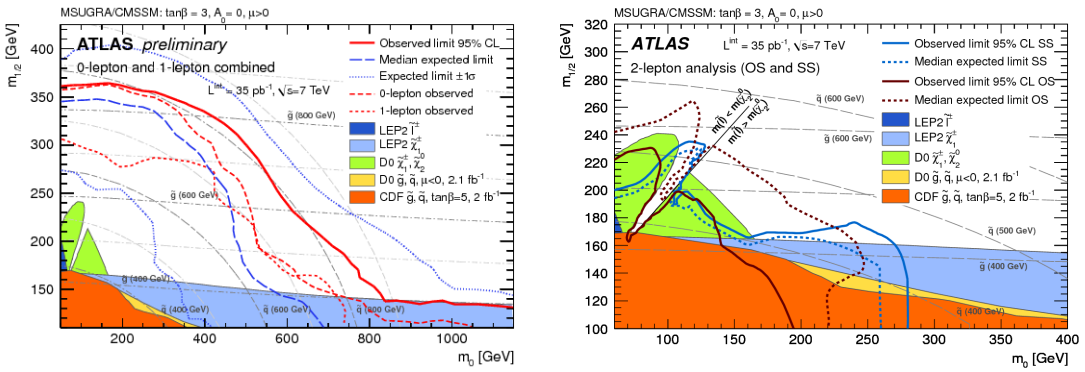

(a) (b)

Figure 1.15: Expected and observed limits for the combined 0- and 1-lepton channels. The blue dashed line corresponds to the expected median 95% C.L. exclusion limit, the dashed-solid blue lines to $\pm 1\sigma$ 95% C.L. limits respectively. The red line represents the combined observed limit. (a) The observed limits for the individual 0-lepton and 1-lepton channels are indicated with red dashed lines. TeVatron and LEP limits on $m_{\tilde{q}}$ and $m_{\tilde{g}}$ are marked for searches in the specific context of MSUGRA/CMSSM, with $\tan\beta = 3$, $A_0 = 0$ and $\mu > 0$, and are also shown for illustration [51]. (b) Expected and observed exclusion limits in MSUGRA for di-lepton searches [52].

model. The red dashed and the blue dotted lines mark the expected limits, respectively.

Finally the limits in the GMSB model have been set by LEP [57–60] and TeVatron [61, 62]. The results of the OPAL collaboration published in [63] are shown in Fig. 1.17.

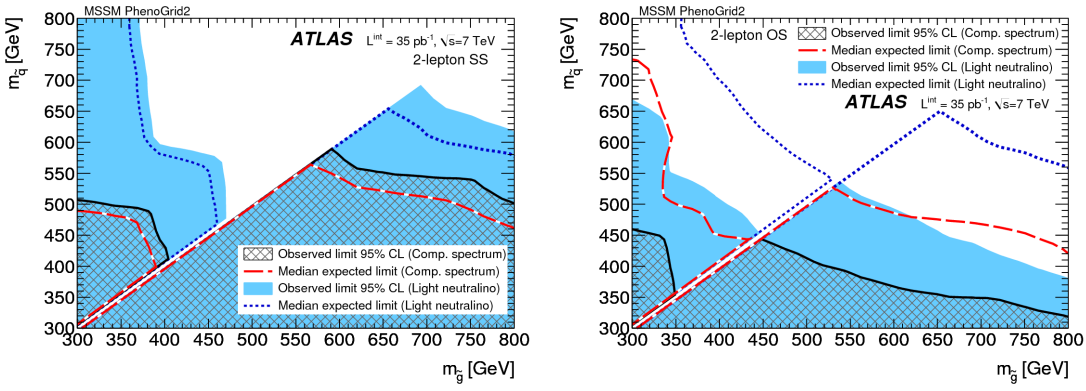

(a) (b)

Figure 1.16: Expected and observed 95% C.L. exclusion limits in the $(m_{\tilde{g}}, m_{\tilde{q}})$ plane for the *PG11* grids described in the text for the same sign (SS) analysis (a) and the opposite sign (OS) analysis (b) [52].

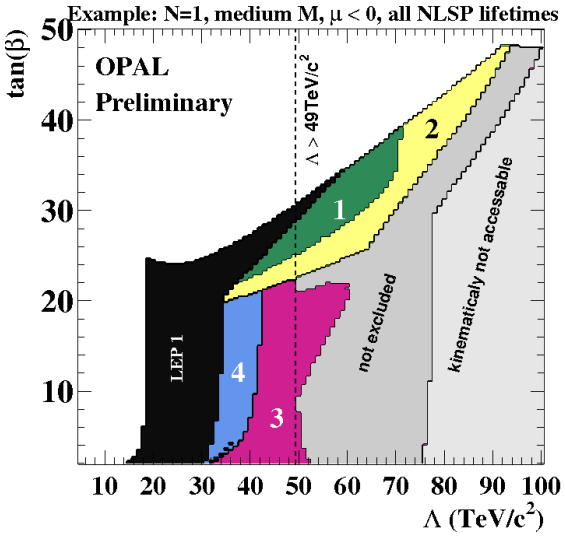

Figure 1.17: Excluded regions in the $\Lambda - \tan\beta$ plane for a fixed set of parameters $N_5 = 1$, medium M_{mes} and $sgn(\mu) < 0$.In the black regions the NLSP is lighter than 45 GeV. These regions were not considered in this analysis. The regions are excluded by: 1 slepton pair-production in the $\tilde{\ell}$ CoNLSP or $\tilde{\tau}$-NLSP scenario, 2 $\tilde{\chi}^0$ pair-production in the $\tilde{\ell}$ CoNLSP or $\tilde{\tau}$NLSP scenario, 3 $\tilde{\ell}$ pair-production in the $\tilde{\chi}_1^0$ NLSP scenario, 4 $\tilde{\chi}^{\pm}$ pair-production in the $\tilde{\chi}_1^0$ NLSP scenario. The dashed vertical line indicates the lowest value of λ which in the particular set of parameters can be excluded for any NLSP lifetime [63].

2 The ATLAS Experiment at the LHC

This chapter gives an overview of the experimental setup at the Large Hadron Collider (LHC) [64]. Therefore the particle collider and the experiments at LHC are briefly described in section 2.1, then the ATLAS detector [65] and its subsystems are described in detail in section 2.2.

2.1 The LHC Collider

The LHC is a proton-proton collider placed at CERN near Geneva, Switzerland. It is a two-ring-superconducting-hadron accelerator with an circumference of 27 km installed in a tunnel between 45 m and 170 m below the surface. The tunnel has been built for the Large Electron Positron collider (LEP) between 1984 and 1989. Building the LHC into the already existing LEP tunnel was strongly influenced by the costs saving by re-using the tunnel and the injection chain (Fig. 2.1).

The most important parameters for a ring collider like the LHC are the beam energy and the number of interactions per bunch crossing since the production rate of a specific physics process rely on those values (Fig. 2.2). In order to maximize the energy of an accelerated proton on a circular path both the radius and the magnetic field have to be maximized. The radius is limited by the already existing tunnel. The magnetic field has been maximized to the edge of the technology available during LHC construction. Such that a maximum energy of 7 TeV per beam can be achieved by the magnetic field of 8.33 T in the deflection magnets. The other parameter, the number of interactions per bunch crossing has been increased up to 40 MHz. This value corresponding to a bunch spacing of 25 ns is incredibly high in comparison to the readout electronics and detector systems, which can be up to ns and μs. The different experiments developed elaborate buffer and trigger systems dealing with those high interaction rates.

The LHC is built to reveal physics beyond the standard model with a center of mass energy up to 14 TeV. In order to collect a sufficient number of interesting events the number of events per second produced in a LHC collision can be calculated:

$$N_{event} = \mathcal{L} \cdot \sigma_{event} \tag{2.1}$$

where σ_{event} is the cross section of a specific physics process and $\mathcal{L}$ the machine luminosity. The machine luminosity depends on the beam parameters only and can be calculated for a Gaussian beam distribution as [64]:

$$\mathcal{L} = \frac{N_b^2 n_B f_{rev} \gamma_r}{4\pi \epsilon_n \beta^*} \cdot F \tag{2.2}$$

where N_b is the number of particles per bunch, n_b the number of bunches per beam, f_{rev} the revolution frequency, γ_r the relativistic gamma factor, ϵ_n the normalized transverse beam emittance, β^* the beta function of the collision point and F the geometric luminosity reduction factor due to the angle of the beam crossing at the interaction point (IP).

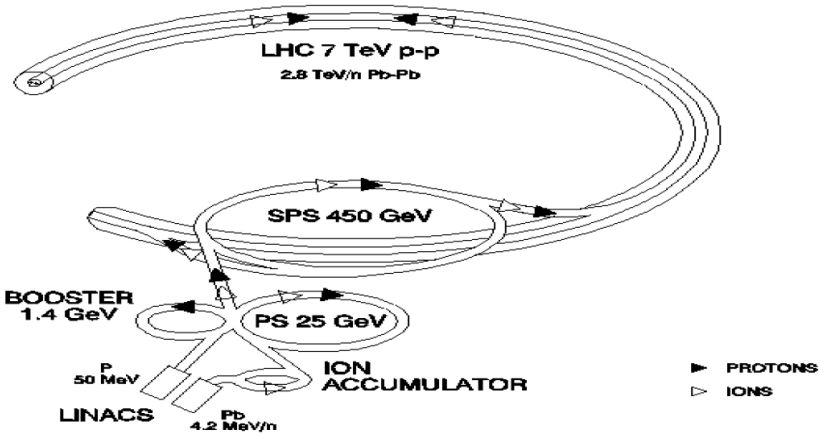

Figure 2.1: The LHC injection chain [66]

In order to investigate rare events like Higgs (Fig. 2.2) or searches for supersymmetry both high beam energies and high beam intensities are required.

The LHC design parameters are a center of mass energy of 14 TeV and an instantaneous luminosity of $10^{34}\,\mathrm{cm^2 s^1}$ for proton-proton collisions. With a design bunch spacing of 25 ns and in average $1.15 \cdot 10^{11}$ protons per bunch 40 million collisions per second are expected. Those are the design parameters for the high luminosity experiments ATLAS [65] and CMS [68]. LHCb [69] is designed to study B-physics aiming for a peak luminosity of $10^{32}\,\mathrm{cm^2 s^1}$. The LHC can be run to accelerate heavy ions as well. A dedicated heavy ion experiment ALICE [70] and the multi purpose experiments ATLAS and CMS are taking data in specific heavy ion runs. The design luminosity for lead-lead ion collisions is $10^{27}\,\mathrm{cm^2 s^1}$ with an energy of 2.8 TeV per nuclei.

Several steps are needed to accelerate the particles up to their final collision energy. During particles pass the injection chain shown in Fig. 2.1 they are accelerated more and more. Protons are injected into the chain from the linacs with an energy of 50 MeV per particle. Then the protons are accelerated via the Proton Synchrotron Booster (PSB) to 1.4 GeV, by the Proton Synchrotron (PS) to 25 GeV and finally by the Super Proton Synchrotron up to 450 GeV. Then the proton beams are injected into the LHC (beam 1 clockwise and beam 2 anti-clockwise). Finally the beams are accelerated up to the collision energy in the LHC ring and brought to collision in the four interaction points in the experiments.

As mentioned above, magnets providing magnetic fields above 8 T are needed in order to keep protons with an energy of 7 TeV on track. The LHC is using a NbTi superconductor magnet technology which has been employed in previous experiments like Tevatron-FNAL [71] and HERA-DESY [72].Only superconductor technology is able to provide constant magnetic fields with high magnetic field strength. Conventional magnets would produce too much heat which would yield a large amount of energy loss. The NbTi Rutherford cables used for the LHC coils are cooled by super-fluid helium at a temperature below 2 K. Comparing to the previous experiments (4.2 K with magnetic field strengths of around 4 T) the working point temperature of the LHC it is a factor 2 colder. This is needed for the higher magnetic field, but it also reduces the heat capacity of the cable such that much lower energy deposition can trigger a quench for a given temperature margin.

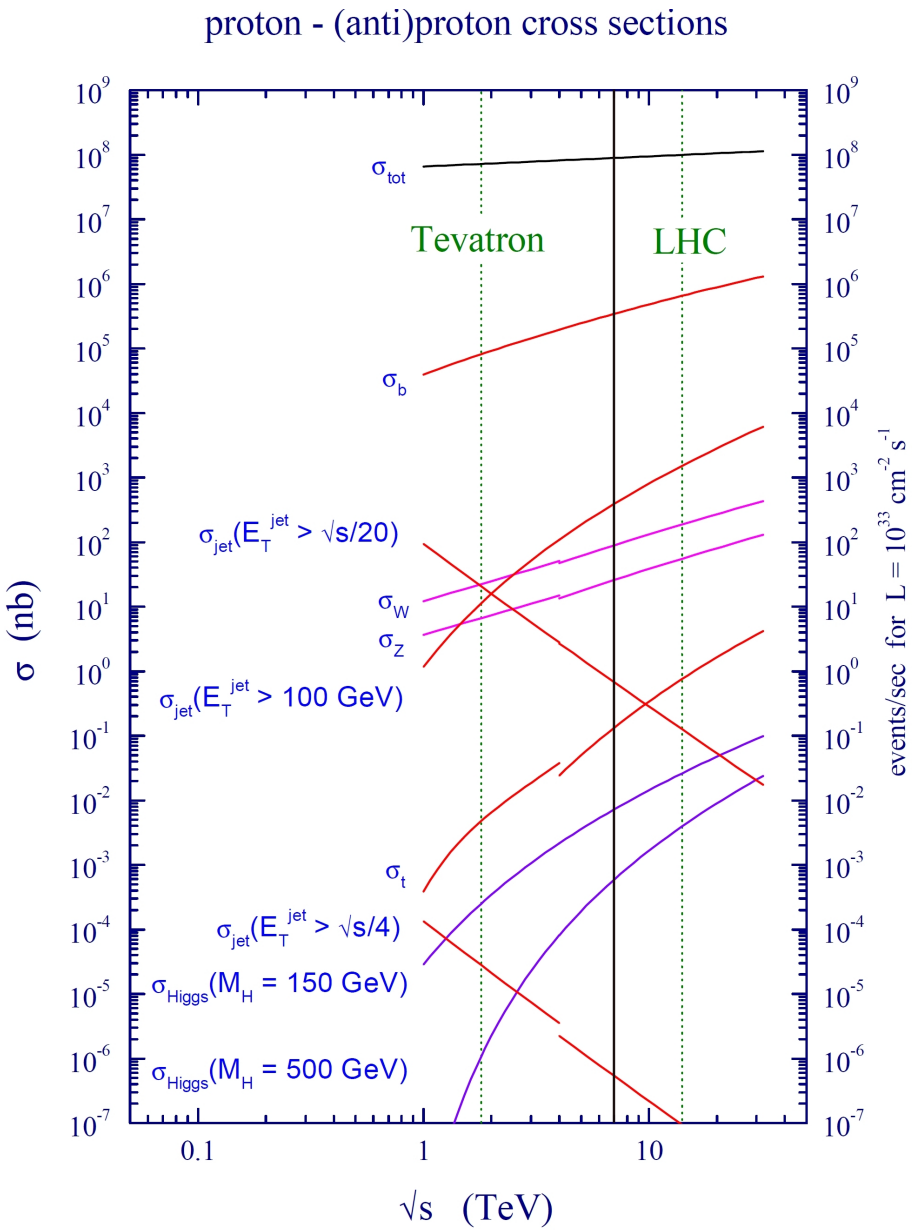

Figure 2.2: The proton-proton cross section and the event rates at the TeVatron and LHC [67]. The cross section in *nb* and the event rate per sec. for a luminosity of $10^{33}\,\mathrm{cm}^{-2}\mathrm{s}^{-1}$ are plotted over the center of mass energy in TeV. At 14 TeV the operation point of the LHC mainly b-quarks will be produced. The cross section of the Higgs boson production, the LHC is searching for, is orders of magnitude lower than the other cross sections shown in this figure.

Table 2.1: Overview of the six experiments at the LHC.

ATLAS:	Is built as multi purpose detector to discover the Higgs boson and find physics beyond the standard model [65].
CMS:	Compact Muon Solenoid Same aim as ATLAS: ATLAS and CMS are built to cross check their results [68].
LHCb:	LHC B-physics experiment Is dedicated to B-physics and will investigate CP-violation [69].
ALICE:	A Large Ion Collider Experiment Investigates quark-gluon plasma produced via heavy ion collisions [70].
TOTEM:	TOTEM is dedicated to the measurement of the total cross section, elastic scattering and diffractive processes [73].
LHCf:	Large Hadron Collider forward experiment LHCf uses forward particles created inside the LHC as a source to simulate cosmic rays in laboratory conditions [74].

An overview of the experimemts at the LHC is given in Tab. 2.1.

The data taking started in 2009 with proton-proton collisions at a center-of-mass energy of 900 GeV. During the commissioning phase two bunches per beam with 5×10^{10} protons per bunch have been brought to collision. The luminosity was around $10^{26}\,\mathrm{cm^2 s^1}$ to $10^{27}\,\mathrm{cm^2 s^1}$. The experiments collected about 1.5 million events. At the end of March 2010 first collisions with a center-of-mass energy of 7 TeV were recorded. The number of protons per bunch have been increased from 5×10^{10} to 1.2×10^{11} with a bunch spacing of 150 ns. In 2010 an integrated luminosity of $48\,\mathrm{pb^{-1}}$ with the highest instantaneous luminosity of $2 \times 10^{32}\,\mathrm{cm^2 s^1}$ has been recorded. At the end of 2010 there were four weeks of data taking with heavy ion collisions delivering an integrated luminosity of $9.7\,\mu\mathrm{b^{-1}}$. The 2011 data taking period is analysed in this study and described in detail in section 3.

.

2.2 The ATLAS Detector

The ATLAS detector is a multi purpose experiment designed to discover the Higgs boson and new physics at the LHC. The possible systems of Higgs decays are driven by the Higgs mass. The allowed rage of predicted Higgs masses [75] allows several decay products so that the detector has to full-fil a variety of performance goals. A light Higgs would decay into two-photon final state, a Higgs around 130 GeV would mainly decay into dibosons which requires a good lepton reconstruction and Higgs to diTau would require a good coverage of forward jets in case of vector boson fusion and a good τ identification. Many new physics scenarios predict missing transverse energy, which can be measured with a full η-ϕ coverage of calorimeters. Precision measurements can be achieved by investigating leptons e.g. in an invariant mass analysis. To cover all those physics goals the requirements on the detector can be summarized as:

- high bunch crossing rate requires fast and radiation-hard electronics and sensors
- high particle flux requires a high detector granularity
- good η-ϕ coverage for missing transverse energy reconstruction

Table 2.2: Performance goals of the ATLAS detector. The units of E and p_T are in GeV [65].

Detector component	Required resolution	η coverage Measurements	Trigger
Tracking	$\sigma_{p_T}/p_T = 0.05\% \oplus 1\%$	$\pm$ 2.5	
Ecal	$\sigma_E/E = 10\%/\sqrt{E} \oplus 0.7\%$	$\pm$ 3.2	$\pm$ 2.5
Hcal (jets)			
barrel & end-cap	$\sigma_E/E = 50\%/\sqrt{E} \oplus 3\%$	$\pm$ 3.2	$\pm$ 3.2
forward	$\sigma_E/E = 100\%/\sqrt{E} \oplus 10\%$	$3.1 < \lvert\eta\rvert < 4.9$	$3.1 < \lvert\eta\rvert < 4.9$
Muon spectro.	$\sigma_{p_T}/p_T = 10\%$ at $p_T = 1$ TeV	$\pm$ 2.7	$\pm$ 2.4

- good hadron calorimeter with a good jet resolution
- good charge momentum resolution for lepton sign based searches and secondary vertexing for b-jets and τ reconstruction
- good muon identification and momentum resolution over a wide range of momenta
- very good electromagnetic calorimeter for electron and photon identification
- high trigger efficiency on low transverse-momentum objects with sufficient background suppression in order to trigger the interesting events

In order to achieve an acceptable precision, the performance goals listed in 2.2 has been addressed with the ATLAS design.

The ATLAS detector is organized in an onion-like structure like many other particle physics experiments. It is symmetric around the z-axis with an barrel part in the center and end-caps on both sides. Figure 2.3 shows the different sub-detectors, which are described in more detail in the following. The innermost part of the ATLAS detector is the tracking system (Sec. 2.2.2) surrounded by a thin superconducting solenoid (Sec. 2.2.1). A second magnetic field is provided by three large superconducting toroids (one barrel and two end-caps) (Sec. 2.2.1) which are arranged around the calorimeter system (Sec. 2.2.3). The outermost layer is the muon system (Sec. 2.2.4) which defines the overall dimension of the detector.

The ATLAS Coordinate System

The ATLAS coordinate system is defined by the x-axis which is the axis pointing from the interaction point to the center of the LHC ring. Perpendicular to the x-axis pointing upwards is the y-axis defined and the z-axis is pointing in direction of the counter-clockwise beam direction.

The azimuthal angle ϕ is defined as the angle around the beam pipe (z-axis) by $\tan\phi = \frac{y}{x}$, which varies from $-\pi$ to π. The polar angle θ is measured from the beam axis (positive z-axis) and defines the pseudo rapidity:

$$\eta = -\ln\left(\tan\frac{\theta}{2}\right). \tag{2.3}$$

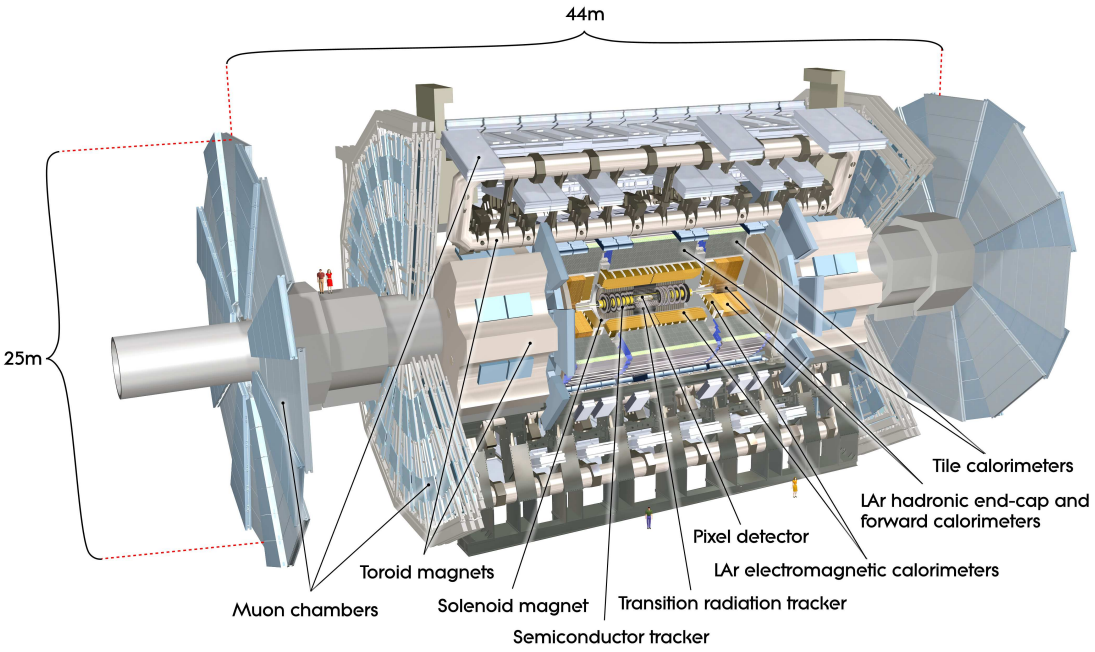

Figure 2.3: The ATLAS detector in a schematic overview. The dimensions of the detector are 25 m in height and 44 m in length. The overall weight of the detector is approximately 7000 tonnes. [65].

Using η instead of the polar angle θ is addressing the unknown initial boost in the z-direction in hadron colliders as $\Delta\eta$ is invariant under Lorentz transformation in approximation for relativistic particles.

The distance between two objects in the $\eta - \phi-$plane is defined as:

$$\Delta R = \sqrt{\Delta\eta^2 + \Delta\phi^2}. \tag{2.4}$$

The transverse energy and transverse momentum of a particle are measured in the x-y-plane e.g. as $p_{\mathrm{T}} = \sqrt{p_x^2 + p_y^2}$ this parameter is Lorentz invariant along the z-axis.

2.2.1 Magnet System

The magnet system of the ATLAS detector [76] provides magnetic fields by four magnets: one solenoid in the barrel and three toroids (one barrel and two end-caps). The geometry of the magnetic windings and tile calorimeter steel are shown in Fig. 2.4(a) and the installed barrel toroid in Fig. 2.4(b). In order to measure the momentum and the charge of a charged particle, a magnetic field is provided. The Lorentz force is bending the track of a charged particle such that the momentum can be measured by the curvature and the charge can be determined by the direction of the deviation.

The solenoid [77] provides an axial field of 2 T which bends charged tracks in ϕ direction. It is built within the Calorimeter system, such that the calorimeter size is not limited by the size of the solenoid. The flux of the solenoid field is returned by the hadronic calorimeter. This design has been chosen to minimize the amount of material in front of the electromagnetic calorimeters to guarantee a good energy resolution. In total it contributes around 0.66 radiation lengths. The solenoid has an axial length of

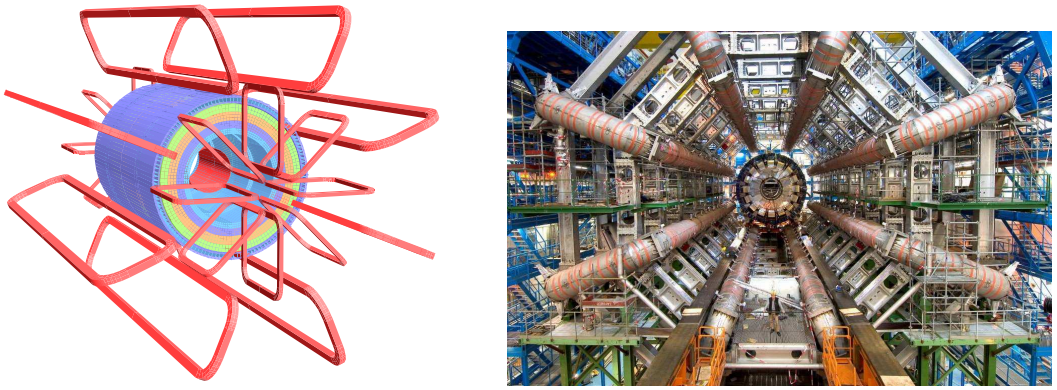

Figure 2.4: (a) Geometry of magnet windings and tile calorimeter steel. The eight barrel toroid coils, with the end-cap coils interleaved are visible. The solenoid winding lies inside the calorimeter volume. The tile calorimeter is modelled by four layers with different magnetic properties, plus an outside return yoke. For the sake of clarity the forward shielding disk is not displayed. (b) Barrel toroid as installed in the underground cavern; note the symmetry of the supporting structure. The temporary scaffolding and green platforms were removed once the installation was complete. The scale is indicated by the person standing in between the two bottom coils [65].

5.8 m and an radius of 2.46 m (inner radius) respectively 2.56 m (outer radius).

The toroids [78, 79] deliver a toroidal field of 0.5 T in the barrel and 1.5 T in the end-caps in order to bend muon tracks in the η direction. As shown in Fig. 2.4(a), each of the toroids in both barrel and end-caps consist of eight coils arranged radially and symmetrically around the z-axis. The end-caps are rotated by 22.5° with respect to the barrel providing a good overlap and optimizing the bending power.

2.2.2 Inner Detector

The Inner Detector (ID) [80] encases the beam pipe. Its purpose is to reconstruct the track of a charged particle in order to measure its momentum, the sign of the charge, and secondary vertices of long-living particles. Therefore, each sub-detector element which is crossed by a charged particle registers the specific space point. By combining those space points, a track can be fitted. By combining tracks pointing to a common origin, vertices can be reconstructed. The magnetic field (B) of the solenoid is bending the track of a charged particle in the $R-\phi$-plane such that the deviation can be exploited to measure the transverse momentum and the sign of the charge. The following expression is an approximation for calculating the transverse momentum:

$$p_{\mathrm{T}} \sim 0.3 \cdot B \cdot R \left[\frac{GeV}{Tm}\right] \tag{2.5}$$

with the magnetic field B in T and the bending radius R in m. A good track resolution can be achieved if a high granularity guarantees precise measurement of space points and a sufficient number of detector layers provide enough space points for the track fitting. Modules with high granularity are extremely expensive and cannot be installed in every ID layer. The ID design accounts for both a sufficient number of detector

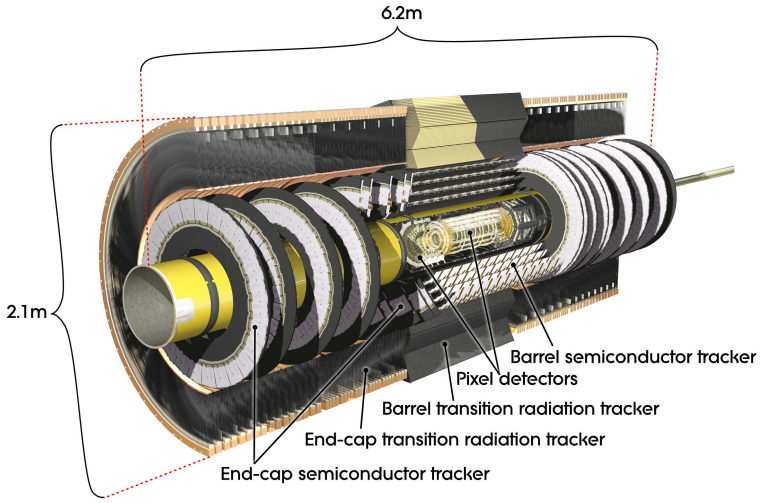

Figure 2.5: The ATLAS Inner Detector (ID). The Pixel Detector with the highest granularity is located near the the interaction point at the center of the ID. It is surrounded by the Silicon Microstrip Detector, which covers a much larger area. Most ID volume is covered by the Transition Radiation Tracker [65].

layers and a high granularity. Therefore, the detector consists of several subsystems with different granularities, such that the inner layers have the highest granularity and precision, but a much smaller surface to cover and the outer layers have to cover a much bigger surface/volume with lower accuracy. The Pixel Detector with the highest granularity is the innermost layer, the semiconductor tracker (SCT) with a slightly lower granularity covers a much larger surface, and the outermost part is covered by a straw tube system, the transition radiation tracker (TRT). Figure 2.5 gives an overview of the different sub-detectors (barrel and end-cap) of the Inner Detector and Fig. 2.6 shows a more detailed drawing of the sensors and the structural elements of the Pixels, SCT, and TRT. The basic properties are summarized in Tab. 2.3.

The readout architecture is optimized for each subsystem separately, but all components are based on the following common principles:

1 The signal in the front-end electronics gets a time-stamp provided by a 40.08 MHz clock synchronized with the LHC bunch-crossing. This tagging is needed to combine all signals from the different sub-detectors associated to the same event.

2 The generated signal is stored in binary or digital buffers for approximately 3.2 μs accounting for the L1 trigger latency.

3 Triggered by the L1 decision (cf. 2.2.5), the transfer of the buffer content associated with the bunch-crossing to the readout driver of the detector has to be provided.

The final readout of the pipelines is handled by the trigger processor, described in Sec. 2.2.5.

Pixel Detector

The Pixel Detector [81] is the innermost sub-detector of the Inner Detector. It consists of three cylindrical layers in the barrel and three discs in each end-cap. It covers the full

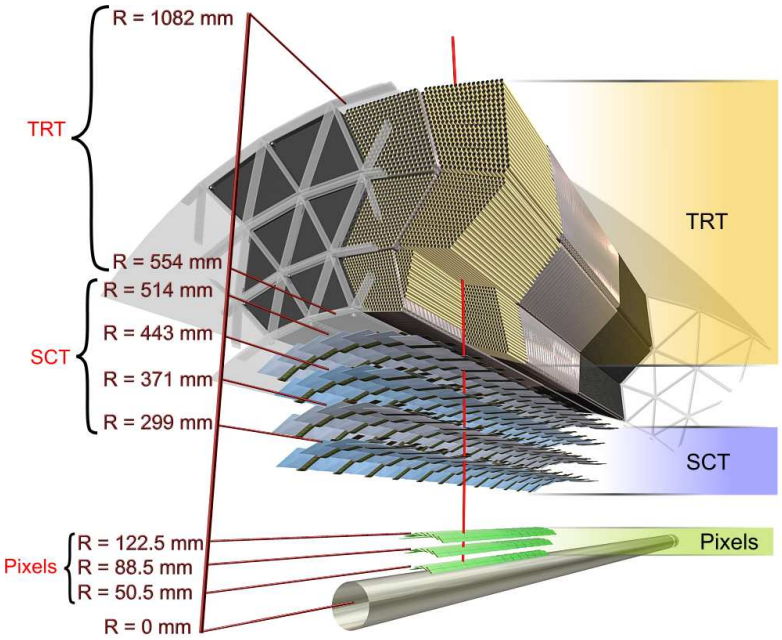

Figure 2.6: Barrel region of the ATLAS Inner Detector. Shown are the three subsystems Pixel, SCT and TRT of the ID. The precise positions of the several layers are registered[65].

Table 2.3: Main parameter of the Inner Detector[65].

	pixel detector	SCT	TRT
coverage	$\|\eta\| < 2.5$	$\|\eta\| < 2.5$	$\|\eta\| < 2.0$
module size	minimum $50 \times 400\,\mu m^2$	6.4 cm long, 80 μm pitch, 40 mradstereoangle	barrel: 144 cm long, end-cap: 37 cm long, 4 mm in diameter
accuracy:			
barrel	10 μm (R-ϕ), 115 μm (z)	17 μm (R-ϕ), 580 μm (z)	130 μm (R-ϕ), no z
end-cap	10 μm (R-ϕ), 115 μm (R)	17 μm (R-ϕ), 580 μm (R)	17 μm (R-ϕ), 580 μm (R)
# of comp.:			
barrel	3 cylindrical layers	4 cylindrical layers	73 straw planes
end-cap	2 × 3 discs	2 × 9 discs	160 straw planes
# of hits	3 pixel hits	4 space points	22 to 40 hits

acceptance region and provides ideally three precision measurements of hits. In total the pixel system consists of 1500 barrel modules and 1000 disc modules. This allows a spatial resolution of 10 μm in R-ϕ-plane in the barrel and the end-caps and 115 μm in z-direction in the barrel and 115 μm in R-direction in the end-caps. The individual layers have a thickness of around 1% of the radiation length. The price for the high granularity is the large number of readout channels. The Pixel Detector has 80.4 million readout channels in total, which is around 90% of all readout channels of the ATLAS detector.The close position of the Pixel Detector to the beam pipe (first layer 50.5 mm measured from the

beam-axis) yields a high radiation dose. The radiation damage reduces the lifetime of the pixel detector such that it has to be replaced after a few years of data-taking depending on the luminosity.

Semiconductor Tracker

The SCT [82] is extending the Pixel Detector in intermediate radial range. It consists of eight strip layers (four space points) which are crossed by each track. Each sensor has a size of $6.36 \times 6.40\,\mathrm{cm}^2$ with 768 readout strips of $80\,\mu$m pitch. Two sensors are daisy-chained and glued together back-to-back with a 40 mrad tilt build a module in order to get a precise measurement in both coordinates. In the barrel region one strip layer is arranged parallel to the beam axis such that a R-ϕ measurement is possible. In the end-cap wheels the strips are arranged radially. Each forward module is 7 cm (innermost radii) respectively 12 cm (outermost radii) long. In total the surface of the SCT detector is $63\,\mathrm{m}^2$. It consists of 4088 modules and 6.2 million readout channels. The accuracy per module is $17\,\mu$m (R-ϕ) and $580\,\mu$m (z) in the barrel and $17\,\mu$m (R-ϕ) and $580\,\mu$m (R) in the end-caps. Tracks can be distinguished, if they are separated by more than $200\,\mu$m.

Transition Radiation Tracker

The outermost layer of the Inner Detector is filled with the Transition Radiation Tracker (TRT) [83]. The TRT is designed as a drift chamber with about 370000 straw tubes with a diameter of 4 mm containing a gas mixture of 70% Xenon, 27% CO_2, and 3% Oxygen which are circulated with $5 - 10$ mbar over-pressure. Both barrel and end-cap straws use tungsten wires plated with $0.5. - 0.7\,\mu$m gold as anode. The wires are directly connected to the front-end electronics. Each track crossing the TRT typically provides at least 36 hits. The TRT only provides R-ϕ information with an accuracy of $130\,\mu$m per straw. The barrel consists of 50000 straws which are installed parallel to the beam axis. The straws are 144 cm long and the wire is divided into two halves at $\eta = 0$. The readout is placed at the end of each tube. The end-caps contain 320000 straws with a length of 37 cm which are installed radially. The readout is placed at the outer radius. 420000 TRT electronic channels provide information about the drift-time measurement to determine the distance of the track from the wire. In addition, the tubes are interleaved with polymeric fibres and foils in order to induce transition radiation of crossing high relativistic particles. When high relativistic particles passing through materials with different permittivities they induce radiation. Electrons for example with energies above 2 GeV induce typically 7 to 10 high threshold hits in the TRT and can be distinguished from low-threshold tracking hits. Those low and high thresholds are used to distinguish between electrons and charged pions.

Performance

Table 2.3 lists some ATLAS ID design parameters like the accuracy of the different modules. The alignment of the ATLAS tracking system has been studied with $\sqrt{s} = 7$ TeV collision data in [84, 85] and the module resolution has been determined. The new *Autumn 2010 Alignment* investigated in [85] is compared to the previous *Spring 2010 Alignment* and the hit-on-track residuals for Pixel, SCT and TRT, barrel and end-cap each, are shown in Fig. 2.7. The distributions for Pixel and SCT are projections onto the local x direction. The determined module resolutions are $\sigma = 9\,\mu$m ($\sigma = 15\,\mu$m) for

the Pixel barrel (end-caps), $\sigma = 25\,\mu$m ($\sigma = 30\,\mu$m) for the SCT barrel (end-caps), and $\sigma = 118\,\mu$m ($\sigma = 132\,\mu$m) for the TRT barrel (end-caps).

Measurements of the performance of the Inner Detector have been studied in [65]. The muon momentum resolution for $1/p_{\mathrm{T}}$ is $0.34\,\mathrm{TeV}^{-1}$ in the barrel region, the resolution of the transverse impact parameter is $10\,\mu$m, the muon charge misidentification is in order of a few percent for p_{T} up to 1 TeV, and the reconstruction efficiency in the barrel is almost 100%. The electron charge misidentification is comparable to the muon charge misidentification, but the electron reconstruction efficiency suffers from material effects such that the reconstruction efficiency is between 70% and 90% at $p_{\mathrm{T}} = 25\,\mathrm{GeV}$. The vertexing has a high efficiency, primary and secondary vertices can be measured with an efficiency of 99% in the presence of low-luminosity pile-up.

2.2.3 Calorimetry

The calorimeters are needed to measure the energy of the final state objects. As the tracking components are designed to absorb as less energy of a crossing particle as possible, the calorimeters are designed to stop and absorb the particles completely. Therefore, the calorimeters are several radiation/interaction length deep and, in case of the ATLAS calorimeter, designed as sampling calorimeters. A sampling calorimeter consists of several layers of active and passive absorber material. In the dense absorber the specific particles interact with the absorber material and cause showers, whereas the active material is measuring the deposited energy. In order to measure both electromagnetically and hadronically interacting particles, an electromagnetic calorimeter is encased by a hadronic calorimeter. As long as a particle is interacting electromagnetically or hadronically, the particle will be absorbed by the calorimeter and the energy can be measured. Only weakly interacting particles can pass the calorimeter system. If a calorimeter with a fine granularity is used, a precise position measurement can be done and matched with geometrical information from the tracking system. The shower shape of a specific decay can be used to distinguish for example electrons from pions or hadronically decaying τ-leptons from QCD-jets.

The ATLAS calorimeter system [86, 87] consists of four different calorimeters: the electromagnetic calorimeter, the hadronic tile calorimeter, the hadronic end-cap calorimeter and the forward calorimeter. Figure 2.8 shows an overview of the ATLAS calorimeter system, the pseudorapidity coverage, granularity, and segmentation in depth of the calorimeters are summarised in Tab. 2.4. The very fine granularity of the EM calorimeter is designed for precision measurements of electrons and pions, whereas the coarser granularity of the other calorimeters is designed to full-fill the requirements of jet reconstruction and missing transverse energy measurements. In order to measure the complete energy of a particle and to avoid punch-throughs into the muons system, the thickness of the calorimeter is important. The EM calorimeter is > 22 (> 24) radiation lengths (X_0) deep in the barrel (end-caps) and the depth of the tile calorimeter is 7.4 interaction lengths (λ). The combination of the thickness of the calorimeter systems and the large η-coverage guarantees a good $E_{\mathrm{T}}^{\mathrm{miss}}$ measurement, which is a crucial variable for many SUSY searches.

Electromagnetic Calorimeter

The electromagnetic calorimeter (ECal) of the ATLAS detector is a lead-liquid-Argon (LAr) calorimeter [86]. The lead layers are the absorber material and the liquid Argon

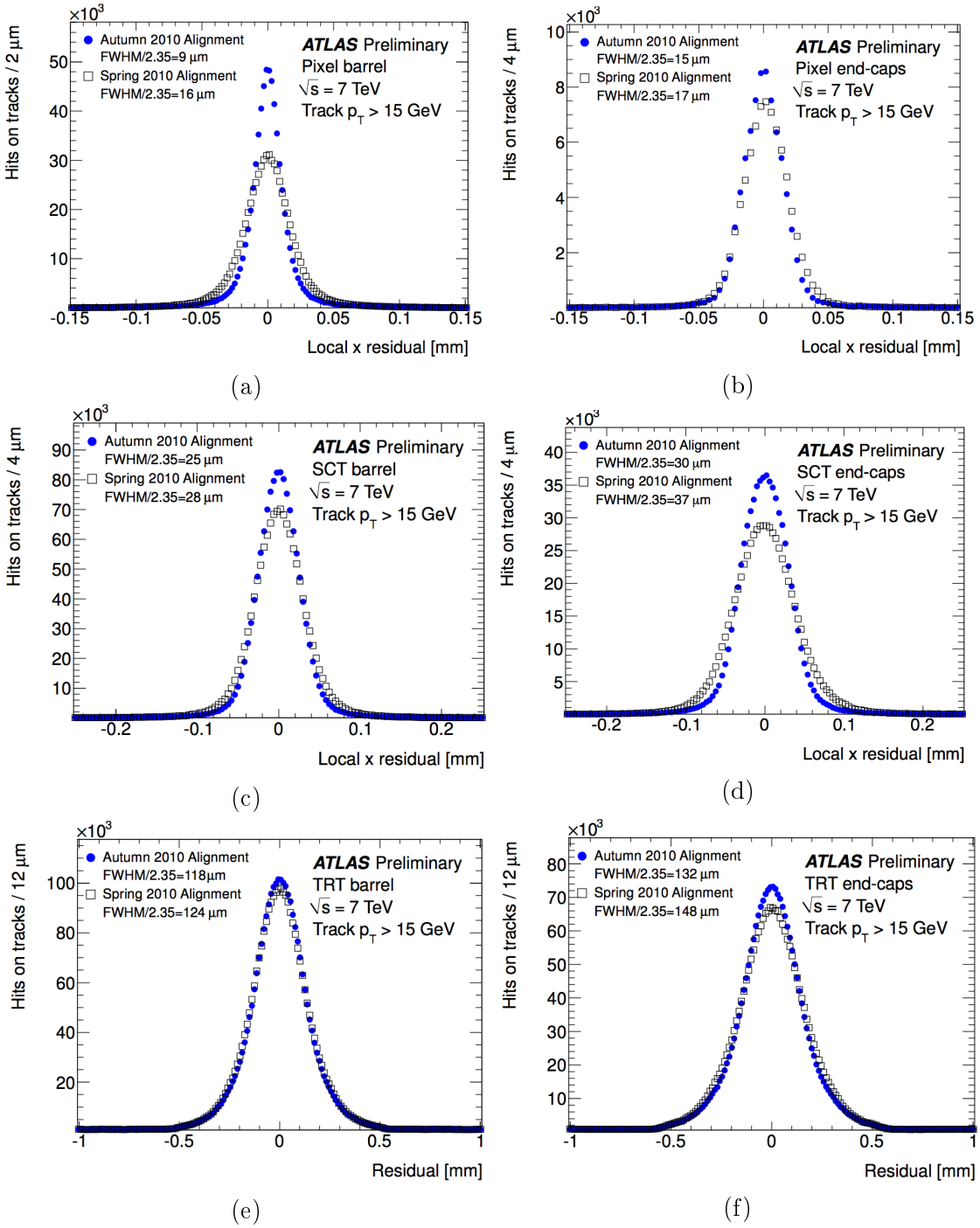

Figure 2.7: Tracking local x residual distributions obtained by reconstructing the jet trigger data sample with the *Spring 2010 Alignment* (open squares) and *Autumn 2010 Alignment* (solid circles). The distributions are integrated over all hits-on-tracks in the Pixel barrel and end-cap modules (a,b), SCT barrel and end-cap modules (c,d), and TRT barrel and end-cap modules (e,f). Tracks are required to have $p_{\mathrm{T}} > 15\,\mathrm{GeV}$ [85].

Table 2.4: Main parameters of the calorimeter system [65].

	Barrel		End-cap	
EM calorimeter				
Number of layers and $\|\eta\|$ coverage				
Presampler	1	$\|\eta\| < 1.52$	1	$1.5 < \|\eta\| < 1.8$
Calorimeter	3	$\|\eta\| < 1.35$	2	$1.375 < \|\eta\| < 1.5$
	2	$1.35 < \|\eta\| < 1.475$	3	$1.5 < \|\eta\| < 2.5$
			2	$2.5 < \|\eta\| < 3.2$
Granularity $\Delta\eta \times \Delta\phi$ versus $\|\eta\|$				
Presampler	0.025×0.1	$\|\eta\| < 1.52$	0.025×0.1	$1.5 < \|\eta\| < 1.8$
Calo 1st layer	$0.025/8 \times 0.1$	$\|\eta\| < 1.40$	0.050×0.1	$1.375 < \|\eta\| < 1.425$
	0.025×0.025	$1.40 < \|\eta\| < 1.475$	0.025×0.1	$1.425 < \|\eta\| < 1.5$
			$0.025/8 \times 0.1$	$1.5 < \|\eta\| < 1.8$
			$0.025/6 \times 0.1$	$1.8 < \|\eta\| < 2.0$
			$0.025/4 \times 0.1$	$2.0 < \|\eta\| < 2.4$
			0.025×0.1	$2.4 < \|\eta\| < 2.5$
			0.1×0.1	$2.5 < \|\eta\| < 3.2$
Calo 2nd layer	0.025×0.025	$\|\eta\| < 1.40$	0.050×0.025	$1.375 < \|\eta\| < 1.425$
	0.075×0.025	$1.40 < \|\eta\| < 1.475$	0.025×0.025	$1.425 < \|\eta\| < 2.5$
			0.1×0.1	$2.5 < \|\eta\| < 3.2$
Calo 3rd layer	0.050×0.025	$\|\eta\| < 1.35$	0.050×0.025	$1.5 < \|\eta\| < 2.5$
Number of readout channels				
Presampler	7808		1536 (both sides)	
Calorimeter	101760		62208 (both sides)	
LAr hadronic end-cap				
$\|\eta\|$ coverage			$1.5 < \|\eta\| < 3.2$	
Number of layers			4	
Granularity			0.1×0.1	$1.5 < \|\eta\| < 2.5$
$\Delta\eta \times \Delta\phi$			0.2×0.2	$2.5 < \|\eta\| < 3.2$
Readout chan.			5632 (both sides)	
LAr forward calorimeter				
$\|\eta\|$ coverage			$3.1 < \|\eta\| < 4.9$	
Numb. of layers			3	
Granularity			FCal1. 3.0×2.6	$3.15 < \|\eta\| < 4.30$
$\Delta x \times \Delta y$ (cm)			FCal1.	$3.10 < \|\eta\| < 3.15$,
			$\sim 4\times$ finer	$4.30 < \|\eta\| < 4.83$
			FCal2. 3.3×4.2	$3.24 < \|\eta\| < 4.50$
			FCal2.	$3.20 < \|\eta\| < 3.24$,
			$\sim 4\times$ finer	$4.50 < \|\eta\| < 4.81$
			FCal3. 5.4×4.7	$3.32 < \|\eta\| < 4.60$
			FCal3.	$3.29 < \|\eta\| < 3.32$,
			$\sim 4\times$ finer	$4.60 < \|\eta\| < 4.75$
Readout chan.			3524 (both sides)	
Scintillator tile calorimeter				
	Barrel		Extended barrel	
$\|\eta\|$ coverage	$\|\eta\| < 1.0$		$0.8 < \|\eta\| < 1.7$	
Numb. of layers	3		3	
Granularity	0.1×0.1		0.1×0.1	
$\Delta\eta \times \Delta\phi$				
Last layer	0.2×0.1		0.2×0.1	
Readout chan.	5760		4092 (both sides)	

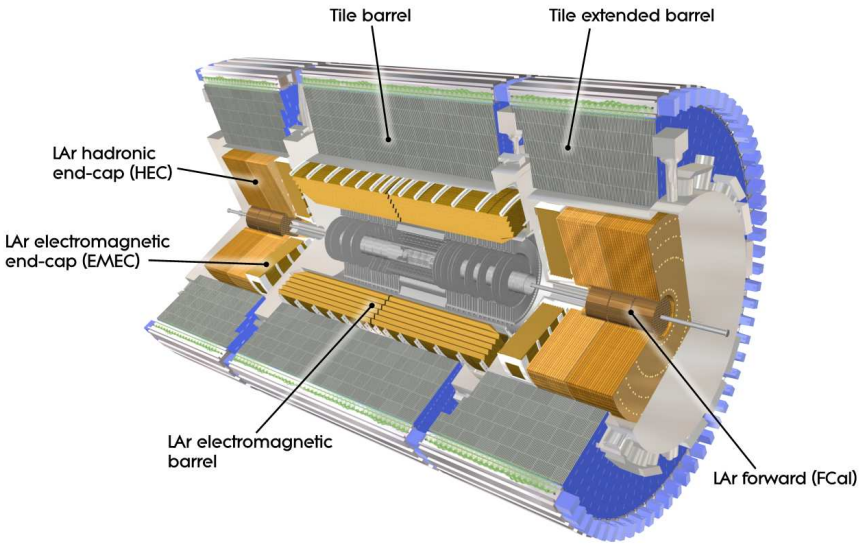

Figure 2.8: The ATLAS Calorimeter system. It contains of the electromagnetic calorimeter (ECal) and the hadronic calorimeter (HCal). The two modules of the ECal are the LAr EM Barrel and the LAr EM Endcap. The HCal consists of the Tile Barrel and the Extended Tile Barrel, the Hadronic End-cap and the Forward Calorimeter near the beam axis [88].

layers serve as active material. The ECal consists of a barrel ($|\eta| < 1.475$) and two end-caps ($1.375 < |\eta| < 3.2$) each covered by their own cryostat. The barrel is split into two parts with a gap of 4 mm at $z = 0$. Both half-barrels are 3.2 m long. The end-caps are divided as well, in a inner wheel covering $2.5 < |\eta| < 3.2$ and an outer wheel covering $1.375 < |\eta| < 2.5$. As shown in Fig. 2.9 the calorimeter is designed in an accordion shape geometry. This provides a complete ϕ uniform coverage without azimuthal cracks. In the calorimeter region ($\eta < 2.5$) which is optimized for precision physics the calorimeter is segmented in three sections in depth (Fig. 2.9). The inner end-cap is divided into two segments in depth with a coarser lateral granularity.

The first segment shown in Fig. 2.9 has a very fine granularity in η which allows to distinguish the photons from neutral pion decays. This is also important to separate single photons from electrons or inside jets or τ-lepton decays. The second layer is 16 radiation lengths deep and absorbs most of the energy. This sampling consists of cubic cells of size $\Delta\eta \times \Delta\phi = 0.025 \times 0.025$. This layer has a much better ϕ resolution than the first sampling and is used to determine the ϕ position of a signal. The third layer is only 2 X_0 thick and is used to determine the leakage into the hadronic calorimeter. In the region of $\eta < 1.8$ a LAr presampler is installed to correct the energy losses of electrons and photons in the Inner Detector, the solenoid, or support structures. It consists of an active LAr layer of thickness 1.1 cm (0.5 cm) in the barrel (end-cap) region.

Performance

The energy resolution has been determined in test-beam measurements [89], simulation studies and for example in the electron performance paper with the 2010 data set [90] (cf. Sec. 4.1.3). The energy resolution from the test-beam has been fitted with the following

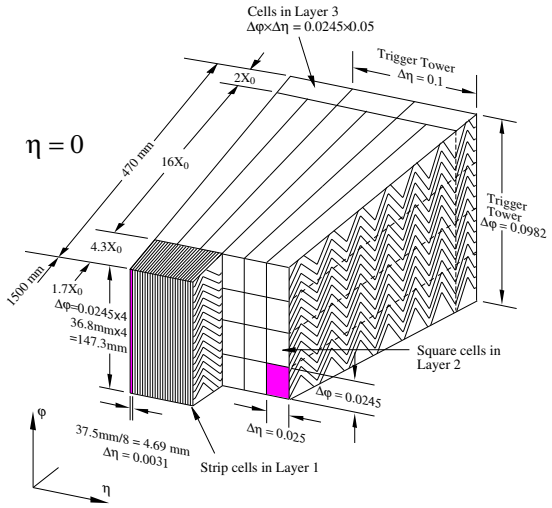

Figure 2.9: The ATLAS Electromagnetic Calorimeter is built in three different layers. The first layer is very high granulated in η to separate γ and π^0 but not in ϕ. Hence the second layer is squared to get an η and ϕ resolution. The third layer the so-called tail catcher registers an occurring leakage of calorimeter [65].

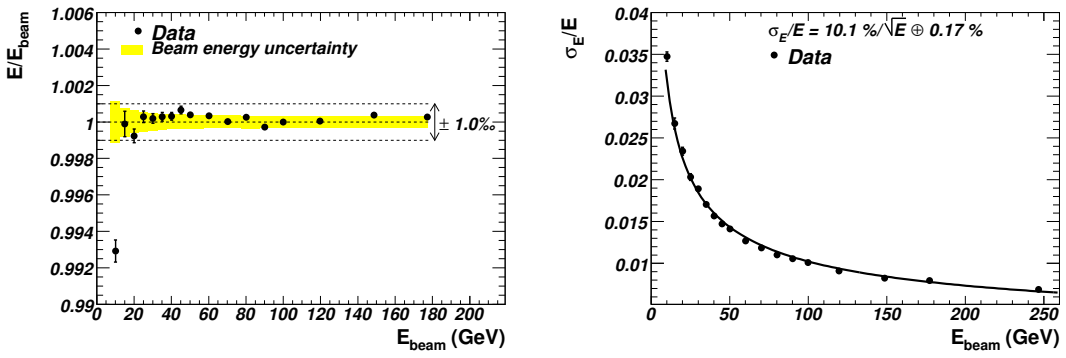

(a) (b)

Figure 2.10: Linearity of response as a function of the electron beam energy, E_{beam}, for a barrel LAr electromagnetic module at $|\eta| = 0.687$. All points are normalised to the value measured at $E_{beam} = 100\,\text{GeV}$. The band represents the total uncertainty on the beam energy measurement (a).The fractional energy resolution as is shown as a function of the electron beam energy, E_{beam}, for a barrel LAr electromagnetic module at $|\eta| = 0.687$. Electronic noise was subtracted from the data before plotting the results. The curve represents the results of a fit to the data using Eq. (2.6) [65].

parametrization [89]:

$$\frac{\sigma(E)}{E} = \frac{a}{\sqrt{E[GeV]}} \oplus b \tag{2.6}$$

where $a = 10\% \cdot \sqrt{E[\text{ GeV}]}$ is a stochastic term and $b = 0.17\%$ is a constant term. The fitted function is shown in Fig. 2.10(a). The energy response is linear within $\pm 0.1\%$ in the energy range form $15\,\text{GeV} - 180\,\text{GeV}$ (cf. 2.10(b)).

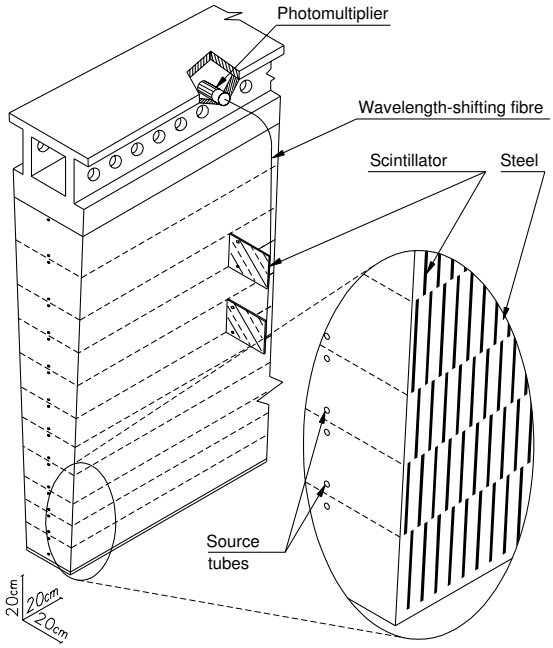

Figure 2.11: Schematic showing how the mechanical assembly and the optical readout of the tile calorimeter are integrated together. The various components of the optical readout, namely the tiles, the fibres and the photo-multipliers, are shown. [65]

Hadronic Calorimeter

The hadronic calorimeter (HCal) [87] is measuring the deposited energy of jets and hadronically decaying τ-leptons. The missing transverse energy is calculated from both the energy deposition in the ECal and in the HCal, therefore it is important to achieve a good η and ϕ coverage.

The **Tile Calorimeter** is placed around the ECal. It consists of a barrel covering $|\eta| < 1.0$ and two extended barrels covering $0.8 < |\eta| < 1.7$. It is a sampling calorimeter with steel as absorber material and scintillating tiles as active material. As shown in Fig. 2.11, the light produced in the scintillators is collected at the edge of each tile. The tiles are read out on both sides by wavelength shifting fibres. The fibres are grouped together and coupled to photo-multipliers. The grouped fibres define a three-dimensional cell structure. Those cells are segmented in three radial sampling depth of $\lambda = 1.5$, $\lambda = 4.1$ and $\lambda = 1.8$. The two inner cells have a dimension in $\Delta\eta \times \Delta\phi$ of 0.1×0.1 and the outer layer of 0.2×0.1.

LAr hadronic end-cap calorimeter (HEC) The active material in the hadronic end-caps is liquid argon, because of the high radiation exposure. Parallel arranged copper plates are used as absorber. The HEC is placed directly behind the end-cap electromagnetic calorimeters and is using the same LAr cyrostats. It consists of two wheels per end-cap. The readout cells are of size $\Delta\eta \times \Delta\phi = 0.1 \times 0.1$ for $|\eta| < 2.5$ and $\Delta\eta \times \Delta\phi = 0.2 \times 0.2$ for larger values in $|\eta|$.

The **LAr forward calorimeter** (FCal) consists of three modules in each end-cap. All of them are using liquid argon as active medium, but they have different absorber materials. The first layer is using copper, it is optimized for electromagnetic measurements.

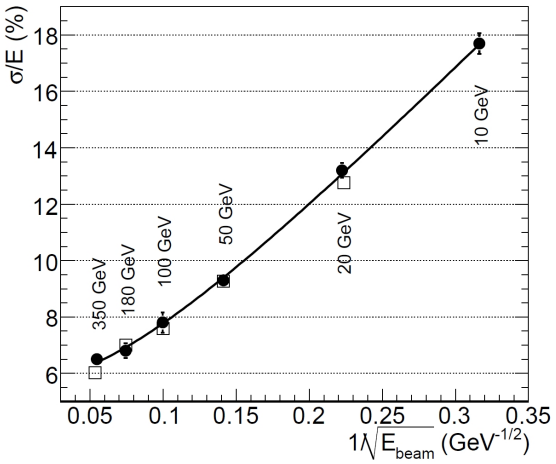

Figure 2.12: The tile-calorimeter-standalone energy resolution for pions impinging on the calorimeter at $|\eta| = 0.35$ (equivalent calorimeter depth 7.9λ), as a function of the beam energy. MC simulation results (Geant4.8.3 QGSP+Bertini models, shown with open squares) are in agreement with data (full circles). The electronic noise contribution is found to be negligible, so that only statistical and constant terms are used in the fit. Note that in the ATLAS configuration the total calorimeter (EM LAr + Tilecal) depth is larger by about 30%, hence the longitudinal leakage is smaller and its contribution to the energy resolution degradation is smaller. The expected constant term for jet energy resolution in ATLAS is typically 2.6% [91].

The outer two modules using tungsten measuring predominantly the energy of hadronic interactions. Each module is 45 cm long, such that the FCal is about 10 radiation length deep in total.

Performance

The tile-calorimeter stand-alone performance has been measured in dedicated test-beam periods [65] at the CERN SPS. The fractional energy resolution σ_E/E for isolated pions reported in [91] has been studied as a function of the test-beam energy and the impact angle. Figure 2.12 shows the measured resolutions for $\eta = 0.35$ and the fit according to Eq. (2.6). The best fit yields $a = (52.9 \pm 0.9)\,\%/\ \mathrm{GeV}^{1/2}$ and $b = (5.7 \pm 0.2)\,\%$. This corresponds to $\sigma_E/E = (14.2 \pm 0.1)\,\%$ at $\eta = 0.25$ and $E = 20\,\mathrm{GeV}$, and $\sigma_E/E = (6.6 \pm 0.1)\,\%$ at $\eta = 0.25$ and $E = 350\,\mathrm{GeV}$, respectively [65].

2.2.4 Muon System

The outermost sub-detector of the ATLAS detector is the muon system [92]. Only weakly interacting particles like muons, neutrinos or particles from new physics should reach the muon spectrometer, while other particles are mostly absorbed by the calorimeter system. In order to get a precise momentum measurement, an additional magnetic field provided by the three toroids (one barrel and two end-caps cf. Sec. 2.2.1) is installed. The muon system consists of four different gaseous detector technologies: monitored drift tubes (MDT), cathode strip chambers (CSC), resistive plate chambers (PRC), and thin-gap chambers (TGC) as shown in Fig. 2.13. The first two systems are used for precision

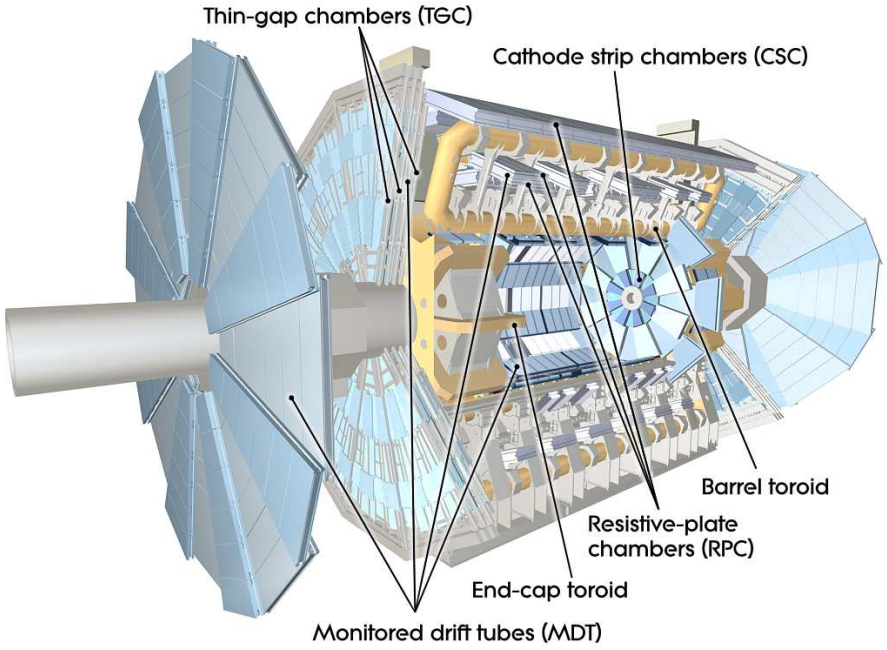

Figure 2.13: The ATLAS Muon system divided in a detection and a trigger system. Both are separated into barrel and end-cap region. The detection system are the Monitored Drift Tubes and the Cathode Strip Chambers and the trigger system are the Resistive Plate Chambers and the Thin Gap Chambers. The end-cap toroids and the barrel toroid produce a 1 T and a 0.5 T magnetic field to deviate the muons for better identification [65].

measurements and the last two technologies are less precise, but much faster, such that they are used as muon detectors for the muon trigger systems.

Precision Tracking Chambers

The precision measurements are performed mainly by the MDTs, they cover the $|\eta|$-range up to 2.7 (except the outermost wheel with $|\eta| < 2.0$). The MDTs consist of three to eight layers of drift tubes. The tubes are filled with a gas mixture of 93% Ar and 7% CO_2 operated at an absolute pressure of 3 bar. They are made of aluminium and have a diameter of 30 mm. The position of the crossing muon is determined by the drift time of electrons to the anode wires which have been produced by ionizing muons. The maximal drift time is 700 ns. The resolution is 80 μm per tube and about 35 μm per chamber.

The forward region is covered by the CSCs. Those are multi-wire proportional chambers with cathode planes segmented into strips in orthogonal directions. The gas mixture used in the CSCs is 30% Ar, 50% CO_2, and 20% CF_4. The track coordinates are determined by induced-charge distributions on the cathode strip. In the bending plane a resolution of 40 μm can be achieved, whereas the transverse plane has a resolution of 5 mm. The lower resolution in the transverse plane is due to the fact that the readout runs parallel to the anode wire. Compared to the MDTs, the CSCs have a better time resolution and high rate capability.

In order to achieve the performance goal of a resolution of 10% for 1 TeV tracks, the position of the wires of the MDTs and the CSCs has to be known with a precision

Table 2.5: Parameters of the four sub-systems of the muon detector. The quoted spatial resolution (columns 3, 4) does not include chamber-alignment uncertainties. Column 5 lists the intrinsic time resolution of each chamber type, to which contributions from signal-propagation and electronics contributions need to be added. Numbers in brackets refer to the complete detector configuration as planned for 2009. [65]

		Chamber resolution (RMS) in			Measure./track		Number of	
Type	Func.	z/R	ϕ	time	barrel	end-cap	chamb.	chan.
MDT	track.	35 mm (z)	-	-	20	20	1088	339k
							(1150)	(354k)
CSC	track.	40 mm (R)	5 mm	7 ns	-	4	32	30.7k
RPC	trig.	10 mm (z)	10 mm	1.5 ns	6	-	544	359k
							(606)	(373k)
TGC	trig.	2 – 6 mm (R)	3 – 7 mm	4 ns	-	9	3588	318k

of better than 30 μm. This is done with a very precise optical laser-based alignment system which monitors the position and deformations of the muon system. In addition track alignment corrections based on methods like tag-and-probe measured in data as described in Sec. 4.2.3 are applied to the different analysis.

Trigger Chambers

The precision measurement muon detectors are not fast enough to be used as trigger. Therefore additional fast trigger chambers have been designed and added to the ATLAS muons system. In the barrel region $|\eta| < 1.05$, RPCs with a time resolution of 1.5 ns have been installed. Those chambers are also gaseous detectors, but they do not use a wire as anode but parallel resistive plates with a distance of 2 mm. An electric field of 4.9 kV/mm is applied in order to measure electrons produced by ionizing tracks.

The end-caps are covered by TGCs ($1.05 < |\eta| < 2.4$) with a time resolution of 4 ns. The TGCs are multi-wire proportional chambers like the CSCs, but with a smaller anode cathode distance and another gas mixture in order to achieve a better time resolution. In addition to the time measurement, it also provides the coordinates of the azimuthal coordinate of the muon track.

Performance

The muon spectrometer performance has been measured in cosmic muons events [93] and in collision data [94, 95]. The results from the collision data study from [95] are described for stand-alone muon tracks and combined tracks from ID and muon spectrometer in detail in Sec. 4.2.

2.2.5 Trigger System

The LHC design bunch crossing rate is 40 MHz with 25 interactions per bunch crossing. This yields an interaction rate of approximately 1 GHz. The capacity for storing data to disc is about 200 Hz. This limit corresponds to an average data rate of $\sim$ 300 MB/s. In order to reduce the amount of data and filtering the interesting events, a dedicated trigger system has been designed. The ATLAS trigger system [96, 97] consists of three

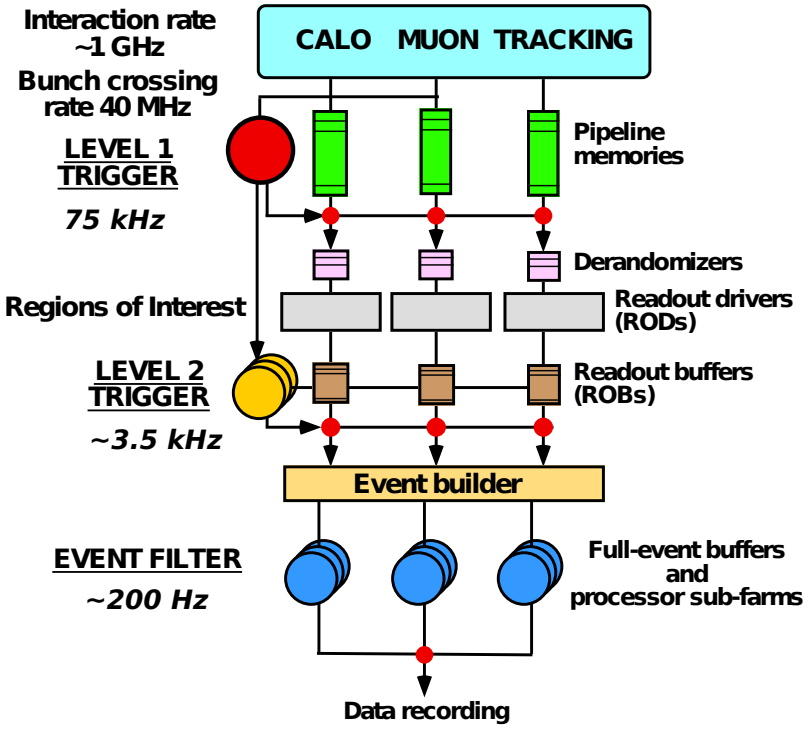

Figure 2.14: The three steps of the ATLAS Trigger System: the **Level 1** trigger, the **Level 2** trigger and the **Event Filter**. It reduces the total data rate from 1 GHz to about 200 Hz [96].

trigger levels: Level 1 (L1), Level2 (L2) and the Event Filter (EF). Each level reduces the amount of data by refining the decisions made by the previous trigger level.

Figure 2.14 shows a schematic of the ATLAS trigger system. Detector signals are buffered in *front end pipelines* during the decision making of the L1 which is implemented in a fast customs electronics analysing a limited amount of event information only. It runs on every bunch crossing, therefore it has to make a decision in 2.5 μs and reduces the rate to < 75 kHz. In addition to the first event filtering the L1 trigger is identifying the *Regions of Interest* (ROI) which are investigated furthermore by the High Level Trigger (HLT) consisting of the L2 trigger and the EF.

The HLT system is software based. It is installed on a computing farm. The system is designed having 500 nodes required for the L2 trigger and 1800 nodes for the EF. If an event is accepted by the L1 trigger, the data from each sub-detector buffered in the readout pipelines are transferred to the detector-specific read out buffers (ROB). ROBs from one or more detector systems, corresponding to detector elements within one ROI, are grouped together into the *Readout Systems* (ROS) which are connected to the HLT network. The L2 trigger analyses the data inside the ROIs via fast custom algorithms. About 2-6% of the total data volume is analysed by the L2 trigger. It has ~ 40 ms for making the decision per event and reduces the rate to < 3.5 kHz.

If an event is accepted by L2, the Event Builder is collecting the event fragments from the ROBs, providing full event information to the EF. The EF is using the same reconstruction algorithms as used for the offline reconstruction. However, EF objects might differ slightly from the offline reconstructed objects, because some calibration and

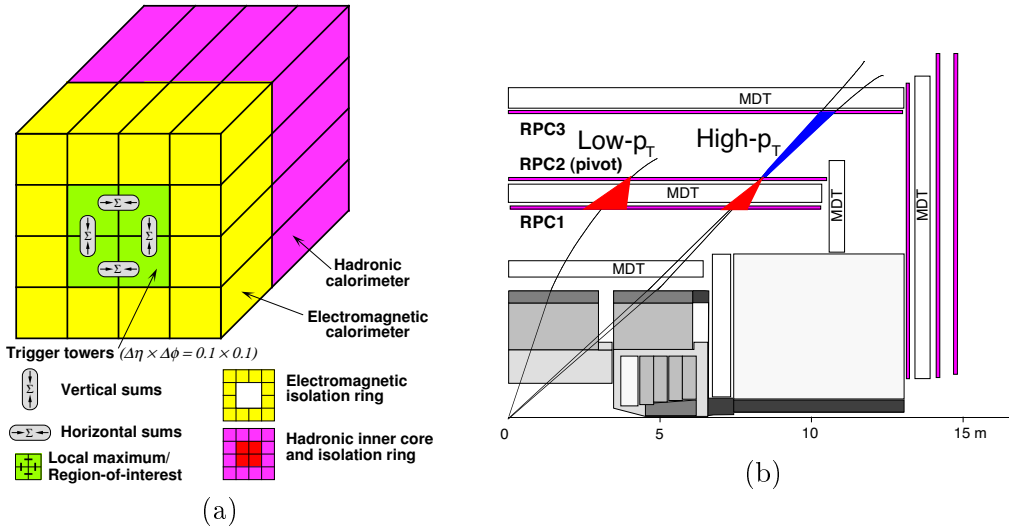

Figure 2.15: The L1 electron/photon and tau trigger algorithms is shown in (a). The RPC's are arranged in three stations: RPC1, RPC2, and RPC3. Also shown are the low-pT and high-pT roads (b) [65].

alignment constants are not adjusted in time for the online decision making. The EF requires in average $\sim 4\,\mathrm{s}$/event for the processing and reduces the rate to $\sim 200\,\mathrm{Hz}$.

Level 1 Trigger

L1 decisions are based on objects with high transverse momentum like muons, electrons, photons, jets, and hadronically decaying tau leptons as well as large missing and total transverse energy. The trigger decision is formed by the Central Trigger Processor (CTP) analysing information from calorimeter trigger towers and dedicated muon trigger layers (cf. Sec. 2.2.4). In addition to the trigger decision, which is made considering the different thresholds and prescales, the CTP is providing the timing signal taken from the LHC bunch crossing. The L1 trigger decision is distributed to the detector-specific read-out systems together with timing and control signals.

The L1 calorimeter decision is based on analogue sums of calorimeter elements within projective regions, so-called *trigger towers*. The trigger towers are of size $\Delta\eta \times \Delta\phi = 0.1 \times 0.1$ in the central part of the calorimeter (cf. Fig. 2.15(a)). The electron/photon trigger algorithm for example, defines a 2×2 trigger tower cluster of interest. If a pair of two neighbours (2×1 or 1×2) exceeds a given threshold, the L1 trigger is fired. Isolation requirements can be applied for tighter selections. Either the 12 cells surrounding the 2×2 cluster are checked for exceeding an isolation-veto threshold, or the 2×2 core of the hadronic cluster behind the interesting electromagnetic cluster is used as a hadronic isolation veto.

The L1 muon decision is based on the muon trigger chambers (cf. Sec. 2.2.4). Those chambers are arranged in three planes, in both barrel and end-caps. The L1 trigger is fired by the muon trigger system if a muon candidate is found in coincidence within different planes. Hits lying within parametrized geometrical muon *roads* (see Fig. 2.15(b)) are considered by forming those coincidences. The minimum muon p_{T} threshold is 6 GeV.

High Level Trigger

The HLT has access to the full calorimeter information, the data from the precision muon chambers, and the Inner Detector hits, in addition to the detector information analysed by the L1 trigger. There is no track reconstruction at L1, because track fitting would be too time consuming for the fast L1 decision. The track fitting is run firstly at L2 where software algorithms are available. Tracking is applied at both L2 trigger and EF only within the ROIs for electron, muon, tau lepton and b-jet signatures. Since the analysis performed in Ch. 6 is based on electron and muon triggers, those algorithms are explained here as examples, more information can be found in [98]:

In order to run the software based algorithms at L2 and EF, trigger framework tools have to be applied to convert the sub-detector specific digital information into input objects like calorimeter cells with energy and geometry. The L2 and EF clustering algorithms have completely different implementations, although they are both software based. As the L2 clustering is optimized for fast processing, the EF clustering is based on the offline software: The L2 clustering is performed within ROIs of size $\Delta\eta \times \Delta\phi = 0.4 \times 0.4$. The cell with most deposited energy in the second calorimeter layer is the seed for cluster. The position is defined as the energy-weighted average of all cell positions. The clustering algorithm, run at EF level, is similar to the offline sliding window algorithm explained in Sec. 4.1.1.

The HLT makes use of the information of the precision chambers (MDT and CSC, cf. Sec 2.2.4), in addition to the information from the muon trigger chambers. The muon candidates found by the L1 trigger are refined by including the precision measurements from the MDTs and CSCs. The L2 trigger investigates muon candidates found by the MS only, combined muons, and isolated muons. In the second case, the algorithm benefits from the ID tracking and combines the MS tracks with the ID tracks. The latter case is starting with combined muon candidates and exploits the calorimeter and tracking information in order to find isolated muons. The EF muon algorithms are using dedicated track extrapolations and fitting methods in order to increase the precision of the muon momentum determination.

As described above, an event has to be accepted by each trigger level before it is finally stored. The criteria for selecting interesting events are pre-defined in so-called trigger menus which define trigger chains. A trigger chain specifies the thresholds and signatures which have to be satisfied by an object triggering an event. The current trigger menus consist of approximately 500 different trigger chains.

The trigger rates must not exceed the capacity of the different trigger levels. In order to record events with high trigger rates like minimum bias events, or events collected for dedicated calibration streams, so-called prescale factors can be applied to each L1 trigger and each HLT chain, such that only 1 in N events is accepted.

The accepted events are written to so-called data streams selected by the trigger system. Three types of *trigger streams* are available: physics streams, calibration streams and one express stream (cf. Data Processing Sec. 3.1.3). The physics streams are inclusive data streams for `egamma`, `muon`, `jetTauEtmiss` and `minBias` selections. An event which is selected by two different triggers corresponding to two different trigger streams, will be written twice, once in each stream. This creates an overlap between streams. Studies at $L = 10^{32}\,\mathrm{cm}^{-2}\mathrm{s}^{-1}$ find significant overlap ($> 1\%$) between two streams for: `egamma-jetTauEtmiss` 14%, `egamma-muon` 2% and `muon-jetTauEtmiss` 4%. The Study presented in Ch. 6 analyses data from the `egamma` and the `muon` stream. In order to

account for the overlap of the streams, a dedicated trigger strategy has been applied (cf. 6.2.1).

Performance

The trigger performance has been studied in [98] for a run in the last pp fill of 2010 data taking (run period I). This particular run had an instantaneous luminosity ranging from $0.85 \times 10^{32}\,\mathrm{cm}^{-2}\mathrm{s}^{-1}$ to $1.8 \times 10^{32}\,\mathrm{cm}^{-2}\mathrm{s}^{-1}$ and an integrated luminosity of $6.4\,\mathrm{pb}^{-1}$. Figure 2.16(a) shows the total L1, L2 and EF output rates as a function of the instantaneous luminosity. The rates have been kept to $\sim 30\,\mathrm{kHz}$ (L1), $\sim 4\,\mathrm{kHz}$ (L2), $\sim 450\,\mathrm{Hz}$ (L1) by adjusting the prescale factors. Each discontinuity of the rates show a change of the prescale factor. The factors for L2 and EF are changed at the same time, the L1 prescale factors are changed individually. It is possible to record data at a significantly higher output rates for a short period of time. During the 2010 data taking, EF rates up to $\sim 600\,\mathrm{Hz}$ have been run successfully. The rates measured in period I are slightly above the design parameters, nevertheless those rates can be processed and stored safely with the current set-up. The total output rates of the different physics streams are shown in Fig 2.16(b).

The total trigger efficiencies in 2010 data taking [98] are greater than 99% for electrons and photons with $E_{\mathrm{T}} > 25\,\mathrm{GeV}$, 94-96% for muons with $p_{\mathrm{T}} > 13\,\mathrm{GeV}$ in regions with full acceptance, greater than 90% for tau leptons with $p_{\mathrm{T}} > 30\,\mathrm{GeV}$, greater than 99% for jets with $E_{\mathrm{T}} > 60\,\mathrm{GeV}$. The missing E_{T} trigger was fully efficient above $100\,\mathrm{GeV}$.

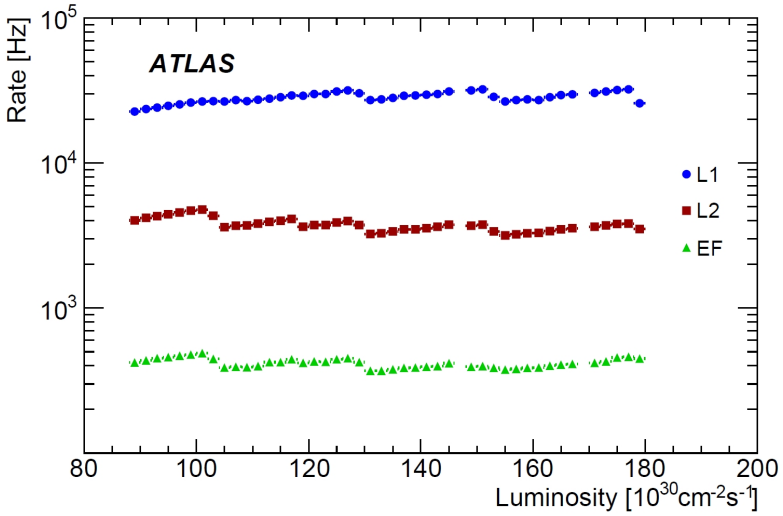

(a)

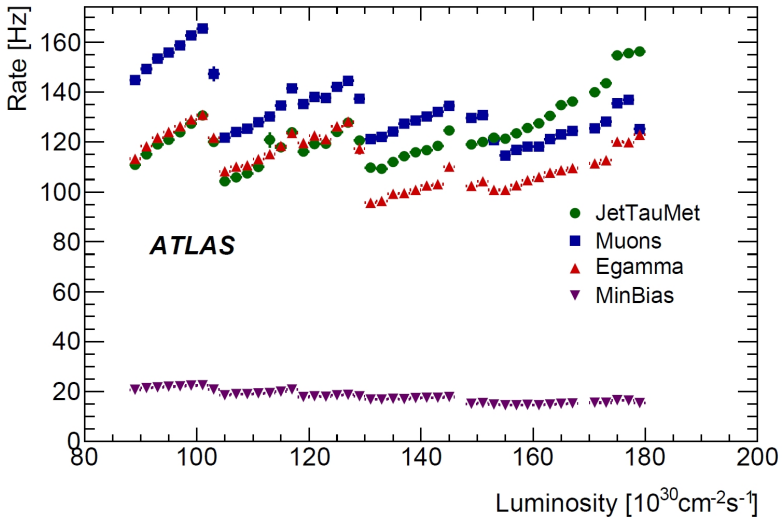

(b)

Figure 2.16: Total output trigger rates as a function of instantaneous luminosity in a sample run from period I for (a) each trigger level and (b) each stream. B-jet triggers are included in the `jetTauEtmiss` stream and B-physics triggers are included in the `muon` stream [98].

3 ATLAS Data Taking and Monte Carlo Generation

The production rate of events like Higgs boson or new physics searches is rather low in comparison to QCD processes or other Standard Model processes, as shown in Fig. 2.2 in Ch. 2. Even after filtering the interesting events by a complex trigger system (Sec. 2.2.5), a huge amount of data needs to be processed and transferred to the different institutes and users such that the data can be analysed.

The information from each detector subsystem has to be readout and combined in order to reconstruct the individual particles. The first part of this chapter addresses the ATLAS data. It gives an overview of the 2011 data taking status and a summary of the ATLAS data quality criteria Sec. 3.1.1. Several data formats are provided by the ATLAS reconstruction software to meet different needs and to reduce the amount of data which is transferred to the institutes all over the world. Those data formats are combined in the ATLAS Event Data Model described in Sec. 3.1.2. Finally, the data processing and reprocessing is described briefly in Sec. 3.1.3.

The second section of this chapter discusses the tasks (Sec. 3.2.1) and implementation (Sec.3.2.2) of the data-driven auto-configuration tool which has been developed as an flexible and uniform tool for an automatized steering of the different data formats and job conditions in the core software as part of this thesis.

After recording and reconstructing the data, individual physics processes have to be understood in order to interpret the results. These processes are simulated with respect to the different behaviour of the interaction within the detector. The third part of this chapter describes the event generation performed by Monte Carlo generators (Sec. 3.3.1), the different Monte Carlo generators used to provide MC used in this study (Sec. 3.3.2), and the simulation of the detector interactions (Sec. 3.3.3).

3.1 ATLAS Data

3.1.1 Data Taking Status and Data Quality

The LHC 2011 period started in March 2011. From March 22nd until October 30th, an integrated luminosity of $5.2\,\mathrm{fb}^{-1}$ of pp-collisions has been recorded by the ATLAS experiment (Fig 3.1(a)). A peak luminosity of $3.65 \times 10^{33}\,\mathrm{cm}^{-2}\mathrm{s}^{-1}$ has been achieved (Fig 3.1(b)).

The quality of the recorded data depends on the reliability of the different sub-detectors and trigger system. Each detector system (Tab. 3.1) and the different ATLAS triggers (Tab. 3.2) have maintained a high efficiency during the so-called stable beam condition. Most detector and magnet systems have an efficiency above 99%. After the 'stable beam' flag is set by LHC, the tracking detectors can ramp up the high-voltage. The efficiencies quoted in Tab. 3.1 do not include the detector dead-times during the ramp up of the tracking detectors. Those inefficiencies are quoted for the ATLAS overall efficiency. The inefficiencies in the LAr calorimeter are mostly due to isolated HV trips and noise

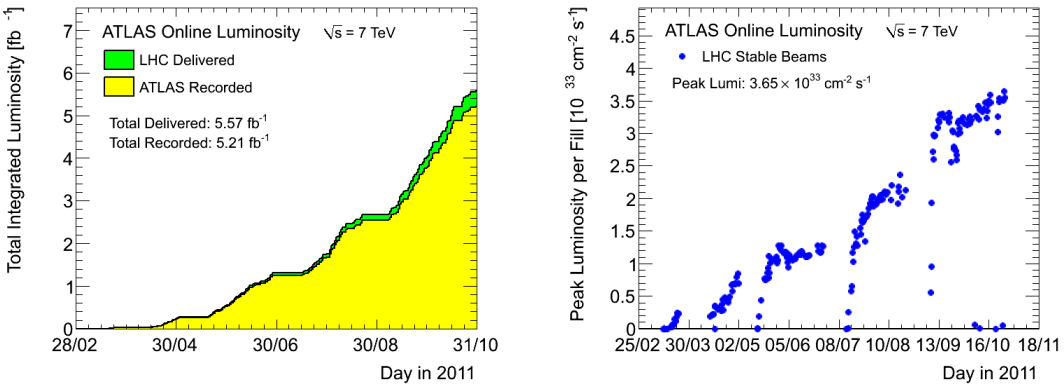

(a) (b)

Figure 3.1: Total integrated luminosity in 2011. (a) The cumulative luminosity delivered to (green), and recorded by ATLAS (yellow) versus the day during stable beams and for pp collisions at 7 TeV centre-of-mass energy in 2011 is shown. The delivered luminosity accounts for the luminosity delivered from the start of stable beams until the LHC requests ATLAS to turn the sensitive detectors off to allow a beam dump or beam studies. Given is the luminosity as determined from counting rates measured by the luminosity detectors. These detectors have been calibrated with the use of the van-der-Meer beam-separation method, where the two beams are scanned against each other in the horizontal and vertical planes to measure their overlap function. (b) The maximum instantaneous luminosity versus day delivered to ATLAS. The luminosity determination is the same as described above for the integrated luminosity. Only the peak luminosity during stable beam periods is shown [99].

bursts. The other small inefficiencies are due to individual isolated problems of a given sub-detector. The efficiency of the ATLAS trigger system quoted in the Tab. 3.2 is almost 100%. The slight inefficiency of the High Level jet trigger is due to a misconfiguration associated with specific calorimeter conditions that occurred during two runs. However, all high events containing p_{T} jets were still successfully triggered and recorded.

A specific ATLAS data quality infrastructure [100] is used to consider the status of each detector subsystem in order to determine the quality of the recorded data. Primary data quality (DQ) flags show the readiness of each detector subsystem in the form of 'traffic lights'. The final analysis is interested in physics objects. Each physics object requires several good primary DQ flags. For example, an electron in the barrel requires the data quality to be good for magnets, tracking subsystem, tracker alignment, and the barrel parts of both electromagnetic and hadronic calorimeter systems. Combined performance and trigger groups have established requirements to declare data as good/flawed/bad for given physics objects (electrons, photons, muons, τs, jets, MET, b-tagging, trigger slices, luminosity determination, etc.) such that complex physics analysis like SUSY searches require to have green light for all objects associated to the physics process they are searching for.

The ATLAS data-taking is divided into runs (nominally an LHC run) and luminosity blocks (LB), discrete periods $60 - 120$ s. The length of the LBs is chosen in order to get stable detector conditions per LB. In order to keep as much data as possible with a sufficient data quality, so called *GoodRunsLists* (GRLs) are provided for each kind of

Table 3.1: Luminosity weighted relative fraction of good quality data delivery by the various ATLAS subsystems during LHC fills with stable beams in pp collisions at $\sqrt{s} = 7\,\text{TeV}$, and after switching the tracking detectors on. Runs between March 13th and August 13th, corresponding to a recorded integrated luminosity of $2.33\,\text{fb}^{-1}$ are accounted. The table corresponds to the DQ tag DetStatus-v25-pro08-v06 for periods B-K2 and DetStatus-v08-pro07 for period A [101].

Inner Tracking Detectors			Calorimeters				Muon Detectors				Magnets	
Pixel	SCT	TRT	LAr EM	LAr HAD	LAr FWD	Tile	MDT	RPC	CSC	TGC	Solenoid	Toroid
99.9	99.9	100	90.0	91.3	94.8	98.2	99.5	99.7	99.9	99.6	99.6	99.4

Luminosity weighted relative detector uptime and good quality data delivery during 2011 stable beams in pp collisions at √s=7 TeV between March 13th and August 13th (in %). The inefficiencies in the LAr calorimeter will largely be recovered in the future.

Table 3.2: Luminosity weighted relative fraction of good quality data delivery by the various components of the ATLAS trigger system during LHC fills with stable beams in pp collisions at $\sqrt{s} = 7\,\text{TeV}$, and after switching the tracking detectors on. Runs between March 13th and June 29th, corresponding to a recorded integrated luminosity of $1.25\,\text{fb}^{-1}$ are accounted. The table corresponds to the DQ tag DetStatus-v18-pro08-v04 for periods B-H and DetStatus-v08-pro07 for period A [101].

Level 1			High Level Trigger						
Muon	Calo	CTP	electron	photon	muon	tau	jet	b-jet	missing E_T
100	100	100	100	100	100	99.5	97.3	99.5	100

Luminosity weighted relative trigger quality delivery during 2011 stable beams in pp collisions at √s=7 TeV between March 13th and June 29th (in %).

analysis. The GRLs contain all luminosity blocks per run with good quality data such that in case of a short incident data which was taken during such a 120 seconds block may be rejected only. After applying the SUSY analysis GRLs to the data taken from March 22nd until June 28th (Ch.6) an integrated luminosity $1035.4\,\text{fb}^{-1}$ of good quality data can be analysed.

3.1.2 Event Data Model

The ATLAS Event Data Model (EDM) [102] foresees different data formats with different detail levels resulting in different file sizes per event (Fig. 3.2(b)): The so-called byte stream (BS) is the raw data which is written on tape. This data format is not used for any kind of data analysis. It is the input format for the offline prompt reconstruction and can be used for data reprocessing (cf. 3.1.3). The detailed reconstructed objects are written in Event Summary Data (ESD) files, for detector and reconstruction studies.

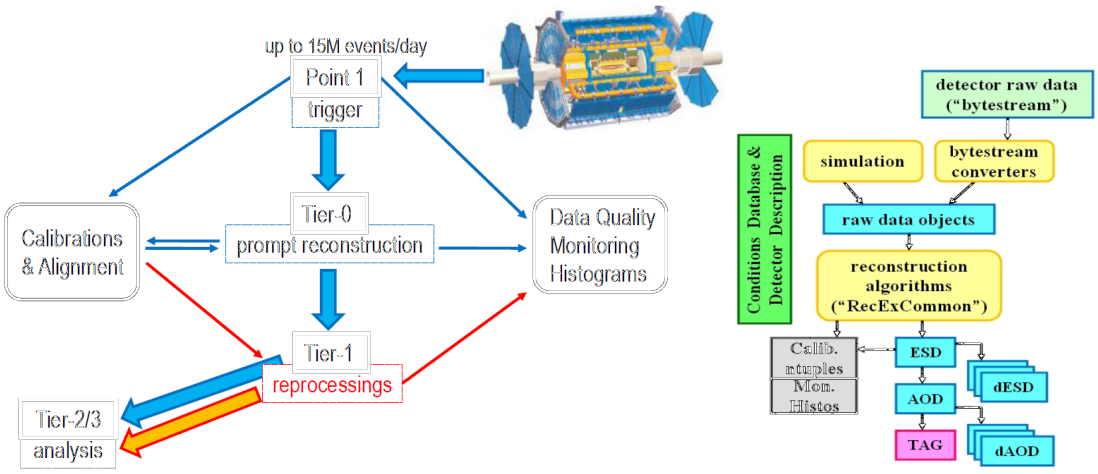

(a) (b)

Figure 3.2: An overview of the ATLAS data flow is shown in (a). The blue arrows illustrate the processing flow. All reconstruction steps are exclusively processed on the Tier0 computing farm. The GRID sites are only used for data transfer and storage. The red arrows mark the reprocessing chain. The re-reconstruction during the reprocessing is performed by the different Tier1 clusters. The ATLAS data formats produced by the ATLAS core reconstruction algorithm (*ReExCommon*) of the ATHENA framework are shown in (b) [103].

Smaller Analysis Object Data (AOD) files are derived from ESD, for physics analysis. TAG, dESD, and dAOD files are provided through further data reduction. TAG allows the selection of individual events by using a kind of *pointer mechanism*. The TAG file contains a specific class of events. In order to analyse these events, the TAG file is pointing to the specific events in AOD files. The dESD and dAOD formats have analysis-specific event filtering further reducing the file sizes. Three different methods for data reduction are implemented: Event skimming, which means that only a specific class of events are written to the data set, uninteresting events are not considered. Another method is the event information thinning, in this case physics objects not necessary for the analysis are not written to the data set. The third method is the so-called slimming, thereby, unnecessary object information is not considered.

3.1.3 Data Processing and Reprocessing Strategy

Events which have passed the ATLAS trigger system are directly reconstructed at the Tier0 computing farm at CERN. The data is processed in so-called *trigger streams* (cf. Sec. 2.2.5). There are three different types of *trigger streams*; the *express stream*, the *calibration streams*, and the four different *physics streams*.

The *express stream* contains about 10% of the data events per run and provides calibration and data quality (DQ) information. The *calibration streams* do not contain complete event information, but partial information from one or more detector sub-systems. These streams are used for detector calibration. Before the full offline reconstruction of a the data runs are processed, the calibration and DQ information have to be available. Therefore, the express streams is proccessed firstly, which is taking a maximum of 36

hours. Afterwards, the reconstruction of the *physics streams* is started using the newly calculated calibration information. The ATLAS reconstruction software ATHENA is providing the different data formats (cf. Fig. 3.2(b)) directly at Tier0. Two copies of the most detailed data formats (ESD) are stored at two different Tier1, the analysis specific data sets are transferred to the Tier2 and Tier3 centers for data analysis (cf. blue arrows Fig. 3.2(a)).

New conditions or configuration parameters can be used for data reprocessing (re-reconstruction of raw data). Reprocessing campaigns are done for two reasons: Firstly, some calibration and alignment parameters can be determined very precisely with dedicated analysis only. After these analysis have been performed, the more precise calibration constants can be taken into account and systematic uncertainties can be reduced. For example the luminosity measurements are done in dedicated *van de Meer* scan (sometimes also called beam separation or luminosity scans) runs [104, 105]. In addition, a complete reprocessing of the recorded raw data is necessary, if the software release is updated and the new version changes the physics results. The reprocessing campaigns are run on the GRID mainly formed by the Tier1 computing centers. The reprocessing is sketched with the orange arrows in Fig. 3.2(a). The same data formates as during the prompt reconstruction are produced.

The Processing, Calibration and Reprocessing of ATLAS Data from LHC Collisions at 7 TeV after the first commissioning phase in 2010 is firstly summarized in [103]. Both, the prompt reconstruction as well as the reprocessing are centrally coordinated reconstruction jobs, such that the derived data formats are provided in a standardized way. The flexible implementation of the ATHENA framework allows the user to modify each reconstruction and identification algorithm and (re)-run the complete reconstruction based on raw data sets if necessary.

3.2 Flexible and uniform Data-Driven Auto-Configuration of ATLAS Reconstruction

The previous sections Event Data Model Sec. 3.1.2 and Data Processing and Reprocessing [103] Sec. 3.1.3 show some tasks of the ATLAS reconstruction software ATHENA. The different detail levels of the ATLAS data formats and the different environments (prompt reconstruction, reprocessing and user analysis) for the reconstruction jobs have to be considered during job configuration. Part of this thesis was the development and commissioning of a flexible and uniform data-driven auto-configuration of the ATLAS reconstruction software. After highlighting the main challenges of the data formats and the job environments, the implementation of the auto-configuration tool is summarized.

3.2.1 Configurations of the Reconstruction Software

As mentioned in Sec. 3.1.2 the reconstruction algorithms have to deal with several data formats. Some conditions are added to the data sets during the prompt reconstruction. This means, that (re)-reconstructions based on formats after ESD level can directly retrieve condition and steering information from the input file. If the reconstruction is run on BS, information like the beam type (cosmic events, collisions, or single beam), magnetic field setup, etc. have to be retrieved either from dedicated data bases or from the task name directly. The main tasks of the auto-configuration tool are the differentiation of the data formats, acquisition of the steering information, and storage

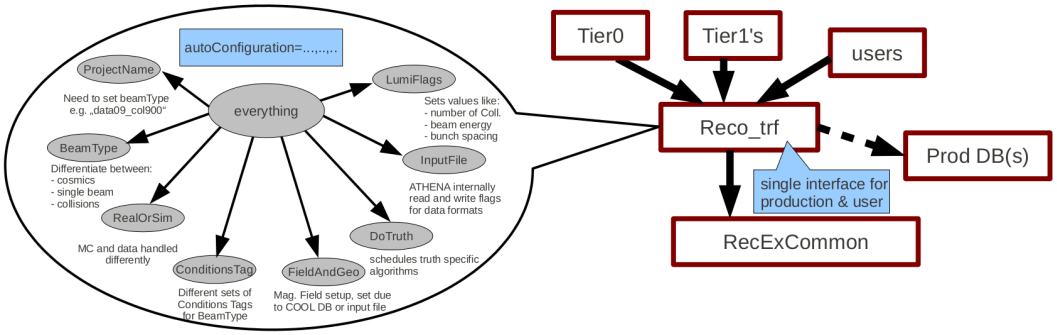

(a) (b)

Figure 3.3: The Auto-configuration tool with specific configuration items is shown in (a). *Reco_Trf* used as common interface for different Tiers and users which is calling the ATLAS core reconstruction algorithm *RecExCommon* is shown in (b) [106].

of the information in the created output file for steering a subsequent reconstruction job without retrieving the information from data bases again, if not necessary. A complete list of all tasks and its implementation is given in Sec.3.2.2.

Input file specific setups are also needed to handle the order of calling the different data formats guaranteeing that only formats with lower detail level are derived from data samples with higher detail level (e.g. ESD $\rightarrow$ AOD $\rightarrow$...).

In addition, the configuration is designed to steer real data and reconstruction jobs of Monte Carlo and detector simulation data sets (cf. Sec. 3.3). Some algorithms are Monte-Carlo specific and cannot be run on data samples. Automated steering of these algorithms can avoid wrongly configured job setups.

This, amongst other configuration tasks, can be achieved by using an input file driven auto-configuration. In order to run complete reconstruction chains (ESD....dAOD) at once, a so-called *Reco_trf* script has been implemented which allows chaining several reconstruction tasks.

Running ATHENA in Different Environments

Originally designed for steering the job configuration of the offline reconstruction at Tier0, additional needs have been addressed during the implementation such that the auto-configuration is able to steer the job configuration during online reconstruction at Tier0, the offline reconstruction on the Tier1 GRID and the user analysis, usually run on the work stations in the different institutes. In order to configure in an identical way, the ATLAS core code for Tier0, Production System (Tier1s), and various user jobs, a common interface is needed. In addition, different job setups have to be specified for running reconstruction jobs of Monte-Carlo simulation, cosmic muon events, single beam setup and collision data.

3.2.2 Implementation of the Auto-Configuration Tool

A fully automated job configuration [106] has to full-fill at least the following tasks: the configured jobs have to run in rather different environments, the Tier0 at CERN, the Tiers

from the GRID, and on institute machines for user analysis. It also has to set up different job configurations according to the different detail levels of the various ATLAS derived data sets. To full-fill those tasks, two tools have been developed. An auto-configuration tool, which handles the setup of the configuration parameters by inspecting the meta-data of each input file and a job transform script *Reco_trf*, which is used as a common interface to call *RecExCommon* (the central ATLAS reconstruction code steering all reconstruction algorithms for the different physics objects) from the different Tiers and the users' analysis in the same way.

The auto-configuration tool is a python based steering algorithm, which reads the meta-data of the input file and/or retrieves some information directly from the ATLAS conditions database to configure setup parameters. These parameters have to be set before a reconstruction job can be launched (Fig. 3.3(a).

The auto-configuration has to be added to the individual job option file. It can be run for prompt reconstruction at Tier0, large scale production jobs on the GRID and even for user analysis. To configure all possible items it can be called as:

```
autoConfiguration=everything,
```

or each item can be added separately to a list:

```
autoConfiguration='BeamType,InputFile,..'.
```

The auto-configuration tool does not override any user specification.

A brief overview of all items that can be auto configured is listed below:

- ProjectName: stored in the *Conditions Objects for LCG* (COOL) data base [107]; can be used to extract the beam type and the beam energy.
- BeamType: internal flag to differentiate between single beam, cosmic data, collision data, and heavy ion runs.
- RealOrSim: differentiates data from Monte-Carlo samples.
- ConditionsTag: according to the magnetic field setups, the express and physics streams as well as for reprocessing various condition tags are available. The condition tags are stored in the conditions data base and in the meta-data of the derived data formats.
- FieldAndGeo: ATLAS has different geometry versions, whereas the appropriate one has to be set before launching a reconstruction job. The correct magnetic field setup has to be chosen according to the detector conditions.
- DoTruth: used to steer Monte-Carlo specific algorithms.
- InputFile: the data format can be set according to the input file.
- LumiFlags: number of collisions and bunch spacing can be configured according to meta-data.

Reco_trf is a single interface which can be used for prompt reconstruction (at Tier0), for MC production, reprocessing (e.g. Tier1), and for user jobs (Fig 3.3 right). Based on the input file and a list of output files, *Reco_trf* can automatically configure one or more chained ATHENA job(s). Combining the data-driven auto-configuration and the common reconstruction interface simplifies the job configuration to a few lines of code:

```
Reco_trf.py
  inputBSFile=data09_900GeV.00142193.physics MinBias.merge.RAW.10evts.data
  autoConfiguration=everything outputESDFile=myESD.pool.root
  outputAODFile=myAOD.pool.root outputDESD_PIXELCOMMFile=PIXELCOMM.pool.root
```

The complete job configurations used during the centrally run production jobs are stored in so-called tags (e.g. f215). The tags are stored for bookkeeping in the ATLAS Metadata Interface (AMI) data base [108] such that each user can rerun reconstruction jobs with identical job option commands. Therefore the *Reco_ trf.py* script has to be executed with the specified AMI tag:

```
Reco_trf.py AMI=f215
```

The complexity and the different purposes of the ATLAS reconstruction software yield a solution requiring two separate tools for job configuration and submission. As described above, a combined development of a data-driven auto-configuration tool and a unified configuration interface *Reco_ trf* has been chosen. Using the *Reco_ trf* interface and the auto-configuration tool, the amount of user interaction respectively the computing shifter interactions at Tier0 during data re-/reconstruction has been minimized. In combination with the stored tags in the production data base, it is very useful for the bookkeeping of the centrally running reconstruction jobs (e.g. users can easily reproduce official reconstruction runs).

3.3 Monte Carlo Events

Event generation and detector simulation is an important tool to design, test, and finally to interpret the results of a particle physics experiments. Before a particle physics experiment is built, many studies are done in order to optimize the design according to the physics case which should be analysed. As a second step, the detector simulation has to be done in close cooperation with testbeam measurements on prototype detector (sub)systems. After data taking has started, Monte Carlo generated samples are needed in order to interpret the results found in data.

The Monte Carlo samples which can be compared to data have to be produced step by step. As shown in Fig. 3.4 (left column), three 'simulation' steps are needed, before the 'Monte Carlo data' can be reconstructed by the ATLAS software like 'real data'. After the physics process is generated (3.3.1), the particle detector interactions have to be simulated (3.3.3), finally the simulated detector hits have to be transformed into the same format as the detector response from the experiment, this is done in the digitization step.

3.3.1 Event Simulation

Calculations in quantum mechanics provide only probabilities of an outcome of an experiment. Using event generators with (pseudo) random numbers many events can be simulated and expected distributions can be provided according to the pdf predictions by QCD. Those distributions can be compared with data distributions in order to interpret the results. The complexity of an particle event is simulated in different steps as shown in Fig. 3.5. There exist several event generators, which slightly differ in the implementation of the individual sub-steps of the event generation. But the basic steps like hard

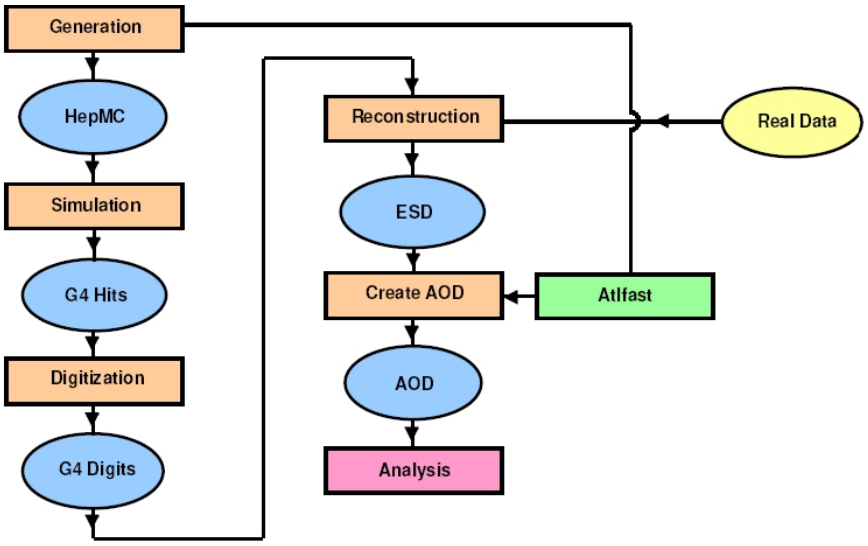

Figure 3.4: The simulation and reconstruction chain of data in the ATLAS framework ATHENA [102]; (blue ellipse) the data formats and (red rectangle) the processes. The left chain describes the event and detector simulation; the right chain the reconstruction and data preparation (this part has to be passed by real data, too (yellow ellipse)). A fast simulation approach is available in order to simulated high statistics in reasonable time (ATLFAST green rectangle). ATLFAST runs the event generation, a simplified detector simulation and the reconstruction in one step [109].

scattering, initial and final state radiation, harmonization, and multiple interactions have to be considered by each implementation such that the concept is described generally as follows:

Hard Scattering

The primary parton interaction of the colliding protons is the hard scattering process (Fig 3.5(a)). It is determined from the matrix elements calculated by perturbation theory. In proton-proton collisions the proton PDF has to be considered during this step. Depending on the individual generator, tree level calculations and or higher order matrix elements are taken into account.

Initial and Final State Radiation

Radiative corrections from QCD and electroweak theory are considered by initial and final state radiation. These corrections can be calculated by the amplitudes of the corresponding matrix elements. Therefore, the Feynman diagrams have to be calculated order by order. Those can be calculated for up to eight partons in the final state giving a quite accurate estimate of the final state multiplicity, but being very time consuming. In case of soft and collinear partons the parton shower approach [110] is applied. The full matrix elements are approximated by simplifying the kinematics such that an arbitary number of branchings of one parton into two or more are used to describe the multijet events. Initial state radiation can be modelled as spacelike parton showers (Fig 3.5(b)), final state radiation as timelike parton showers (Fig 3.5(c)).

Multiple Interactions

Multiple (parton) interactions can occur in proton-proton collision due to the fact that protons consist of more than one parton. If an additional interaction of the two partons associated to the same protons takes place, a second hard scattering process has to be modelled (Fig 3.5(c) black gluon-gluon interaction). The leftovers of the protons (proton-parton from hard scattering) carrying part of the total energy, are colour connected to the rest of the interaction and have to be considered in the calculation (Fig 3.5(e)).

Hadronization

The description of gluon radiation and the interaction of colour-charged particles by the QCD perturbation theory works fine when considering short distances, but it breaks down when confinement becomes dominating (Theory chapter...). Then the hadronization of colour-charged particles into colourless hadrons takes place. This process has to be described by phenomenological models. Monte Carlo generators use different techniques to describe the hadronization. *Pythia* for example uses the so called *string fragmentation model* [111]. In this model, two partons which have been produced together are connected via a one-dimensional string. When the partons are moving apart an increasing amount of energy is stored as potential energy in the string. If the stored energy reaches a certain threshold, the string can break by producing a colourless quark-antiquark pair. Depending on the invariant mass of the string pieces, this process can happen iteratively until only on-shell hadrons are left (Fig. 3.5(f)). The hadrons may decay further via hadronic showers, or directly interact with the detector. As this heavily depends on the detector design this step is not modelled by the event generator, but by the detector simulation GEANT4 described in Sec. 3.3.3.

3.3.2 Event Generators

Pythia

Pythia [113] is used to generate several processes at different colliders. It provides $2 \to 1$, $2 \to 2$, and $2 \to 3$ leading order processes for Standard Model and beyond Standard Model physics. A variety of incoming particles can be processed: pp, $p\bar{p}$, e^+e^-, and $\mu^+\mu^-$. The basic steps needed for a complete event generation described in detail in Sec. 3.3.1 are explained according to the *Pythia* implementation. Even though it is implemented as a general event generator taking into account each step of particle collisions, it can also be used as a showering and hadronization program in other event generator programs not having implemented this step internally. The *string fragmentation model* described above is implemented via the *Lund fragmentation framework* [111].

Herwig

Herwig [114] is a general purpose Monte Carlo generator as *Pythia*. It designed for high-energy processes with particular emphasis on QCD parton showers. Several incoming particles can be processed: hard lepton-lepton, lepton-hadron, and hadron-hadron scattering as well as soft hadron-hadron collisions. The special features of the *Herwig* implementation are: The QCD jet evolution with soft gluon interferences is taken into account via angular ordering. It takes into account colour coherences of partons in all

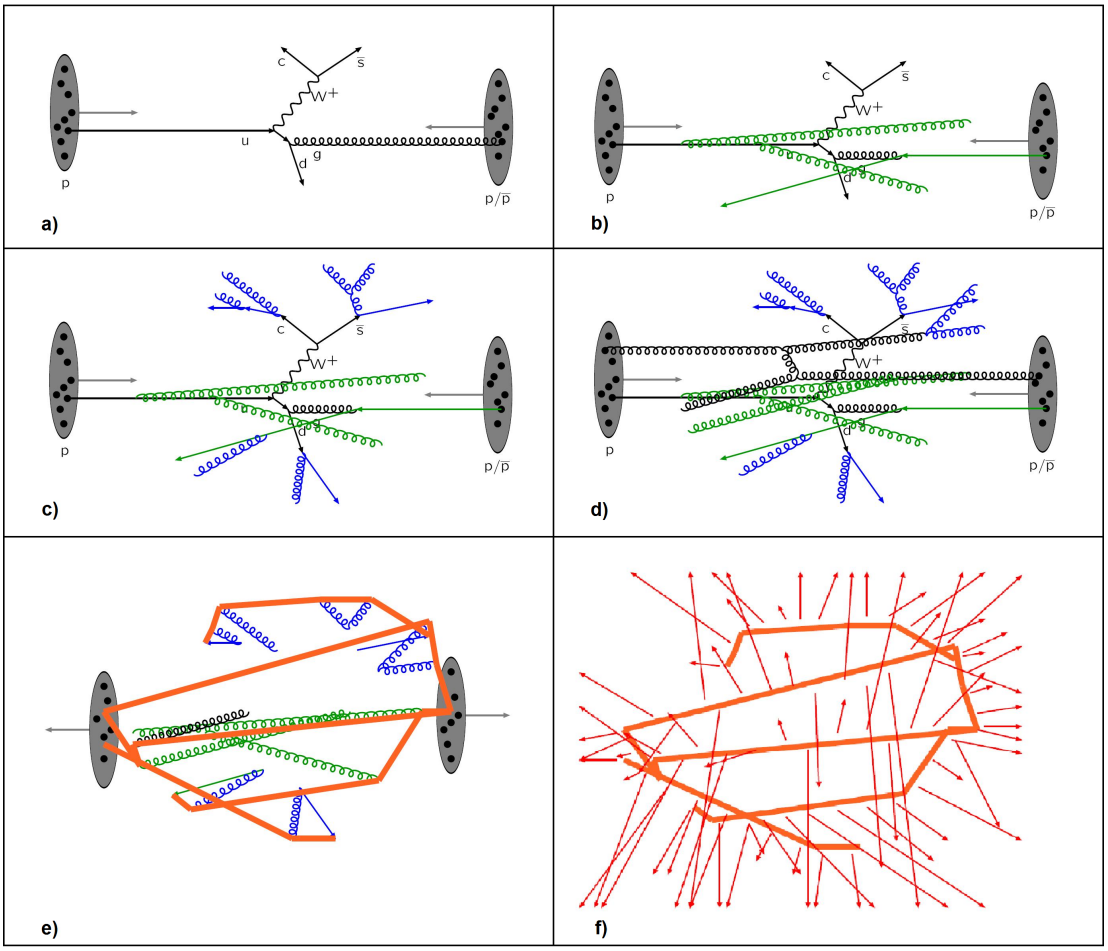

Figure 3.5: Example the individual steps of MC event simulation as it is implemented in *Pythia* [112]: (a) The hard sub-process of a pp collision can be described by matrix elements. The produced intermediate W-boson decays hadronically.(b) Initial state radiation can be described as spacelike parton showers (here gluon radiations in green). (c) Final state radiation can be described as timelike parton showers (in blue). (d) Protons contain multiple partons. If more than one parton of a proton interacts via a hard process it is called multiple interactions (shown in black + initial- (green) and final (blue) radiation) (e) Finally, all coloured particles and beam remnants are connected by colour confinement strings (red). (f) Primary hadrons are produced from the string fragments. Unstable hadrons decay further.

hard subprocesses, azimuthal correlations between and within jets due to gluon interferences and polarization. It provides a cluster model based on non-perturbative gluon splitting for jet hadronization and for soft and underlying hadronic events. The program also includes a Les Houches Accord [110] interface allowing users to implement other processes and use external PDFs.

Especially for SUSY processes an additional interface to *Isajet* [115] is implemented to import supersymmetric mass spectra and branching ratios. In addition, there are also many MSSM processes with and without R-parity violation included since *Herwig* 6.1 [116].

Alpgen

Alpgen [117] is an event generator particularly designed for hadronic collisions with emphasis on multiparton hard processes. Therefore, the final states with a large multiplicity of hard and well separated jets like at the LHC can be modelled with high precision. In order to provide an accurate prediction of the final state particle multiplicity, an exact calculation for the partonic matrix element in leading order is used. Events are generated on parton level with the full information on their colour and flavour structure, enabling the evolution of the partons into fully hadronized final states. The development of the partonic cascades with the subsequent transformation of the partons into observable hadrons is not implemented within *Alpgen*. Instead, the program stores the event information into files according to the event format established by the Les Houches convention. Then Monte Carlo generators like *Pythia* or *Herwig* are run to finalize the event generation including the hadronization step.

MC@NLO

The *MC@NLO* [118] package is based on the *Herwig* event generator such that is is using the *Herwig* showering and hadronization steps. It allows the incorporation of next-to-leading order (NLO) QCD matrix elements into a parton shower framework. Due to the NLO calculations of the hard sub-processes, it provides good results for multiple soft and collinear emissions. Due to the fact that both the NLO matrix elements and the daisy-chained showering algorithm are describing soft emissions, double counting of the radiated partons need to be avoided. This feature is accounted for by the production of events with negative event weights, typically $\sim 15\%$ of all generated events have a negative weight.

In the appendix A.2 a complete list (Tab. A.2-A.4) with all Monte Carlo samples used in the analysis provided by the specific event generator can be found.

3.3.3 Detector Simulation GEANT4

The GEomentry ANd Tracking (GEANT4) program [119] is a tool-kit of detector description and simulation tools. Even though it was originally designed for high energy particle physics it has also been adopted in medical and biological science, as well as for radio-protection and astronautics. It simulates the passing of particles through matter. In case of the ATLAS experiment, GEANT4 was used for design studies, and for detector and reconstruction optimization. The detector simulation is crucial to study and understand real data since not all effects and (in)efficiencies of the detector can be estimated from data only.

The hadrons and long living particles generated with an event generator as described in Sec. 3.3.1 pass through the detector and interact with active and passive detector material. As described in Ch.2.2, different sub-detectors consisting of different materials are needed to reconstruct the variety of particles produced in proton-proton collisions. To get a detector simulation as precise as possible, every component of the ATLAS detector, its material composition, and its position has to be considered by the detector simulation tool. Especially the magnetic field has to be measured very precisely, both in force and geometry, in order to simulate the deflection of charged particles due to the magnetic field.

The position of every interaction of a generated particle in the simulated detector is recorded and stored as a hit. In the last step of the event simulation, all hits have to be

transferred into signals corresponding to the actual output of the individual sub-detector readout systems. This transfer is done during the digitization. In addition to the digits, which are modelled to look like real data, the truth information, the original Monte Carlo generator identity, is stored in the Monte Carlo samples as well. This can be used to study reconstruction algorithms and the efficiencies of specific analysis tools.

Real and Monte Carlo data is reconstructed by the ATLAS reconstruction software identically. The different reconstruction methods have been optimized for different elementary particles. Those methods and their performance are described in detail for the physics object needed for this analysis in the following chapter.

4 Object Reconstruction and Identification

The analysis performed in this thesis is a search for supersymmetry with di-leptons in the final state and missing transverse energy. The event selection is based on jets, missing transverse energy, and exactly two leptons. The reconstruction and identification of electrons (Sec. 4.1), muons (Sec. 4.2), jets (Sec. 4.3) and missing transverse energy (Sec. 4.4) are described in detail in this chapter.

4.1 Electron

The reconstruction of electron objects is split into a so-called reconstruction and an identification step. The first step described in Sec. 4.1.1 aims to provide electron candidates with a high efficiency. The cut based identification provides *loose*, *medium* and *tight* selections, optimized at different working points to achieve electron signal efficiencies of 90%, 80% and 70%, with a background suppression of O(500), O(5000) and O(50000) respectively.

The measurement of invariant mass distributions, as performed in this thesis, relies on a good electron energy scale and energy resolution. The methods and cross checks applied to determine the electron energy scale correction factors (SF) and the constant term in the electron energy resolution are described in Sec. 4.1.3. Finally, the measurement of electron efficiencies using $Z \to ee$ events is summarized in Sec. 4.1.4.

4.1.1 Reconstruction

The electron reconstruction is seeded with an energy deposition in the electromagnetic calorimeter which is then matched to an extrapolated track from Inner Detector. A *sliding window* algorithm of 3×5 cells shown in Fig. 4.1(a), scans the EM middle layer cells in $\eta \times \phi$. If the cluster energy exceeds 2.5 GeV (Fig. 4.1(b)) and the cluster is within the tracking acceptance of the ID ($|\eta| < 2.5$), the tracks are extrapolated from their last measured point to the second layer of the ECal. If the extrapolated track lies within $\Delta\eta \times \Delta\phi = 0.05 \times 0.1$ of the cluster center, the track is matched to the cluster and the cluster is rebuilt by using 3×7 (5×5) cells in the barrel (end caps) (cf. Fig. 4.1 c). If there is more than one track which could be matched to the cluster, the track with the smallest $\Delta R = \sqrt{\Delta\eta^2 + \Delta\phi^2}$ is chosen as best match. Tracks with silicon hits have priority, because tracks without silicon hits are more likely to originate from converted photons. Figure 4.1 shows the cluster matching variables before and after 2010 alignment corrections have been applied.

The cluster energy of an electron candidate is the sum of the energy deposited in front of the EM calorimeter, the energy deposited in the calorimeter inside the cluster, the energy deposited around the cluster (lateral leakage), and the energy deposited beyond the EM calorimeter (longitudinal leakage). Afterwards, information from both the final cluster and the tracks are used to derive the four-momentum of the electron candidate.

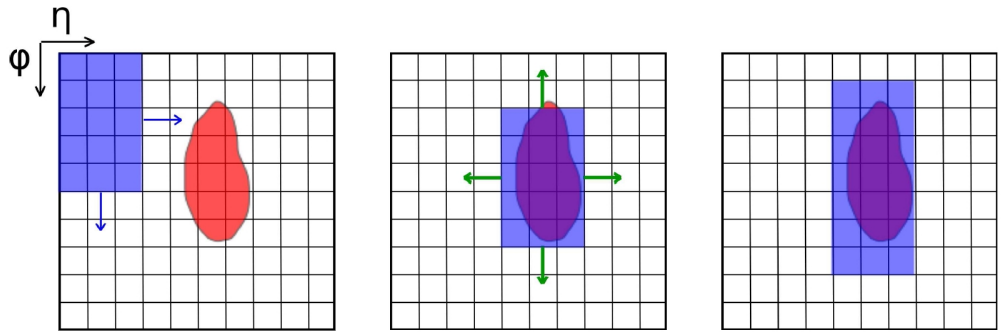

(a) (b) (c)

Figure 4.1: Electron clusters are defined by a *sliding window* algorithm. A 3 × 5 cells big window is scanning the EM middle layer cells in $\eta \times \phi$ (a). If the energy exceeds 2.5 GeV and an associated track is found, the cluster is rebuilt by using 3 × 7 (5 × 5) cells in the barrel (end caps) (b) Then the rebuilt cluster is used for determine the energy c) [120]

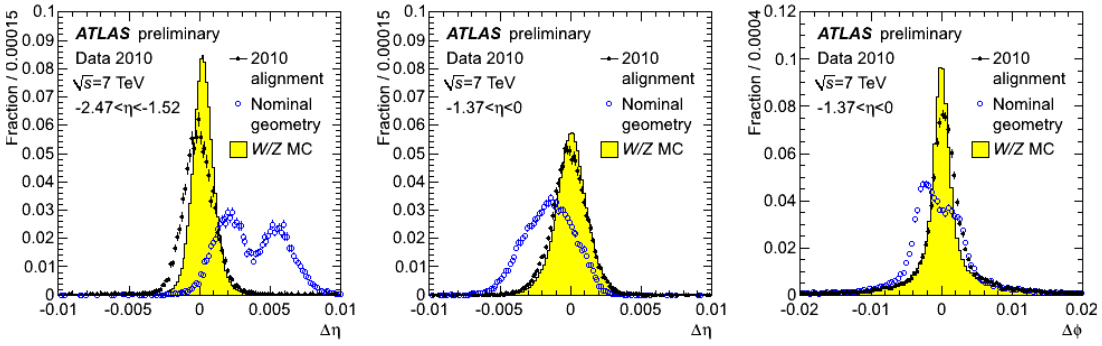

(a) (b) (c)

Figure 4.2: Track cluster matching variables of electron candidates from W-boson and Z-boson decays for reconstruction with nominal geometry and after the 2010 alignment corrections have been applied: (a) $\Delta\eta$ distributions for -2.47 < η < -1.52 and (b) -1.37 < η < 0; (c) $\Delta\phi$ distributions for -1.37 < η < 0. The MC prediction with perfect alignment is also shown [90].

The energy is taken from the cluster and the η and ϕ components are taken from the track, if the track has more then four silicon hits. Otherwise, the η direction is provided by the cluster η-pointing. Forward electron candidates ($|\eta| > 2.5$) do not have a track-match, and in this case, all parameters are derived from the cluster information for clusters with a transverse energy $E_{\mathrm{T}} > 5\,\mathrm{GeV}$.

4.1.2 Identification

The reconstructed electron candidates are identified via a cut-based selection using calorimeter, tracking and combined variables. The cut-based selections are optimized for a good separation between signal electrons, background electrons and jets faking electrons. Three sets of cuts have been provided for *loose*, *medium* and *tight* selections, based on different working points for a background suppression of O(50), O(500) and

Table 4.1: Definition of variables used for *loose*, *medium* and *tight* electron identification cuts for the central region of the detector with $|\eta| < 2.47$ [90].

Type	Description	name
Loose selection		
Acceptance	- $\|\eta\| < 2.47$	
Hadronic leakage	- Ratio of E_T in the first layer of the hadronic calorimeter to E_T of the EM cluster (used over the range $\|\eta\| < 0.8$ and $\|\eta\| > 1.37$)	R_{had1}
	- Ratio of E_T in the hadronic calorimeter to E_T of the EM cluster(used over the range $\|\eta\| > 0.8$ and $\|\eta\| < 1.37$)	R_{had}
Second layer of EM calorimeter	- Ratio in h of cell energies in 3×7 versus 7×7 cells	R_η
	- Lateral width of the shower	ω_{η_2}
Medium selection (includes loose)		
First layer	- Total shower width	$\omega_{s\,tot}$
of EM calorimeter	- Ratio of the energy difference associated with the largest and second largest energy deposit over the sum of these energies	E_{ratio}
Track quality	- Number of hits in the pixel detector (≥ 1)	n_{pixel}
	- Number of hits in the pixels and SCT (≥ 7)	n_{Si}
	- Transverse impact parameter (< 5 mm)	d_0
Track matching	- $\Delta\eta$ between the cluster and the track (< 0.01)	$\Delta\eta$
Tight selection (includes medium)		
Track matching	- $\Delta\phi$ between the cluster and the track (< 0.02)	$\Delta\phi$
	- Ratio of the cluster energy to the track momentum	E/p
	- Tighter $\Delta\eta$ cut (< 0.005)	$\Delta\eta$
Track quality	- Tighter transverse impact parameter cut (< 1 mm)	d_0
TRT	- Total number of hits in the TRT	n_{TRT}
	- Ratio of the number of high-threshold hits to the total number of hits in the TRT	HT_{frac}
Conversions	- Number of hits in the b-layer (≥ 1)	n_{BL}
	- Electron candidates matching to reconstructed photon conversions are rejected	

O(50000) studied in MC.

The *loose* selection is based on shower shape variables of the EM calorimeter middle layer and hadronic leakage variables.

The *medium* selection also considers variables from the EM strip layers, track quality requirements, and track-cluster matching.

The *tight* selection adds E/p, TRT particle identification, and a b-layer hit requirement suppressing converted photons.

The cuts are optimized in 10 bins of η and 11 bins of cluster E_{T} from 5 GeV to greater than 80 GeV. An overview of the electron identification variables used for *loose*, *medium* and *tight* selections is given in Tab. 4.1.

There are no tracking detectors installed in the forward region ($2.5 < |\eta| < 4.9$), and therefore, no tracking information is available. Consequently, the forward electron identification is based on cluster moments and shower shapes only. The good transverse and longitudinal segmentation provides a good discrimination power against hadrons, but it is not possible to distinguish between electrons and photons.

4.1.3 Electron Energy Scale and Resolution

The aim of the analysis performed in this thesis is to measure the invariant mass distribution of di-lepton events, and, if SUSY is realised in nature, fit the endpoint of the mass distribution and extract the mass difference of the SUSY particle. This precision measurement requires a good knowledge of the electromagnetic energy scale and resolution. Methods to determine the energy scale and resolution using di-electron decays of Z and J/Ψ particles are described briefly in the following, the complete study is documented in [90].

Electron Energy Scale

Based on the precise Z line shape [121] measurements from the LEP experiments, the electron energy can be calibrated according to the Z shape. The residual mis-calibration can be parametrized as:

$$E^{meas} = E^{true}(1 + \alpha_i) \tag{4.1}$$

where E^{meas} is the energy measured by the calorimeter after MC-based energy scale corrections, E^{true} is the true electron energy, and α_i measures the deviation from perfect calibration. The energy scale correction factor α is determined by minimizing a unbinned log-likelihood function considering the compatibility of the invariant mass of an event with the Z line shape.

The resulting energy scale correction factor is plotted in Fig. 4.3(a) as function of η. The different detector components are added to the plot demonstrating the effect of the boundaries of the different components on the correction factor. The variations within the detector elements are due to several effects related to electronic calibration and additional material in front of the calorimeters. Figure 4.3(b) shows the calibration factor derived from $J/\Psi \to ee$ data after applying the correction factors derived from $Z \to ee$ data. Energy deposition in detector components are considered in the detector simulation. Imperfect knowledge of material in front of the calorimeters affects the energy measurement and contributes to the scale factor uncertainty as shown in Fig. 4.4(a).

The E/p distribution can be fitted with a Crystal Ball function extracting the energy scale factor $\alpha_{E/p}$ as cross check to the method described above. This method is dominated by systematic uncertainties due to its fit procedure. A comparison of $W \to e\nu$ data using the E/p distribution with the results from the baseline method using the invariant masses of $Z \to ee$ and $J/\Psi \to ee$ data is shown in Fig. 4.4(b). Both methods are in good agreement.

Electron Energy Resolution

The relative energy resolution is determined based on the 2010 data set in [90]. The formula parameterizing the relative energy resolution depends on three parameters:

$$\frac{\sigma_E}{E} = \frac{a}{\sqrt{E}} \oplus \frac{b}{E} \oplus c \tag{4.2}$$

with the sampling term a, the noise term b and the constant term c.

Due to the limited statistics from 2010, only the constant term c is determined by analysing the measured and predicted invariant mass resolution from $Z \to ee$ decays. The sampling term is more dominate at low energies. Due to the good agreement of α

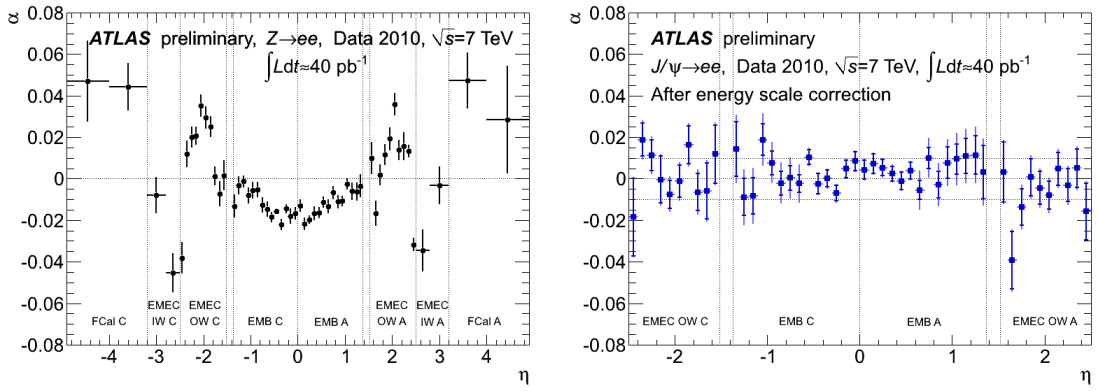

(a) (b)

Figure 4.3: The α energy scale correction factors as a function of the pseudorapidity of the electron cluster derived from fits (a) to $Z \to ee$ data and (b) to $J/\Psi \to ee$ data. The uncertainties of the $Z \to ee$ measurement are statistical only. The $J/\Psi \to ee$ measurement was done after the $Z \to ee$ calibration shown on the left has been applied. Its results are given with statistical (inner error bars) and total (outer error bars) uncertainties. The boundaries of the different detector parts are indicated by dotted lines [90].

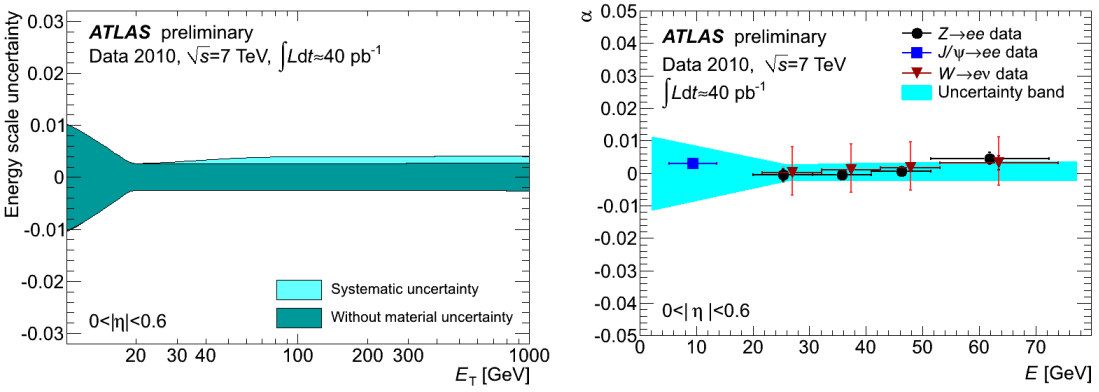

(a) (b)

Figure 4.4: Systematic uncertainty on the electron energy scale with and without the uncertainty due to the amount of passive material in front of the EM calorimeter for the regions of $|\eta|$ <0.6 in the barrel with the smallest systematics (a). The α energy scale correction factor as a function of the electron energy for $|\eta|$ <0.6 determined by the baseline calibration method using $Z \to ee$ (circles) and $J/\Psi \to ee$ (square) decays and by the E/p method using $W \to e\nu$ decays (triangles) (b). For the $Z \to ee$ data points, the inner error bar represent the statistical uncertainty and the outer gives the combined error when bin migration effects are also included. The error on the $J/\Psi \to ee$ measurements are statistical only. The band represents the systematic errors on the energy scale for the baseline calibration method. For the E/p method, the inner error bar represents the statical and the outer the total uncertainty [90].

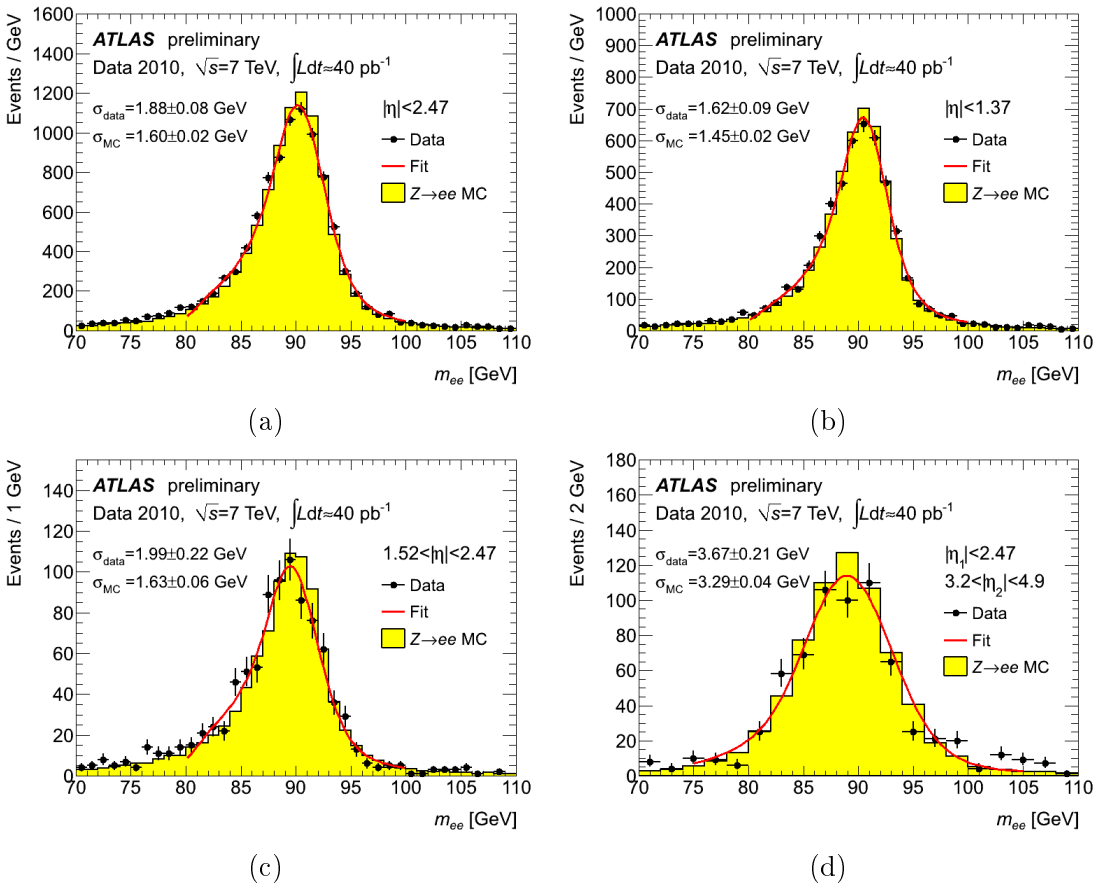

Figure 4.5: Reconstructed di-electron mass distributions for the $Z \to ee$ selection in different pseudorapidity regions after the $Z \to ee$ calibration described in [90] has been applied. The transition region $1.37 < |\eta| < 1.52$ is excluded. The data (dots with statistical error bars) are compared to the signal MC expectation (filled histogram). The fits of a Breit-Wigner convoluted with a Crystal Ball function are shown (full lines). The Gaussian width (sigma) of the Crystal Ball function is given both for data and MC simulation [90].

(the energy scale correction factor) with 0 derived from $J/\Psi \to ee$ decays, after applying the $Z \to ee$ correction factors, the sampling term is assumed to be well described within an uncertainty of 10%. The effect of the noise term cancels out at first order, due to the fact that the noise description in MC is derived from calibration runs in data.

Based on the fits shown in Fig. 4.5, the energy resolution and finally the constant term c are derived. The fits are performed using a Breit-Wigner convoluted with a Crystal Ball function. The resolution is taken from the Gaussian component of the Crystal Ball function, fixing the Breit-Wigner width to the measured Z width of 2.49 GeV [90].

The result of the measured constant term c of the energy resolution extracted from the $Z \to ee$ peak is listed for the different calorimeter regions in Tab. 4.2.

4.1.4 Performance

The performance study summarized in this section is documented in the ATLAS paper [90]. The correction factor needed in order to take into account different efficiency

Table 4.2: Measured effective constant term c from the observed width of the $Z \to ee$ peak for different calorimeter regions [90].

	Effective constant term, cdata
EMB	1.2 % ± 0.1% (stat) $^{+0.5\%}_{-0.6\%}$ (syst)
EMEC-OW	1.8% ± 0.4% (stat) ± 0.4% (syst)
EMEC-IW	3.3% ± 0.2% (stat) ± 1.1% (syst)
FCal	2.5% ± 0.4% (stat) $^{+1.0\%}_{-1.5\%}$ (syst)

terms for single electrons is given by:

$$C = \epsilon_{event} \cdot \alpha_{reco} \cdot \epsilon_{ID} \cdot \epsilon_{trig} \cdot \epsilon_{isol} \tag{4.3}$$

with the efficiency of the event selection cuts (ϵ_{event}), the basic reconstruction efficiency (α_{reco}), the efficiency of the identification cuts relative to the reconstruction efficiency (ϵ_{ID}), and the trigger and isolation efficiency with respect to all reconstructed and identified electron candidates (ϵ_{trig} and ϵ_{isol}).

Figure 4.6 shows the results of a tag and probe analysis studying the electron identification efficiencies for *medium* and *tight* selections in $Z \to ee$ decays. The integrated identification efficiency is 94.7 % ± 0.4%(stat) ± 1.5%(sys) in data and 96.3% in MC, corresponding to a ratio of 0.984 for the *medium* selection, and 80.7 % ± 0.5%(stat) ± 1.5%(sys) in data and 78.5% in MC, corresponding to a ratio of 1.028 for the *tight* selection.

4.2 Muon

The estimation of the quality of reconstructed muons relies on the muon reconstruction efficiency, the muon isolation efficiency and the muon momentum resolution. The results for the muon reconstruction and isolation efficiency presented below are derived from 2010 data sets after the autumn reprocessing with improved detector calibration and alignment [94]. The efficiencies calculated are binned in η, ϕ and p_{T} . The different materials and detector technologies used in the different $\eta - \phi$ regions (Fig. 4.7) yield significant differences in the muon reconstruction efficiencies in the $\eta - \phi$-plane.

The muon momentum resolution was determined from the first pass reconstruction corresponding to an integrated luminosity of 40 pb^{-1} of 2010 data with preliminary calibration and alignment [95]. Therefore, the measured resolution is poorer than its design value [88] of better than 3% over a wide p_T range and 10% at $p_{\mathrm{T}} = 1\,\mathrm{TeV}$.

4.2.1 Reconstruction Efficiency

The ATLAS reconstruction software provides three different classes of muon objects:

Stand-alone (SA) muons: Those muons are reconstructed by the muon spectrometer, only. The impact parameter of the muon track is derived by extrapolating the muon track back to the beam line.

Combined (CB) muons: If both Inner Detector (ID) and muon spectrometer (MS) reconstruct the muon track independently and both tracks can be matched successfully, the muon is defined as CB muon.

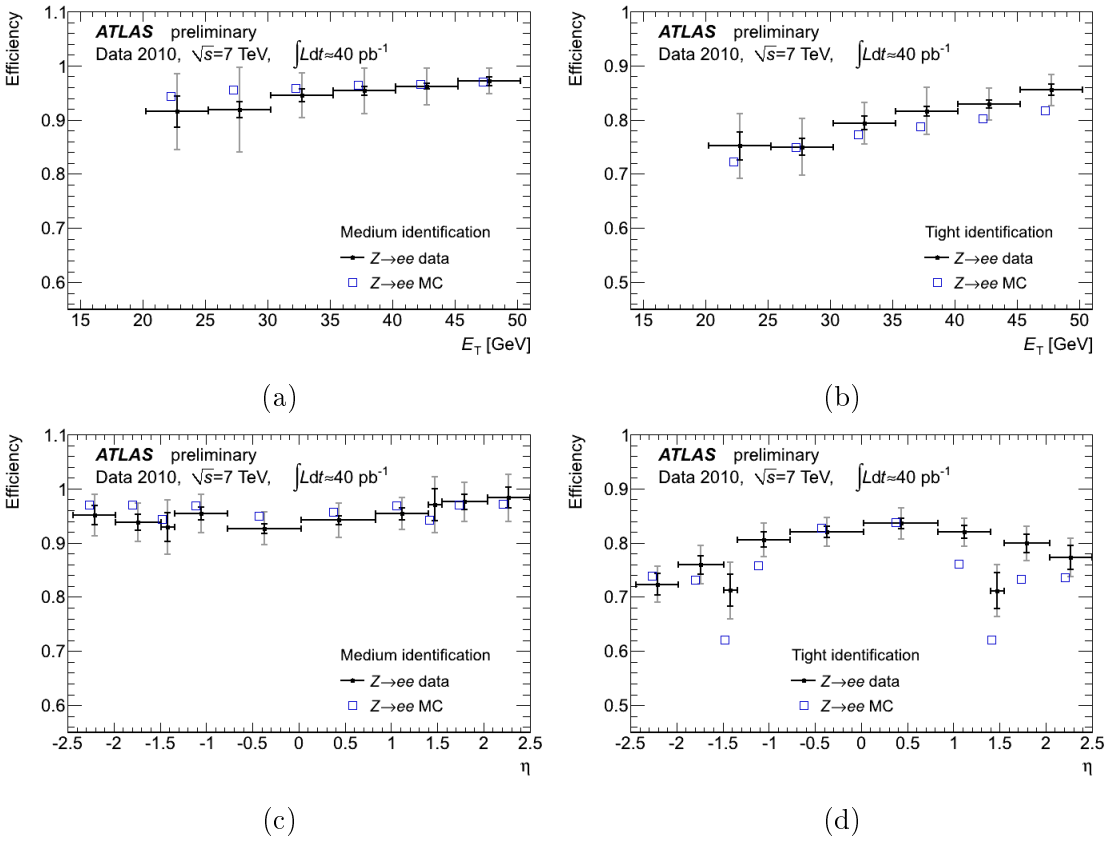

Figure 4.6: Efficiencies measured from $Z \to ee$ events and predicted by MC for medium (a,c) and tight identification (b,d) as a function of E_{T} (a,b) integrated over $|\eta| < 2.47$ excluding the transition region $1.37 < |\eta| < 1.52$ and as function of η (c,d) integrated over $20 < E_{\mathrm{T}} < 50\,\mathrm{GeV}$. The results for the data are shown with their statistical (inner error bars) and total (outer error bars) uncertainties. The statistical error on the MC efficiencies plotted as open squares is negligible.

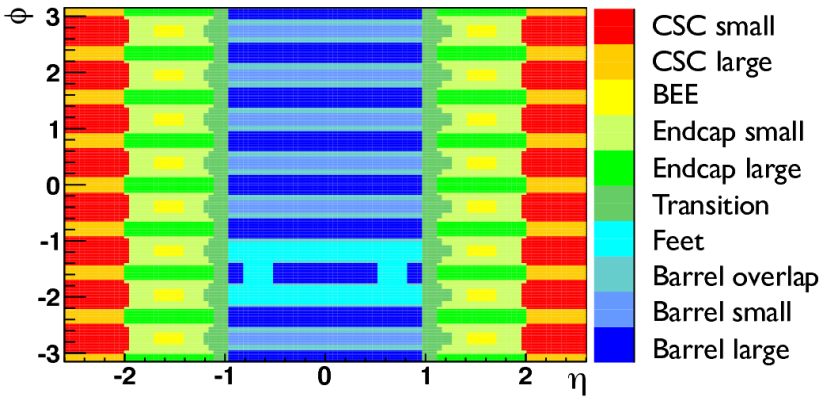

Figure 4.7: The detector regions. Regions in the $\eta - \phi$ map with the same colour code are grouped into a single detector region [94].

Segment tagged (ST) muons: If a good ID track can be extrapolated and associated to a track segment found in the MS, the muon is defined as ST muon.

The latter class shows a higher efficiency than the CB muons, because it can recover muons which do not cross enough precision chambers in the MS. The ATLAS reconstruction provides two different algorithm chains for reconstructing CB and ST muons; Chain 1 (*Staco*) and Chain 2 (*MuID*). All results shown in this section used the *Staco* algorithm, because the analysis performed in Ch. 6 is based on *Staco* muons only.

The reconstruction efficiencies for CB and ST muons are both products of the ID reconstruction efficiency, the MS reconstruction efficiency and the ID-MS track matching. Both efficiencies, the ID muon reconstruction efficiency and the combined MS and matching efficiency, can be determined via a tag-and-probe method. For this, $Z \to \mu\mu$ decays are selected requiring two oppositely charged isolated tracks with an invariant mass near the Z-boson mass. The tag object must be trigged and reconstructed as a CB muon.

The ID efficiency can be extracted from stand-alone muon probes. The ID efficiency is then defined as the fraction of stand-alone muon probes which can be associated to a ID track.

The MS and matching efficiency is determined via ID track probes. It is the fraction of ID tracks which can be associated to MS tracks. The probe-muon matching is successful:

- if the probe is an ID track and both tracks (ID and MS track) have the same charged and $R_{\text{cone}} \leq 0.01$ between extrapolated ID track and MS track
- or the probe is a SA muon and $R_{\text{cone}} \leq 0.05$.

The analysis performed in [94] gives an average ID reconstruction efficiency of $(99.1 \pm 0.1)\%$ and an average CB muon reconstruction efficiency of $(93.8 \pm 0.2)\%$.

The detector regions with partial coverage like *barrel large*, *feet*, and *transition* defined in Fig. 4.7 can be recovered by combining CB and ST muon reconstruction as shown in Fig. 4.8. The overall efficiency for CB plus ST muon reconstruction is $(98.0 \pm 0.1)\%$.

4.2.2 Isolation Efficiency

The muon isolation efficiency is studied in the similar way to the analysis described above for the reconstruction efficiency; the only change is the definition of the probe muon. The probe is defined as an isolated CB muon with $p_{\text{T}} > 20\,\text{GeV}$ passing some additional track quality criteria [94]. Two definitions of isolation with various isolation cuts are studied in [94], only the tightest selections are shown in Fig. 4.9:

- The **track isolation** is defined as the fraction of the sum of p_{T} of all charged track particles in a cone of $R_{\text{cone}} < 0.3$ around the probe direction divided by the p_{T} of the probe.
$$\frac{\sum p_{\text{T}}\ (R_{\text{cone}} < 0.3)}{p_{\text{T}}\ (\mu)} < 0.1 \tag{4.4}$$
- The **calorimeter isolation** is defined as the ratio of the transverse energy deposition (E_{T}) in a cone of $R_{\text{cone}} < 0.3$ around the probe direction divided by the probe p_{T} . The calorimeter isolation energy is corrected for muon energy loss.
$$\frac{E_{\text{T}}\ (R_{\text{cone}} < 0.3)}{p_{\text{T}}\ (\mu)} < 0.1 \tag{4.5}$$

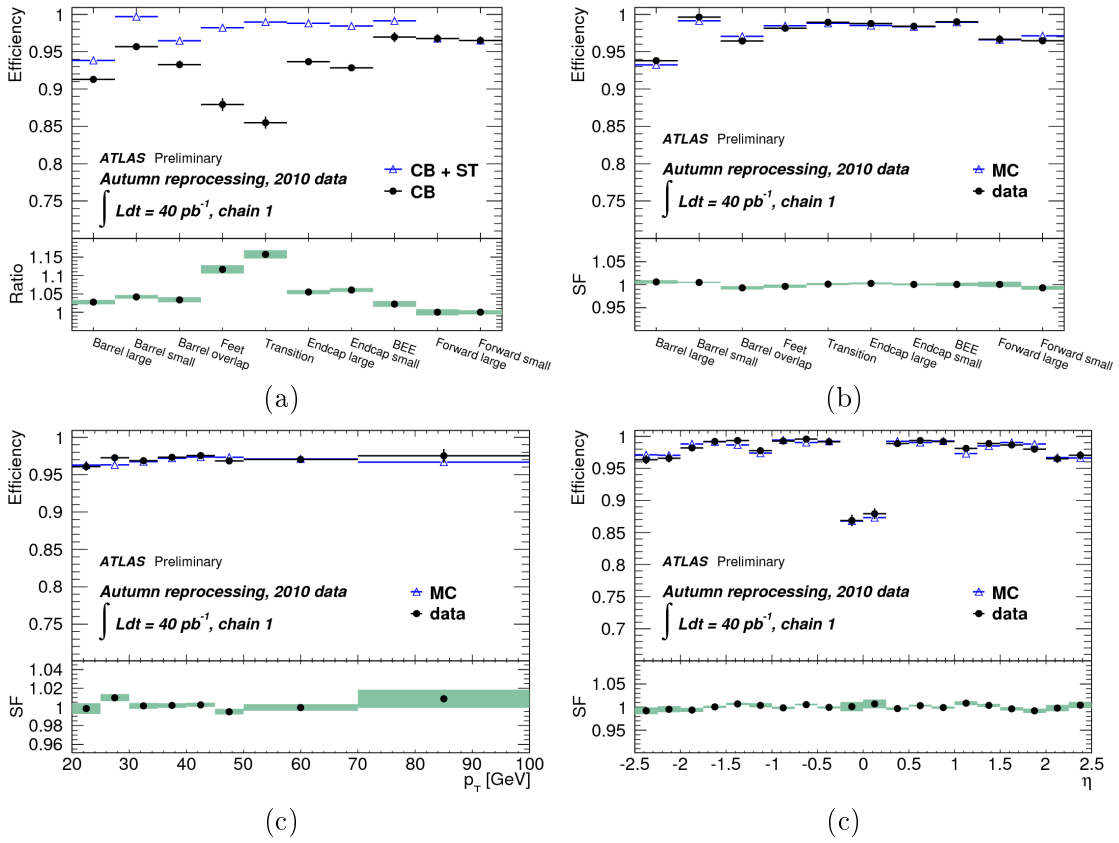

Figure 4.8: Efficiencies for CB plus ST muons (open circles) in comparison to those for CB muons only (dots) are shown for the different detector regions(a). Efficiencies for CB plus ST muons, obtained from data with background correction (dots) and Monte Carlo simulation of the signal (open triangles) are shown for the different detector regions(b), as a function of muon p_{T} (c), and as a function of muon η(d) [94].

The probe is isolated in both cases if the isolation fraction is smaller than 10% (20% also studied in [94]). Both distributions in Fig. 4.9 show excellent agreement between data and Monte Carlo. The drop in the isolation efficiency at low p_{T} is due to the definition of the isolation; the sums of p_{T} and E_{T} depend only weakly on the probe p_{T} such that the isolation fraction increases with decreasing probe p_{T} .

4.2.3 Muon Momentum Resolution

The relative muon momentum resolution depends on the amount of material in front of the muon detector, the intrinsic spatial resolution, and the alignment. The muon momentum resolution study done in [95] separates the detector in four η regions as shown in Fig. 4.7:

- Barrel - covering $0 < |\eta| < 1.05$,
- Transition region - covering $1.05 < |\eta| < 1.7$,
- End-caps - covering $1.7 < |\eta| < 2.0$ and

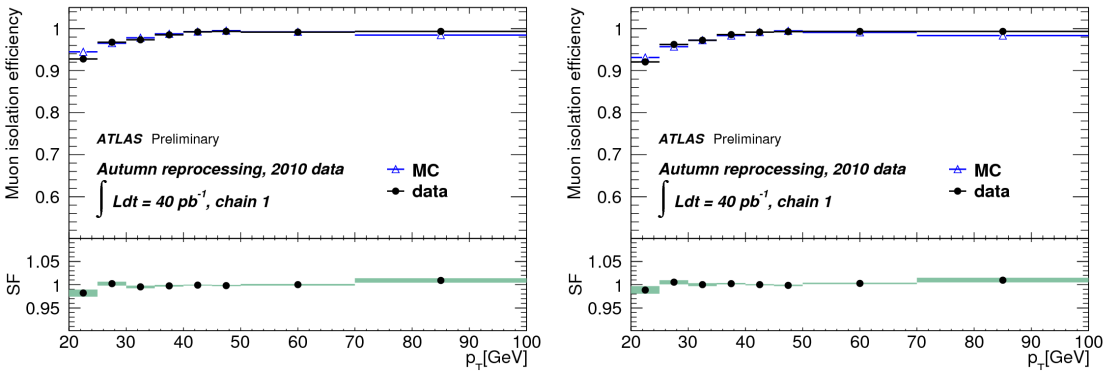

(a) (b)

Figure 4.9: Muon isolation efficiency in $Z \to \mu\mu$ events for different isolation requirements. The Monte Carlo prediction includes Z signal and background processes. Track isolation efficiency for track isolation fraction smaller than 10% (a) and calorimeter isolation efficiency for calorimeter isolation fraction smaller 10% (b) [94].

- CSC/no TRT - covering $2.0 < |\eta| < 2.5$.

The momentum resolution in MS can be parametrized as follows for a fixed η:

$$\frac{\sigma(p)}{p} = \frac{p_0^{MS}}{p_{\mathrm{T}}} \oplus p_1^{MS} \oplus p_2^{MS} \cdot p_{\mathrm{T}} \tag{4.6}$$

where p_0^{MS} is the coefficient related to the energy loss in the calorimeter, p_1^{MS} to the multiple scattering, and p_2^{MS} to the intrinsic spatial resolution, which depends on the alignment. A comparable parametrization with the same notation can be given for the ID tracks:

$$\frac{\sigma(p)}{p} = p_1^{ID} \oplus p_2^{ID} \cdot p_{\mathrm{T}} \tag{4.7}$$

for muons at higher $|\eta| < 1.9$ the polar angle θ must also be considered:

$$\frac{\sigma(p)}{p} = p_1^{ID} \oplus p_2^{ID} \cdot p_{\mathrm{T}} \ \cdot \frac{1}{\tan^2\theta} \tag{4.8}$$

The muon momentum resolution is determined from $Z \to \mu\mu$ events [95]. The width of the invariant mass of di-muons is a convolution of the natural Z width and the muon momentum resolution. The di-muon invariant mass is measured for MS and ID tracks separately. Both shapes are fitted with a convolution of the Z lineshape and two Gaussian distributions modelling the detector resolution effects. The momentum correction parameters are determined using a Monte Carlo template technique. A series of distributions of the resolution contribution to the di-muon invariant mass width and the relative difference of the muon momentum measurements in ID and MS are created for different momentum resolutions. By matching those distributions to the one found in data, the momentum correction factors have been fitted. By adding quadratically the uncorrected simulated resolution terms of Eq. (4.6)-(4.8) to the correction found by the template fits, the resolution correction parameters listed in Tab.4.3 have been determined.

Table 4.3: Resolution parametrization as defined in Equations (4.6)-(4.8) in the MS and ID. The measurements are obtained by adding the correction parameters in quadrature to the uncorrected momentum resolution from simulation.

	MS			ID	
η region	p_0^{MS} (TeV)	p_1^{MS} (%)	p_2^{MS} (GeV^{-1})	p_1^{ID} (%)	p_2^{ID} (TeV^{-1})
barrel	0.23 ± 0.01	3.75 ± 0.10	0.24 ± 0.04	1.60 ± 0.32	0.49 ± 0.04
transition	0	8.80 ± 0.46	0.30 ± 0.16	2.60 ± 0.54	0.95 ± 0.10
end-caps	0	4.77 ± 0.35	0.23 ± 0.12	3.40 ± 0.58	1.39 ± 0.05
CSC/no TRT	0.17 ± 0.02	4.87 ± 0.65	0.90 ± 0.25	4.10 ± 0.50	0.140 ± 0.004

Based on those parameters, the momentum resolution as a function of p_{T} for two (barrel and CSC) of the four η regions defined above are shown for MS and ID tracks in Fig. 4.10. The corrected momentum resolution parameters have to be considered in Monte Carlo simulation in order to get a precise data distribution description. Figure 4.11 shows the invariant mass distribution of $Z \to \mu\mu$ events for MS tracks only, ID tracks only and combined tracks from data and MC after correcting the simulated muon p_{T}. By varying these parameters, the systematic uncertainty on ID and MS momentum resolution can be estimated for different analyses. In Ch. 6 it is described, how those systematics are considered in the di-lepton analysis performed in this thesis.

4.3 Jets

The jet reconstruction is done in three steps. First, the energy deposition in the calorimeter cells are grouped together building calorimeter objects with four momentum information. This is done during the calorimeter reconstruction described in Sec. 4.3.1. Then the reconstructed calorimeter objects are analysed by the so-called jet finder (Sec. 4.3.2), providing calorimeter jets. Finally, the calorimeter jets have to be corrected to the jet energy scale reflecting the original physics object energy and momentum, unfolded from detector effects (Sec. 4.3.3). The analysis performed in Cp. 6 is based on so-called *AntiKt4Topo* jets. Therefore, the topological clustering [122] and the anti-k_T jet finding [123] are described in detail in this section. Other implementations for calorimeter reconstruction and jet finding algorithms are implemented in the ATLAS reconstruction software and a description of these can be found in [124]. Specific jet cleaning cuts, applied in the analysis described in Cp. 6, have been developed by the ATLAS Jet performance group [125]. These cuts are summarized in Sec.4.3.4. The performance of the jet reconstruction studied in [126] is briefly described in Sec. 4.3.5.

4.3.1 Calorimeter Reconstruction - Topological Clustering

The topological clustering provides three dimensional calorimeter clusters. The algorithm is seeded by calorimeter cells with a large *signal-to-noise* ratio (typically $|E_{cell}| > 4 \cdot \sigma_{noise}$). The *signal-to-noise* ratio is defined as the ratio of the deposited energy in the calorimeter cell over the RMS of the energy deposition measured in random events. Then all neighbouring cells with a signal to noise ratio of $2 \cdot \sigma_{noise}$ are added. Finally, all neighbouring cells are added (no signal noise ratio requirment $|E_{cell}| > 0 \cdot \sigma_{noise}$). This is the so-called *420* topocluster configuration used for hadronic topocluster reconstruction.

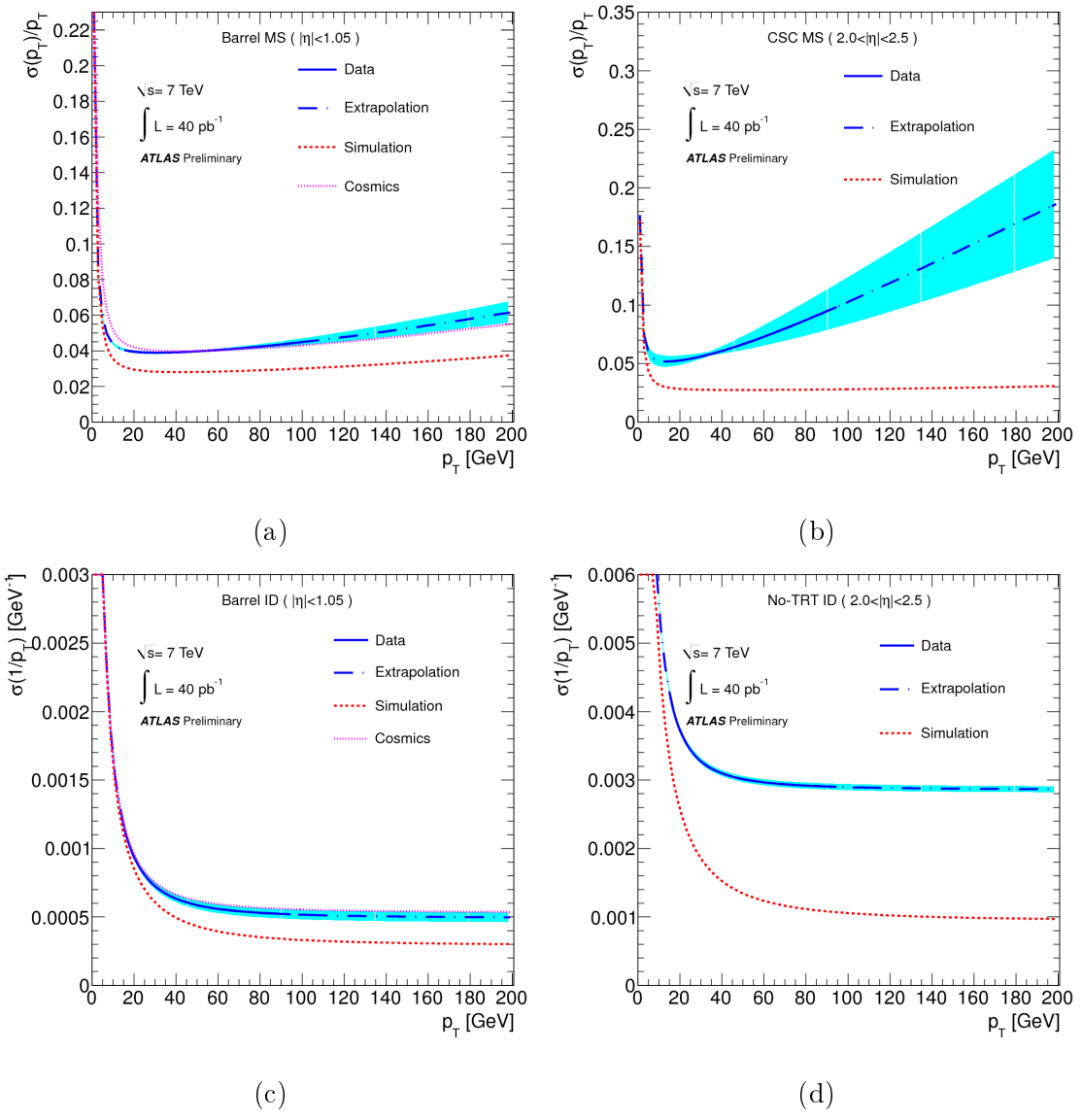

Figure 4.10: Resolution curve from the fitted parameter values of the Muon Spectrometer (a,b) and the Inner Detector (c,d) in collision data and simulation as a function of the muon p_T, for the *barrel* region $0 < |\eta| < 1.05$ (a,c) and for the *forward* region $2.0 < |\eta| < 2.5$ (b,d). The solid blue line shows determinations based on data and is continued as dashed line for the extrapolation to p_{T} ranges not accessible in this analysis. The shaded band represents the sum in quadrature of the statistical and systematic uncertainties. For the case of the barrel, a comparison with the curve obtained from the fitted parameters from cosmic ray data is overlaid for comparison [95].

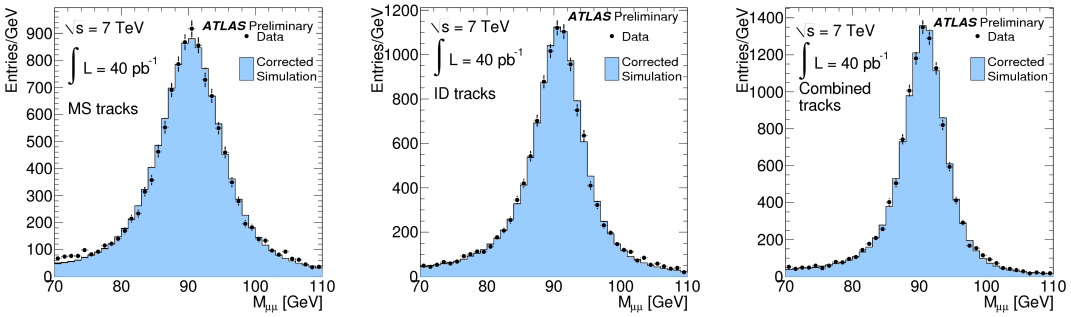

(a) (b) (c)

Figure 4.11: Di-muon invariant mass comparison between collision data (dots) and simulation (full histogram) in the Z boson mass range, after correcting the simulated muon p_{T} by the parameters derived in this study. The distribution is integrated over the full range of η. The Muon Spectrometer momentum measurement is shown in (a), the Inner Detector momentum measurement in (b) and the combined muons in (c) [95].

The noise is computed cell-by-cell. It varies by orders of magnitude in η, between the calorimeter subsystems and due to pile-up. After the *topoclusters* are created a *cluster splitter* searches the topoclusters for local maxima. If such a maximum is found, it is used as seed for another iteration of topological clustering.

The jet finding algorithm needs physical four-momenta as input format. Therefore the topoclusters have to be transformed into massless pseudoparticles based on the energy sum of all cluster cells and the direction, defined as the vector originating from the center of the ATLAS coordinate system pointing to energy-weighted barycenter of the topocluster.

4.3.2 Jet Finding - Anti-k$_T$ Algorithm

The anti-k$_T$ [123] jet finder is a sequential recombination algorithm which analyses all pairs (ij) of four-momentum objects provided by the calorimeter reconstruction in terms of their relative momenta squared:

$$d_{ij} = max(k_{T,i}^2, k_{T,j}^2)\frac{R^2}{\Delta R_{ij}^2} \tag{4.9}$$

$$d_i = k_{T,i}^2 \tag{4.10}$$

with $k_{T,i,j}^2$ the four momentum of object i and j,ΔR_{ij}^2 the relative distance between i and j and R the fixed cone radius. The ATLAS reconstruction software provides *AntiKtTopo* jets for distance parameters $R = 0.4$ (narrow) and $R = 0.6$ (wide). The narrow jet cone is optimized for $W \to jj$ decays in dense environments like $t\bar{t}$ and SUSY event topologies, the wide cone jets are studied in inclusive jet cross section measurements.

The minimum of all d_{ij} and d_i (momentum squared relative to the beam) is found. If d_i is the minimum, it is defined as a calorimeter jet and it is removed from the input list. If a combination of two calorimeter objects d_{ij} is found as the minimum, i and j are combined as a new object k by four-momentum recombination. Both objects i and j are removed from the input list and replaced by k. This procedure is repeated until all

objects are removed from the input list.

Performance studies and scale uncertainty measurements rely on Monte Carlo comparisons. Due to the input format of the jet finder, truth jets based on the true Monte Carlo four-momenta of the vector sum of generated hadrons can be processed like calorimeter clusters.

The resulting calorimeter jets are reconstructed at electromagnetic scale, such that these jets have to be calibrated to the hadronic scale and additional jet energy scale corrections accounting for noise, pile-up, algorithm effects, etc. have to be applied in order to form physics jets at parton level.

4.3.3 Jet Energy Scale Calibration

The ATLAS calorimeter energy scale is calibrated according to electromagnetic showers validated in test-beam measurements [91, 127–131]. The electromagnetic energy scale has been studied and corrected as described in Sec. 4.1.3. The goal of the jet energy scale calibration is to correct the energy and the momentum of the measured calorimeter jets to the hadronic scale. Various detector effects have to be considered by the jet energy calibration:

- partial measurement of energy deposition
- energy loss in dead detector material
- calorimeter leakage
- signal losses during clustering and jet reconstruction

A calibration scheme called *EM+JES calibration* [124, 132] applies jet-by-jet corrections as a function of the jet energy at em scale and the pseudorapidity.

The EM+JES Calibration

The calibration is done in three steps:

1. Subtraction of average additional energy due to pile-up. This correction is applied at the electromagnetic scale as the first step of the calibration scheme. The corrections are determined from minimum bias data as a function of η and the number of primary vertices.

2. Correction of the jet position considering the primary vertex position. As mentioned above, the direction of calorimeter jets is derived as the barycenter of the cluster pointing to the center of the ATLAS coordinate system. The cluster is corrected considering the primary vertex of the event, recalculating each topocluster so that it points to the primary vertex.

3. Correction of the reconstructed jet energy by comparing the kinematics of reconstructed and truth jets.

Energy Scale Uncertainties

After calibrating the nominal inclusive Monte Carlo samples as a closure test, the jet energy and the track p_{T} response show small deviations. This implies that the kinematics of the calibrated calorimeter jets are not fully restored to that of the corresponding truth jets. Uncertainties due to various effects have to be taken into account:

- JES calibration method (non-closure)
  The same correction is used for both energy and transverse momentum assuming a zero jet mass. A non-zero jet mass will lead a bias in the p_{T} calibration. This uncertainty amounts to 2% for low p_T^{jet} jets, smaller than 1% for $p_T^{jet} < 30\,\mathrm{GeV}$ in the barrel, and smaller than 1% in the end-caps.

- calorimeter response
  The dominant effect in the response uncertainty is due to particles with $p > 400\,\mathrm{GeV}$. The test-beam response has been measured for pions with $20 < p < 350\,\mathrm{GeV}$ [133]. The uncertainty varies between 1.5% and 4%.

- Detector simulations
  - Noise threshold
    As described in Sec. 4.3.1, the topoclustering is based on a signal-to-noise ratio. Due to time-dependent noise changes in data, discrepancies between simulated noise and real noise can lead to differences in cluster shapes. The contribution is below 2% at low p_{T} and can be neglected completely above $p_T^{jet} > 45\,\mathrm{GeV}$.
  - Additional dead material
    Additional dead material can lead to jet energy losses. Several MC samples with additional detector material (up to 5%) in the ID and calorimeter have been simulated. Contributions up to 1% have been found.

- Event modelling
  - Alpgen+Herwig+Jimmy
    Different modelling of the hard sub-process and soft processes has been studied with different MC generators. Differences in pdfs, cluster fragmentation, underlying event implementation, etc. have been considered. Uncertainty contributions up to 2% have been found.
  - PYTHIA Perugia 2010
    This is a specific PYTHIA generator tune optimized to hadron collider data with increased final state radiation. A further uncertainty of 2% is considered in the JES uncertainty due to this modelling.

A detailed study of all uncertainties is performed in [132]. The resulting jet energy scale systematic uncertainties are shown in Fig. 4.12.

4.3.4 Jet Cleaning

Misreconstructed jets or fake jets due to hardware problems, beam conditions, and cosmic ray showers have been observed. Based on the first study from 2010 [125], which was performed on the first $0.3\,\mathrm{nb}^{-1}$ data at $\sqrt{s} = 7\,\mathrm{TeV}$, several jet quality criteria have been established for the rejection of jets not originating from proton-proton collisions.

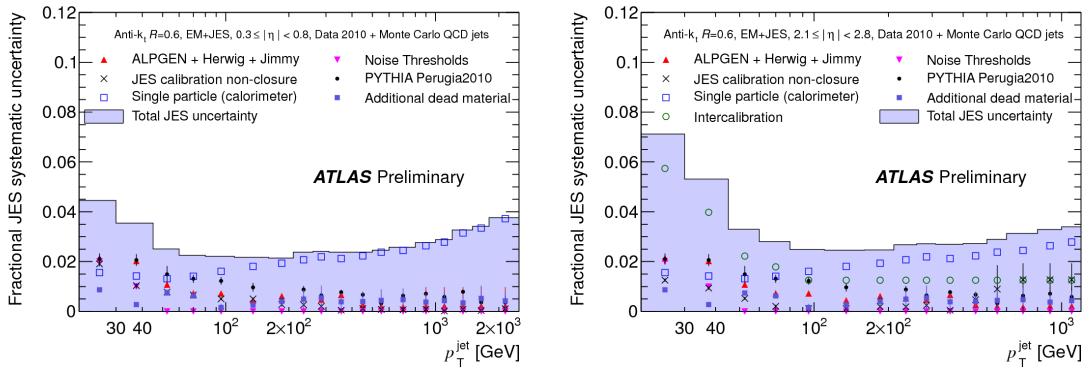

(a) (b)

Figure 4.12: Fractional jet energy scale systematic uncertainty as a function of p_{T} for jets in the pseudorapidity region $0.3 < |\eta| < 0.8$ in the calorimeter barrel (a) and in the pseudorapidity region $2.1 < |\eta| < 2.8$ (b). The total uncertainty is shown as the solid light blue area. The individual sources are also shown, with uncertainties from the fitting procedure if applicable [132].

Table 4.4: Jet quality criteria for rejection jets not originating from proton-proton collisions

	loose	medium = loose OR
HEC spikes	$(HEC_{frac} > 0.5$ and $\lvert HEC_{Quality}\rvert > 0.5)$ or $\lvert neg.E\rvert > 60\,\mathrm{GeV}$	$HEC_{frac} > 1 - \lvert HEC_{Quality}\rvert$
EM coherent noise	$EM_{frac} > 0.95$ and $\lvert LAr_{Quality}\rvert > 0.8$ and $\lvert\eta\rvert < 2.8$	$EM_{frac} > 0.9$ and $\lvert LAr_{Quality}\rvert > 0.8$ and $\lvert\eta\rvert < 2.8$
non-collision background and cosmics	$\lvert t\rvert > 25\,\mathrm{ns}$ or $(EM_{frac} < 0.05$ and $Ch_{frac} < 0.05$ and $\lvert\eta\rvert < 2)$ or $(EM_{frac} < 0.05$ and $\lvert\eta_{jet@emscale}\rvert \geq 2)$ or $(F_{Max} > 0.99$ and $\lvert\eta_{jet@emscale}\rvert < 2)$	$\lvert t\rvert > 10\,\mathrm{ns}$ or $(EM_{frac} < 0.05$ and $Ch_{frac} < 0.1$ and $\lvert\eta\rvert < 2)$ or $(EM_{frac} < 0.95$ and $Ch_{frac} < 0.05$ and $\lvert\eta_{jet@emscale}\rvert < 2)$

Single cell jets in the HEC can be caused by sporadic noise burst in the HEC leading to a jet with most energy deposited in only one cell. The energy fraction in the HEC, HEC_{fraq}, and the $HEC_{Quality}$, which is a measure for the difference between the measured pulse shape and the predicted pulse shape used to reconstruct the cell energies, address this kind of fakes. Bad quality jets in the ECal are caused by rare noise bursts in the EM calorimeter. The fraction of energy in the electromagnetic calorimeter EM_{frac}, the maximum energy fraction in one calorimeter layer f_{max}, and the $LAr_{Quality}$ (comparable to the $HEC_{Quality}$) distinguish this kind of fakes. Out-of-time jets, for example energy depositions from photons produced by cosmic muon events, are suppressed by the jet time, computed as the energy squared cells mean time t_{jet}. Two different working points for bad jets (*loose* and *medium*) have been defined. All selection criteria are listed in Tab. 4.4. The analysis performed in Ch. 6 rejects events with one or more loose bad jet.

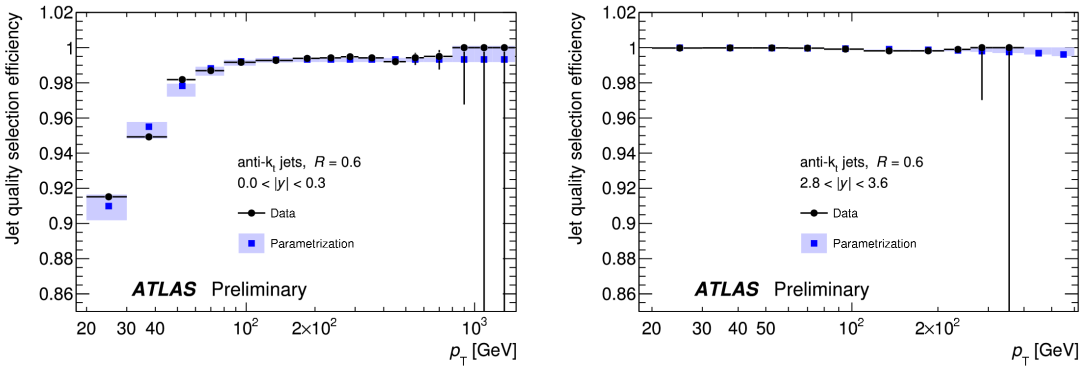

(a) (b)

Figure 4.13: Jet identification efficiency as a function of p_{T} for anti-k$_T$ jets with R = 0.6 for the rapidity regions $|y| < 0.3$ (a) and $2.8 < |y| < 3.6$ (b). The black circles indicate the efficiency measured in-situ using a tag-probe method, while the blue squares and the shaded band indicates the parametrized central value and the systematic uncertainty on the efficiency obtained by varying the tag jet selection. The turn-on is due to harder jet cleaning cuts for low-p_{T} jets [126].

4.3.5 Performance

The jet identification efficiency is studied in [126], using a tag-and-probe method on di-jet events analysing the full 2010 dataset. The di-jet event selection requires the leading jet to be within $|y| < 4.4$ and $p_{\mathrm{T}} < 30\,\mathrm{GeV}$ and to have at least a second leading jet within $|y| < 4.4$ and $p_{\mathrm{T}} < 20\,\mathrm{GeV}$. Jet quality criteria as described in Sec. 4.3.4 are applied to reject jets not coming from proton-proton collisions. The test sample requires a tag jet within $|\eta| < 2.0$, which is back-to-back ($\Delta\phi > 2.6$) and p_{T} -balanced with the probe jet. The jet selection efficiency and the systematic uncertainty on the efficiency is shown for two η bins in Fig. 4.13. The overall jet inefficiency is below 5% at jet $p_{\mathrm{T}} = 20\,\mathrm{GeV}$ and decreases with increasing jet p_{T} . The efficiency is above 99% for jets with $p_{\mathrm{T}} > 100\,\mathrm{GeV}$.

4.4 Missing Transverse Energy

The missing transverse energy is defined as the momentum imbalance in the transverse plane to the beam axis. A conservation of the momentum in this plane is expected. This variable is important for many beyond Standard Model physics searches, because in many new physics models, massive particles are expected to escape the detector like neutrinos. Those particles can be measured only indirectly via the missing transverse energy.

The vector momentum of the missing transverse energy is defined as the negative vector sum of all particles detected in the collision.

4.4.1 Reconstruction

The energy deposition in the calorimeters and the measurements in the muon spectrometer are considered separately:

$$E_{x(y)}^{miss} = E_{x(y)}^{miss,calo} + E_{x(y)}^{miss,\mu} \tag{4.11}$$

The missing $E_{\mathrm{T}}^{\mathrm{miss}}$is calculated as:

$$E_T^{miss} = \sqrt{(E_x^{miss})^2 + (E_y^{miss})^2} \tag{4.12}$$

The $E_T^{miss,calo}$ terms are derived from the calorimeter cells calibrated to the energy scale according to the associated physics objects like electrons, photons, hadronically decaying τ-leptons, and jets. The $E_T^{miss,calo,\mu}$ term depends on the isolation of the reconstructed muon (see below). Cells associated to clusters, but not matched to any physics objects, are taken into account in the $E_T^{miss,CellOut}$ term. The $E_T^{miss,calo}$ is calculated as follows:

$$E_{x(y)}^{miss,calo} = E_{x(y)}^{miss,e} + E_{x(y)}^{miss,\gamma} + E_{x(y)}^{miss,\tau} + E_{x(y)}^{miss,jets} + E_{x(y)}^{miss,softjets} + E_{x(y)}^{miss,calo,\mu} + E_{x(y)}^{miss,CellOut}. \tag{4.13}$$

Each term is calculated from the negative sum of the calibrated objects (Sec. 4.4.2):

$$E_x^{miss} = -\sum_{i=1}^{N_{cell}^{term}} E_i \sin\theta_i \cos\phi_i \tag{4.14}$$

$$E_y^{miss} = -\sum_{i=1}^{N_{cell}^{term}} E_i \sin\theta_i \sin\phi_i \tag{4.15}$$

where E_i is the scaled energy deposition, θ_i the polar angle, and ϕ_i the azimuthal angle of cell i. All cells belonging to a specific object with a pseudorapidity $|\eta| < 4.5$ are considered. The jet term is split into $E_{x(y)}^{miss,jets}$ and $E_{x(y)}^{miss,softjets}$. The first term is reconstructed from jets with calibrated $p_{\mathrm{T}} > 20\,\mathrm{GeV}$ and the second term from jets with $7 < p_{\mathrm{T}} < 20\,\mathrm{GeV}$.

The muon term ($E_{x(y)}^{miss,\mu}$) is calculated from the momentum of selected muons with $|\eta| < 2.7$. In the pseudorapidity region $|\eta| < 2.5$ only CB muons are considered. As described in Sec. 4.2, the energy loss in the calorimeter of muons is taken into account for the ID to MS extrapolation of CB muons, if the muons is well isolated. Therefore the muon terms have to be calculated differently for isolated and non-isolated muons. The muon is defined as isolated if $R_{\mathrm{cone}} > 0.3$ to the next reconstructed jet in the event. Then the energy loss is considered in the CB muon and the $E_{x(y)}^{miss,calo,\mu}$ is not added to the calorimeter term in order to avoid double counting. Otherwise, the muon term is calculated from the MS track and the energy loss in the calorimeter is taken into account in the calorimeter term: $E_{x(y)}^{miss,calo,\mu}$. In the outer pseudorapidity region $2.5 < |\eta| < 2.7$ the MS momentum is used for both isolated and non-isolated muons and $E_{x(y)}^{miss,calo,\mu}$ is added to the calorimeter term.

4.4.2 Calibration

The cells are calibrated according to the parent object identity. The identification cuts and the calibration schemes are listed below:

- $E_{x(y)}^{miss,e}$ Electrons are identified as *medium* electrons with $p_{\mathrm{T}} > 10\,\mathrm{GeV}$ and calibrated as described in Sec. 4.1.

- $E_{x(y)}^{miss,\gamma}$ Photons are identified with *tight* selection [134] and $p_{\mathrm{T}} > 10\,\mathrm{GeV}$, due to the low photon purity, no calibration is applied.
- $E_{x(y)}^{miss,\tau}$ τ-leptons are required to be identified with *tight* selection criteria [135] and $p_{\mathrm{T}} > 10\,\mathrm{GeV}$. The calibration is applied according to the local hadronic calibration (LCW) [136] (see below).
- $E_{x(y)}^{miss,softjets}$ Softjets are reconstructed jets (anti-k$_T$ with R=0.6 more details 4.3.2) with $7 < p_{\mathrm{T}} < 20\,\mathrm{GeV}$ calibrated with the LCW calibration scheme.
- $E_{x(y)}^{miss,jets}$ Jets are reconstructed as described in Sec. 4.3 with $p_{\mathrm{T}} > 20\,\mathrm{GeV}$, calibrated with LCW and applied jet energy scale factors in Sec. 4.1.3.
- $E_{x(y)}^{miss,cellOut}$ The cellOut terms consider calorimeter cells with energy deposition, not matched to physics objects, but matched to topoclusters. They are calibrated with the LCW scheme.

The LCW calibration scheme weights each calorimeter cell according to the topology (electromagnetic or hadronic cluster), the cluster energy, and the cell energy density. Afterwards, corrections for non-active material and unclustered calorimeter energy are made.

4.4.3 Performance

Detailed performance studies are presented in [137] based on minimum bias events, di-jet events, $Z \to ll$ events, and $W \to l\nu$ events corresponding to integrated luminosities of 0.3 nb^{-1}, 600 nb^{-1}, and 36 pb^{-1} respectively.

Direct measurements of the $E_{x(y)}^{miss}$ resolution as function of $\sum E_{\mathrm{T}}$ are performed in $Z \to ll$ and QCD jet events. Assuming values of $E_{x(y)}^{miss}$ equal to zero in those events, the resolution is derived from the width of the combined distribution ofE_x^{miss} and E_y^{miss} in bins of $\sum E_{\mathrm{T}}$. The resolution is fitted with a functions

$$\sigma = k \cdot \sqrt{\sum E_{\mathrm{T}}} \tag{4.16}$$

with k quantifying the resolution of $E_{\mathrm{T}}^{\mathrm{miss}}$. The resolutions derived from data for minimum bias, QCD di-jet and $Z \to ll$ events are shown in Fig. 4.14(a). Comparable results calculated from MC samples are shown in Fig. 4.14 (b).

The $E_{\mathrm{T}}^{\mathrm{miss}}$resolutions studied in different channels are in good agreement in both the data channels and the MC simulations. The resolution $\sigma/\sqrt{\sum E_{\mathrm{T}}}$ is about $0.5\,\mathrm{GeV}^{1/2}$.

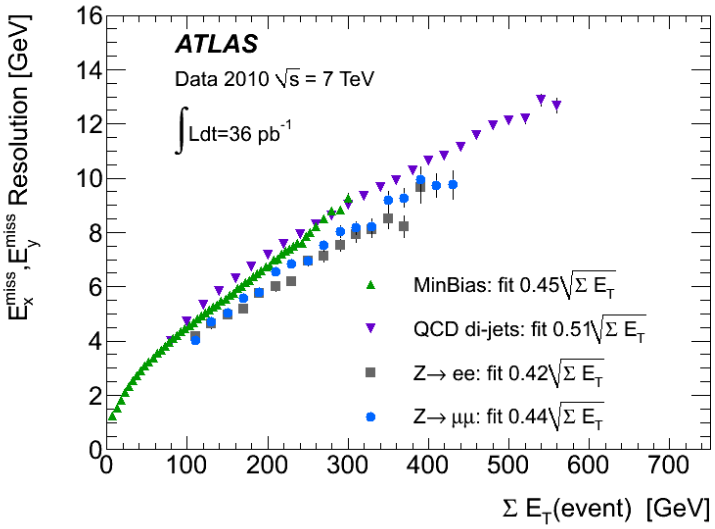

(a)

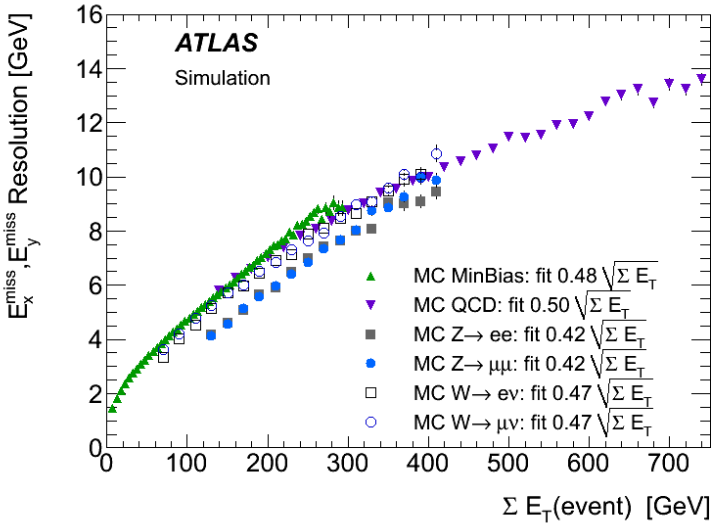

(b)

Figure 4.14: E_x^{miss} and E_y^{miss} resolution as a function of the total transverse energy in the event calculated by summing the p_{T} of muons and the total transverse energy in the calorimeter in data at $\sqrt{s} = 7\,\mathrm{TeV}$ (a) and MC (b). The resolution of the two $E_{\mathrm{T}}^{\mathrm{miss}}$components is fitted with a function $\sigma = k \cdot \sqrt{\sum E_{\mathrm{T}}}$ and the fitted values of the parameter k, expressed in $\mathrm{GeV}^{1/2}$, are reported in the figure [137].

5 Analysis Strategy

The analysis described in this thesis is a search for R-Parity conserving SUSY models. The three different models under investigation have common kinematic features even though they have different phenomenologies as explained in detail in Ch. 1.2.1. R-Parity conservation requires that each vertex in the Feynman diagram must have even number of SUSY particles. According to that rule, SUSY particles (sparticles) can only be produced in pairs, they can only decay into another SUSY plus an SM particle, and every SUSY decay chain must end with the lightest supersymmetric particle (LSP). Both sparticles produced at the SUSY production vertex decay via decay chains like the mSUGRA example shown in Fig. 5.1. The neutralino ($\tilde{\chi}_1^0$) is the LSP in the case of mSUGRA models, and the gravitino ($\tilde{G}$) in the case of GMSB. The LSP escapes the detector without any interaction in both scenarios, such that all models analysed in this thesis have final states with significant missing transverse energy ($E_{\mathrm{T}}^{\mathrm{miss}}$). The number of sparticle decays in one decay chain depends on the mass hierarchy and the branching ratios (BR), which differ depending on the SUSY parameters. Leptons are produced in the following decay chains with gauginos ($\tilde{\chi}$):

$$\tilde{\chi}_i^0 \rightarrow l^{\pm}\nu\tilde{\chi}_j^{\mp} \tag{5.1}$$
$$\tilde{\chi}_i^{\pm} \rightarrow l^{\pm}\nu\tilde{\chi}_j^0 \tag{5.2}$$
$$\tilde{\chi}_i^0 \rightarrow l^{\pm}l^{\mp}\tilde{\chi}_j^0 \tag{5.3}$$
$$\tilde{\chi}_i^{\pm} \rightarrow l^{\pm}l^{\mp}\tilde{\chi}_j^{\pm} \tag{5.4}$$

with $i > j$. According to Eqs. (5.1)-(5.4), there are two different ways for exactly 2 leptons to be produced in the final state of a SUSY event:

1. two decays like in Eq. (5.1), and/or Eq. (5.2) happen in one event
2. exactly one decay-chain, like in Eq. (5.3) or Eq. (5.4) is involved

In the first case, two same or different-flavour leptons with the same or opposite charge (sign) are produced. The latter case produces exactly 2 leptons with same-flavour and opposite-sign.

The Flavour Subtraction(FS) Analysis performed in this thesis, aims to measure the excess of opposite-sign same-flavour lepton pairs (OSSF) over opposite-sign different-flavour lepton pairs (OSDF). This method is an interesting tool to measure SUSY particle mass differences and to suppress flavour symmetric background efficiently.

This chapter gives an overview of the analysis strategy. After explaining the idea of flavour subtraction (OSSF-OSDF) in general, the power of the FS method for SM background suppression is shown in Sec. 5.1.1. Correlated systematics are reduced by FS as derived in Sec. 5.1.2 and in Sec. 5.1.3 the use of FS to account for combinatorial SUSY backgrounds is explained.

The second part of this chapter (Sec. 5.2) describes the differences in kinematics between the final states of Standard Model background processes and different SUSY

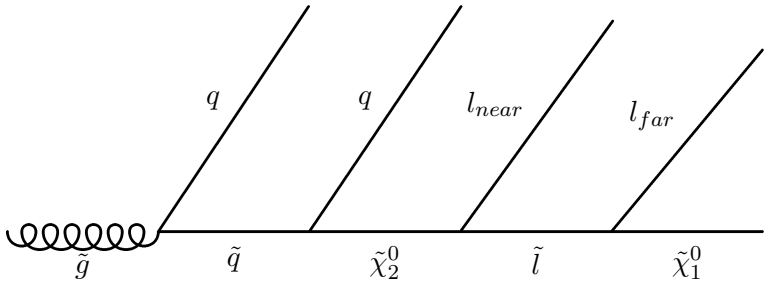

Figure 5.1: Typical SUSY decay chain (e.g. in mSUGRA models) with the neutralinos ($\tilde{\chi}_1^0$) as LSP . In case of the GMSB scenario, the gravitinos ($\tilde{G}$) is the LSP. In contrast to mSUGRA the next-to-lightest sparticle (NLSP) is highly constrained by the GMSB parameters.

benchmark points for the SUSY models studied in this thesis. Firstly, the different SM backgrounds with di-lepton final states are summarized in Sec. 5.2.1 with respect to the features of FS. Then the so-called SUSY *signal grids* and corresponding benchmark points are introduced in Sec. 5.2.2. A *signal grid* is a parameter space, usually in two dimensions, in which two parameters are varied while the other free parameters of the SUSY scenario are fixed. The analysis, for a given signal region, is performed for each point in the *signal grid* and compared to the results observed in data. Finally, the kinematic distributions with the best separation power between SUSY and SM backgrounds are discussed in Sec. 5.2.3. The signal regions studied in the analysis in Ch. 6, are defined, based on this Monte Carlo study.

5.1 Flavour Subtraction

The excess of identical flavour events over those of different-flavour is quantified by using the variable $\mathcal{S}$, introduced in [52].

$$\mathcal{S} = N^{true}_{e^{\pm}e^{\mp}} + N^{true}_{\mu^{\pm}\mu^{\mp}} - N^{true}_{e^{\pm}\mu^{\mp}} \tag{5.5}$$

Flavour symmetric events are expected to cancel after FS, such that $\mathcal{S} = 0$. However, particles interacting within the detector and different acceptances for triggering, reconstruction and identification of electrons and muons affect the total number of $N_{l^{\pm}l^{\mp}}$ events, meaning that in practise even flavour symmetric processes will not cancel completely after FS. Therefore, differences in the lepton trigger, reconstruction and identification efficiencies must be taken into account in the subtraction. The true numbers of events are multiplied by the following efficiencies:

$$N(e^{\pm}e^{\mp}) = (1-(1-\tau_e)^2)\cdot\epsilon_e\cdot\epsilon_e\cdot N^{true}_{ee} \tag{5.6}$$
$$N(\mu^{\pm}\mu^{\mp}) = (1-(1-\tau_\mu)^2)\cdot\epsilon_\mu\cdot\epsilon_\mu\cdot N^{true}_{\mu\mu} \tag{5.7}$$
$$N(e^{\pm}\mu^{\mp}) = (1-(1-\tau_e)(1-\tau_\mu))\cdot\epsilon_e\cdot\epsilon_\mu\cdot N^{true}_{e\mu} \tag{5.8}$$

with τ_e and τ_μ the electron and muon trigger efficiencies, and ϵ_e and ϵ_μ the reconstruction and identification efficiency for electrons and muons respectively. Replacing the true

number of expected di-lepton events in Eq. (5.5) with the measured numbers, the excess of same-flavour events can therefore be calculated as:

$$\mathcal{S} = \frac{N(e^{\pm}e^{\mp})}{(1-(1-\tau_e)^2)\cdot\epsilon_e\cdot\epsilon_e} + \frac{N(\mu^{\pm}\mu^{\mp})}{(1-(1-\tau_\mu)^2)\cdot\epsilon_\mu\cdot\epsilon_\mu} - \frac{N(e^{\pm}\mu^{\mp})}{1-(1-\tau_e)(1-\tau_\mu)\cdot\epsilon_e\cdot\epsilon_\mu} \quad (5.9)$$

Assuming a constant reconstruction and identification efficiency for all muons and electrons, the formula can be simplified by introducing the ratio $\beta = \frac{\epsilon_e}{\epsilon_\mu}$. This simplification induces an extra systematic which will be discussed in detail in the systematic section (Sec. 6.6). Equation (5.9) therefore becomes:

$$\mathcal{S} = \frac{N(e^{\pm}e^{\mp})}{\beta(1-(1-\tau_e)^2)} - \frac{N(e^{\pm}\mu^{\mp})}{1-(1-\tau_e)(1-\tau_\mu)} + \frac{\beta N(\mu^{\pm}\mu^{\mp})}{(1-(1-\tau_\mu)^2)} \quad (5.10)$$

The trigger efficiencies τ_e and τ_μ and β, the ratio of reconstruction efficiencies ϵ_e/ϵ_μ, must be determined for data and Monte Carlo samples separately. Their determination is described in the analysis chapter, in Sec. 6.2.3 and Sec. 6.7 respectively.

5.1.1 Standard Model Background Suppression

The most important feature of the flavour subtraction is the suppression of flavour symmetric background processes, such as $t\bar{t}$ or SUSY backgrounds of di-lepton pairs from different decay chains as explained in Sec. 5.1.3. The amount of same-flavour and different-flavour events is expected to be equal, given the underlying physics, and this is also reflected at the event generator level:

$$\left(N_{e^{\pm}e^{\mp}} + N_{\mu^{\pm}\mu^{\mp}} = N_{e^{\pm}\mu^{\mp}} + N_{\mu^{\pm}e^{\mp}}\right)_{t\bar{t}}. \quad (5.11)$$

After considering the differences in trigger, reconstruction and identification efficiencies as explained in Sec. 5.1 in Eq. (5.10), the corrected flavour symmetric events cancel out completely after flavour subtraction within statistical uncertainties. This is demonstrated in Fig. 5.2 for $t\bar{t}$ events as a proof of principle.

However, this method cannot remove background from flavour asymmetric processes, and so selection cuts must be applied to remove these and to reduce the number of background events, such that the signal after subtraction is not completely dominated by statistical fluctuations. The FS method is applied on MC $Z \to \ell\ell$ events in Fig. 5.3. The remaining distribution still shows a clear Z mass peak. Individual FS studies (Fig.B.1-B.4) for each SM background, introduced in Sec. 5.2.1, are attached to the appendix B. Several kinematic distributions are investigated, and the distributions with best separation power are discussed in Sec. 5.2.3. These are used for defining signal regions, in order to find sub-samples with only remaining flavour symmetric background contributions, such that the FS can expose any flavour excess of new physics models.

5.1.2 Reduction of Systematics Effects

Another advantage of subtracting the different-flavour contribution from the same-flavour contribution is the reduction of correlated systematics, e.g. the jet energy scale uncertainty, jet resolution, etc.

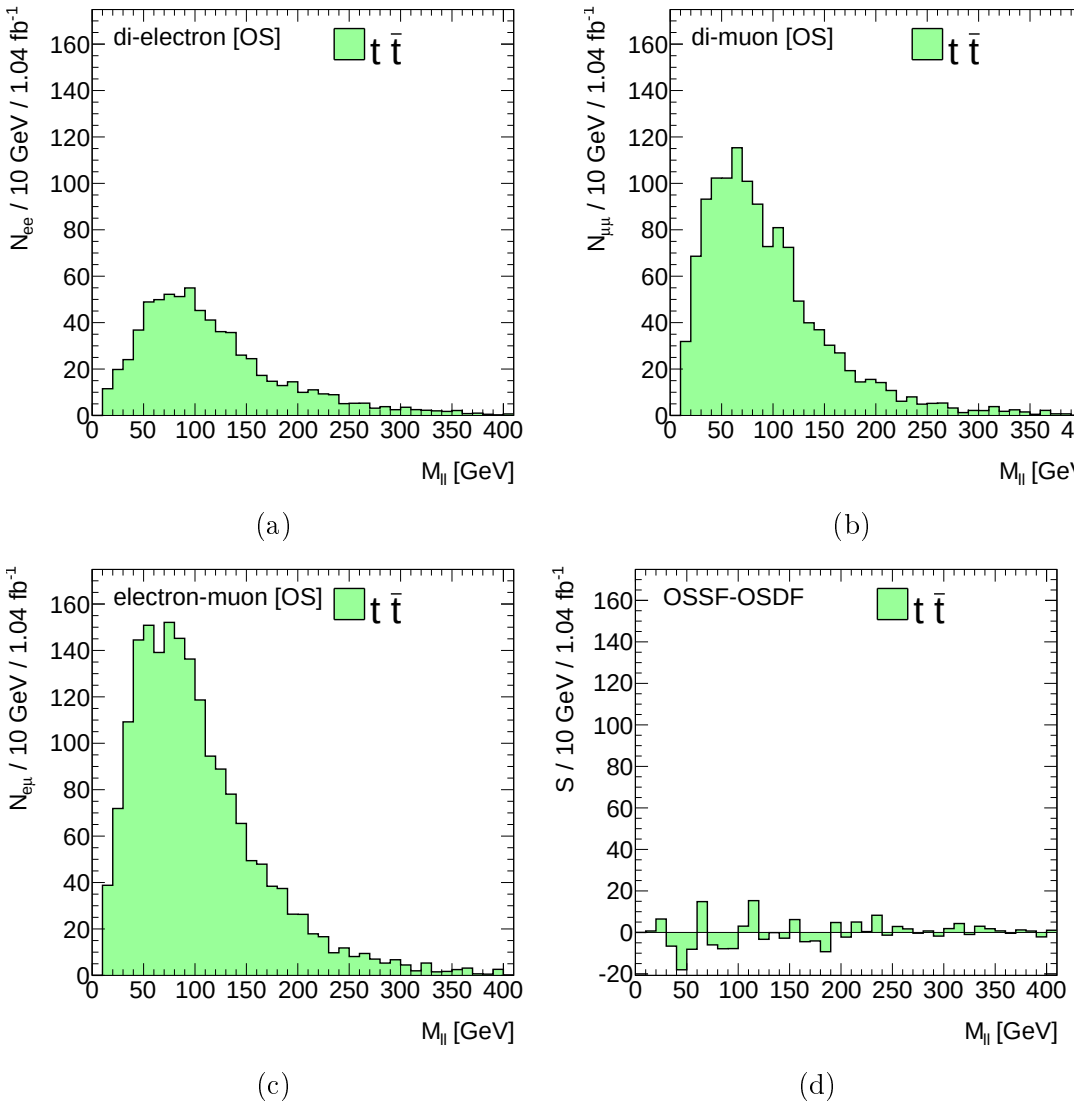

Figure 5.2: The FS applied to the event selection directly after the *exactly 2 opposite-sign leptons* cut on the $t\bar{t}$ sample only. The invariant mass distributions of N_{ee}(a) is added to the $N_{\mu\mu}$(b) distribution then, the different-flavour sample $N_{e\mu}$(c) is subtracted . The trigger, reconstruction, and identification efficiencies are considered as explained above. The distribution of $\mathcal{S}$ after the subtraction is shown in (d).

$$\begin{aligned}
\Delta\mathcal{S} &= \mathcal{S}^{nom.} + \mathcal{S}^{sys.} && (5.12)\\
&= (N_{ee}^{nom.} + N_{\mu\mu}^{nom.} - N_{e\mu}^{nom.}) + (N_{ee}^{sys.} + N_{\mu\mu}^{sys.} - N_{e\mu}^{sys.}) && (5.13)\\
&= (N_{ee}^{nom.} + N_{ee}^{sys.}) + (N_{\mu\mu}^{nom.} + N_{\mu\mu}^{sys.}) - (N_{e\mu}^{nom.} + N_{e\mu}^{sys.}) && (5.14)\\
&= \Delta N_{ee} + \Delta N_{\mu\mu} - \Delta N_{e\mu} && (5.15)
\end{aligned}$$

A detailed summary of all considered systematic effects is discussed in the analysis chapter in Sec. 6.6. Although FS reduces correlated systematics, it introduces additional

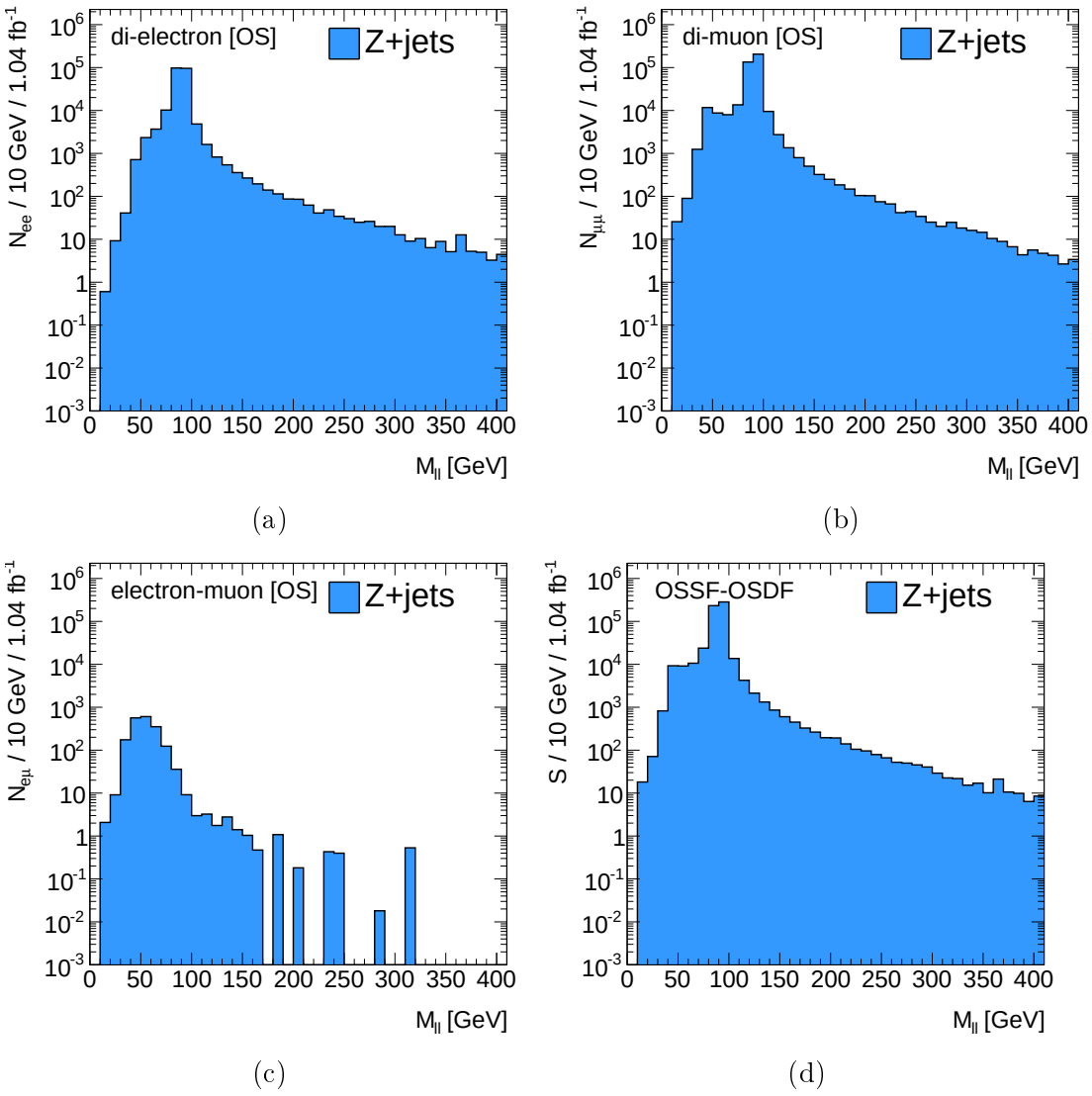

Figure 5.3: The FS is applied to the event selection directly after the *exactly 2 opposite-sign leptons* cut on the $Z \to \ell\ell$ sample only. The invariant mass distributions of N_{ee}(a) is added to the $N_{\mu\mu}$(b) distribution then, the different-flavour sample $N_{e\mu}$(c) is subtracted. The trigger, reconstruction, and identification efficiencies are considered as explained above. The distribution of $\mathcal{S}$ after the subtraction is shown in (d).

systematic effects due to the simplification of the $\mathcal{S}$ variable in Eq. (5.10), which have to be taken into account. The ratio of the of electron and muon reconstruction and identification efficiencies (β) is not constant over p_{T} or over all physics processes, inducing an extra systematic which is studied in detail and considered appropriately. The trigger efficiencies are constant over the physics processes and the p_{T} -range under study, but vary within two different ηregions due to the design of the ATLAS muon spectrometer. Nevertheless, the two additional systematic effects are negligible, such that the gain due to the reduction of correlated systematics obtained by using the FS improves the overall systematics.

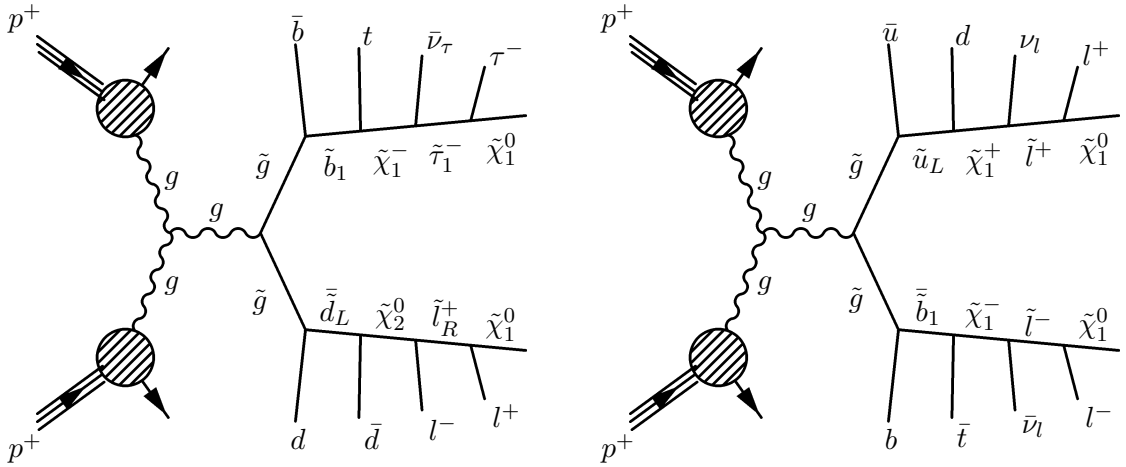

Figure 5.4: Feynman diagram of SUSY events with di-lepton final states. The di-leptons within one decay chain are shown in (a). The invariant mass distribution of these events are studied in detail in order to extract SUSY particle mass differences. The Feynman diagram in (b) has to be considered as combinatorial background.

5.1.3 Exploiting Kinematic Mass Edges

If SUSY is discovered, observables must be measured in order to determine the underlying SUSY parameters and the SUSY scenario. Assuming a R-parity conserving model, each sparticle will decay via SUSY decay chains (cf. Fig. 5.1) into the LSP, which will escape the detector. The missing constraints from the two escaping neutralinos impedes the complete kinematic reconstruction of the SUSY event and therefore SUSY masses cannot be measured directly. Nevertheless, the invariant mass spectrum of opposite-sign leptons can be exploited by measuring the endpoint of the distribution. Opposite sign di-leptons produced in

$$\tilde{\chi}_2^0 \to \tilde{\ell}^{\pm}\ell^{\mp} \to \ell^{\pm}\ell^{\mp}\tilde{\chi}_1^0 \tag{5.16}$$

decays (cf. Fig. 5.1) have an invariant mass spectrum determined by the masses of the contributing sparticles. Figure 5.5(a) shows the invariant mass distribution of the decay chain from Eq. (5.16) for the SU4 benchmark point (the SUSY parameters of this point are explained in detail in Sec. 5.2.2). The endpoint is clearly visible by eye at $\sim 54\,\mathrm{GeV}$. A possible Feynman diagram is shown in Fig. 5.4(a). Taking into account that not all true leptons originate from the decay chain in Eq. (5.16), the combinatorial background due to opposite-sign leptons from different decay chains must be considered (cf. Fig 5.4(b)). In this case, the shape of the opposite-sign same-flavour di-lepton invariant mass distribution still contains the triangular shape due to the leptons from Eq. (5.16), but the endpoint is smeared by additional SUSY background. This combinatorial SUSY background can be suppressed by the FS method. The generator-level distribution of OSSF-OSDF true di-lepton pairs from all possible productions in SU4 is shown as open circles in Fig. 5.5(c). Figure 5.5(e) finally, shows the same plot after detector simulation and reconstruction (filled circles). The reconstruction simulation does not change the distribution as much as the combinatorial SUSY background. Applying the FS after considering the combinatorics the endpoint of the invariant mass distribution can be clearly separated from background. The resulting edge of $m_{\ell\ell}$-distribution can be fitted and the endpoint can be determined (cf. Eq (1.52)) as explained in Sec. 1.2.4.

The invariant mass of the di-leptons is one observable needed in order to determine

SUSY parameters, but the theoretical calculation for the endpoint has three free parameters ($m^2_{\ell\ell}(m^2_{\tilde{\chi}^0_2}, m^2_{\tilde{\ell}}, m^2_{\tilde{\chi}^0_1})$ cf. Eq. (1.52)). Exploiting only one observable yields an under-determined expression. Another interesting observable is the invariant mass of the di-lepton system plus the jet from the quark originating directly before the $\tilde{\chi}^0_2$in the decay chain (cf. Fig. 5.1). The endpoint of this distribution depends on four SUSY mass parameters: $m^2_{\ell\ell}(m^2_{\tilde{q}}, m^2_{\tilde{\chi}^0_2}, m^2_{\tilde{\ell}}, m^2_{\tilde{\chi}^0_1})$. Three of the four parameters are the same as in the previous expression. In adding the jet to the invariant mass from the di-leptons, two challenges arise: Firstly, the correct jet has to be selected. As shown in the Feynman diagram in Fig. 5.1, more than one jet may be reconstructed in an event. The second problem is that the different squarks have different masses. The histograms in the right column in Fig. 5.5 show the truth invariant mass peak in the hatched area. The expected endpoint is calculated for the squark mass with the highest branching ratio for decaying into the $\tilde{\chi}^0_2$. The distribution with the open circles includes all true di-lepton pairs combined with the selected jet. This selection is done as follows: Two invariant masses are calculated, each including one of the two leading p_{T} -jets. The jet with the lower invariant mass of the jet-lepton-lepton system is chosen. This ensures that the endpoint which should be estimated with this technique is not shifted towards higher values. In case of insufficient statistics, the method might underestimate the endpoint. Nevertheless, it has been observed that this selection achieved the best performance. The filled circles show the same distributions after detector simulation and reconstruction.

The Feynman diagram in Fig. 5.1 shows two additional possibilities of combining the final state particles in order to extract more event information. By combining the jet with the lepton next to it (ℓ_{near}) and with the other lepton (ℓ_{far}), two more observables can be measured ($m^2_{q\ell_{near}}(m^2_{\tilde{q}}, m^2_{\tilde{\chi}^0_2}, m^2_{\tilde{\ell}})$ and $m^2_{q\ell_{far}}(m^2_{\tilde{q}}, m^2_{\tilde{\chi}^0_2}, m^2_{\tilde{\ell}}, m^2_{\tilde{\chi}^0_1})$). On the assumption that the best jet was selected for the m_{Jetll} invariant mass distribution, the same jet is used for the $m_{q\ell_{near}}$ and $m_{q\ell_{far}}$ distribution. Due to the fact that there is no way of distinguishing between lepton near and lepton far, both combinations are calculated, $m_{q\ell_1}$ and $m_{q\ell_2}$. The smaller invariant mass is defined as $m_{q\ell_{low}}$ and the larger invariant mass as $m_{q\ell_{high}}$, such that the endpoints are calculated as

$$m^2_{q\ell_{low}} = min\left(m^2_{q\ell_{near}}, m^2_{q\ell_{far}}\right), \tag{5.17}$$

$$m^2_{q\ell_{high}} = max\left(m^2_{q\ell_{near}}, m^2_{q\ell_{far}}\right). \tag{5.18}$$

Figure 5.6 shows the invariant mass distributions for $q\ell_{low}/q\ell_{high}$ at generator level (a/b), after considering combinatorial SUSY background and jet finding (c/d), and after detector simulation and reconstruction (e/f).

If the endpoints of the four distributions can be fitted successfully, four observables can be measured for an equation system with four free parameters. These endpoints can therefore be analysed by SUSY fit programs like *Fittino* [138] and the SUSY parameters can be constrained.

5.2 Kinematics of Standard Model Processes and Different SUSY Models

The flavour subtraction analysis is an exclusive analysis searching for same-flavour leptons. New physics can be found, if the kinematic distributions measured in data are well

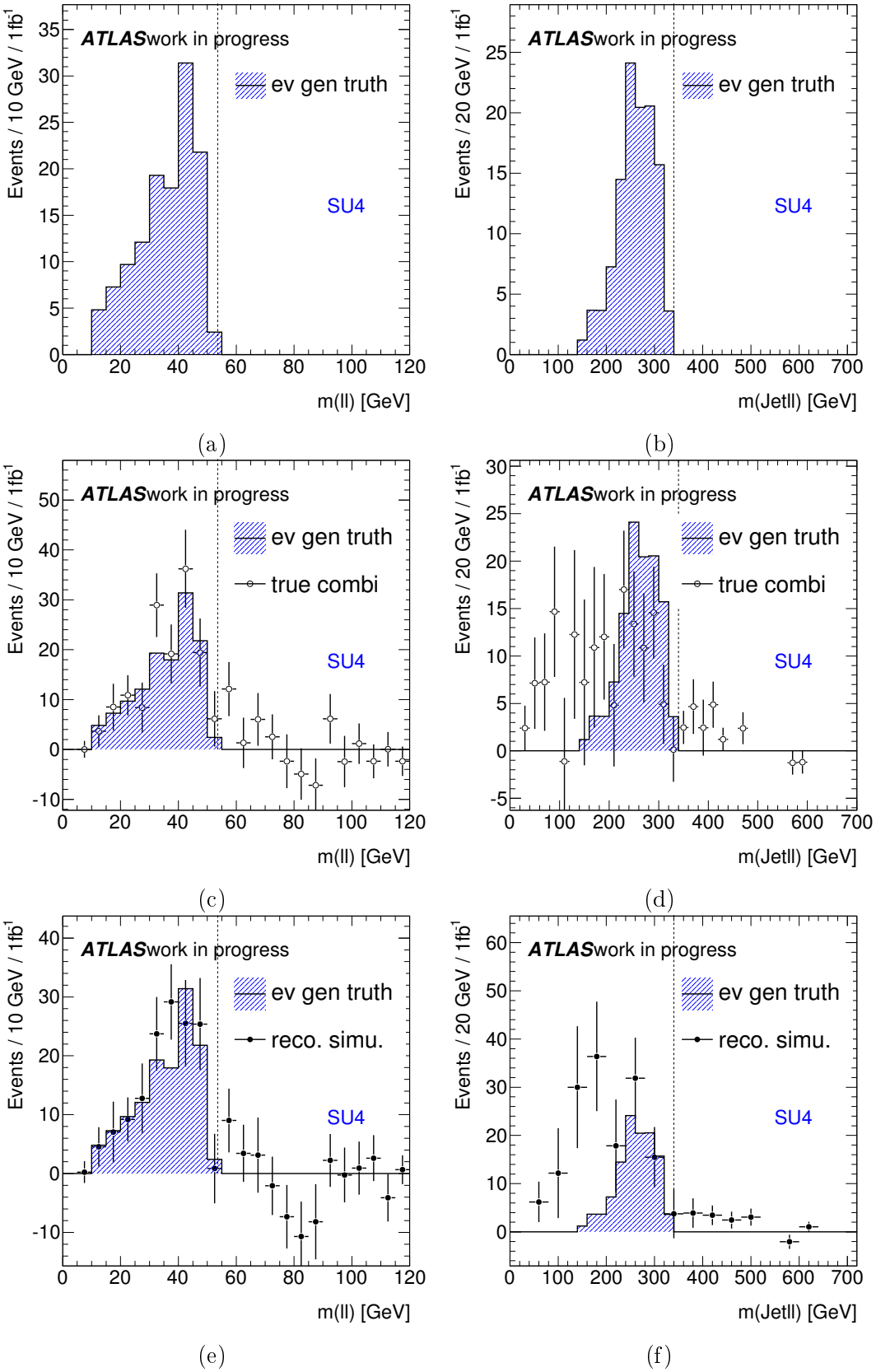

Figure 5.5: Invariant mass distributions in SU4 for m(ll) left column and m(Jetll) right column. (a) and (b) are based on the generator truth information, (c) and (d) consider combinatorial SUSY background from different decay chain and (e) and (f) show the distributions after detector simulation and reconstruction.

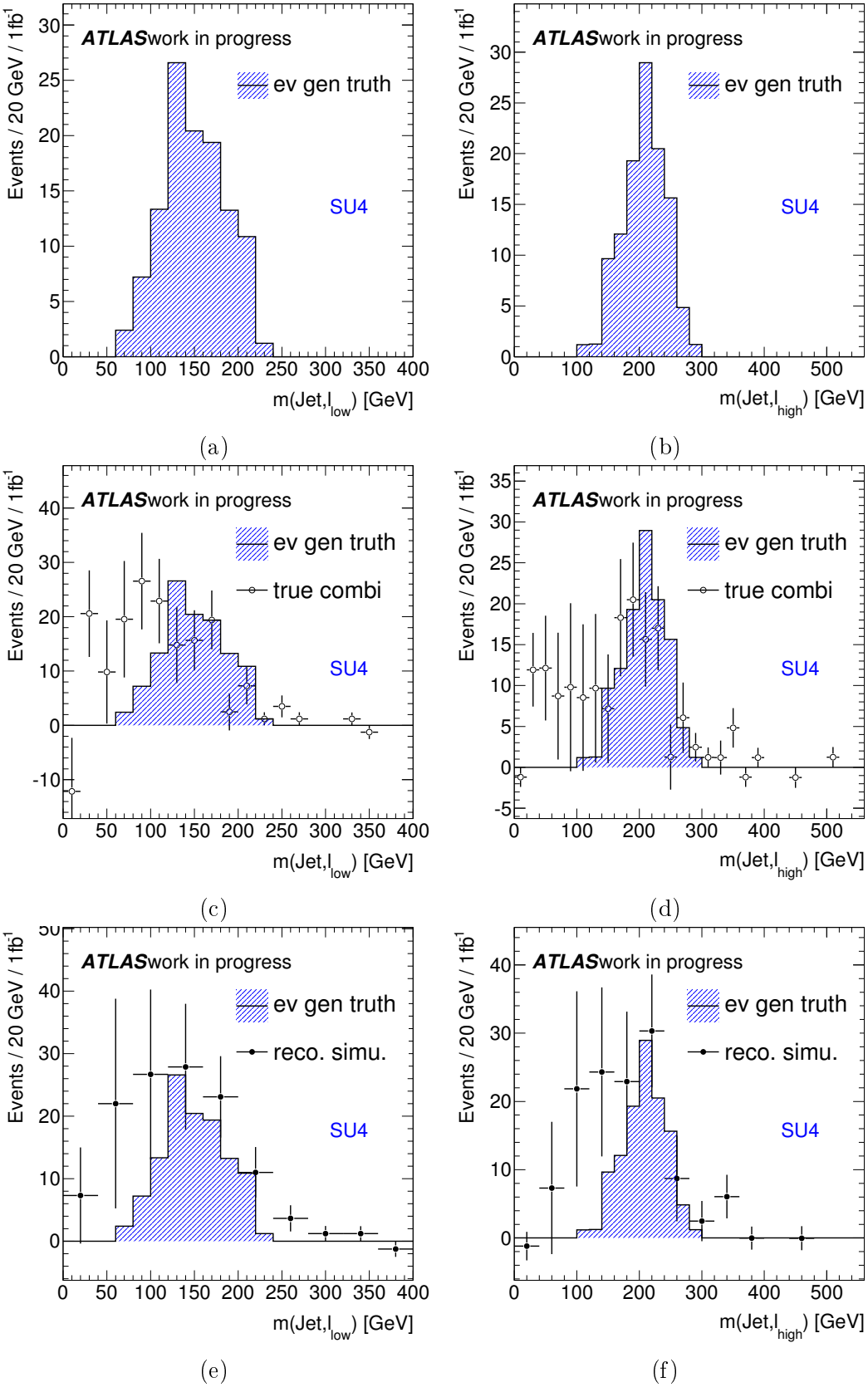

Figure 5.6: Invariant mass distributions in SU4 for m(Jet,l_{low}) left column and m(Jet,l_{high}) right column. (a) and (b) are based on the generator truth information, (c) and (d) consider combinatorial SUSY background from different decay chance and (e) and (f) show the distributions after detector simulation and reconstruction.

understood, by observing differences in comparison to the distributions expected from Standard Model processes. To achieve this, the Standard Model and SUSY processes are generated with Monte Carlo generators as described in Sec. 3.3. After the detector response has been simulated and the reconstruction algorithms applied, resulting in the same output formats for both MC samples and real data, the distributions can be compared.

Specific event selections have to be defined in order to suppress Standard Model processes (background) and keep as many simulated SUSY signal events as possible (for example a high signal-to-background ratio). These selection criteria are usually defined in so-called Monte Carlo studies. In the following section, the Standard Model processes with exactly 2 leptons in the final state are described in detail. These processes have to be separated from potential SUSY signals. In order to estimate the differences between SUSY signals and SM background, benchmark points for each SUSY model under investigation in this thesis were simulated and their kinematic variables are compared to the SM distributions.

5.2.1 Standard Model

The relevant SM processes which have to be distinguished from a potential SUSY signal have to be studied in detail. Only SM processes with di-lepton final states or final states that might be reconstructed as di-leptons are considered in the following. In order to simulated the expected number of event per process as precisely as possible, the production cross sections which have been measured in different experiments are taken into account.

Due to the fact that all physics processes have different production cross sections as shown in Fig. 2.2 but the amount of simulated MC events do not necessarily reflect this. The correct number of expected events coming from a specific process can be achieved by normalizing the different samples to the same integrated luminosity. The histograms shown in this section are weighted to $1.04\,\mathrm{fb}^{-1}$ matching the total integrated luminosity of data analysed in Ch. 6.

Z+Jets and Drell-Yan

After applying the data quality cuts and requiring exactly two tight and isolated (cf. Sec. 6.4.1), opposite-sign leptons ($e^{\pm}e^{\mp}$, $e^{\pm}\mu^{\mp}$ or $\mu^{\pm}\mu^{\mp}$), from Z-boson decays are the main contribution to the selected sample.

The production cross section for Z/γ^* has been measured in ATLAS as $\sigma^{tot}_{Z/\gamma^*} \cdot BR(Z/\gamma^* \to ee) = 0.952 \pm 0.010(\mathrm{stat}) \pm 0.026(\mathrm{syst}) \pm 0.032(\mathrm{lumi}) \pm 0.019(\mathrm{acc})$ nb [139]. Z/γ^* decay into two leptons:

$$Z/\gamma^* \to \ell^+\ell^- \tag{5.19}$$

$$Z/\gamma^* \to \tau^+\tau^- \to \ell^+\nu_\ell\bar{\nu}_\tau\ell^-\bar{\nu}_\ell\nu_\tau \tag{5.20}$$

with $l = e, \mu$. Following the laws of lepton flavour and charge conservation, Z/γ^* always decays into same-flavour opposite-sign pairs ($e^{\pm}e^{\mp}$, $\mu^{\pm}\mu^{\mp}$ or $\tau^{\pm}\tau^{\mp}$). Due to the fact that electron and muon final states in Eq. (5.19) do not decay any further, only same-flavour events are produced ($e^{\pm}e^{\mp}$ and $\mu^{\pm}\mu^{\mp}$). This is important for the flavour subtraction, because of this asymmetry (only same-flavour pairs), the Z/γ^* contribution has to be suppressed by selection cuts before applying the flavour subtraction.

The second Eq. (5.20) shows the decay into a di-tau pair. If both tau leptons decay leptonically, all processes $e^{\pm}e^{\mp}$, $e^{\pm}\mu^{\mp}$ and $\mu^{\pm}\mu^{\mp}$ investigated in this analysis are produced. The same branching ratios (BR) for $\tau^- \to e(\mu)^-\bar{\nu}_{e(\mu)}\nu_\tau$ yield a flavour symmetric contribution from $Z \to \tau\tau$ decays. After applying the FS, these contributions will cancel each other out.

Equation (5.19) does not have a natural source of $E_{\mathrm{T}}^{\mathrm{miss}}$, and so the $E_{\mathrm{T}}^{\mathrm{miss}}$ distributions is expected to be small. Additional jets produced in the proton-proton collision and detector effects like unmeasured jet and electron p_{T} (i.e. due to final-state-radiation or bremsstrahlung effects in case of electrons) might lead to significant $E_{\mathrm{T}}^{\mathrm{miss}}$ contributions. The kinematics which can be used to suppress Z/γ^* processes are discussed in detail in Sec. 5.2.3.

Di-Boson - WW, WZ and ZZ

Di-boson processes are divided into three different groups, WW, WZ and ZZ. Each di-boson process produces opposite-sign di-lepton pairs and neutrinos, such that selection criteria on leptons and $E_{\mathrm{T}}^{\mathrm{miss}}$ are fulfilled.

The production cross section for W^+W^- events is measured in ATLAS [140] and found to be $\sigma^{tot}_{W^+W^-} = 48.2 \pm 4.0(\mathrm{stat}) \pm 6.4(\mathrm{syst}) \pm 1.8(\mathrm{lumi})$ pb. The fully leptonic WW decays which are the only relevant WW decays for the di-lepton search are:

$$W^+W^- \to \ell^+\nu_\ell\ell^-\bar{\nu}_\ell \tag{5.21}$$
$$W^+W^- \to \tau^+\tau^- \to \ell^+\nu_\ell\bar{\nu}_\tau\ell^-\bar{\nu}_\ell\nu_\tau \tag{5.22}$$

with $\ell = e, \mu$. These decays have exactly the same final states as the $Z \to \ell\ell$ decays, with additional neutrinos. But the leptons originate from different W bosons, therefore they are not connected via lepton flavour conservation consequently, the produced events are flavour symmetric and cancel each other out after FS. This contribution is therefore very small.

The measured WZ production cross section at LHC is $\sigma^{tot}_{WZ} = 21.1^{+3.1}_{-2.8}(\mathrm{stat}) \pm 1.2(\mathrm{syst})$ $^{+0.9}_{-0.8}(\mathrm{lumi})$ pb [141]. The relevant WZ di-boson process decays leptonically as follows:

$$W^{\pm}Z \to q\bar{q}\ell^+\ell^- \tag{5.23}$$
$$W^{\pm}Z \to q\bar{q}\tau^+\tau^- \to \ell^+\nu_\ell\bar{\nu}_\tau\ell^-\bar{\nu}_\ell\nu_\tau \tag{5.24}$$

with $\ell = e, \mu$. The final states are identical to the $Z \to \ell\ell$ decays, because the leptons originate from the Z bosons. The additional W-boson has to decay hadronically, in order to produce exactly 2 leptons in the final state. The $W^{\pm}Z \to \tau\tau$ decays are flavour symmetric and can be suppressed by the FS. The $W^{\pm}Z \to \ell\ell$ remain like the $Z \to \ell\ell$ events, and have to suppressed by selection cuts.

The ZZ production cross section is $\sigma^{tot}_{ZZ} = 8.5^{+2.7}_{-2.3}(\mathrm{stat})$ $^{+0.4}_{-0.3}(\mathrm{syst}) \pm 0.3(\mathrm{lumi})$ pb [142] which is much smaller than $Z \to \ell\ell$. It has the same relevant decays as the single Z-boson decays:

$$ZZ \rightarrow \ell^+\ell^-\nu_\ell\bar{\nu}_\ell \tag{5.25}$$
$$ZZ \rightarrow \tau^+\tau^-\nu_\ell\bar{\nu}_\ell \rightarrow \ell+\nu_\ell\bar{\nu}_\tau\ell^-\bar{\nu}_\ell\nu_\tau\nu_\ell\bar{\nu}_\ell \tag{5.26}$$
$$ZZ \rightarrow \ell+\ell^- q\bar{q} \tag{5.27}$$

with $\ell = e, \mu$. In order to have exactly 2 leptons in the final state, one Z decays leptonically into ($e^\pm e^\mp$, $\mu^\pm\mu^\mp$ or $\tau^\pm\tau^\mp$) and the other Z decays either hadronically, or into a di-neutrino pair. The decays via di-tau leptons is flavour symmetric, but the decays Eq. (5.26) and Eq. (5.27) cannot be subtracted via the FS. In addition, neutrinos are produced in Eq. (5.26), which yields a larger $E_{\mathrm{T}}^{\mathrm{miss}}$ spectrum for fully leptonic ZZ decays.

Fully Leptonic $t\bar{t}$ Decay

The top quark pair production cross-section is determined in the ATLAS experiment based on a statistical combination of measurements of di-lepton and single-lepton final states at $\sqrt{s} = 7\,\mathrm{TeV}$ as $\sigma_{t\bar{t}}^{tot} = 176 \pm 5(\mathrm{stat})^{+13}_{-10}$ (syst) ± 7 (lumi) pb [143]. The leptonic $t\bar{t}$ decay has exactly the same final state as the WW di-boson decays, with additional b-jets:

$$t\bar{t} \rightarrow W^+ b\, W^- \bar{b} \rightarrow \ell^+\nu_\ell b\, \ell^-\bar{\nu}_\ell\bar{b} \tag{5.28}$$

with $\ell = e, \mu$. The signature of $t\bar{t}$ events, large $E_{\mathrm{T}}^{\mathrm{miss}}$ and two opposite-sign leptons in the final state, cannot be distinguished easily from most signals of R-parity conserving SUSY models. Due to its large cross section in comparison to the boson production cross sections, $t\bar{t}$ is the main contribution after applying medium $E_{\mathrm{T}}^{\mathrm{miss}}$ cuts. In case of $t\bar{t}$ background, the flavour subtraction is most efficient, because even in the presence of a large $t\bar{t}$ contribution, the processes cancel out almost completely after FS. This demonstrated in Fig. 5.2 in Sec.5.1.

Single Top

The total predicted single top and anti-top production cross section $(t, \bar{t})$ are $64.6^{+3.3}_{-2.6}$ pb [144] for the leading t-channel process, 15.7 ± 1.4 pb [145] for top with associated W-boson (Wt) production, and $4.6 \pm 0.3\ pb$ [146] for the s-channel. The t-channel production cross section has been measured in ATLAS using $0.70\,\mathrm{fb}^{-1}$ of data [147] and found to be $\sigma_t = 90^{+32}_{-22}\,\mathrm{pb}$. Only one lepton is produced in the leptonic top decay:

$$t \rightarrow Wb \rightarrow \ell\nu_\ell b. \tag{5.29}$$

If the top is produced in association with a W-boson, and the W-boson also decays leptonically, the final state will have two opposite-sign leptons. This process is also flavour symmetric and can be suppressed by the FS. The other top decays only contribute if a jet is misidentified as lepton, therefore the single top contribution is negligible.

W+Jets

The W^+ and W^- production cross section have been measured by ATLAS [139] as $\sigma_{W+}^{tot} \cdot BR(W \rightarrow e\nu) = 6.063 \pm 0.023(\mathrm{stat}) \pm 0.108(\mathrm{syst}) \pm 0.206(\mathrm{lumi})$

± 0.104(acc)nband $\sigma^{tot}_{W^-} \cdot BR(W \to e\nu) = 4.191 \pm 0.020$(stat) ± 0.085(syst) ± 0.142(lumi) ± 0.084(acc) nbrespectively. The W BR in electrons or muons is 10.75% each:

$$W^+ \to \ell + \nu_\ell \tag{5.30}$$
$$W^+ \to \tau^+\nu_\tau \to \ell^+\nu_\tau\bar{\nu}_\ell \tag{5.31}$$

W-boson decays produce single leptons and $E_{\mathrm{T}}^{\mathrm{miss}}$ final states. W+jets events contribute to the selected events, if an additional fake-lepton is measured.

QCD - and Fake Estimation

Processes which couple via the strong interaction are favoured at hadron colliders like the LHC, where the QCD event production cross section is of the order of μb. Even following the tight lepton selection criteria chosen in order to suppress QCD fakes, the huge cross section yields a large number of QCD MC events. The amount of simulated Monte Carlo QCD events is not sufficient to make any statistical reliable estimates, therefore the QCD and W+jet *fake* events are estimated in data. These data driven fake estimations are used in the analysis for plotting and for comparing numbers. The method is explained in detail in Sec. 6.5.1. QCD events are not considered in the Monte Carlo study in this chapter.

5.2.2 SUSY Model Grids and Benchmark Points

mSUGRA - SU4

The mSUGRA breaking reduces the number of free parameters to the following five: The common scalar mass at the GUT scale m_0, the common gaugino mass at the GUT scale $m_{1/2}$, the common trilinear scalar coupling (Higgs-SFermion-SFermion coupling) A_0, the ratio of the vacuum expectation values of the Higgs field $\tan\beta$, and the sign of the higgsino mass term μ (cf. Sec. 1.2.3).

The mSUGRA grid is a set of variations of m_0 and $m_{1/2}$ with fixed values for:

$$A_0 = 0\,\mathrm{GeV},\ \tan\beta = 10,\ \text{and}\ \mu > 0.$$

The production cross section of SUSY events in this $m_0 - m_{1/2}$ parameter space varies from 783 pb for low m_0 and $m_{1/2}$ to 0.7 fb for high m_0 and $m_{1/2}$ (cf. Fig. 5.7).

The mSUGRA benchmark point (*SU4*) has the following parameters:

$$m_0 = 200\,\mathrm{GeV},\ m_{1/2} = 160\,\mathrm{GeV}\ A_0 = 0\,\mathrm{GeV},\ \tan\beta = 10,\ \text{and}\ \mu > 0.$$

Setting all mSUGRA parameters to specific values allows the calculation of the mass hierarchies and BR for all SUSY processes valid for a given point. These values can be derived with programs like *ISAJET* [115]. The mass hierarchy for the SU4 point is plotted in Fig.5.8. The heaviest SUSY particle is the stop squark ($\tilde{t}_2$) with $m_{\tilde{t}_2} = 447.4\,\mathrm{GeV}$, whereas the lightest sparticle is the neutralino with $m_{\tilde{\chi}^0_1} = 60.7\,\mathrm{GeV}$. The main contribution to flavour excess in SU4 comes from the $\tilde{\chi}^0_2$decay:

$$\tilde{\chi}^0_2 \to \ell^\pm\ell^\mp\tilde{\chi}^0_1. \tag{5.32}$$

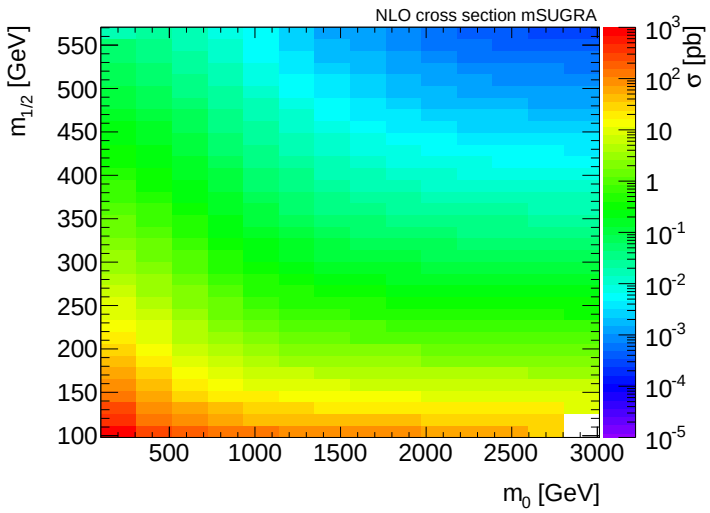

Figure 5.7: NLO production cross section for mSUGRA grid shown in the $m_0 - m_{1/2}$ hyperplane.

The $\tilde{\chi}_2^0$ decays with a BR of 12.4% into a di-lepton pair and a $\tilde{\chi}_1^0$. This decay is suppressed in comparison to the $\tilde{\chi}_2^0$ decaying into di-tau leptons and $\tilde{\chi}_1^0$ (BR: 50.8%). The $\tilde{\chi}_2^0$ is wino-like and therefore preferably couples to left-handed sparticles. The left-handed slepton ($\tilde{e}_\mathrm{L}$ and $\tilde{\mu}_\mathrm{L}$) is heavier than the $\tilde{\chi}_2^0$, such that the left-handed fraction of the mixing $\tilde{\tau}_1$ is the most favoured decay sparticle of the $\tilde{\chi}_2^0$. Nevertheless, if SU4 is realized in nature, the di-lepton channel is a good candidate to measure this decay chain, because the tau lepton reconstruction is based on hadronically decaying taus only (BR: $\sim 65\%$) and has a reconstruction and identification efficiency of $\epsilon \sim 30\%$ [148] which is lower than the electron and the muon reconstruction efficiencies.

Even though this particular point is already excluded by direct SUSY searches, it is still used as benchmark point because its mass hierarchy, the couplings, and the decay kinematics can be used universally as a typical mSUGRA scenario. The number of simulated SUSY events for the SU4 point is much larger than the number of events in any other grid point. Therefore, all studies are based on the benchmark point in order to benefit from the larger statistics.

Phenomenological Grids - Light Neutralino and Compressed Spectrum

Phenomenological models have been introduced in the theory chapter in Sec. 1.2.3. Those models are constrained by the SUSY masses only, such that 5 mass parameters determine the complete decay signatures. The phenomenological grids simulated in 2011 studied in this thesis are constrained further, such that an enhanced lepton production is expected. Additional relations between the $\tilde{\chi}_2^0$, the $\tilde{\ell}$, and the minimum of the $\tilde{g}$ and $\tilde{q}$ masses, reduce the free parameters to: $m_{\tilde{g}}$, $m_{\tilde{q}}$, and $m_{\tilde{\chi}_1^0}$. Two different sets of parameter spaces have been simulated, the so-called light neutralino (LN) and the compressed spectrum (CS) grids. In both parameter spaces, $m_{\tilde{q}}$ and $m_{\tilde{g}}$ are varied, with fixed $m_{\tilde{\chi}_2^0}$, $m_{\tilde{\ell}}$, and $m_{\tilde{\chi}_1^0}$, such that the parameter space can be plotted as $m_{\tilde{g}}$-$m_{\tilde{q}}$-planes. The masses and dependencies are listed in Tab. 5.1. Figure 5.9 shows the next-to-leading-order (NLO) production cross section for both grids and the positions of the chosen benchmark points,

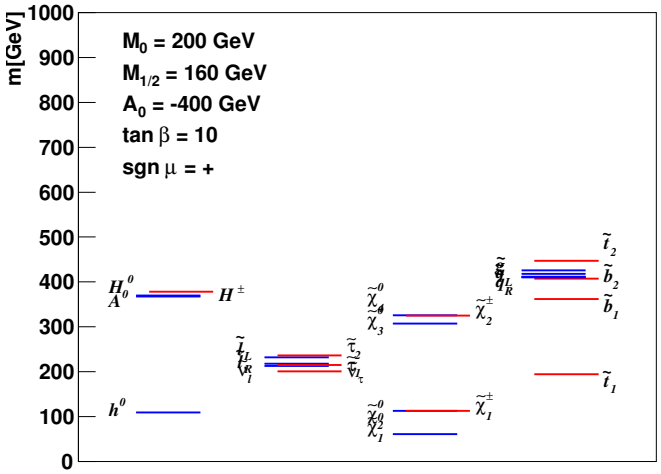

Figure 5.8: Mass hierarchy derived with *ISAJET* [115] for the SU4 benchmark point with the following SUSY parameters: $m_0 = 200\,\text{GeV}$, $m_{1/2} = 160\,\text{GeV}$, $A_0 = -400\,\text{GeV}$, $\tan\beta = 10$, and $\mu > 0$.

Table 5.1: Pheno grids and benchmark points. The light neutralino grid has a fixed neutralino mass of $m_{\tilde{\chi}_1^0} = 100\,\text{GeV}$ and the other masses are determined by the squark and gluino masses. In the compresses spectrum (CS) GRID, all masses are calculated as relations to the squark and gluino masses.

Light neutralino (LN) GRID and benchmarkpoint					
	$m_{\tilde{g}}$[GeV]	$m_{\tilde{q}}$[GeV]	$m_{\tilde{\chi}_2^0}$[GeV]	$m_{\tilde{\ell}}$[GeV]	$m_{\tilde{\chi}_1^0}$[GeV]
GRID	-	-	$min(m_{\tilde{g}}, m_{\tilde{q}})$ $-100\,\text{GeV}$	$(m_{\tilde{\chi}_2^0} + m_{\tilde{\chi}_1^0})/2$	100
PG11 LN	600	610	500	300	100

compressed spectrum (CS) GRID and benchmarkpoint					
	$m_{\tilde{g}}$[GeV]	$m_{\tilde{q}}$[GeV]	$m_{\tilde{\chi}_2^0}$[GeV]	$m_{\tilde{\ell}}$[GeV]	$m_{\tilde{\chi}_1^0}$[GeV]
GRID	-	-	$min(m_{\tilde{g}}, m_{\tilde{q}})$ $-50\,\text{GeV}$	$(m_{\tilde{\chi}_2^0} + m_{\tilde{\chi}_1^0})/2$	$min(m_{\tilde{g}}, m_{\tilde{q}})$ $-150\,\text{GeV}$
PG11 CS	600	610	550	500	450

PG11 LN and *PG11 CS*.

Both points are slightly higher in the $\tilde{q}$ and the $\tilde{g}$ mass than the excluded region determined in the analysis using the ATLAS data of 2010 [52]. Large mass differences between the neutralinos and the slepton yield larger tails in the $E_{\text{T}}^{\text{miss}}$ and the lepton momenta distribution (cf. *PG11 LN* distributions in Fig. 5.12 and Fig. 5.13). Both signatures can be distinguished easily from SM background and therefore this model is favoured for SUSY searches. The drawback of the large mass differences is an expected invariant mass endpoint at $m_{\ell\ell} = 377.1\,\text{GeV}$. In order to fit an endpoint at high $m_{\ell\ell}$ values, high statistics are required.

The smaller mass differences of the minimum of $\tilde{q}$ and $\tilde{g}$ mass to the $\tilde{\chi}_2^0$ mass, the $\tilde{\chi}_2^0$ mass to the $\tilde{\ell}$ mass, and the $\tilde{\ell}$ mass to the $\tilde{\chi}_1^0$ mass yield a much smaller phase space

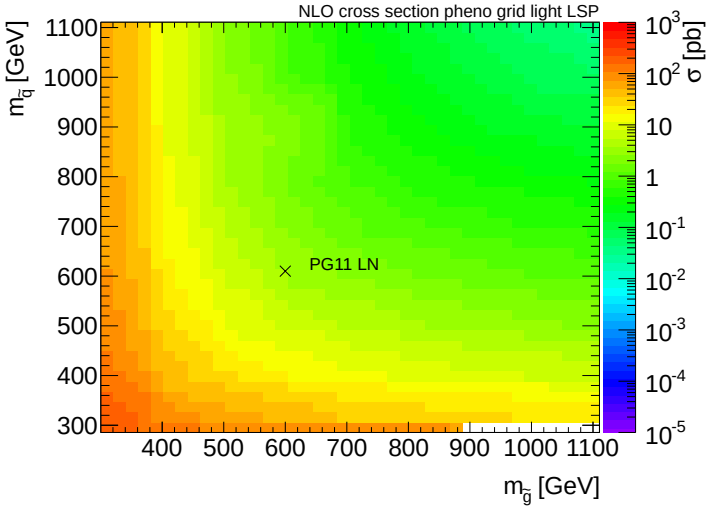

(a)

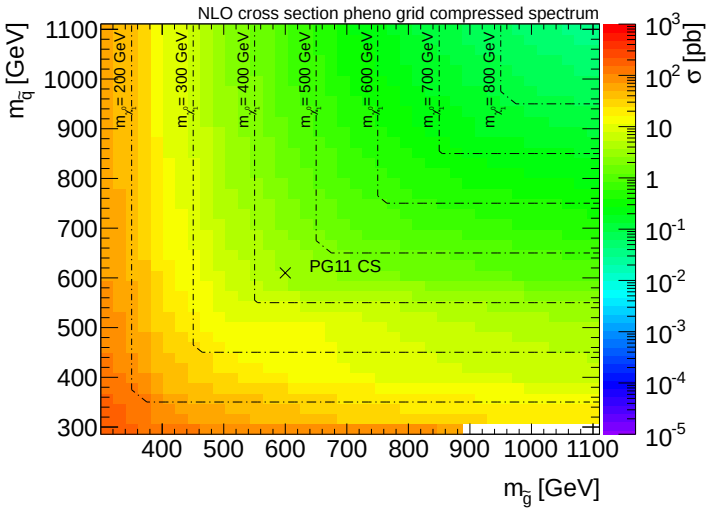

(b)

Figure 5.9: NLO production cross section for *PG 11* light LSP (a) and compressed spectrum (b) GRIDs in $m_{\tilde{g}} - m_{\tilde{s}}$-hyperplane.

for the produced SM particles in the compressed spectrum in comparison to the light neutralino points. The resulting CS kinematics are very similar to the $t\bar{t}$ distribution and can hardly be distinguished from SM processes. In this case, the FS provides a powerful tool for signal background separation. The *PG11 CS* model point has another challenging feature; the expected endpoint of the invariant mass $m_{\ell\ell} = 99.9\,\text{GeV}$ lies directly in the Z-peak region. Fitting an endpoint in this region requires good $Z \to \ell\ell$ background suppression.

GMSB - GMSB6

The reduced free parameters of the GMSB scenario are the scale of the SUSY breaking Λ, the ratio of the two Higgs expectation values at the electroweak scale $\tan\beta$, the messenger

mass scale M_{mes}, the number of equivalent messenger fields N_5, the ratio of the gravitino mass to its value for a breaking scale C_{grav} and the sign of the Higgsino mass term μ. The GMSB GRID is simulated with fixed values for:

$$M_{mes} = 250\,\text{TeV},\ N_5 = 3,\ C_{grav} \geq 1,\ \text{and}\ \mu = 1$$

and a variation of Λ between $10 - 80\,\text{TeV}$ and $\tan\beta$ between 2 and 50. The cross section decreases with Λ from 100 pb at $\Lambda = 10\,\text{GeV}$ to 0.01 pb for $\Lambda = 75\,\text{TeV}$ as shown in Fig 5.10.

The NLSP is mainly constrained by N_5, $\tan\beta$ and Λ. For $N_5 = 1$ and small values of $\tan\beta$, the NLSP is the $\tilde{\chi}_1^0$. In this case, the $\tilde{\chi}_1^0$decays into a photon and a $\tilde{G}$. Those events are dominated by photon final states. The GMSB GRID shown in Fig 5.10 is generated with $N_5 = 3$; there the NLSP is a stau or another slepton. Three regions with varying $\tan\beta$ can be distinguished: In the low $\tan\beta$, the $\tilde{\ell}_\text{R}$are the NLSPs ($\tilde{e}_\text{R}$, $\tilde{\mu}_\text{R}$). Most decay chains end with an $\ell$and the $\tilde{G}$, such that up to four leptons in the final state are expected. The $\tilde{\ell}_\text{R}$and the $\tilde{\tau}_1$are almost degenerate in mass in the medium $\tan\beta$ region; there, all kind of sleptons exist as NLSP in parallel (*CoNLSP*-region)[1] and decay directly into the $\tilde{G}$. For large values of $\tan\beta$, the NLSP is always the $\tilde{\tau}$. The region of small λ and large $\tan\beta$ is theoretically excluded.

The GMSB6 benchmark point is chosen as:

$$\Lambda = 40\,\text{TeV},\ \tan\beta = 30,\ M_{mes} = 250\,\text{TeV},\ N_5 = 3,\ C_{grav} = 1,\ \text{and}\ \mu = 1.$$

lying in the $\tilde{\tau}_1$-NLSP region. The $\tilde{\tau}_1$can be produced by various decays: 43% (9%) of the $\tilde{\tau}_1$are produced in $\tilde{\chi}_1^0(\tilde{\chi}_2^0)$ decays, 28 % in decays of the right-handed sleptons and 13% in the decay of the lightest chargino ($\tilde{\chi}_1^\pm$) [149]. Each decay chain ends with at least one τ-lepton and the gravitino:

$$\tilde{\chi^0}_{1,2} \rightarrow \tau^\pm\tilde{\tau}_1^\mp \rightarrow \tau^\pm\tau^\mp\tilde{G} \quad (5.33)$$

$$\tilde{\ell}_\text{R} \rightarrow \ell^\pm\tau^\pm\tilde{\tau}_1^\mp \rightarrow \ell^\pm\tau^\pm\tau^\mp\tilde{G} \quad (5.34)$$

$$\tilde{\chi}_1^\pm \rightarrow \nu_\tau\tilde{\tau}_1 \rightarrow \tau^\pm\tilde{G} \quad (5.35)$$

The complete mass hierarchy is shown in Fig. 5.11, again calculated with *ISAJET*. The di-lepton analysis is sensitive to the events with exactly two leptonic τ-lepton decays or two leptons from slepton decays. The GMSB events do not decay into the preferred final states for this analysis. Nevertheless, even in this environment, the flavour subtraction can be applied successfully.

5.2.3 Signal Regions and Kinematic Distributions

Several kinematic distributions are exploited in order to find signal regions with sufficient signal to background ratio.

Kinematics for SM and SUSY Benchmark Points

All pre-selection cuts (up to the *exactly 2 leptons + flavour* cut) described in Sec. 6.4 are applied on the Monte Carlo samples used to provide the kinematic distributions shown in

[1] the *CoNLSP*-region is defined as $|m_{\tilde{\ell}_\text{R}} - m_{\tilde{\tau}_1}| < m(\tau)$

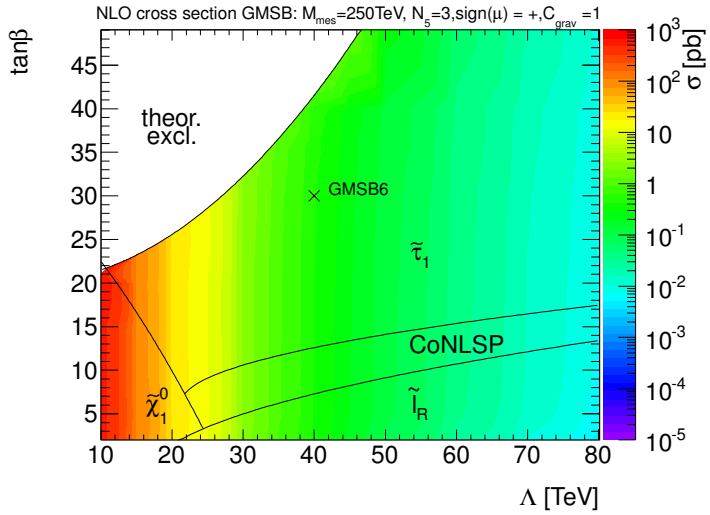

Figure 5.10: NLO production cross section for GMSB GRID shown in the $\Lambda - \tan\beta$-hyperplane. The different NLSP regions and the theoretically excluded area are highlighted [150].

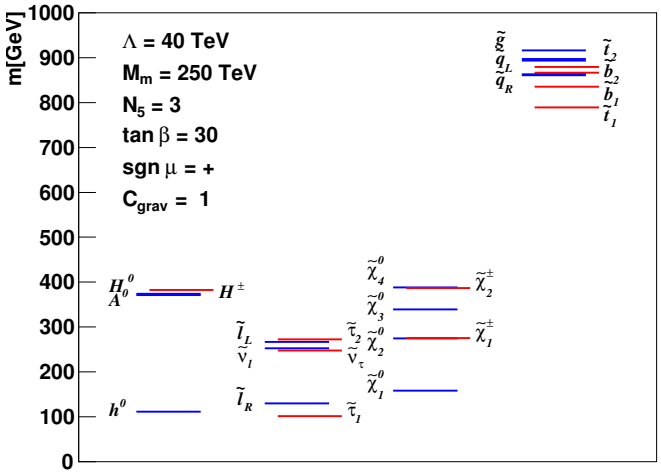

Figure 5.11: Mass hierarchy derived with *ISAJET* [115] for the GMSB6 benchmark point with the following SUSY parameters: $\Lambda = 40\,\text{TeV}$, $\tan\beta = 30$, $M_{mes} = 250\,\text{TeV}$, $N_5 = 3$, $C_{grav} = 1$, and $\mu = 1$.

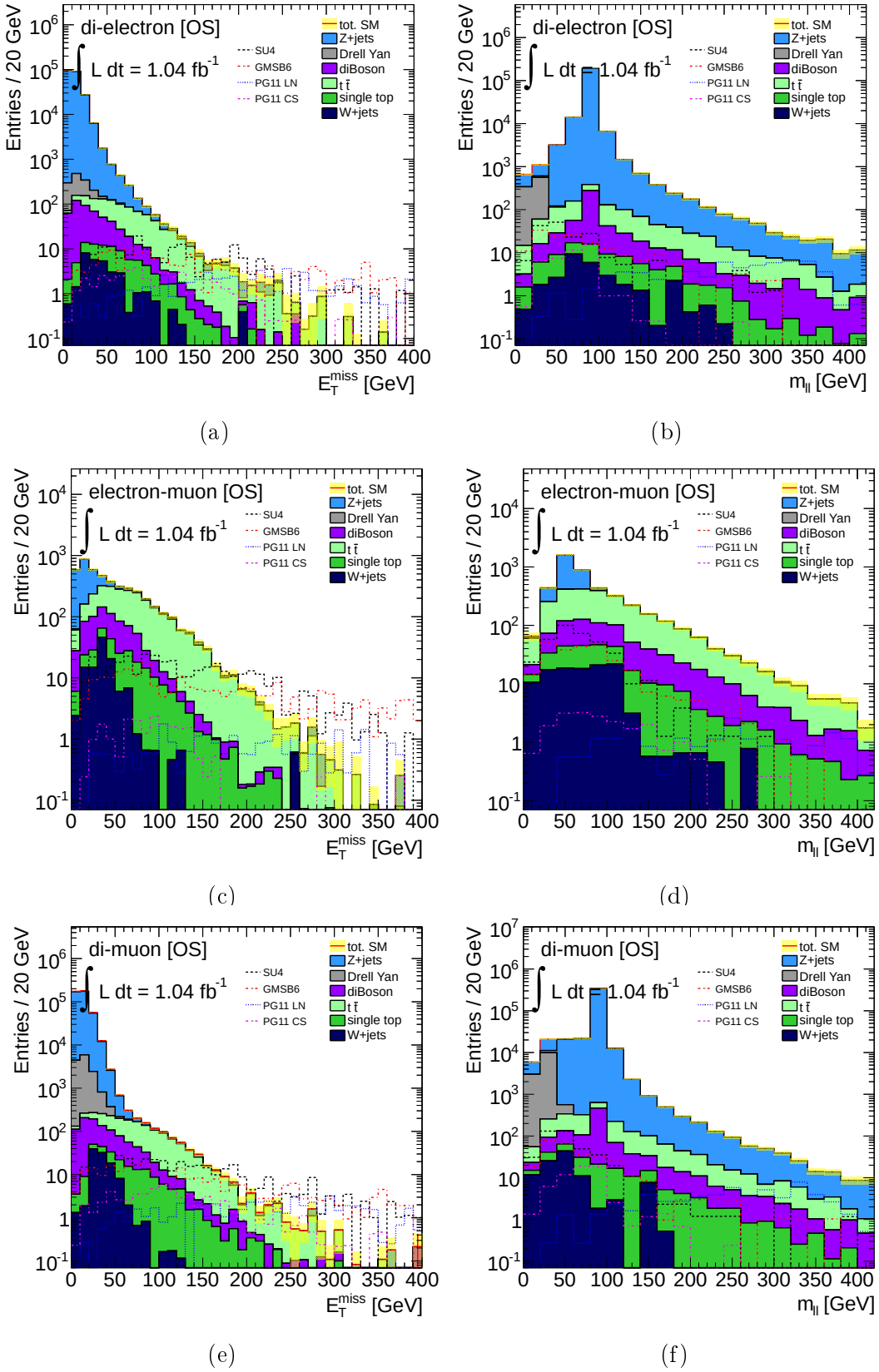

Figure 5.12: The missing transverse energy (a,c,e) and the invariant mass distributions (b,d,f) are shown for the SM background processes stacked and for four SUSY benchmark points as dotted lines. All pre-selection cuts described in Sec. 6.4 up to the *exactly 2 leptons + flavour* cut are applied.

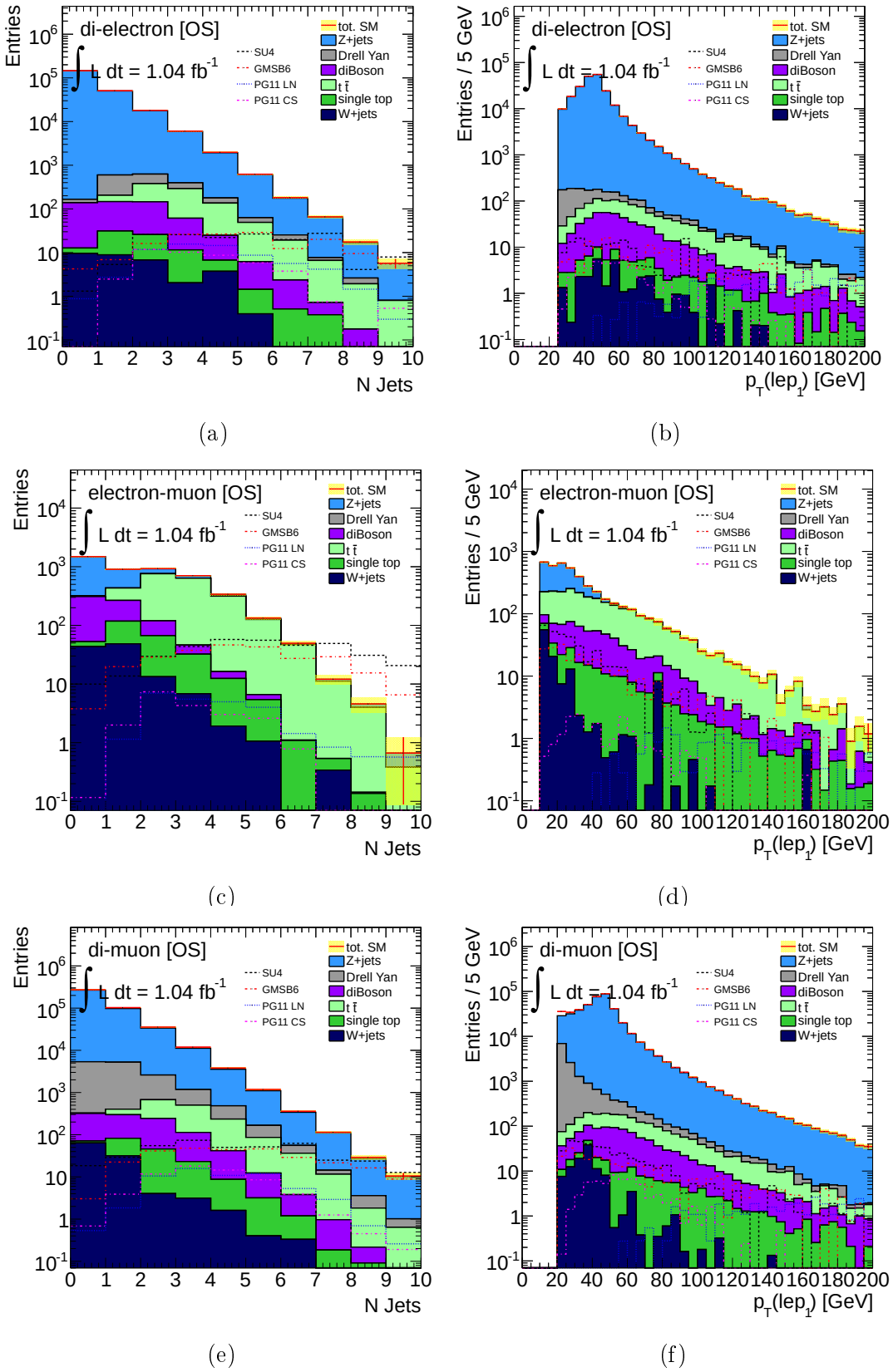

Figure 5.13: The number of jets for $e^{\pm}e^{\mp}$(a), $e^{\pm}\mu^{\mp}$ (c) and $\mu^{\pm}\mu^{\mp}$ (e) events are shown in the left column and the leading lepton momenta in the right column (b,d, and f) for the SM background processes stacked and for four SUSY benchmark points as dotted lines. All pre-selection cuts described in Sec. 6.4 up to the *exactly 2 leptons + flavour* cut are applied.

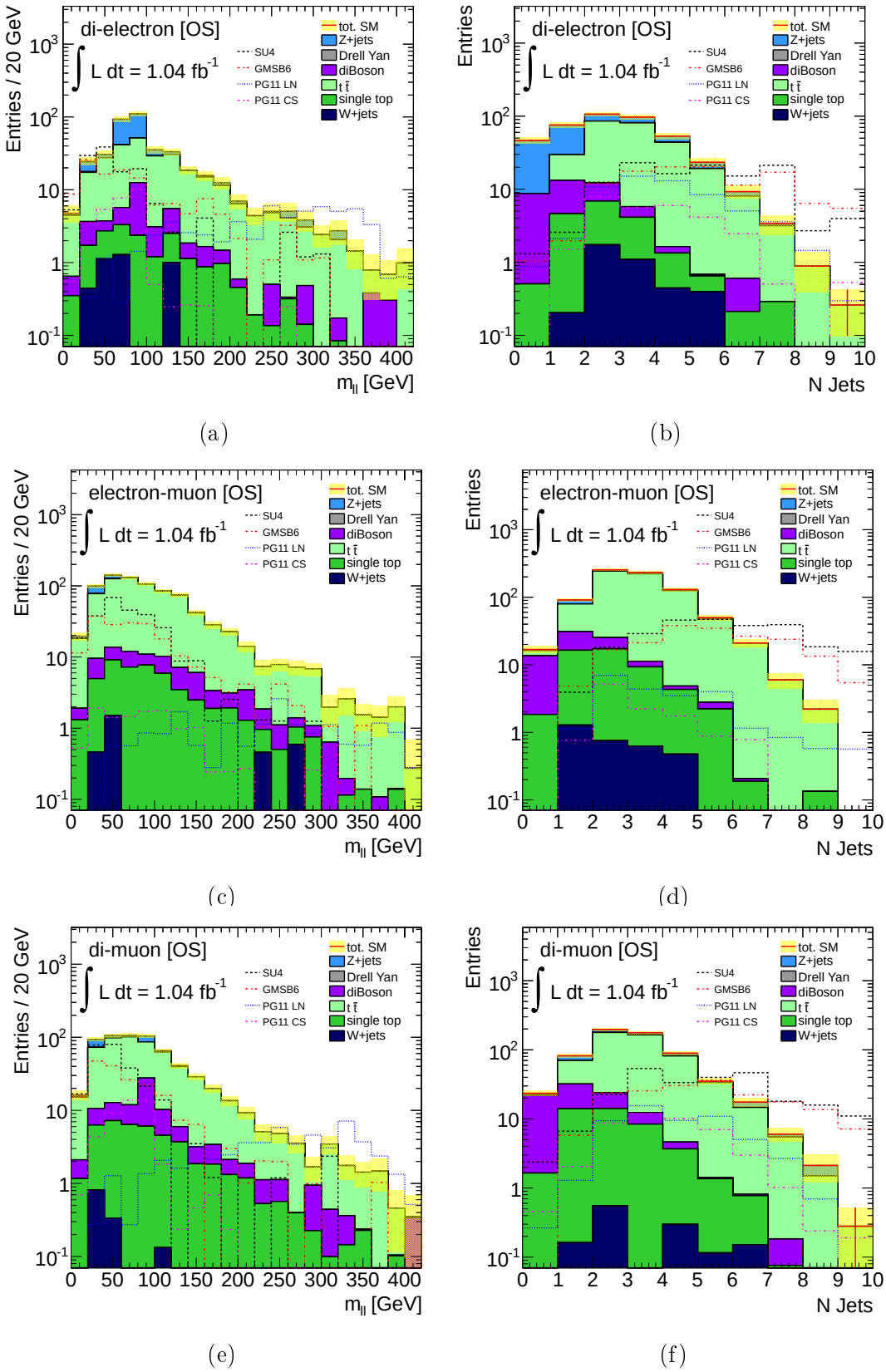

Figure 5.14: Invariant mass (a,c,e) and number of jet distrubutions (b,d,f) are shown for the SM background processes stacked and for four SUSY benchmark points as dotted lines. All pre-selection cuts described in Sec. 6.4 up to the *exactly 2 leptons + flavour* cut and a cut on the missing transverse energy ($E_{\mathrm{T}}^{\mathrm{miss}} > 80\,\mathrm{GeV}$) are applied.

this section. The Standard Model processes introduced in Sec. 5.2.1 are shown stacked on top of each other with a total statistical uncertainty shown as a yellow band. A benchmark point for each SUSY GRID used for providing SUSY model specific limits in Ch. 7, is plotted as dashed/dotted line.

Figure 5.12 shows the $E_{\mathrm{T}}^{\mathrm{miss}}$ distributions of $e^{\pm}e^{\mp}$(a), $e^{\pm}\mu^{\mp}$(c) and $\mu^{\pm}\mu^{\mp}$(e) in the left column. As described above (cf. 5.2.1), the Z/γ^{*} decays have no natural sources for $E_{\mathrm{T}}^{\mathrm{miss}}$. The distributions peak at $E_{\mathrm{T}}^{\mathrm{miss}} = 0\,\mathrm{GeV}$. SM processes with significant $E_{\mathrm{T}}^{\mathrm{miss}}$ are $t\bar{t}$, di-boson and single top. Whereas $t\bar{t}$ has the biggest contribution at high $E_{\mathrm{T}}^{\mathrm{miss}}$ values, the different SUSY benchmark points show flat $E_{\mathrm{T}}^{\mathrm{miss}}$ distributions. Tight cuts on $E_{\mathrm{T}}^{\mathrm{miss}}$ give a good signal-background discrimination. Nevertheless, cutting too tightly on $E_{\mathrm{T}}^{\mathrm{miss}}$ should be avoided in order to avoid suppressing SUSY signal too much.

The di-lepton invariant mass distributions are shown in Fig. 5.12, right column. The flavour symmetric plots ($e^{\pm}e^{\mp}$(b) and $\mu^{\pm}\mu^{\mp}$(f)) are dominated by the $Z \to \ell\ell$. The same order of magnitude for $t\bar{t}$, di-boson and single top can be seen in the high $\mathrm{m}_{\ell\ell}$regions. The production rates for SM processes are orders of magnitude higher than the SUSY benchmark points, such that invariant mass edges, expected in same-flavour lepton final states SUSY models, cannot be distinguished without further selection cuts.

The number of jets is plotted in Fig. 5.13, left column. The Z/γ^{*} and di-boson distributions peak at low jets multiplicity, whereas $t\bar{t}$ decays usually produce two or more jets. For $t\bar{t}$, the number of events decreases with higher jets multiplicity, whereas the SUSY signals with long decays chains, SU4 and GMSB6, show an almost flat jets multiplicity distribution for $N_{jets} > 2$. The PG benchmark points peak around three and four jets.

The leading-lepton momentum distributions are dominated by Z and Drell-Yan. The Drell-Yan lepton p_{T} peaks at low momenta, while the leptons originating in Z-boson decays peak at $p_{\mathrm{T}} \sim 45\,\mathrm{GeV}$, which is half of the Z-boson mass. The large values of the *PG11 LN* lepton momentum distribution is driven by the large mass differences of the neutralinos and the slepton (cf. Sec 5.2.2). The other benchmark points show similar lepton distributions to the SM backgrounds, such that an additional lepton p_{T} cut does not have good signal-background discrimination power.

The invariant mass of the di-leptons ($\mathrm{m}_{\ell\ell}$) and the number of jet distributions are reinvestigated after applying a medium $E_{\mathrm{T}}^{\mathrm{miss}}$ cut of $E_{\mathrm{T}}^{\mathrm{miss}} \geq 80\,\mathrm{GeV}$ (cf. Fig. 5.14 left, right column respectively). The overwhelming $Z \to \ell\ell$ contribution can be reduced significantly. The asymmetry between $Z \to ee$ and $Z \to \mu\mu$ can be explained by the larger $E_{\mathrm{T}}^{\mathrm{miss}}$ tail in the $Z \to ee$ events, caused by additional $E_{\mathrm{T}}^{\mathrm{miss}}$ of electron energy losses for example from bremsstrahlung. The $Z \to ee$ can be suppressed further by applying either a Z-veto, accepting only events with $\mathrm{m}_{\ell\ell} < 80\,\mathrm{GeV}$ or $\mathrm{m}_{\ell\ell} > 100\,\mathrm{GeV}$, or by applying a number of jets cut with $N\,jets \geq 2$. The remaining $t\bar{t}$ and single top events are flavour symmetric and can be suppressed by the FS.

Signal Regions

The signal regions strategy is two-fold; a pair of orthogonal loose $E_{\mathrm{T}}^{\mathrm{miss}}$ signal regions and a tight $E_{\mathrm{T}}^{\mathrm{miss}}$ signal region have been chosen. The loose-$E_{\mathrm{T}}^{\mathrm{miss}}$ regions allow the study of phase space regions not covered by the inclusive analysis and the exploitation of the invariant mass distributions for searching mass edges, since using a loose-$E_{\mathrm{T}}^{\mathrm{miss}}$ cut increases the possible signal statistics. As long as the flavour asymmetric backgrounds are under control, the $e\mu$ channel can be used for the suppression of combinatorial background in the same-flavour channels. According to the kinematics discussed in Sec. 5.2.1, the following signal regions have been chosen:

- **FS-SR1:** $E_{\mathrm{T}}^{\mathrm{miss}} > 80\,\mathrm{GeV}$ with *Z-veto*,
  (accepting only events with $\mathrm{m}_{\ell\ell} < 80\,\mathrm{GeV}$ or $\mathrm{m}_{\ell\ell} > 100\,\mathrm{GeV}$)
- **FS-SR2:** $E_{\mathrm{T}}^{\mathrm{miss}} > 80\,\mathrm{GeV}$ and number of jets: $N_{Jets} \geq 2$

The $E_{\mathrm{T}}^{\mathrm{miss}}$ cut used is lower than that used in the analysis in [52] ($E_{\mathrm{T}}^{\mathrm{miss}} > 100\,\mathrm{GeV}$). The additional cuts need to be applied in order to suppress the FS irreducible background of Z boson decays; they are not optimized to suppress the flavour symmetric $t\bar{t}$ background. It is important to study both signal regions and not only one, because they are complementary in the sense that SUSY might be realized in nature with a low number of jets (e.g. in direct gaugino production scenarios) or with invariant mass edges lying within the $\mathrm{m}_{\ell\ell}$-veto region between $80\,\mathrm{GeV} < \mathrm{m}_{\ell\ell} < 100\,\mathrm{GeV}$, like *PG11 CS* for example. SUSY final states with low $E_{\mathrm{T}}^{\mathrm{miss}}$, $\mathrm{m}_{\ell\ell} > 80\,\mathrm{GeV}$ and $\mathrm{m}_{\ell\ell} < 100\,\mathrm{GeV}$ and low number of jets cannot be distinguished from SM processes.

In addition, a tight $E_{\mathrm{T}}^{\mathrm{miss}}$ signal region requiring high missing transverse energy only, has been chosen, in order to increase the significance of a potential SUSY signal with regards to the total background. The signal region is defined as:

- **FS-SR3:** $E_{\mathrm{T}}^{\mathrm{miss}} > 250\,\mathrm{GeV}$

After applying a $E_{\mathrm{T}}^{\mathrm{miss}} > 250\,\mathrm{GeV}$ cut, the only significant SM background comes from $t\bar{t}$ decays, cf. Fig 5.12, left column. This signal region is inspired by the 2010 analysis [52]. Another advantage of the tight $E_{\mathrm{T}}^{\mathrm{miss}}$ signal region is that the inclusive di-lepton analysis is also studying this signal region. Therefore, the fully data-driven background estimates obtained for the inclusive search can be used for the main backgrounds.

A study was done in order to check the gains in the three signal regions with regards to signal region defined in the analysis performed on the ATLAS data of 2010 [52]. Figure 5.15 presents a rough estimate of the expected significance for the FS-SR1 (a,b), FS-SR2 (c,d), and FS-SR3 (e,f) (no systematic uncertainties are taken into account) supposing the irreducible background is perfectly controled (or completely supressed) for the Pheno GRIDs with light LSP and the compressed spectrum (cf. Sec. 5.2.2). The significance is defined as the ratio of the flavour subtraction value $\mathcal{S}$ (cp. Eq. (5.10)) of the SUSY sample over the square-root of the expected background in all the 3 di-lepton channels. This approximation is equivalent to the assumption of complete control of the irreducible background.

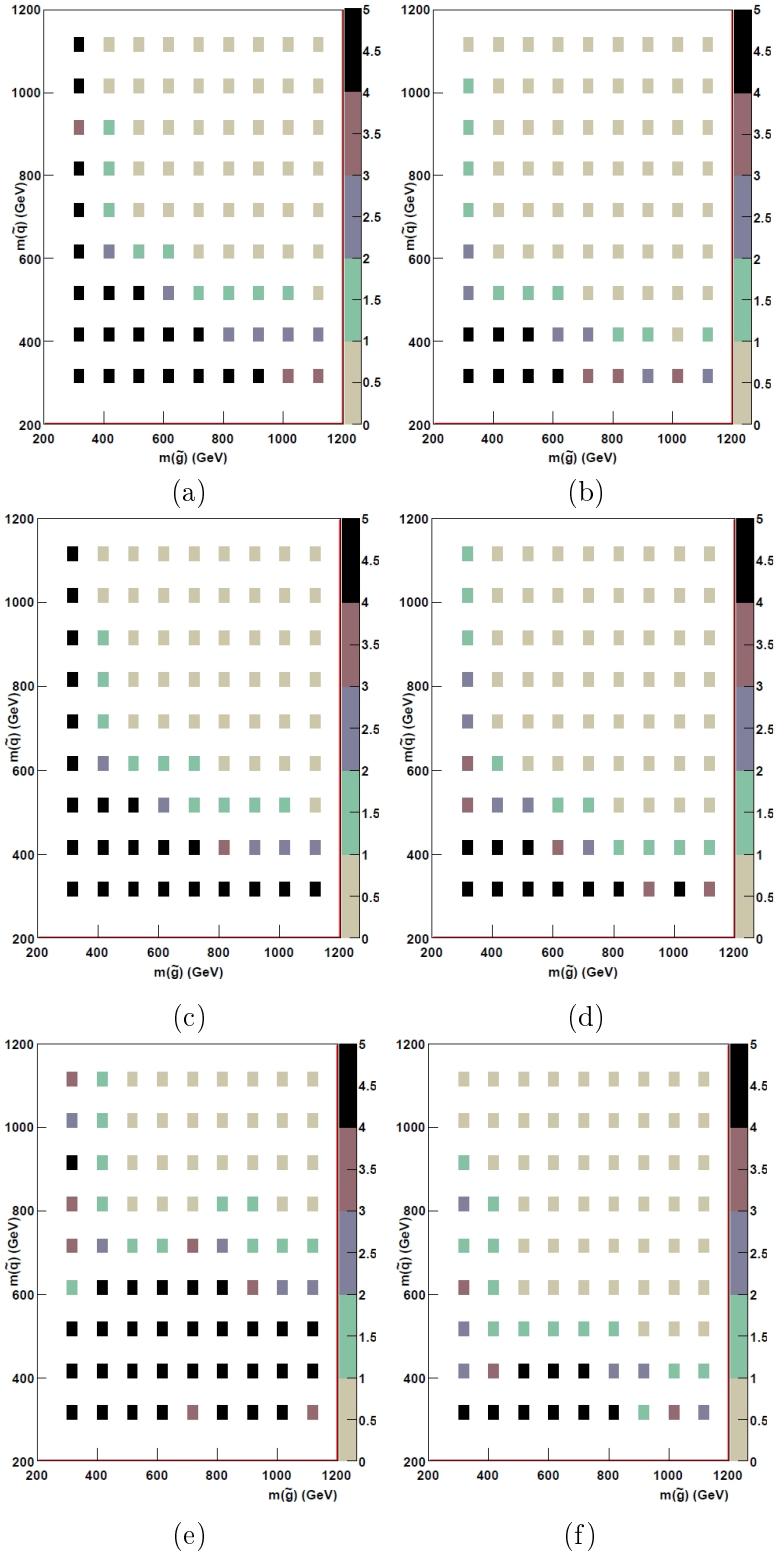

Figure 5.15: Simplified estimation of expected significance for both PG grids (LN and CS) for the different signal regions FS-SR1:(a), (b), FS-SR2:(c), (d), and FS-SR3:(e), (f). The expect signal significance is given in standard deviations (σ). Here the significance is estimated as the ratio of the flavour subtraction on the SUSY sample over the square-root of the expected background in all the 3 di-lepton channels. This approximation is equivalent to the assumption of complete control of the irreducible background [151].

6 Flavour Subtracting Analysis

The analysis performed in this thesis has been published as one of three di-lepton analyses in the paper: *Searches for supersymmetry with the ATLAS detector using final states with two leptons and missing transverse momentum in* $\sqrt{s} = 7\,\text{TeV}$ *proton-proton collisions* [152] detailed information can be found in the ATLAS internal document [151].

This chapter is organized as follows. The first section gives an overview of the analysed data-sets and the simulated Monte Carlo samples. The trigger strategy, the trigger reweighting tool and the trigger efficiency measurements are explained in Sec. 6.2. Before the object definition and the event selections are introduced in Sec. 6.4, the Monte Carlo re-scaling strategy applied to reproduce pile-up effects seen in data, is described in Sec. 6.3. The data-driven, semi data-driven, and Monte Carlo based background estimation methods are explained in Sec. 6.5. In Sec. 6.6 the systematic uncertainties are evaluated. Before summarizing the results of the flavour subtraction (FS) analysis, the ratio of the lepton reconstruction and identification efficiencies (β) is determined in Monte Carlo and data and its systematics are studied in Sec. 6.7.

6.1 Data and Monte Carlo Samples

The analysis described in this thesis is performed on derived AOD datasets. The so-called *SUSYD3PDs* have been provided by the ATLAS central production system (cf. Sec 3.1.3). Both data and Monte Carlo Samples have been processed by the *SUSYD3PDMaker*, an ATLAS software package providing ROOT [153] ntuples with SUSY analysis specific event and particle information.

6.1.1 Data

The ATLAS detector recorded $5.21\,\text{fb}^{-1}$ of integrated luminosity from March 22nd 2011 until October 31st 2011 (cf. Fig. 6.1). The datasets analysed in this thesis were recorded between March 22nd and June 28th, corresponding to the amount of analysed data shown at the*XXV International Symposium on Lepton Photon Interactions at High Energies (Lepton Photon 11)* conference held at the Tata Institute of Fundamental Research in Mumbai, India. The datasets contain the data runs 178044 to 184169 (data-taking periods B-G). A detailed list can be found in the appendix in Tab. A.1.

The Good Runs List (GRL) selection defined by the official Data Preparation Group, based on a list of good quality data (cf. Sec. 3.1.1), is applied on the recorded data sets. The total integrated luminosity of the sample, after GRL selection, is $1035.18\,\text{pb}^{-1}$ for the `egamma` stream and $1035.04\,\text{pb}^{-1}$ for the `muon` stream, both sets have a luminosity uncertainty of 3.7% [104].

6.1.2 Monte Carlo

All Monte Carlo samples used in this analysis are from the official *mc10b* Monte Carlo production. Detailed tables listing the dataset number, the used Monte Carlo generator,

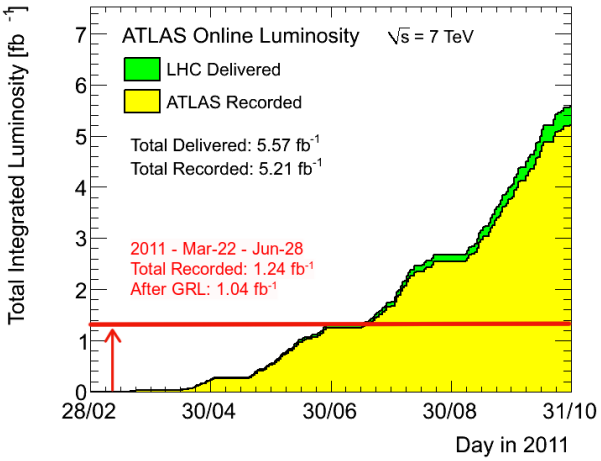

Figure 6.1: Total integrated luminosity in 2011. The cumulative luminosity delivered to (green), and recorded by ATLAS (yellow) versus the day during stable beams and for pp collisions at 7 TeV centre-of-mass energy in 2011 is shown. The total recorded luminosity is $5.2\,\text{fb}^{-1}$. For the analysis presented in this thesis the first $1.24\,\text{fb}^{-1}$ of the recorded data of the 2011 data taking is considered. After the Good Runs List (GRL) selection, which guarantees a sufficient data quality, the total integrated luminosity of this sample is $1.04\,\text{fb}^{-1}$ [99].

and the corresponding cross sections are given in the appendix in Tab.A.2-A.4 for Z-samples, $t\bar{t}$, single top, W-samples, and di-boson respectively.

The Monte Carlo samples are re-weighted to match the integrated luminosity corresponding to the value found in data. According to the final state, the event is either weighted to the integrated luminosity of the `egamma` stream or to the integrated luminosity of the `muon` stream.

6.2 Trigger

The ATLAS data is processed in so-called streams (as introduced in the ATLAS Trigger Section in Sec. 2.2.5). The analysis is based on di-electron, di-muon and electron-muon pairs. The challenge for this analysis is to combine the `egamma` and the `muon` stream in a way, such that events, recorded in both streams (the streams are inclusive event selections based on the triggered objects) are not counted twice. Therefore the trigger strategy described below was designed to take into account possible overlaps. On the other hand, the Monte Carlo samples are not divided in different streams such that no specific care to avoid overlaps is needed.

6.2.1 Trigger Strategy

The selection of the interesting events for the analysis is based on single lepton triggers. The electron trigger requires a medium electron with $p_{\text{T}} > 20\,\text{GeV}$ at the EF trigger level (*EF_e20_medium*), and the muon trigger requires a muon with transverse momentum above the p_{T} -threshold at 18 GeV at the EF trigger level (*EF_mu18*). The *EF_e20_medium* trigger items are used to select both data and Monte Carlo events. In case of the muon trigger, a more elaborate trigger reweighting tool is applied on the

Table 6.1: List of trigger items for Data and Monte Carlo.

Trigger	Data	MC
electron	*EF_e20_medium*	*EF_e20_medium*
muon	*EF_mu18*	trig reweighting tool based on *EF_mu18*

Monte Carlo events (cf. Sec.6.2.2) in order to emulate the trigger efficiency in data found for the *EF_mu18* trigger. Such a tool was not (yet) available for the electron trigger, but due to the high electron trigger efficiency (close to 100%) the fraction of Monte Carlo events rejected at Trigger level is an acceptable loss of Monte Carlo statistics.

The following trigger strategy is applied:

- The $e^{\pm}e^{\mp}/e^{\pm}e^{\pm}$ (di-electron) events are taken from the `egamma` stream in data, and must satisfy the electron trigger. There must be exactly two selected electrons and no selected muons. Only events with leading offline electrons p_{T} greater than 25 GeV are considered in order to select trigger objects lying in the so-called trigger plateau with comparable (maximum) trigger efficiency.
- The $\mu^{\pm}\mu^{\mp}/\mu^{\pm}\mu^{\pm}$ (di-muon) events are taken from the `muon` stream in data and must satisfy the muon trigger. There must be exactly two selected muons and no selected electrons. The muon trigger efficiency plateau is reached for muons with p_{T} larger than 20 GeV. Therefore the leading offline muons must satisfy a $p_{\mathrm{T}} > 20$ GeV cut.
- Different flavour $e^{\pm}\mu^{\mp}/e^{\pm}\mu^{\pm}$ events are taken from both streams. Either the event for which there is an offline electron with $p_{\mathrm{T}} > 25$ GeV in the `egamma` stream, firing an electron trigger is taken, or the event is taken from the `muon` stream, for which the muon trigger is fired, the offline muon $p_{\mathrm{T}} > 20$ GeV, and electron trigger selection has failed. The selected events must have exactly one electron and one muon.

The same trigger strategy is applied on Monte Carlo samples. The only difference between data and Monte Carlo is that the Monte Carlo samples are not separated in streams, therefore no double counting of simulated events has to be avoided.

6.2.2 Trigger Re-weighting Tool

The triggers are defined achieving maximum trigger efficiencies. Nevertheless, fiducial regions and p_{T} thresholds yield trigger inefficiencies. The usual procedure to account for those inefficiencies is to rely on the trigger simulation in the MC and apply scale factors to correct for differences between the simulated and the measured trigger response. The disadvantage of this method is that the statistics of the simulated events is already reduced due to the trigger simulation only. In the case of the muon triggers, up to 20% of the simulated data is rejected due to the trigger simulation. This is a big loss of statistics.

The trigger reweighting tool [154] does not rely on trigger simulation: it extracts the trigger efficiency from data and applies weights to the MC events directly. Thereby the full set of simulated events used for the MC distributions. Each event is weighted with

a proper factor reflecting the probability that the trigger has selected this specific event. In addition, the uncertainties on the measured trigger efficiencies are directly propagated to the analysis.

As mentioned above, no electron trigger reweighting was available for this analysis. Considering the higher electron trigger efficiency of more than $> 95\%$ the improvement in statistics of MC electron events would be of 5% at most after applying a reweighting. Therefore, the development of a trigger reweighting tool was concentrated on the muon trigger in first place, because there the improvement in statistics is much higher.

6.2.3 Trigger Efficiency

As discussed above, the different physics streams (`egamma` stream and `muon` stream) are selected according to the lepton triggers (electron, muon respectively). The electron and the muon trigger are completely orthogonal, thus the two streams can be used directly for the determination of the trigger efficiencies. The muon trigger efficiency is studied in the `egamma` stream data sample and the electron trigger efficiency in the `muon` stream.

In data, the trigger efficiencies are determined as the ratio of events selected by the tight event selection (cf. Sec. 6.4) and where one lepton has fired the appropriate trigger over all events after tight event selection. The trigger efficiencies in Monte Carlo samples are defined as the number of events with selected lepton and appropriate trigger divided by all events containing a selected lepton. Following these procedures, the trigger efficiencies have been determined as:

- Monte Carlo: τ_e: 98.74 % $\pm$ 0.01%, τ_μ: 80.01 % $\pm$ 0.02%
  (τ_μ: barrel: 70.90% $\pm$ 0.02%, end-cap: 86.56% $\pm$ 0.01%),
- Data 2011: τ_e: 96.35 % $\pm$ 0.14 % τ_μ: 79.32 % $\pm$ 0.60%
  (τ_μ: barrel: 72.94% $\pm$ 0.89 %, end-cap: 87.54% $\pm$ 0.75%)

The large discrepancy between the electron and muon trigger efficiencies is caused by the ATLAS design. A small gap at $\eta = 0$ between two trigger chamber elements and the necessity of space for the feet carrying the ATLAS barrel region (cf. Fig 4.7) yield regions which are not covered by muon trigger chambers, and so decreases the overall muon trigger efficiency.

Figure 6.2 shows the electron (a) and muon (b) trigger efficiencies determined in orthogonal trigger streams. The muon trigger efficiency is averaged over barrel and end-cap contributions. The difference in muon trigger efficiencies between barrel and end-caps comes from the different technologies used in the different detector regions (cf. Sec 2.2.4).

These results are compatible with those found with a different technique described in [155].

6.3 Monte Carlo Pile-Up Reweighting

For the 2011 data taking the bunches in the LHC are grouped in bunch trains with an in-train bunch separation of 50 ns. Due to these bunch-trains the so-called out-of-time pile-up - overlapping signals in the detector from different bunch crossings - plays an important role. Considering this train configuration in the pile-up correction, the number of interactions averaged across all bunch crossing IDs per luminosity block $\langle\mu\rangle|_{LB,BCID}$

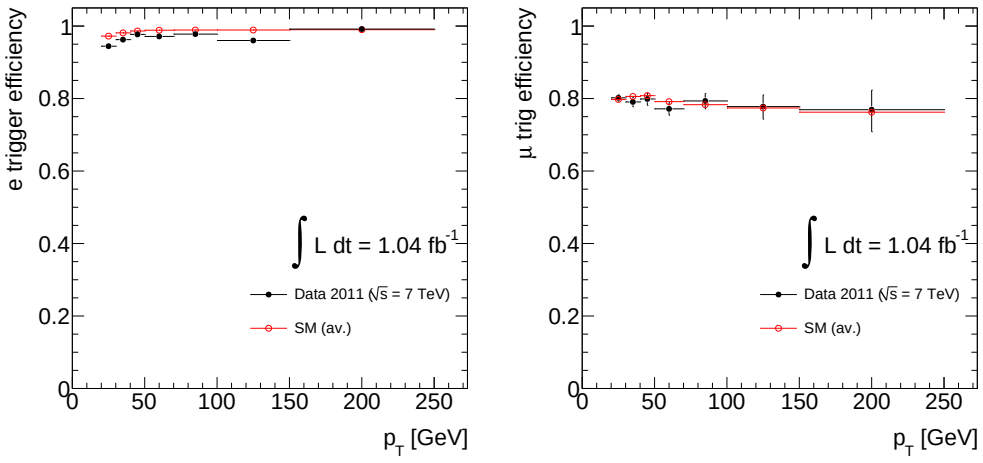

(a) (b)

Figure 6.2: Trigger efficiencies for electron(a) and muon(b) trigger.

is a more accurate description than the number of good primary vertices per event which has been used as a measure for pile-up in [151].

The Monte Carlo samples have been produced before the current data taking period started. A bunch spacing of 50 ns has been expected and therefore taken into account for simulation. The distributions of $\langle\mu\rangle$ are shown in Figure 6.3 for the `egamma` and `muon` stream separately. The Monte Carlo samples have to be reweighted in order to model precisely the pile-up conditions which have been found in reconstructed data.

All Monte Carlo samples are produced with the same fixed $\langle\mu\rangle$ distribution (see Figure 6.3). The $\langle\mu\rangle$ distributions in data are provided by the *iLumiCalc* tool [156]. The distributions used for this analysis have been provided with the following setup: Athena release 16.6.6 and LumiBlockComps-00-04-09. The pile-up weights then have been extracted with the package PileupReweighting-00-00-13. The weights used in the analysis are listed in Table 6.2.

In order to prove that the shape is not affected by the event selection the distribution of the averaged number of interactions is plotted at different event selection cuts. Figure 6.4 shows three $\langle\mu\rangle$ distributions after pile-up correction. First Standard Model events without cuts, second after trigger selection and finally after signal lepton selection. Those distributions are in good agreement for both egamma and muon selections.

6.4 Object Definition and Event Selection

6.4.1 Object Definitions

In this section the definitions of all objects used in the analyses are briefly summarized. A detailed description of electron, muon, jet and $E_{\mathrm{T}}^{\mathrm{miss}}$ reconstruction algorithms, and their performance is given in Ch. 4.

Electrons

The electron candidate can be selected with the standard (cluster based) or the soft electron (track based) algorithm. It must satisfy *medium* requirements based on shower

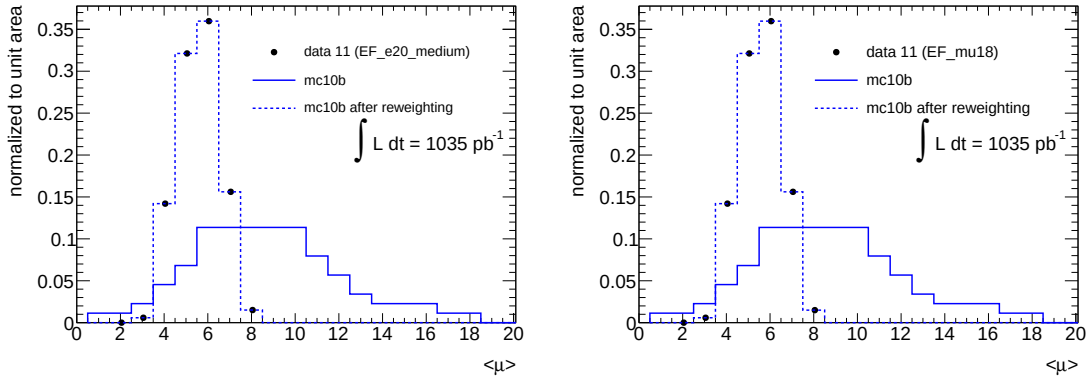

(a) (b)

Figure 6.3: Distribution of $\langle\mu\rangle|_{LB,BCID}$, the number of interactions averaged per luminosity block and bunch crossing ID. The simulated distributions for the Monte Carlo samples are shown for both `egamma`(a) and `muon` stream(b) separately. The data distributions (black dots) and Monte Carlo distributions (mc10b) after pile-up reweighing (blue dotted) are in perfect agreement.

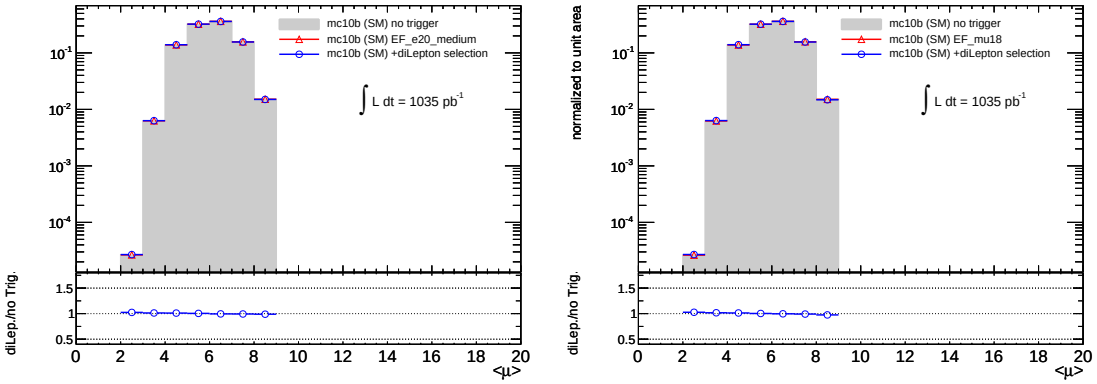

(a) (b)

Figure 6.4: Reweighted Monte Carlo $\langle\mu\rangle|_{LB,BCID}$ distributions are shown for egamma (a) and muon (b) selections separately after different event selection cuts. Filled area Standard Model Monte Carlo after reweighting before any selection cut, red triangle after trigger selection and blue circles after signal lepton selection. The ratios plots show the distributions after di-Lepton selection over the distributions without any cuts.

shape variables of the EM calorimeter middle layer, hadronic leakage variables, variables from the EM strip layers, track quality, and track-cluster matching (cf. Tab. 4.1 in Ch. 4). Selected electrons must have $p_{\mathrm{T}} > 20\,\mathrm{GeV}$ and $|\eta_{cl}| < 2.47$ (η of the electron cluster). In order to guarantee a good electron quality, the electron quality flag has to be marked as *okay* and the electron must not belong to a bad cluster. If any electron falls within $0.2 < \Delta R < 0.4$ of a selected jet, the electron is rejected.

Signal electrons must be identified with the egamma *tight* selection (cf. Tab. 4.1) and satisfy further isolation requirements. The variable ($p_{T,cone20}$) is a measure of the transverse momentum found in a cone of $\Delta R = 0.2$ around a given track. If the ratio of

Table 6.2: Weights for pile-up reweighting based on GRL for `egamma` and `muon` stream for the runs 178044-184169 and the corresponding triggers *EF_ e20medium* and *EF_ mu18*.

$\langle\mu\rangle$	`egamma` stream	`muon` stream
0	0	0
1	0	0
2	0.00218	0.00218
3	0.25886	0.25890
4	3.12420	3.12463
5	4.71067	4.71132
6	3.16552	3.16595
7	1.37379	1.37384
8	0.13261	0.13157
9	0	0
10	0	0

the transverse momentum around a given track over the track p_{T} is $p_{T,cone20}/p_T < 0.10$, the track or the associated electron is defined as isolated.

The leading electron in the event have to have $p_{\mathrm{T}} > 25\,\mathrm{GeV}$ if the event is selected by the electron trigger, as discussed in Sec. 6.2.

Electron energies in Monte Carlo are re-scaled using an ATLAS algorithm called `EnergyRescalerTool` [157]. This is done in order to emulate the electron energy response as precisely as possible. Electrons in data are calibrated using the same tool.

Muons

Selected muons must be reconstructed by the `Staco` muon reconstruction algorithm [158] either as combined or as segment-tagged muon (cf. 4.2.1). They must satisfy $p_{\mathrm{T}} > 10\,\mathrm{GeV}$ and $|\eta| < 2.4$. The muon selection requires at least one B-layer hit (when such a hit is expected generally), at least 2 Pixel hits plus dead Pixel sensors along the track in total, at least 7 SCT hits plus dead SCT sensors along the track in total, and at most 2 Pixel holes plus SCT holes in total. The muon is rejected, if it lies within the Inner Detector TRT region ($\eta< 1.9$) and the number of TRT outliers and TRT hits in total is less than 6. If the sum of the TRT outliers and the TRT hits is greater than 6, then the TRT outliers should not form more than 90% of the sum. For cosmic muon background suppression requirements on the distance to the primary vertex in $z_0 < 1.0\,\mathrm{mm}$ and in $d_0 < 0.2\,\mathrm{mm}$ must be satisfied by all selected muons. More details can be found in Sec. 6.5.4. The muon is rejected, if it lies in a cone of $\Delta R = 0.4$ within a selected jet.

The leading signal muon must have $p_{\mathrm{T}} > 20\,\mathrm{GeV}$ if the event is triggered by a muon trigger decision. Additionally, all signal region muons must be isolated, satisfying a track based isolation, $p_{T,cone_{20}} < 1.8\,\mathrm{GeV}$. The $p_{T,cone_{20}}$ is defined as described in the electron object definition. Muons in Monte Carlo are smeared with p_T and η-dependent scale-factors. The study performed in order to find those scaling factors is described briefly in Sec. 4.2.3.

Jets

This analysis uses the *Anti-Kt4Topo* jet definition [123]. These jets are reconstructed with the anti-k_T jet finder algorithm with a distance parameter $R = 0.4$, based on topological clusters [122] (both topological clustering and anti-k_T jet finder are described in detail in Sec. 4.3). The jet energy is calibrated with the *EMJES* calibration (cf. Sec 4.3.3).

The jets must have $p_{\mathrm{T}} > 20\,\mathrm{GeV}$ and lie within $|\eta| < 2.8$. They must not lie within a cone of $\Delta R = 0.2$ to a selected electron. Removing jets overlapping with signal electrons is necessary to reject jet candidates which have been faked by electrons. If any jet, which survives this overlap-requirement, is classified as a *loose* bad jet (cf. Jet Cleaning Sec. 4.3.4), the event is rejected.

Missing Transverse Energy

The missing transverse energy ($E_{\mathrm{T}}^{\mathrm{miss}}$) is defined as the momentum imbalance in the transverse plane w.r.t. the beam axis. It is calculated as the absolute value of the vector sum of the transverse momenta of the reconstructed objects (jet and leptons).

The $E_{\mathrm{T}}^{\mathrm{miss}}$ algorithm used in this analysis is the *MET_Simplified_RefFinal*. It sums the cells energies of clusters associated to jets calibrated at the EM+JES scale with $p_{\mathrm{T}} > 20\,\mathrm{GeV}$, leptons, non-isolated STACO muons, and topological clusters not belonging to pre-cited objects (CellOut term) calibrated at the EM scale. Further details and performance studies are briefly described in Sec. 4.4.

The components of missing transverse energy are calculated separately in the central, endcap and forward regions of the detector. As a final step, the $E_{\mathrm{T}}^{\mathrm{miss}}$ term is corrected for p_{T} of all the muons passing the object selection.

Event Selection and CutFlow

As first step of the event selection, the data quality is checked using the Good Runs List (GRL), provided by the official Data Preparation Group. The GRL contains the number of the luminosity blocks per run with good quality data. Only events passing this data quality check are analysed.

An additional data quality information is given by the LAr quality assessment. The event is rejected if a *LAr error* is detected. As this kind of detector effect is not simulated, the LAr quality requirement cut is only applied to data. Due to dead Front-End-Board (FEB) electronics in the LAr calorimeter (from period-E onwards), the data in the $\eta - \phi$-region ($-0.1 < \eta < 1.5$ and $-0.9 < \phi < -0.5$) cannot be used. Therefore events in data and Monte Carlo are rejected if they contain a jet with $p_{\mathrm{T}} > 20\,\mathrm{GeV}$ or a good electron (that satisfies object selection) pointing to this $\eta - \phi$ region.

After applying basic data quality selections, the trigger selections are applied separately for the `egamma` and the `muon` stream, as discussed in Sec 6.2.1.

In order to guarantee a good jet quality, several jet quality criteria have been established based on studies in [125] (cf. *JetCleaning* Sec. 4.3.4). An event is rejected if it has at least one *LooseBad* that is failing the jet quality criteria *loose* (cf. Tab 4.4).

The first primary vertex, the vertex with the highest p_{T} sum of the associated tracks, is required to have at least 5 tracks. Since the d_0 and z_0 of the muons considered in the analysis are calculated using the first primary vertex, this cut reduces the chance of selecting a cosmic event (cf. Sec 6.5.4).

In addition, the event is rejected if a least one muon is failing the cosmic rejection cuts (cf. Sec. 6.5.4).

Table 6.3: Number of observed events in data at various stages of the cutflow for opposite-sign events. Bottom table is giving a short description of the cut selections.

Cuts	`egamma` stream		`muon` stream
Total	1.066406e+08		75659176
GRL	89803544		63933884
LArError	89795608		63928384
LArHoleVeto	87779928		63258744
Trig	58408348		40994184
JetClean	58165620		40822164
GoodVertex	57986432		40634840
CosmicVeto	57972488		39343888
	ee	$e\mu$	$\mu\mu$
Exactly 2lepton+flavour	354391	37994	515014
sign	338803	512106	22750
$m_{ll} > 12\,\text{GeV}$	336538	16908	464349
signal leptons	237899	5901	444934
$E_{\text{T}}^{\text{miss}} > 80\,\text{GeV}$	522	858	673
FS SR-1	344	750	551
FS SR-2	336	741	567
FS SR-3	2	8	3

GRL	GoodRunLists selection.
LArError	Select events with no error from LAr quality assessment.
LArHoleVeto	Reject events if an electrons or a jet's η and ϕ points to the dead-FEB region of LAr calo.
Trig	Selecting events with appropriate trigger requirements cf. Sec. 6.2.
JetClean	Reject events if it has at least one jet failing the jet quality criteria.
GoodVertex	Select events where the first primary vtx in the event has at least 5 tracks.
CosmicVeto	Reject event that has at least one muon failing the cosmic rejection cuts.
Exactly 2lepton+flavor	At this stage select events with exactly two leptons and specific flavors
sign	Select events according to the sign of the two leptons.
mll	Select events with invariant mass of the two leptons to be more than 12 GeV.
signal leptons	Apply isolation criteria to the leptons and apply *tight* ID to the electrons.

At this step, all quality and cleaning cuts are applied, and the 'final' event selection, specified for the final states under investigation in this analysis can be adopted. Therefore exactly two leptons satisfying the leading p_T requirements described in the object definition are selected. The $e\mu$ (different-flavour) events are taken from both streams `egamma` and `muon` stream, the same-flavour events are taken from their individual streams according to the trigger strategy, discussed in Sec. 6.2.1.

The events are then classified according to the sign of the two leptons. A cut on the low invariant mass distribution $m_{ll} > 12\,\text{GeV}$ removes events with low-mass resonances, which are poorly modelled by the available Monte Carlo, but un-likely to be supersymmetric events. The signal leptons are required to be tight and isolated. Event weights are applied to each signal electron or muon (in Monte Carlo events only) to correct for the differing electron and muon reconstruction efficiencies in data and Monte Carlo.

The signal regions are defined in Sec. 5.2.3. Each signal region has a missing transverse energy cut at $E_{\text{T}}^{\text{miss}} > 80\,\text{GeV}$ or greater (FS-SR3), in order to remove SM backgrounds like QCD and $Z \to \ell\ell$ decays. The detailed event selection cuts discussed in the previous section are summarized in the cutflow table in Tab. 6.3. The number of events after each cut is listed separately for each di-lepton channel.

6.4.2 Kinematic Comparisons

Figure 6.5 shows the inclusive distributions for the combined di-lepton channels $e^{\pm}e^{\mp}$, $e^{\pm}\mu^{\mp}$ and $\mu^{\pm}\mu^{\mp}$ for (a) transverse missing energy ($E_{\text{T}}^{\text{miss}}$), (b) di-lepton invariant mass ($\text{m}_{\ell\ell}$), (c) p_{T} of the leading lepton, (d) p_{T} of the sub-leading lepton, (e) Number of jets with $p_{\text{T}} > 20\,\text{GeV}$, and (f) p_{T} of the leading jet. Figures 6.6-6.9 show the same distributions separated into the different di-lepton channels. Processes like QCD events with less than two true leptons have to be considered as 'Fakes'. Due to the limited statistics of the simulated QCD events, the *Fakes* are estimated directly from data via a matrix method as described in detail in Sec. 6.5.1. The other Standard Model backgrounds which are plotted here are taken from Monte Carlo simulations. The data is shown as black dots with statistical errors (68% Poissonian confidence limits) while the Monte-Carlo and the *Fake* contributions are stacked and presented in different colours. The red MC line is the sum of all the SM backgrounds. The yellow error band on the MC represents the statistical, cross section, luminosity uncertainties and jet energy scale and jet energy resolution uncertainties. Below the distributions, a ratio plot of data divided by the total MC background is shown. The inclusive di-lepton plots in Fig. 6.5 are published in [152] all plots in Fig 6.6-6.9 are internally published in [151].

The inclusive plots show good agreement between data and SM predictions. The biggest contributions to the total uncertainty are the jet energy scale and the jet energy resolution uncertainties. This can be seen at high $E_{\text{T}}^{\text{miss}}$-values in Fig. 6.5(a) and in the big uncertainty band in Fig. 6.5(e) for large jet multiplicities. Both tails are also effected by decreasing statistics, therefore the jet uncertainties are not the only reason for the bigger uncertainties.

The $E_{\text{T}}^{\text{miss}}$ distribution for $e^{\pm}e^{\mp}$ in Fig. 6.6(a) shows some small discrepancies in $E_{\text{T}}^{\text{miss}}$ around 100 GeV and in the tails. The major differences have been spotted in the $Z \to \ell\ell$ control region, this disagreement can be explained by the underestimation of the $E_{\text{T}}^{\text{miss}}$ from $Z \to ee$ decays in MC. The good agreement in the $Z \to \mu\mu$ channel led to the investigation of additional sources of $E_{\text{T}}^{\text{miss}}$ in the $Z \to ee$ channel. Bremsstrahlung or final state radiation with undetected photons can explain the difference between the $Z \to ee$ and the $Z \to \mu\mu$ channel, because the muons do not have such losses. This behaviour

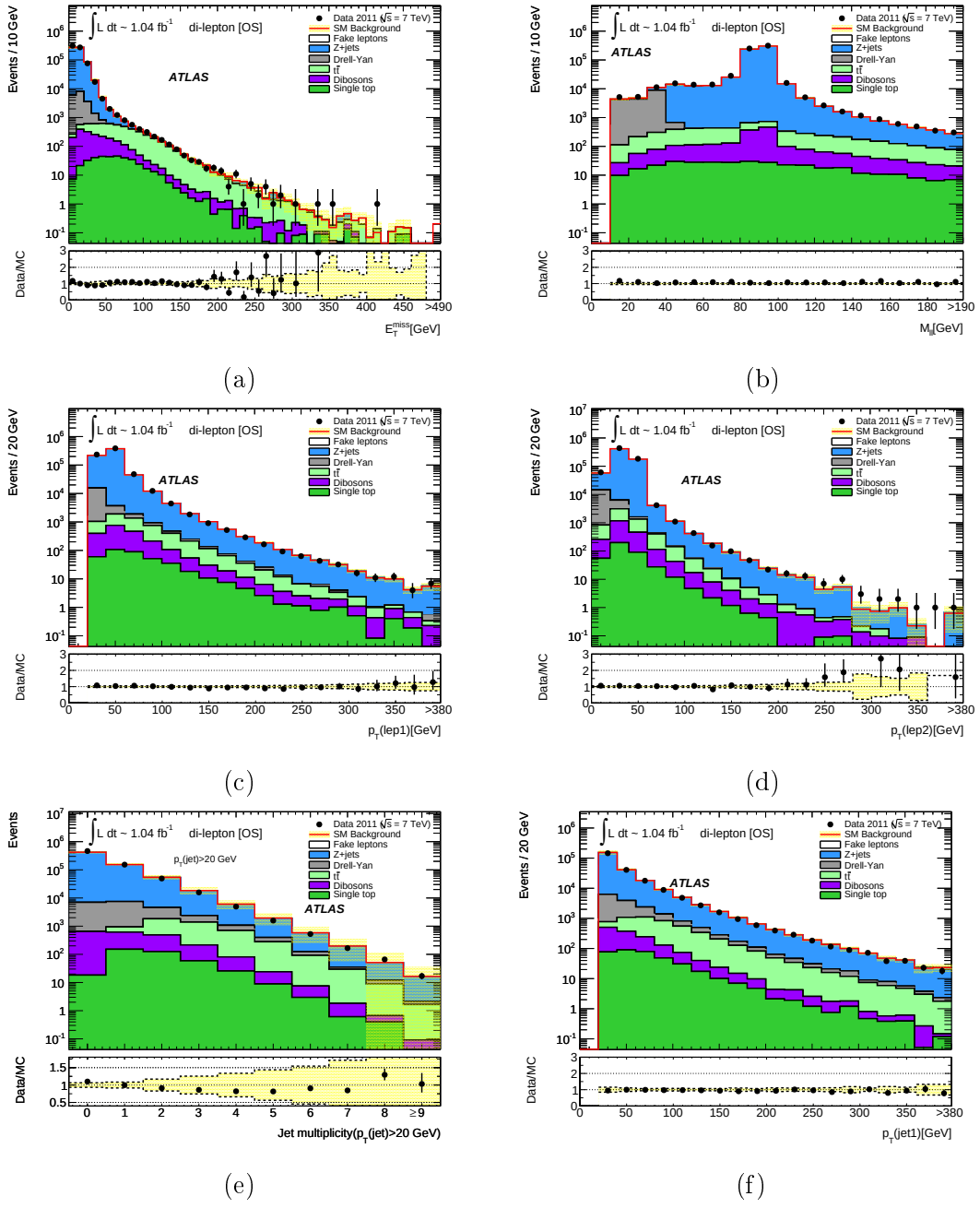

(a) (b) (c) (d) (e) (f)

Figure 6.5: Inclusive opposite-sign ($e^{\pm}e^{\mp}$, $e^{\pm}\mu^{\mp}$ and $\mu^{\pm}\mu^{\mp}$ together) distributions are shown after *signal leptons* cut of the, (a) transverse missing energy ($E_{\mathrm{T}}^{\mathrm{miss}}$), (b) di-lepton invariant mass ($\mathrm{m}_{\ell\ell}$), (c) p_{T} of the highest p_{T} lepton, (d) p_{T} of the next-highest p_{T} lepton, (e) Number of jets with $p_{\mathrm{T}} > 20\,\mathrm{GeV}$, and (f) p_{T} of the highest p_{T} jet. Errors on data points are statistical, while the error band on the MC represents the statistical, cross section, luminosity uncertainties and jet energy scale and jet energy resolution uncertainties. In the bottom histogram the black data points, and the yellow uncertainty band, have been divided by the total MC to show whether the fractional deviation of the data from the MC lies within the uncertainty band. The red MC line is the sum of all the SM backgrounds. The component labelled *Fakes* is evaluated using data as described in 6.5.1. All plots are published in [152].

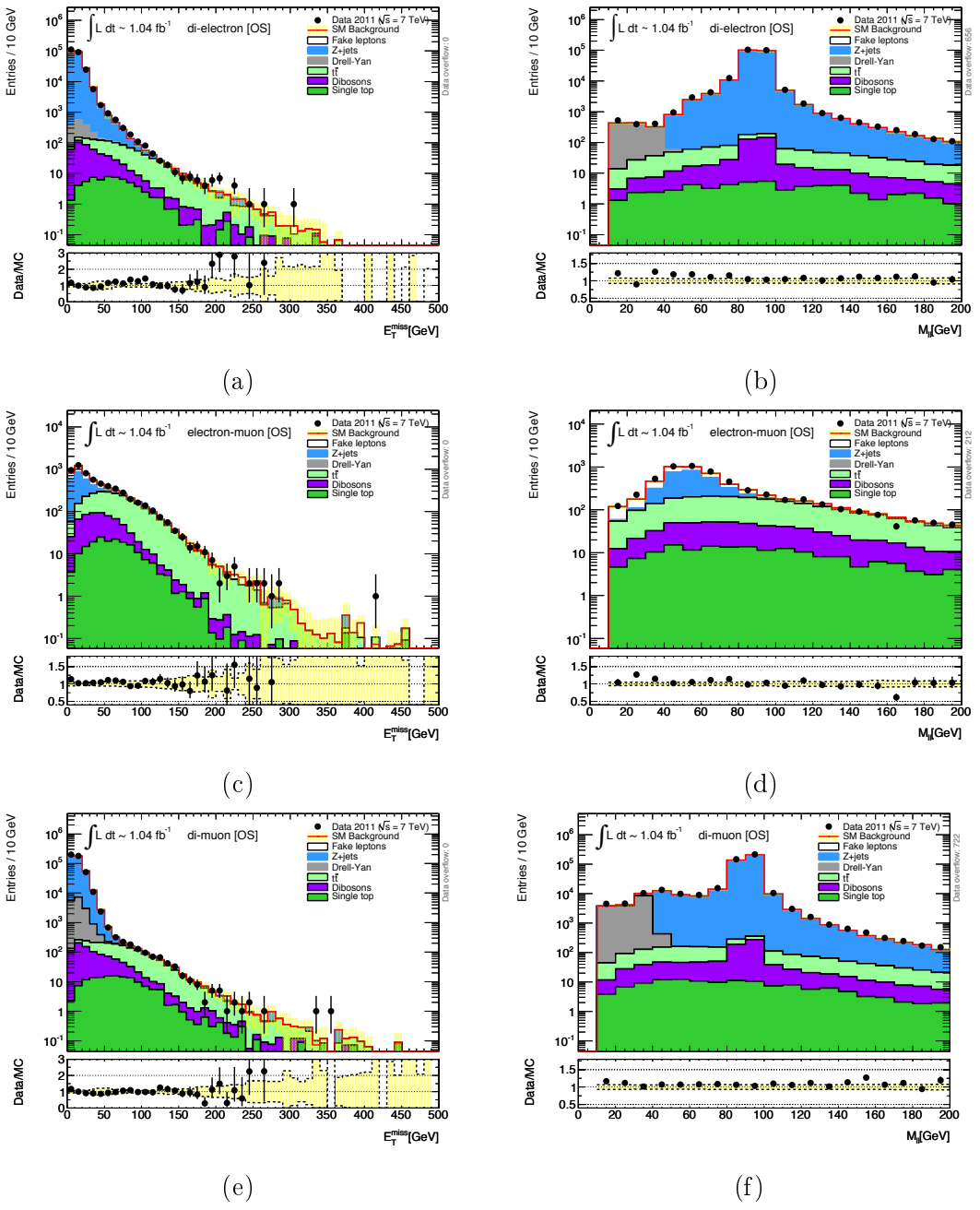

Figure 6.6: The opposite-sign distributions of missing transverse energy ($E_{\mathrm{T}}^{\mathrm{miss}}$) and di-lepton invariant mass distributions ($\mathrm{m}_{\ell\ell}$) are shown after *signal leptons* cut for each lepton channel, separately: (a) $E_{\mathrm{T}}^{\mathrm{miss}}(e^{\pm}e^{\mp})$, (b) $\mathrm{m}_{\ell\ell}(e^{\pm}e^{\mp})$, (c) $E_{\mathrm{T}}^{\mathrm{miss}}(e^{\pm}\mu^{\mp})$, (d) $\mathrm{m}_{\ell\ell}(e^{\pm}\mu^{\mp})$, (e) $E_{\mathrm{T}}^{\mathrm{miss}}(\mu^{\pm}\mu^{\mp})$, and (f) $\mathrm{m}_{\ell\ell}(\mu^{\pm}\mu^{\mp})$, Errors on data points are statistical, while the error band on the MC represents the statistical, cross section, luminosity uncertainties and jet energy scale and jet energy resolution uncertainties. In the bottom histogram the black data points, and the yellow uncertainty band, have been divided by the total MC to show whether the fractional deviation of the data from the MC lies within the uncertainty band. The red MC line is the sum of all the SM backgrounds. The component labelled *Fakes* is evaluated using data as described in 6.5.1. All plots are internally published in [151].

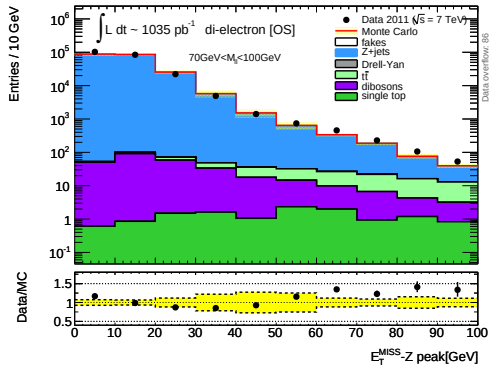

(a)

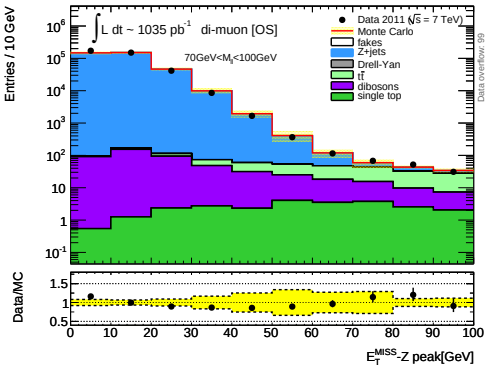

(b)

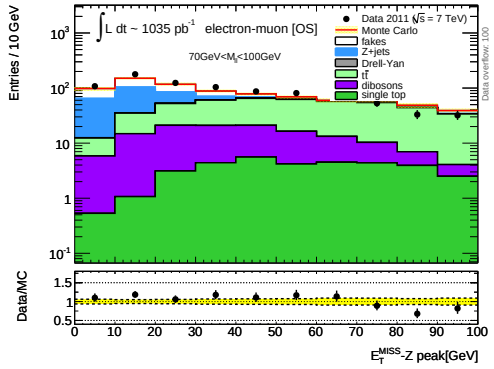

(c)

Figure 6.7: Distributions of the transverse missing energy ($E_{\mathrm{T}}^{\mathrm{miss}}$) of two-lepton events in data and Monte Carlo in the Z mass peak ($70 - 100\,\mathrm{GeV}$). The two lepton events are divided into the two opposite-sign channels ee (a), $\mu\mu$ (b), and $e\mu$ (c). Errors on data points are statistical errors, error band on Monte Carlo represents the statistical, cross-section, luminosity uncertainties and JES, JER. The black data points, and the uncertainty band (yellow), have been divided by the total Monte Carlo to show whether the fractional deviation of the data from the Monte Carlo lies within the uncertainty band. All Monte Carlo is normalised to luminosity and cross-section with the exception of the fake component which is an entirely data-driven estimate. The red Monte Carlo line is the sum of all the Standard Model backgrounds. All plots are internally published in [151].

has been studied in detail in appendix D.1. Figure 6.7 shows the $E_{\mathrm{T}}^{\mathrm{miss}}$ distribution for each channel after selecting the invariant mass of the di-leptons around the Z-boson mass ($70\,\mathrm{GeV} < \mathrm{m}_{\ell\ell} < 100\,\mathrm{GeV}$). Above $E_{\mathrm{T}}^{\mathrm{miss}} > 60\,\mathrm{GeV}$ the data over Monte Carlo ratio in $Z \to ee$ show some discrepancies.

Both the leading lepton and sub-leading momentum distributions in Fig. 6.8 shown good agreement between data and MC. The tails in the high p_{T} regions of the sub-leading lepton show some discrepancies, which are due to the decreasing statistics. The same-flavour distributions are dominated by the $Z \to \ell\ell$ decays.

The jet distributions, number of jets with $p_{\mathrm{T}} > 20\,\mathrm{GeV}$ and the leading jet p_{T} , in Fig 6.9 show comparable behaviour for the different final states. In Fig 6.9 (b) and (f) for

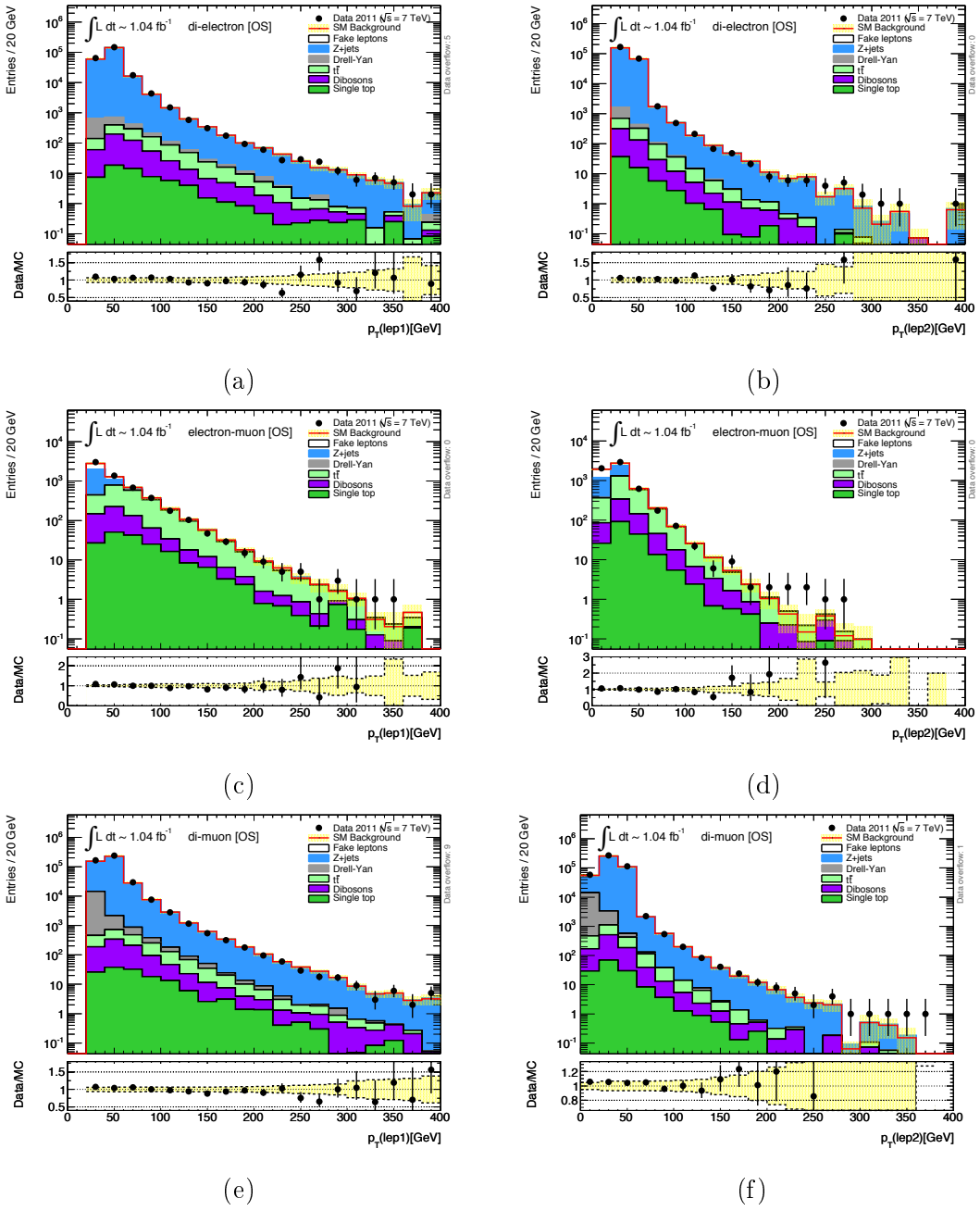

Figure 6.8: The opposite-sign distributions of the highest p_{T} lepton ($p_{\mathrm{T}\ lep,1}$) and the next-highest p_{T} lepton ($p_{\mathrm{T}\ lep,2}$) momentum distributions are shown after *signal leptons* cut for each lepton channel, separately: (a) $p_{\mathrm{T}\ lep,1}$ ($e^{\pm}e^{\mp}$), (b) $p_{\mathrm{T}\ lep,2}$ ($e^{\pm}e^{\mp}$), (c) $p_{\mathrm{T}\ lep,1}$ ($e^{\pm}\mu^{\mp}$), (d) $p_{\mathrm{T}\ lep,2}$ ($e^{\pm}\mu^{\mp}$), (e) $p_{\mathrm{T}\ lep,1}$ ($\mu^{\pm}\mu^{\mp}$), and (f) $p_{\mathrm{T}\ lep,2}$ ($\mu^{\pm}\mu^{\mp}$), Errors on data points are statistical, while the error band on the MC represents the statistical, cross section, luminosity uncertainties and jet energy scale and jet energy resolution uncertainties. In the bottom histogram the black data points, and the yellow uncertainty band, have been divided by the total MC to show whether the fractional deviation of the data from the MC lies within the uncertainty band. The red MC line is the sum of all the SM backgrounds. The component labelled *Fakes* is evaluated using data as described in 6.5.1. All plots are internally published in [151].

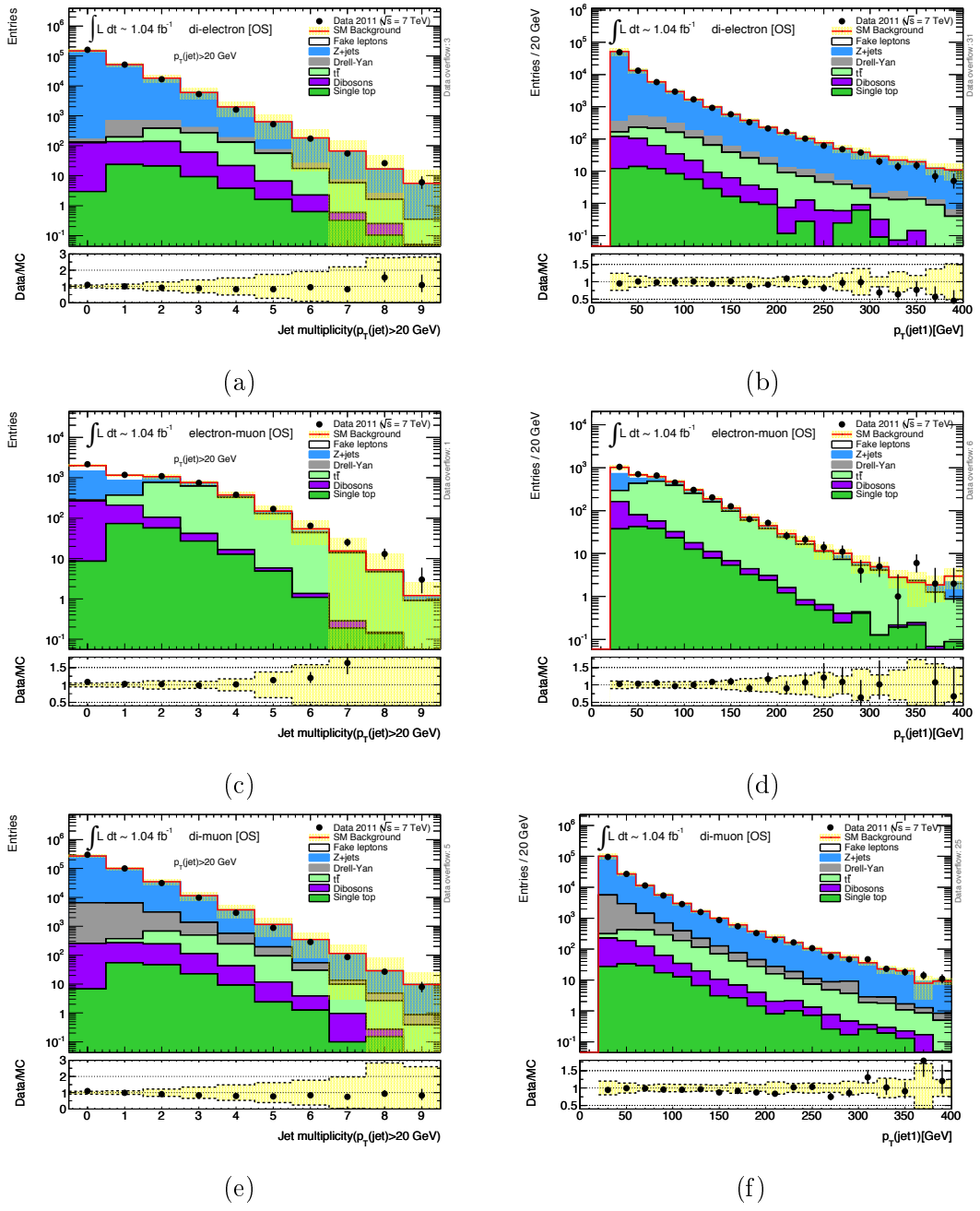

Figure 6.9: The opposite-sign distributions of the number of jets with $p_{\mathrm{T}} > 20\,\mathrm{GeV}$ (N jets) and momentum distributions of the highest p_{T} jet ($p_{\mathrm{T}\ jet,1}$) are shown after *signal leptons* cut for each lepton channel, separately: (a) N jets ($e^{\pm}e^{\mp}$), (b) $p_{\mathrm{T}\ jet,1}$ ($e^{\pm}e^{\mp}$), (c) N jets ($e^{\pm}\mu^{\mp}$), (d) $p_{\mathrm{T}\ jet,1}$ ($e^{\pm}\mu^{\mp}$), (e) N jets ($\mu^{\pm}\mu^{\mp}$), and (f) $p_{\mathrm{T}\ jet,1}$ ($\mu^{\pm}\mu^{\mp}$), Errors on data points are statistical, while the error band on the MC represents the statistical, cross section, luminosity uncertainties and jet energy scale and jet energy resolution uncertainties. In the bottom histogram the black data points, and the yellow uncertainty band, have been divided by the total MC to show whether the fractional deviation of the data from the MC lies within the uncertainty band. The red MC line is the sum of all the SM backgrounds. The component labelled *Fakes* is evaluated using data as described in 6.5.1. All plots are internally published in [151].

example, the difference in the p_{T} cut between electrons and muons is clearly visible in the difference of the amount of Drell-Yan events, softer muon p_{T} cut yield higher Drell-Yan contributions.

6.5 Standard Model Background Estimation

6.5.1 Fake Backgrounds

The Matrix Method

Events from processes with no or less than two true leptons might be selected due to jets or non-isolated leptons faking signal leptons, e.g. W+jets, or QCD events. Especially, the (di-jet) QCD events which have a high production cross section, and so can only be simulated with insufficient statistics need to be estimated in data. While W+jet events usually have one true and one faked lepton, the QCD events are selected by two faked leptons.

These fake backgrounds are estimated using a Matrix method as given in Eq. (6.1). Therefore a sample with *looser* identification criteria has to be defined. The number of real-real (N_{RR}), real-fake (N_{RF}), fake-real (N_{FR}), and fake-fake(N_{FF}) events in a given signal region can be estimated, by counting the number of events in the appropriate control region passing the tight-tight (N_{TT}), tight-loose (N_{TL}), loose-tight (N_{LT}) and loose-loose (N_{LL}) criteria, if the ID efficiency[1] (r) and the fake-rate (f) are known.

$$\begin{bmatrix} N_{TT} \\ N_{TL} \\ N_{LT} \\ N_{LL} \end{bmatrix} = \begin{bmatrix} rr & rf & fr & ff \\ r(1-r) & r(1-f) & f(1-r) & f(1-f) \\ (1-r)r & (1-r)f & (1-f)r & (1-f)f \\ (1-r)(1-r) & (1-r)(1-f) & (1-f)(1-r) & (1-f)(1-f) \end{bmatrix} \begin{bmatrix} N_{RR} \\ N_{RF} \\ N_{FR} \\ N_{FF} \end{bmatrix} \tag{6.1}$$

The ID efficiency is calculated as:

$$r = \frac{2 \cdot \frac{N_{TT}}{N_{Tl}+N_{lT}+N_{TT}}}{1 + \frac{N_{TT}}{N_{Tl}+N_{lT}+N_{TT}}} \tag{6.2}$$

in a true lepton enriched (Z control region) environment, while the fake-rates are simply calculated as the ratio of the number of events passing the tight selections over all events in a fake (QCD) enriched control region:

$$f = \frac{N_T}{N_L} = \frac{N_T}{N_l + N_T}. \tag{6.3}$$

In all equations (l) denotes a lepton that pass the *loose* selection but fails the *tight* selection, (L) a lepton which passes at least the *loose* selection and (T) a lepton which passes the *tight* selection. r and f are the ID efficiency and the fake rate respectively.

[1] here the ID efficiency is defined as the probability of a loose real lepton passing the tight criteria

Definition of Loose Selections

In order to be able to estimate the fake rate, the event selections are loosened. This is achieved by inverting the isolation criteria for electrons and muons. The electrons identification is relaxed further, by requiring *medium* electron selection only. The tight selections are the default tight lepton identification selections used in the analysis, the loose lepton selection is defined in order to enhance the lepton (fakes) from QCD processes.

ID Efficiencies and Fake Rates

The ID efficiency is extracted from a Z control region selected from events with exactly 2 leptons of opposite-sign and same-flavour, and with invariant mass within 5 GeV of the nominal Z mass of 91.2 GeV. At least one lepton (the tag lepton) has to pass the *tight* requirements.

The fake rates are studied in two different sets of QCD control regions: a set of one-lepton QCD control regions and a set of two-lepton opposite-sign QCD control regions (cf. Tab. C.1 and Tab. C.2 in the appendix). Both type of regions have to be analysed for muons and electrons separately. At least one lepton has to fail the tight selection (the anti-tag lepton) as baseline fake requirement. Several cuts have been tested (cf. Tab. C.1 and Tab. C.2 in the appendix) in order to define the final control region. The control regions have been chosen as a compromise of fake rate stability, purity, and statistics.

The purity is estimated by subtracting the amount of Monte Carlo events from other processes counted in a given QCD control region from the measured number of events in data in this region:

$$\text{purity} = \frac{N^{\text{dilep}}_{\text{data}} - N^{\text{dilep}}_{\text{non-QCD}}}{N^{\text{dilep}}_{\text{data}}} \quad \sim \quad \frac{N^{\text{dilep}}_{\text{QCD}}}{N^{\text{dilep}}_{\text{data}}} \tag{6.4}$$

The fake estimations are completely data driven. The Monte Carlo samples are only used to cross-check the control region purity.

The muon fake rates are determined in a two-lepton opposite-sign QCD control region with a missing transverse energy cut of $E_{\text{T}}^{\text{miss}} < 30\,\text{GeV}$ (cf. Tab. C.2 in the appendix). The electron fake rates are derived in the one-lepton QCD control region with the following selection cuts: $E_{\text{T}}^{\text{miss}} < 30\,\text{GeV}$, $\Delta\phi_{E_{\text{T}}^{\text{miss}},l} < 0.5$, and $N_j \geq 1$ (cf. Tab. C.1).

The ID efficiency and the fake rates for muon and electron fakes are quoted in Tab. 6.4.

Table 6.4: The selected fake rates and efficiencies including statistical error for the selected rates used in the fake estimation. The purity is only shown for the selected fake rates. All numbers are quoted in percent.

	ID efficiency	Fake rate	
	Rate	Rate	Purity
Electrons	86.15 ± 0.059	10.96 ± 0.02	94.94
Muons	98.58 ± 0.015	47.63 ± 1.26	98.54

Systematic Uncertainties

Three sources of systematic uncertainties are considered: variations from the choice of the control region, the p_{T} dependency of the fake rates and impurities in the control region.

For muons the same sign two-lepton regions R9 and R2 (cf. Tab. C.2) are taken into account as up and down variation of the fake rate. The variation of the fake rate for electrons is determined by using the one-lepton control regions R7 and R4 (cf. Tab. C.1) as up and down variation. The systematic is derived as the averaged difference of f_{max} and f_{min} from the nominal fake rate.

In order to estimate the systematic uncertainty due to the p_{T} dependency the relative error of r and f as function of p_{T} is considered.

Contamination of (real) leptons from SM background processes like W+jets in the one lepton or Z+jets or $t\bar{t}$ in the two-lepton QCD control region does contribute to higher fake-rates, because the real leptons pass the tight selection criteria. By subtracting the real leptons originating in processes different from QCD, the fake rate would be reduced. Especially in the one-lepton QCD control region (R10), the purity in the tight sample is 63%. The remaining contributions are W and Z events. After subtracting the real lepton events, the fake-rate would drop from 11% to 7%. This impurity has to be considered as systematic uncertainty, because the MC subtraction is not applied on the nominal fake estimation. The purity of the two-lepton QCD control region is 98%, this region is therefore much less affected by this systematic.

A complete table of all systematics is given in the appendix (cf. Tab. C.3). To obtain the total systematic uncertainty the individual systematics are added in quadrature.

Results

Tables 6.5 summarizes the results of the *Fake* estimates. The estimates are obtained using a constant fake-rate in η and p_{T} , and efficiency from the selected QCD control regions one-lepton *R10* for electrons, and same-sign di-muon *R3* for muons. The systematic uncertainty reflects effects described in the subsection 6.5.1. The systematic uncertainties of the p_T dependency, the variation of QCD control region and the MC subtraction of real-lepton contribution from non-QCD processes. Additional Tables in the appendix show the details of the estimates for each signal region and channel.

Table 6.5: Estimated fake (Est fake) contribution and number of observed events (data) in the flavour-subtraction signal regions FS-SR1 FS-SR2 and FS-SR3 for the di-lepton channels $e^{\pm}e^{\mp}$, $e^{\pm}\mu^{\mp}$ and $\mu^{\pm}\mu^{\mp}$.syst and stat

	$e^{\pm}e^{\mp}$		$e^{\pm}\mu^{\mp}$		$\mu^{\pm}\mu^{\mp}$	
	Est fake	data	Est fake	data	Est fake	data
FS-SR1	5.27±2.393±1.71	344	30.22±5.585±6.12	750	21.76±4.911±6.12	551
FS-SR2	1.50±0.662 ±1.52	336	32.26±7.699 ±6.30	741	19.38±5.788 ±5.72	567
FS-SR3	0.17±0.083 ±0.19	2	0.92±0.167 ±0.96	8	-0.08±0.015 ±0.03	3

6.5.2 $Z/\gamma \rightarrow$ ll+jets

Method

The contribution from Z/γ^* in a given signal region is determined by a semi-data driven technique. The number of Z/γ^* is measured in a Z/γ^* enhanced control region in data. The expected number of events in the signal region is extrapolated to the signal region by Eq. (6.5). The transfer factor from the control region to the signal region is determined with Monte Carlo simulations as the ratio of expected number of Z/γ^* events in the signal region over the number of expected Z/γ^* events in the control region (cf. (6.6)).

$$N_{Z/\gamma^*}^{\mathrm{est,SR}} = \beta \cdot N_{Z/\gamma^*}^{\mathrm{data,CR}} \tag{6.5}$$

$$\beta = \frac{N_{Z/\gamma^*}^{\mathrm{MC,SR}}}{N_{Z/\gamma^*}^{\mathrm{MC,CR}}}. \tag{6.6}$$

The number of $N_{Z/\gamma^*}^{\mathrm{data,CR}}$ events in data is corrected by non-Z/γ^* contributions as given in Eq. (6.7).

$$N_{Z/\gamma^*}^{\mathrm{data,CR}} = \left(N^{\mathrm{data}} - N_W^{\mathrm{MC}} - N_{t\bar{t}}^{\mathrm{MC}} - N_{\mathrm{singleTop}}^{\mathrm{MC}} - N_{\mathrm{dibosons}}^{\mathrm{MC}}\right)^{\mathrm{CR}}, \tag{6.7}$$

where the number of W + jets (N_W^{MC}), $t\bar{t}$($N_{t\bar{t}}^{\mathrm{MC}}$), single top ($N_{\mathrm{singleTop}}^{\mathrm{MC}}$) and dibosons ($N_{\mathrm{dibosons}}^{\mathrm{MC}}$) events in the control region are estimated using the MC predictions.

The technique relies on the successful modelling of the $E_{\mathrm{T}}^{\mathrm{miss}}$ distribution in Z/γ^*+jets events by Monte Carlo (in both the $e^{\pm}e^{\mp}$ and $\mu^{\pm}\mu^{\mp}$) channels.

Z/γ^* Control Region

The control region used for this estimation selects events with: $81 < m_{ll} < 101\,\mathrm{GeV}$ and $E_{\mathrm{T}}^{\mathrm{miss}} < 20\,\mathrm{GeV}$. This technique is only used to estimate the Z/γ^*+jets contribution in the $e^{\pm}e^{\mp}$ and $\mu^{\pm}\mu^{\mp}$ channels. Monte-Carlo is used to estimate the number of events in the $e^{\pm}\mu^{\mp}$ channel, due to low statistics.

Systematics

The total uncertainty on the estimates is a result of statistical uncertainties from the MC and of several sources of systematic uncertainties. As the method is largely based on MC expectations, all sources of systematic uncertainties discussed in Sec. 6.5.1 have to be considered. This includes: jet energy scale (JES) variation (both upward and downward), jet energy resolution variation , and changes in the energy scale of the leptons. By varying the JES, electron energy scale (EES), and muon energy resolution (both in the MS and in the ID), and propagating the changes to the $E_{\mathrm{T}}^{\mathrm{miss}}$ a systematic uncertainty can be assessed. The larger of the upward/downward variation for jet and lepton energy scale changes are considered in the total systematic. Furthermore, as the control region is always defined by an upper bound on the missing E_T ($E_{\mathrm{T}}^{\mathrm{miss}} < 20\,\mathrm{GeV}$), variation of this cut was also considered as a potential source of uncertainty. By varying the $E_{\mathrm{T}}^{\mathrm{miss}}$ cut by 5 GeV around its nominal value, it is determined that the systematic has a negligible effect.

Results

The predicted number of events in each opposite-sign channel, in the signal regions defined for the flavour subtraction analysis, are detailed in Table 6.6. For each signal region the estimate in the $e^{\pm}\mu^{\mp}$ channel is taken from Monte Carlo expectation (denoted *using exp.* in the tables). An additional table containing the number of events in the control regions and the transfer factors β can be found in the appendix (cf. Tab. C.12).

Table 6.6: Expected and predicted numbers of Z/γ^*+jets events in each opposite-sign channel, in the flavour-subtraction signal regions. When two errors are quoted, the first one is the systematic error and the second the statistical. The MC numbers have statistical errors only.

	$e^{\pm}e^{\mp}$	$e^{\pm}\mu^{\mp}$	$\mu^{\pm}\mu^{\mp}$
Exp.MC SR1	80.952±4.795	40.814±5.713±3.207	37.647±2.636
Pred. SR1	85.944±4.580±5.096	using exp.	40.924±10.458±2.866
Exp.MC SR2	50.95±3.66	29.09±5.64±2.68	42.77±2.92
Pred. SR2	45.62±11.76±3.31	using exp.	37.95±4.89±2.60
Exp.MC SR3	0.012±0.007	1.028±0.023±0.420	0.75±0.24
Pred. SR3	0.012±0.672±0.007	using exp.	0.81±0.06±0.26

6.5.3 Fully Leptonic $t\bar{t}$

The fully leptonic $t\bar{t}$ contribution to the signal region is estimated with a semi data-driven technique as the Z/γ^* estimation described above. The number of top-tagged events in data in a control region is determined by using the so-called *contransverse* mass top tagger technique [159, 160]. Then, the number of top-tagged events, corrected by non-$t\bar{t}$ Monte Carlo background events counted in the control region, is extrapolated into the signal region. The transfer factor is derived from $t\bar{t}$ Monte Carlo, as the ratio events in the SR over the events in the CR. The procedure is summarised in Eq. (6.8).

$$(N_{tt})_{SR} = \left((N^{tag}_{data})_{CR} - (N^{tag}_{non-tt,MC})_{CR}\right) \frac{(N_{top,MC})_{SR}}{(N^{tag}_{top,MC})_{CR}} \tag{6.8}$$

where $(N_{data})_{CR}$ is the number of events observed in a control region dominated by top pair events, $(N_{non-tt,MC})_{CR}$ is the number of non-$t\bar{t}$ events in the control region, estimated from either Monte Carlo or data-driven techniques, $(N_{top,CR})_{MC}$ is the number of $t\bar{t}$ events estimated from Monte Carlo in the control region, and $(N_{top,SR})_{MC}$ is the number of events estimated from Monte Carlo in the signal region under consideration.

The *contransverse* mass tagger is described in the following. The loose $E_{\mathrm{T}}^{\mathrm{miss}}$ cut for the flavour subtraction signal regions FS-SR1 and FS-SR2 leads to problems in finding a suitable control region for this technique. Therefore, the semi-data driven $t\bar{t}$ background estimation is only available for the tight FS-SR3 signal region, in FS-SR1 and FS-SR2, the $t\bar{t}$ contribution is estimated from Monte Carlo simulation. In the following, the denoted CR is always the control region for the estimation of $t\bar{t}$ contribution for signal region FS-SR3.

Description of the Top Tagging Method

The *contransverse* mass was first introduced in [159]. It is the measurement of an analytical combination of the masses for two pair produced heavy states (δ) decaying into a set of visible decay products (χ_i) and invisible particles (α). In top decays, there are three different heavy state decays, following this definition:

$$\delta \rightarrow \chi + \alpha \tag{6.9}$$

$$t \rightarrow jet + W \tag{6.10}$$
$$b \rightarrow l + \nu \tag{6.11}$$
$$t \rightarrow (jet, l) + \nu \tag{6.12}$$

The *contransverse* mass is defined as:

$$\begin{aligned} m^2_{CT}(\chi_1, \chi_2) &= [E_{\mathrm{T}}\ (\chi_1) + E_{\mathrm{T}}\ (\chi_2)]^2 - [p_{\mathrm{T}}\ (\chi_1) - p_{\mathrm{T}}\ (\chi_2)]^2 \\ &= m^2_{\chi_1} + m^2_{\chi_2} + 2\left[E_{\mathrm{T}}\ (\chi_1) \cdot E_{\mathrm{T}}\ (\chi_2) + p_{\mathrm{T}}\ (\chi_1) \cdot p_{\mathrm{T}}\ (\chi_2)\right] \end{aligned} \tag{6.13}$$

If $m(\chi_1) = m(\chi_2) \equiv m(\chi)$, m_{CT} possesses an endpoint:

$$m^{max}_{CT}\left[m^2(\chi)\right] = \frac{m^2(\chi)}{m(\delta)} + \frac{m^2(\delta) - m^2(\alpha)}{m(\delta)} \tag{6.14}$$

Following the Eq. (6.10)-(6.12), three *contransverse* masses can be constructed: $m_{CT}(j,j)$, $m_{CT}(l,l)$, and $m_{CT}(jl,jl)$. Their endpoints can be calculated by substituting (δ, α) with (W,ν), (t,W), and (t,ν), respectively. The endpoint calculation performed above is only valid if the initial particle is produced in rest-frame, otherwise, m_{CT} is also a function of the vector sum of the transverse momenta of the visible particles upstream of the system for which the *contransverse* mass is calculated. The net transverse mass of the upstream objects can be quantified with the variable p_b [160]. This boost can be considered by not cutting directly on m^{max}_{CT}, but by requiring, that the m_{CT} variable lies below the appropriate curve in the ($\mathrm{m}_{CT}(\chi)$, $\mathrm{p}_b(\chi)$) plane. The corresponding vector sum of the transverse momenta of the upstream objects can be calculated as follows:

$$p_b(l_1, l_2) = \left|-p_{\mathrm{T}}\ (l_1) - p_{\mathrm{T}}\ (l_2) - E^{\mathrm{miss}}_{\mathrm{T}}\right| \tag{6.15}$$
$$p_b(j_1, j_2) = \left|-p_{\mathrm{T}}\ (l_1) - p_{\mathrm{T}}\ (l_2) - p_{\mathrm{T}}\ (j_1) - p_{\mathrm{T}}\ (j_2) - E^{\mathrm{miss}}_{\mathrm{T}}\right| \tag{6.16}$$

The m_{CT} top tagger requirements are:

- The event should have at least $N_{jet} \geq 2$, $p_{\mathrm{T}} > 20\,\mathrm{GeV}$.
- All the 2 jets permutations with $p_{\mathrm{T}}\ (j) > 20\,\mathrm{GeV}$ and $p_{\mathrm{T}}\ (j_1) + p_{\mathrm{T}}\ (j_2) + p_{\mathrm{T}}\ (l_1) + p_{\mathrm{T}}\ (l_2) > 100\,\mathrm{GeV}$ are considered.
- $\mathrm{m}_{CT}(l_1, l_2)$ has to be in the appropriate area of the $m_{CT}(l_1, l_2), p_b(l, l))$-plane.
- All the pairs ($(\mathrm{j}_i,\mathrm{l}_1)$,$(\mathrm{j}_k,\mathrm{l}_2)$) that satisfy both $m(j_i, l_1) < 155\,\mathrm{GeV}$ and $m(j_k, l_2) < 155\,\mathrm{GeV}$ are considered.

- At least one combination with $m_{CT}(j,j)$ in the allowed area of the $(m_{CT}(j,j), p_b(j,j))$-plane has to be found.
- For all the combinations passing the previous cuts $m_{CT}(jl,jl)$ should be compatible with $t\bar{t}$.

Events which have one permutation of two jets fulfilling the conditions above are tagged as top-like event. The top tagging efficiency depends on the choice of the control region, but it is approximately 87%. The rejection factor for other SM processes is roughly 73%.

Control Region - Selection and Observed Events

The complete event selection up to the *signal lepton* cut is applied in order to have similar cuts on the control sample in comparison to the signal sample. The only additional cut which has to be applied, is the requirement of the tagging algorithm, that the event contains at least two jets with $p_{\mathrm{T}} > 20\,\mathrm{GeV}$. Figure 6.10 shows the $E_{\mathrm{T}}^{\mathrm{miss}}$ distributions for ee, $e\mu$ and $\mu\mu$ channel for events passing the top tagger requirements. The control region is defined by $E_{\mathrm{T}}^{\mathrm{miss}}$ cuts only:

- **CR:** $60\,\mathrm{GeV} < E_{\mathrm{T}}^{\mathrm{miss}} < 100\,\mathrm{GeV}$ for $e\mu$ pairs
  and $80\,\mathrm{GeV} < E_{\mathrm{T}}^{\mathrm{miss}} < 100\,\mathrm{GeV}$ for same-flavour lepton pairs.

The lower $E_{\mathrm{T}}^{\mathrm{miss}}$ has to be applied to reduce the $Z \to \ell\ell$background, which is dominating this region in case of same-flavour events (Figure 6.10(a) and (c)). In the $e\mu$ pair events a slightly looser $E_{\mathrm{T}}^{\mathrm{miss}}$ cut can be applied ($E_{\mathrm{T}}^{\mathrm{miss}} > 60\,\mathrm{GeV}$). The upper cut on $E_{\mathrm{T}}^{\mathrm{miss}}$ is fixed to avoid a possible contamination from signal.

The observed number of events in the control region in data and Monte Carlo are listed in Tab. 6.7. Good agreement between the expected and observed number of events in the control region results in a top scaling factor close to 1.

Table 6.7: Expected and observed event counts in the data-driven top control region.

Control region	CR
data	1010
$t\bar{t}$	848.3
Wt	48.2
Z / γ + jets	66.0
diboson	22.2
fakes	39
Total expected	1023.7
Total non-$t\bar{t}$	175.4

Systematic Uncertainties

The $t\bar{t}$ yield in the SR is calculated with Eq. (6.8); all the three terms in this equation contribute to the uncertainty of the estimated number of events. The first term, the number of counted events in data in the control region, is affected by statistical uncertainty. For the second term the contamination of the control region from non-$t\bar{t}$ events,

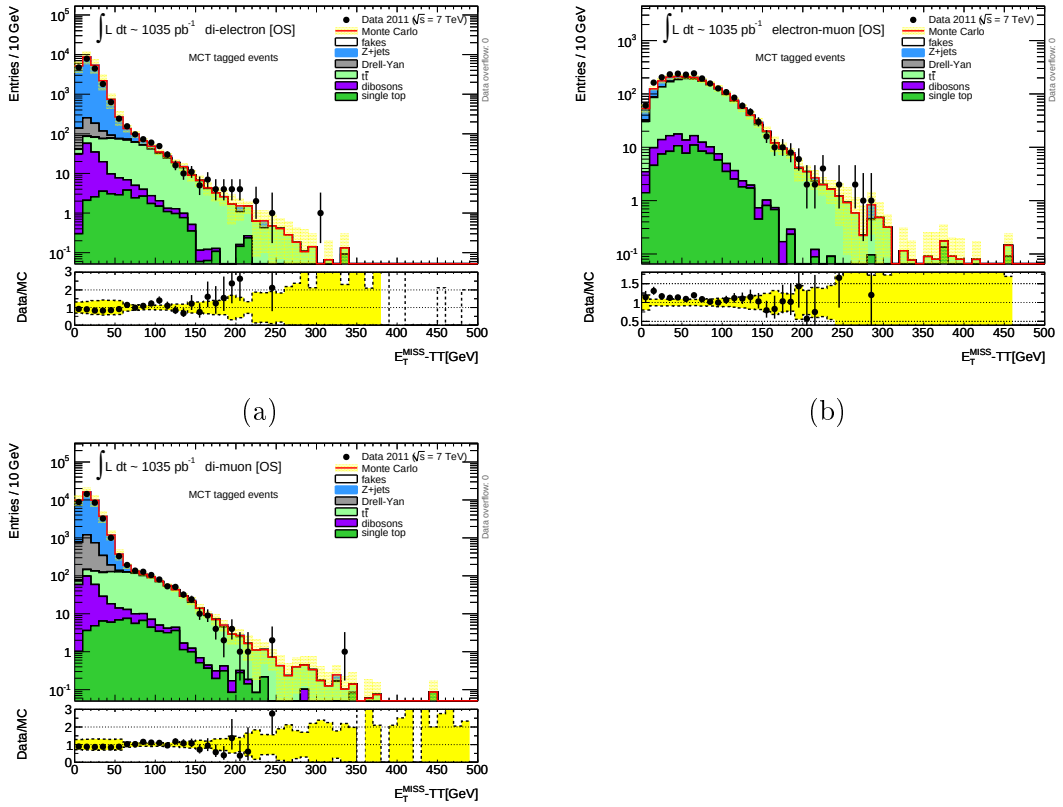

Figure 6.10: Distribution of $E_{\mathrm{T}}^{\mathrm{miss}}$ for events passing the top tagger requirement. The distributions are shown separately for electron pairs (upper left), muon pairs (upper right) and $e\mu$ pairs (lower left).

the uncertainties of the jet energy scale, the jet energy resolution, the luminosity, and the limited Monte Carlo statistics are considered in the total systematic uncertainty. The third term is the extrapolation factor derived from $t\bar{t}$ Monte Carlo samples. The jet energy scale, the jet energy resolution, the limited Monte Carlo statistics, uncertainties of the Monte Carlo generator and ISR/FSR effects are considered. Detailed tables are attached to the appendix for jet energy scale, jet energy resolution, ISR/FSR effects and uncertainties due to different MC generators in Tab. C.13, respectively.

All systematic uncertainties considered in the $t\bar{t}$ background estimation are summarized in Tab 6.8. The jet energy scale uncertainties on the $(N_{top,MC})_{SRxx}/(N_{top,MC}^{tag})_{CR}$ (SRxx denotes the different lepton channels) and on the non-$t\bar{t}$ background in the control region, which are completely anti-correlated, are added linearly, all other systematics are added in quadrature.

Results

Table 6.9 summarizes the estimated $t\bar{t}$ background in the flavour subtraction signal regions. In case of the loose $E_{\mathrm{T}}^{\mathrm{miss}}$ regions FS-SR1 and FS-SR2, no data-driven $t\bar{t}$ estimation is possible, because the $80 < E_{\mathrm{T}}^{\mathrm{miss}} < 100\,\mathrm{GeV}$ region is part of the $t\bar{t}$ control region. Only for this signal region Monte Carlo predictions are available. The data-driven estimates

Table 6.8: Uncertainties on the estimate of the $t\bar{t}$ background in the signal and control region.

	SR & CR
Statistical (CR, observed)	3.8%
Statistical (CR, expected)	3.8%
Statistical ($t\bar{t}$ MC)	6.0%
Statistical (non-$t\bar{t}$ MC)	0.4%
JES ($t\bar{t}$ MC)	10.6%
JES (non-$t\bar{t}$ MC)	3.4%
JER ($t\bar{t}$ MC)	0.6%
JER (non-$t\bar{t}$ MC)	0.9%
luminosity (non-$t\bar{t}$ MC)	0.7%
cross sections (non-$t\bar{t}$ MC)	1.6%
CR fake uncertainty	0.7%
generator	15.6%
ISR/FSR	20.0%
total (expected)	26.7%
total (observed)	26.7%

for FS-SR3 are in good agreement with the simulated Monte Carlo events.

Table 6.9: Expected and predicted numbers of fully-leptonic $t\bar{t}$ events in each opposite-sign channel, in the flavour-subtraction signal regions, obtained using the m_{CT} and kinematic top-taggers (where possible, neither method can predict the top contribution in the region with $80 < E_{\mathrm{T}}^{\mathrm{miss}} < 100\,\mathrm{GeV}$). The errors quoted below, are firstly (syst.) and secondly (stat.) uncertainties.

	$e^{\pm}e^{\mp}$	$e^{\pm}\mu^{\mp}$	$\mu^{\pm}\mu^{\mp}$
Exp.MC SR1	131.0±17.9±5.5	390.0±46.1±9.6	277.7±30.8±7.6
Pred. SR1	using exp.	using exp.	using exp.
Exp.MC SR2	146.7±20.3±5.8	419.4±52.5±9.9	289.8±35.4±7.8
Pred. SR2	using exp.	using exp.	using exp.
Exp.MC SR3	1.72±0.67±0.72	3.03±0.84±0.82	1.91±0.65±0.69
Pred. SR3 (m_{CT})	1.25±0.38±0.06	3.34±1.02±0.15	2.19±0.67±0.10

6.5.4 Cosmic Contamination

The selection cuts for the cosmic muon suppression are chosen as the distances from the primary vertex in z- and R-direction: $|z_0^{PV}| < 1.0$ mm and $|d_0^{PV}| < 0.2$ mm. It has been found that the distance of cosmic muons in average is much larger than the chosen cuts. In order to estimate the number of cosmic muons in this signal-like muon region (signal region), the number of muons in a cosmic muon enhanced region (control region) is determined and extrapolated into the signal region. The control region is based on an inverted $|z_0^{PV}|$ cut. The other muon selection cuts are applied as described in object

definition (cf Sec. 6.4.1). In a first step, only the trigger, vertex, and cleaning cuts are applied on the cosmic muon enhanced sample.

Two methods have been developed in order to estimate the number of cosmic muons in the signal region.

Method A

The first method assumes a flat distribution of cosmic muons in z-direction. The number of muons are counted in a control region which is defined by low and high bounds in z-direction: $T_\ell < |z_0^{\mathrm{PV}}| < T_h$ mm. The contribution in the signal region is estimated by scaling the number of muons in the control region by the ratio of the areas with respect to the signal region:

$$N_{\mathrm{cosmics}}(|z_0^{\mathrm{PV}}| < 1 \text{ mm}) = \frac{1 \text{ mm}}{|T_\ell - T_h| \text{ mm}} \times N_{\mathrm{muons}}(T_\ell < |z_0^{\mathrm{PV}}| < T_h \text{ mm}) \qquad (6.17)$$

with T_ℓ,T_h the lower and upper bound of the control region. By varying the bounds of the control region, the systematic uncertainty on the choice of the control region can be determined. Table 6.10 shows the results for different control regions and the estimated number of cosmic muons in $|z_0^{\mathrm{PV}}| < 1$ mm. If the lower bound of the control region is too small, the control sample is contaminated by collision-like muons. This increases the estimated number of cosmic muons in the signal region artificially. Method A predicts $6.1 \pm 1.4(\mathrm{stat}) \pm 1.3(\mathrm{syst})$ cosmic muons events within $|z_0^{\mathrm{PV}}| < 1$ mm in events with 2 muons, if only loose event selection criteria are applied.

Table 6.10: Number of observed muons in the control region and corresponding estimation of cosmics at $|z_0^{\mathrm{PV}}| < 1$ mm using method A) described in the text on $1.04\,\mathrm{fb}^{-1}$ of data for different control region definitions. Uncertainties are statistical only.

	N_{muons}		$N_{\mathrm{cosmics}}(\lvert z_0^{\mathrm{PV}}\rvert < 1$ mm$)$	
T_l	T_h			
	$\lvert z_0^{\mathrm{PV}}\rvert < 100$ mm	$\lvert z_0^{\mathrm{PV}}\rvert < 150$ mm	$\lvert z_0^{\mathrm{PV}}\rvert < 100$ mm	$\lvert z_0^{\mathrm{PV}}\rvert < 150$ mm
$\lvert z_0^{\mathrm{PV}}\rvert > 1$ mm	2114	2242	21 ± 2	15.0 ± 1.6
$\lvert z_0^{\mathrm{PV}}\rvert > 5$ mm	576	704	6.1 ± 1.4	4.9 ± 1.0
$\lvert z_0^{\mathrm{PV}}\rvert > 10$ mm	541	669	6.0 ± 1.3	4.8 ± 1.0

Method B

The distribution shown in Fig. 6.11 and the muon counts in the first control region in Tab. 6.10 indicate that the assumption of a flat muon distribution in $|z_0^{\mathrm{PV}}|$ is not true for small values. Therefore, a Gaussian fit of the $|z_0^{\mathrm{PV}}|$ distribution has been performed and the value at low $|z_0^{\mathrm{PV}}|$ is determined by this fit. The lower bound of the fit is $T_l = |z_0^{\mathrm{PV}}| > 1$, and the upper bound has been varied for the systematic determination ($T_h = |z_0^{\mathrm{PV}}| < 100$, 150 and 200 mm). The results of method B are summarised in Tab. 6.11 and they are in good agreement with the results from method A. Choosing the conservative estimate, method b gives $5.4 \pm 0.4(\mathrm{stat}) \pm 0.5(\mathrm{syst})$ cosmic muons for $|z_0^{\mathrm{PV}}| < 1$ mm with loose event selection criteria.

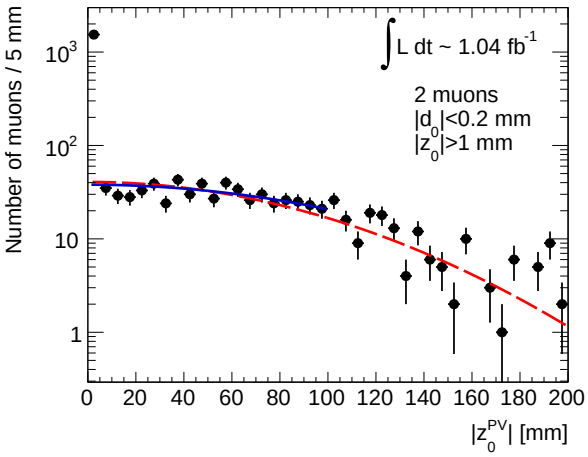

Figure 6.11: Distribution of $|z_0^{\mathrm{PV}}|$ for muons with $|d_0^{\mathrm{PV}}| < 0.2$ mm and $|z_0^{\mathrm{PV}}| > 1$ mm. Two different Gaussian fits are shown.

Table 6.11: Estimation of cosmics at $|z_0^{\mathrm{PV}}| < 1$ mm using method B) described in the text on 1.04 fb^{-1} of data for different control region definitions. Uncertainties are obtained from the errors in the fit parameters.

$T_l = \|z_0^{\mathrm{PV}}\| > 1$ mm	est in $\|z_0^{\mathrm{PV}}\| < 1$ mm
$T_h = \|z_0^{\mathrm{PV}}\| < 100$ mm	5.4 ± 0.4
$T_h = \|z_0^{\mathrm{PV}}\| < 150$ mm	5.1 ± 0.3
$T_h = \|z_0^{\mathrm{PV}}\| < 200$ mm	4.9 ± 0.3

Result

In order to get an estimate of cosmic muons in the signal regions used in the analysis, the additional event selection cuts (e.g. $E_{\mathrm{T}}^{\mathrm{miss}} > 80\,\mathrm{GeV}$ or greater) have to be applied on the cosmic enhanced control sample as well. If the additional cuts are applied, no cosmic muon is observed in the control region any more. An upper limit on the number of cosmic muons in the control region can be set to $N_{\mathrm{muons}}^{\mathrm{CR}} < 1.32$ with 68% C.L.. Performing a Gaussian fit on the $E_{\mathrm{T}}^{\mathrm{miss}}$ distribution of the muons in the control region the contribution of cosmic muons in the signal region with default event selection criteria is estimated as $N_{\mathrm{cosmics}}^{\mathrm{SR}} < 10^{-3}$ before any additional jet cut.

- **Method A** control region($N_{\mathrm{muons}}^{\mathrm{CR}}$)$< 1.32$ at 68% C.L.
  $N_{\mathrm{cosmics}}^{\mathrm{SR}} < 1.32 \cdot \frac{1mm}{95mm} = 0.014$.
- **Method B** cosmic muons at $|z_0^{\mathrm{PV}}| < 1$ mm with $E_{\mathrm{T}}^{\mathrm{miss}} > 100\,\mathrm{GeV}$
  $N_{\mathrm{cosmics}}^{\mathrm{SR}} < 10^{-3}$

6.5.5 Single Top and Di-bosons

Compared to Z/γ^* and $t\bar{t}$, the contributions from di-bosons and single top backgrounds are rather small. In most of the signal regions the contributions are smaller than 5%. Therefore, both single top and di-bosons backgrounds are estimated purely using Monte

Carlo simulation. The Monte Carlo samples used to determine the background contributions in the signal regions are listed in the appendix in Tab. A.2 and Tab. A.4 for single top and di-bosons samples, respectively. The systematic uncertainties are determined by varying the jet energy scale, the jet energy resolution, the electron energy scale, the MS and ID component of the muon tracking, and considering the luminosity and the cross section uncertainties.

Single Top

The main contribution of single top decays to di-lepton final states originates in top production processes with an associated W-boson. As explained in the analysis strategy chapter in Sec. 5.2.1, this process is flavour symmetric and will cancel out after flavour subtraction (cf. Fig. B.1 in the appendix). The predicted numbers of single top events in the flavour subtraction signal regions are given in Tab. 6.12.

Table 6.12: Expected numbers of single-top events in each opposite-sign channel, in the flavour-subtraction signal regions. First error quoted is the systematic uncertainty determined as described in Sec. 6.6. Second error is MC statistics only.

	$e^{\pm}e^{\mp}$	$e^{\pm}\mu^{\mp}$	$\mu^{\pm}\mu^{\mp}$
Exp.MC SR1	12.45±1.80±0.89	40.80±4.64±1.65	36.83±3.84±1.53
Exp.MC SR2	9.89±1.86±0.81	31.52±4.57±1.45	27.36±3.69±1.31
Exp.MC SR3	0.11±0.05±0.11	0.47±0.16±0.16	0.48±0.09±0.17

Di-Bosons

All di-bosons processes (WW, WZ and ZZ) can contribute to the di-lepton final states. The only process which is flavour symmetric and thereby cancel out after FS is the WW decay. WZ and ZZ remain after FS (cf. Fig. B.3 in the appendix.). The predicted numbers of di-bosons events in the flavour subtraction signal regions are given in Tab. 6.13.

Table 6.13: Expected numbers of di-bosons (WW, WZ and ZZ) events in each opposite-sign channel, in the flavour-subtraction signal regions. First error quoted is the systematic uncertainty determined as described in Sec.6.6. Second error is MC statistics only.

	$e^{\pm}e^{\mp}$	$e^{\pm}\mu^{\mp}$	$\mu^{\pm}\mu^{\mp}$
Exp.MC SR1	14.32±1.91±1.79	34.23±4.36±2.76	31.36±3.57±2.43
Exp.MC SR2	7.69±3.11±1.13	11.09±4.79±1.51	14.98±5.10±1.42
Exp.MC SR3	0.54±0.07±0.29	0.04±0.03±0.03	0.67±0.31±0.25

Table 6.14: Additional uncertainties which have to be considered for the JES due to pile-up effects.

	$0< \eta <2.1$	$2.1< \eta <4.5$
$20 < p_{\mathrm{T}} < 50\,\mathrm{GeV}$	5%	7%
$50 < p_{\mathrm{T}} < 100\,\mathrm{GeV}$	2%	3%
$p_{\mathrm{T}} > 100\,\mathrm{GeV}$	no add. uncertainty	

6.6 Evaluation of Systematic Uncertainties

Several sources of systematic uncertainties have to be considered in the analysis. The general systematic uncertainties are discussed below, the flavour subtraction specific systematics which have to be taken in account by the subtraction are described in Sec. 6.8.

6.6.1 Luminosity

The uncertainty on the luminosity is taken to be 3.7% [161].

6.6.2 Cross Section

The uncertainty due to the cross-section is taken to be 5% for most Monte Carlo samples considered - this being consistent with the quoted cross-section uncertainties in Section 6.1.2. The two exceptions to this are: QCD and $t\bar{t}$. For QCD, a cross-section uncertainty of 100% is assigned to account for the expected poor-modelling of fake events in Monte Carlo. An uncertainty of $+6.9\%, -9.5\%$ is assigned on the $t\bar{t}$ cross-section based on [162, 163] ($164.6\ \mathrm{pb}^{+11.4}_{-15.7}$).

6.6.3 Jet Energy Scale (JES)

This is the asymmetric uncertainty due to the scaling of the jet energy *upwards* or *downwards*. The uncertainty due to the JES is evaluated using a software package called `MultijetJESUncertaintyProvider`[164] which gives the uncertainties on the JES as a function of jet p_{T} and η based on the detail study of the jet energy scale and its uncertainty [132] summarized in Sec. 4.3.3. In order to take into account the significant increase of out-of-time pile-up in 2011, a pile-up correction factor has to be applied on the uncertainty provided by the `MultijetJESUncertaintyProvider`. The relative JES-pile-up uncertainties in Tab. 6.14 are derived from the expected difference from data and MC of the jet offset calculated from the mean tower energy in the zero-bias stream [165].

6.6.4 Jet Energy Resolution (JER)

The JER uncertainty is evaluated following the recommendations given in [166]. Each jet is smeared according to a Gaussian distribution, with unit mean, and a width, sigma, given by the p_T (in GeV) dependant resolution function (Eq. (6.18)):

$$0.55\sqrt{\frac{(4.6)^2}{p_T^2} + \frac{0.846^2}{p_T} + 0.064^2} \tag{6.18}$$

The JER uncertainty package provides JER uncertainties up to $p_{\mathrm{T}} = 500\,\mathrm{GeV}$ and $|\eta| = 2.8$. An extra absolute uncertainty of 7% is considered, if the jets is in the region of $|\eta| > 2.8$

6.6.5 Electron Energy Scale and Resolution

This is an asymmetric uncertainty due to the scaling *up* or *down* of the electron energy scale. [157]. The electron energy is smeared using a Gaussian distribution with a p_{T} (in GeV) and η dependent sigma [157]. The function (Eq. (6.19)) is given by:

$$\sqrt{(S(1+\Delta S)\sqrt{E_{cl}})^2 + (C(1+\Delta C)E_{cl})^2 - (S\sqrt{E_{cl}})^2 - (CE_{cl})^2} \tag{6.19}$$

where S and C are the sampling and constant terms, 0.1 and 0.007 respectively. The uncertainty on the sampling term, ΔS, is 0.2, and the uncertainty on the constant term, ΔC, 1% in the barrel and 4% in the end-cap.

6.6.6 Muon Momentum Resolution

The uncertainty of the muon momentum resolution is considered by smearing the track resolution separately in the MS ($\mu_{MS\uparrow\downarrow}$) and in the ID ($\mu_{ID\uparrow\downarrow}$) based on the muon momentum resolution measurements [95] briefly summarized in Sec. 4.2.3. The smearing procedure is provided by the an ATLAS specific software package called `MuonMomentumCorrections` recommended by the *muon combined performance group* [167].

6.6.7 Missing Transverse Momentum

Systematic uncertainties on the reconstructed objects, like jet energy resolution, the jet energy scale or the muon momentum resolution also affect the missing transverse energy calculation. Therefore, the $E_{\mathrm{T}}^{\mathrm{miss}}$-term has to be corrected by the smeared objects in the systematics studies in order to consider the all systematic effects.

6.7 Lepton Reconstruction Efficiency

The differences in the reconstruction and trigger efficiencies for electrons and muons have to be considered in the flavour subtraction, as described in detail in Sec. 5.1. Equation (5.10) uses a simplification of the ratio (β) of the reconstruction (reco) and identification (ID) efficiencies. This section gives an overview of the determination of β in data. The $Z \to \ell\ell$ decays provide clean di-lepton samples, which can be isolated easily from other processes. Differences in the event topology between $Z \to \ell\ell$, $t\bar{t}$ and di-boson events, yield small differences in the reco and ID efficiencies. Therefore, the differences between these processes are studied in Monte-Carlo and considered as additional systematic when applying the flavour subtraction.

6.7.1 Determination of β - Monte Carlo Studies

The reco and ID efficiency is defined as the ratio of reconstructed and identified leptons matched to a true lepton over the sum of all true leptons. Therefore, only the true leptons in the detector acceptance regions of the reconstruction algorithms are taken

Table 6.15: Reconstruction and identification electron ϵ_e and muon ϵ_μ efficiencies and ratio β for several SM processes.

process	ϵ_e	ϵ_μ	β
W+Jets	0.661 ± 0.000	0.897 ± 0.000	0.738 ± 0.001
diBoson	0.689 ± 0.002	0.884 ± 0.002	0.779 ± 0.003
TTbar	0.688 ± 0.002	0.820 ± 0.002	0.839 ± 0.003
Z+Jets	0.667 ± 0.000	0.913 ± 0.000	0.731 ± 0.000

into account. This means true electrons with $p_{\mathrm{T}} > 20\,\mathrm{GeV}$ and $|\eta| < 2.47$ and muons with $p_{\mathrm{T}} > 10\,\mathrm{GeV}$ and $|\eta| < 2.4$.

The electron efficiencies only differ within 1%, but the muon efficiencies show larger differences (c.f. Fig. 6.12). These discrepancies can be explained by the difference in the procedure of the overlap removal for electrons and muons, discussed in Sec. 6.4.1. The muon efficiency is reduced in events with more activity in the detector like $t\bar{t}$ or SUSY events. The differences in the muon efficiencies yield deviations in β. The variation of the β values according to different physics processes have to be taken into account as systematic when applying the flavour subtraction.

6.7.2 Data driven β Determination

The Standard Model process $Z \to l^- l^+$ can be exploited to determine the ratio of the lepton reconstruction and identification efficiencies in data. Therefore a Z-control region with enhanced Standard Model Z decays is defined (cf. Tab. 6.16). On top of the dilepton event selection a missing transverse energy cut ($E_{\mathrm{T}}^{\mathrm{miss}} < 40\,\mathrm{GeV}$) and $\mathrm{m}_{\ell\ell}$-cut around the Z mass peak ($85\,\mathrm{GeV} < \mathrm{m}_{\ell\ell} < 95\,\mathrm{GeV}$) are applied. By dividing the number of e^+e^- by the number of $\mu^+\mu^-$ events, β can be estimated. This ratio has to be corrected for the different trigger efficiencies which have been determined before (cf. Sec. 6.2.3).

$$\beta = \sqrt{\frac{N_{ee}}{N_{\mu\mu}} \cdot \frac{1-(1-\tau_\mu)^2}{1-(1-\tau_e)^2}} \tag{6.20}$$

with the electron trigger efficiency τ_e and the muon trigger efficiency τ_μ respectively.

- Monte Carlo: $\beta = 0.7463 \pm 0.001$

- Data 2011: $\beta = 0.7464 \pm 0.002$

These values are in good agreement. The difference in β for the different Standard Model processes can be taken as systematic uncertainty. $\Delta\beta = 0.042$. The variation of β as a function of p_{T} is shown in Fig. 6.12. It is not possible to consider the p_{T} dependency in the flavour subtraction calculation. Therefore, β is considered as a constant value over the complete p_{T} -range. The systematic error which is induced by this simplification is taken into account as additional systematic uncertainty. The maximal variation of the $\beta(p_{\mathrm{T}})$ in the control region is described as a Gaussian distribution. The width of the Gaussian distribution is taken as systematic uncertainty: $\Delta\beta_{p_T} = 0.05$.

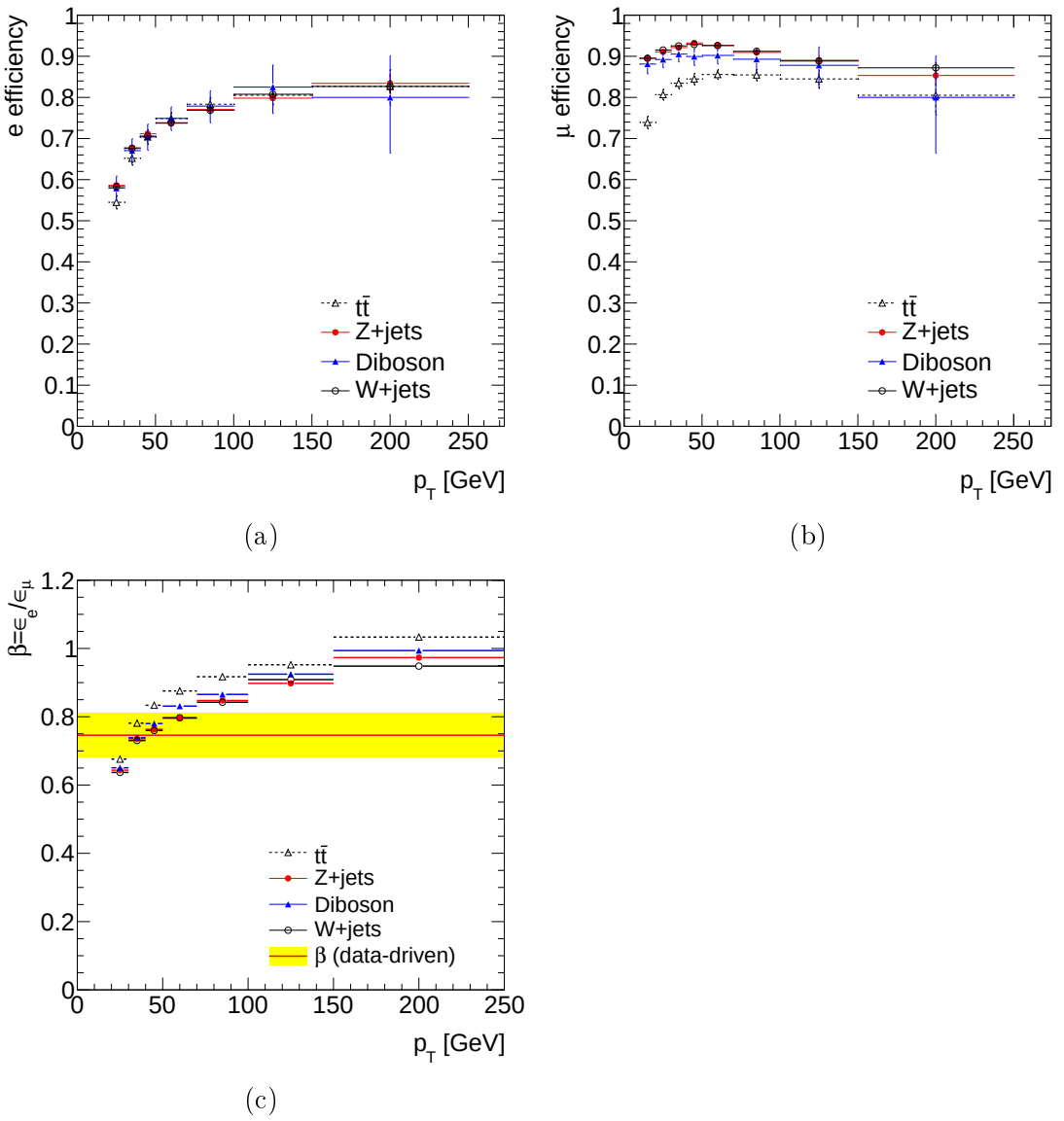

Figure 6.12: Reconstruction and identification efficiencies for electrons (a) and muons (b) and the ratio β (c) for several MC processes. (c) inludes the average β value determined form data and the uncertanity taking into account the variation of $\beta(\mathrm{p}_T)$.

6.8 Results

This section summarises the results of the opposite-sign observations in each of the three flavour channels ($e^{\pm}e^{\mp}$, $e^{\pm}\mu^{\mp}$ and $\mu^{\pm}\mu^{\mp}$) analysed in terms of a flavour subtraction to quantify the *excess* of identical flavour events over those of different-flavour in the data (and make comparisons with the expectation from Monte Carlo). The flavour subtraction methods are described in detail in Sec. 5.1. The results are published in [155] and with more details ATLAS internally in [151]. The results of the flavour subtraction analysis with the ATLAS 2010 datasets only are published in [52].

The observed values in data and the results of the different SM background estimations

Table 6.16: Z control region for data driven β determination for the ee and $\mu\mu$ channel. The contributions to signal regions are quoted with (sys.) and (stat.) uncertainties, data driven fake estimation has statical uncertainties only.

cut	$Z \to ee$ CR mll(85,95)	$Z \to \mu\mu$ CR mll(85,95)
Z+jets	161220.84 ±6253.90 ±271.04	285452.17 ±17486.83 ±341.91
$t\bar{t}$	10.82 ±1.10 ±2.07	17.86 ±3.26 ±2.41
diBoson	176.19 ±8.44 ±3.33	292.12 ±18.37 ±4.01
Drell Yan	0.00 ±0.00 ±0.00	0.00 ±0.00 ±0.00
singleTop	1.80 ±0.41 ±0.39	2.28 ±0.35 ±0.38
SM all	161409.65 ±6261.67 ±271.07	285764.41 ±17506.73 ±341.95
data 2011	168960.00	299466.00

(cf. 6.5) are listed as the number of $e^{\pm}e^{\mp}$ events, $N(e^{\pm}e^{\mp})$, the number of $e^{\pm}\mu^{\mp}$ events, $N(e^{\pm}\mu^{\mp})$, and the number of $\mu^{\pm}\mu^{\mp}$ events, $N(\mu^{\pm}\mu^{\mp})$ in two moderate and one high $E_{\mathrm{T}}^{\mathrm{miss}}$ signal regions (FS-SR1, FS-SR2 and FS-SR3, defined in Sec. 5.2.3) in Tab. 6.17.

The Standard Model background estimations are in good agreement with the measured numbers of events, in each channel and for all signal regions. Therefore, no significant excess has been observed. Figure 6.13 shows the distributions of $e^{\pm}e^{\mp}$, $e^{\pm}\mu^{\mp}$ and $\mu^{\pm}\mu^{\mp}$ for FS-SR1 (a,c,d) and FS-SR2 (b,d,e), respectively. Due to the lack of statistics in the high $E_{\mathrm{T}}^{\mathrm{miss}}$ signal region (FS-SR3), it is not possible to plot meaningful distribution. A small excess (maximum less the 2σ) of data over SM predictions is found around the expected Z-boson invariant mass peak in the $e^{\pm}e^{\mp}$-channel in both regions FS-SR1 (a) and FS-SR2 (b). The deviation can be explained by an underestimation of $E_{\mathrm{T}}^{\mathrm{miss}}$ in Z+jets or di-boson events. The Monte Carlo simulated Z+jets and di-boson events have less missing transverse energy. The study on this effect is summarised in the appendix D.1. Final-state radiation photons from electrons which are pointing to the LAr hole cause extra missing transverse momentum, which is not simulated in MC, nor vetoed in data. Therefore the number of events with medium missing transverse energy is underestimated in MC when comparing with data. The muons are not affected by final-state radiation hence the di-muon $E_{\mathrm{T}}^{\mathrm{miss}}$ distributions for MC are in good agreement with data.

Flavour Subtraction Specific Systematics

Detailed studies of systematics have been done both for Monte Carlo samples and data driven estimates. The results from Monte Carlo based systematic studies are listed in Tab. D.2-D.4 for the three channels ee, $e\mu$ and $\mu\mu$ separately. One takes the biggest contribution of each of the (up/down) variations in $\mathrm{JES}_{\uparrow\downarrow}$, $\mu_{\uparrow\downarrow}$ and $\mathrm{E}_{e\uparrow\downarrow}$ systematic effects for the computation of the total systematic. The systematics which are correlated amongst the different lepton channels, e.g. the jet energy resolution or the jet energy scale, are reduced due to the subtraction method.

When applying the flavour subtraction, the uncertainties of β, τ_e and τ_μ have to be

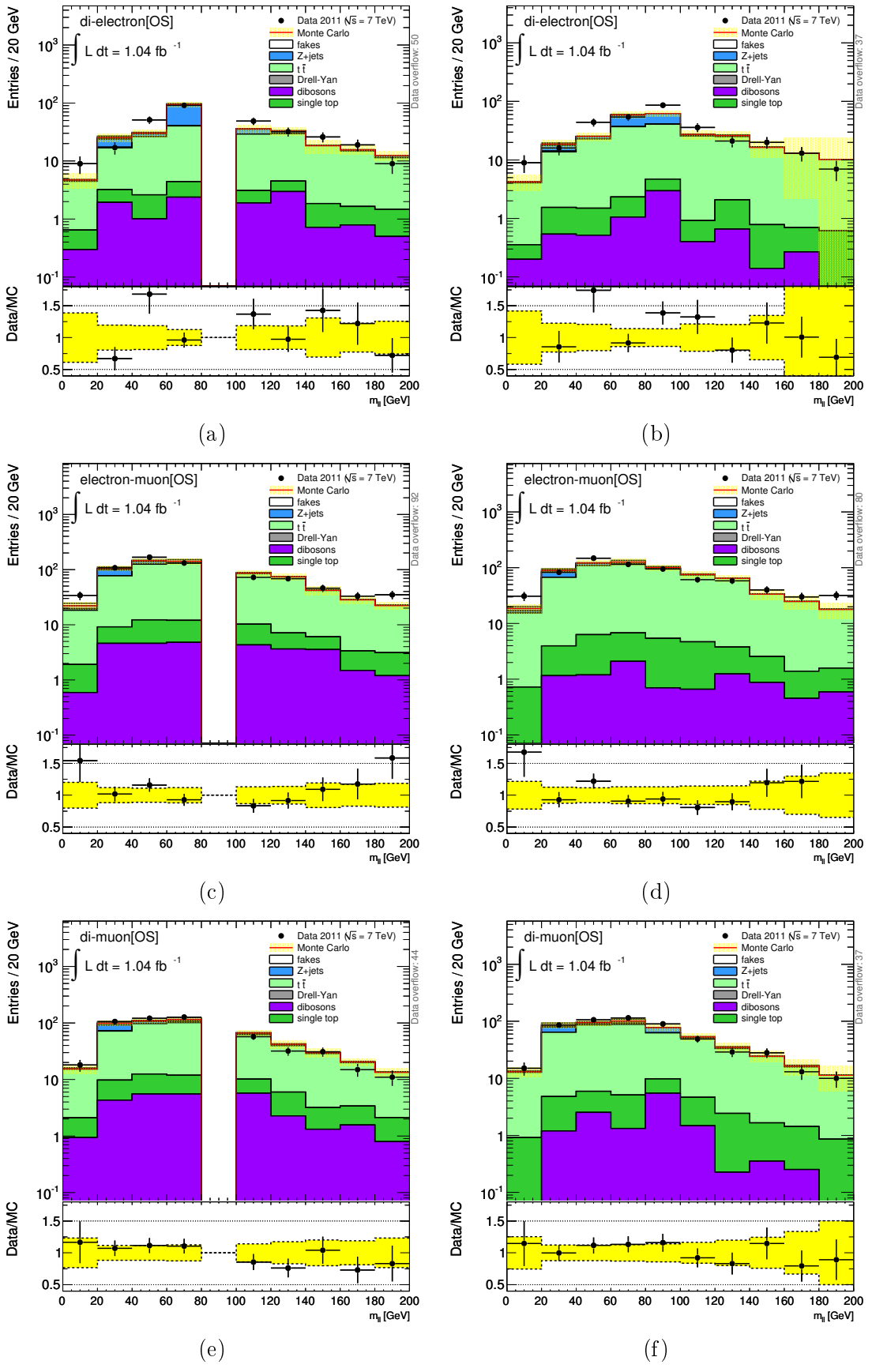

Figure 6.13: Data and Monte Carlo distributions for the three channels OS $e^{\pm}e^{\mp}$, $e^{\pm}mu^{\mp}$ and $\mu^{\pm}\mu^{\mp}$ channels respectively in FS-SR1 (a,c,d) and FS-SR2 (b,d,f)

Table 6.17: The predicted and observed numbers of events in each flavour subtraction signal region. These background contributions are evaluated using the techniques described in Section 6.5. The first and second errors on the SM background events statistical and systematic respectively

OS-FS [FS-SR1]	$e^{\pm}e^{\mp}$	$e^{\pm}\mu^{\mp}$	$\mu^{\pm}\mu^{\mp}$
$t\bar{t}$	198±8±19	581±14±48	418±11±29
Z/γ^*+jets	86±5±5	41±3±6	41±3±11
Fakes	5±2±2	30±6±6	22±6±5
Dibosons	14±2±2	34±3±4	32±2±3
single top	13±1±1	41±2±3	37±2±2
Standard Model	316±10±19	727±16±49	549±14±31
Cosmic rays	$< 10^{-3}$	$< 10^{-3}$	$< 10^{-3}$
Observed	344	750	551
OS-FS [FS-SR2]	$e^{\pm}e^{\mp}$	$e^{\pm}\mu^{\mp}$	$\mu^{\pm}\mu^{\mp}$
$t\bar{t}$	220±9±23	624±15±62	437±12±35
Z/γ^*+jets	46±3±12	29±3±6	38±3±5
Fakes	2±2±1	32±6±8	19±6±6
Dibosons	8±1±3	11±2±5	15±1±5
single top	10±1±2	32±2±4	27±1±3
Standard Model	286±10±26	728±16±63	537±13±36
Cosmic rays	$< 10^{-3}$	$< 10^{-3}$	$< 10^{-3}$
Observed	336	741	567
OS-FS [FS-SR3]	$e^{\pm}e^{\mp}$	$e^{\pm}\mu^{\mp}$	$\mu^{\pm}\mu^{\mp}$
$t\bar{t}$	1.8±0.1±0.5	5.1±0.2±1.4	3.3±0.1±0.9
Z/γ^*+jets	0.01±0.01±0.67	1.03±0.42±0.02	0.81±0.26±0.06
Fakes	0.17±0.19±0.08	0.92±0.96±0.17	-0.08±0.03±0.01
Dibosons	0.54±0.29±0.07	0.04±0.03±0.03	0.67±0.25±0.31
Single-top	0.11±0.11±0.05	0.47±0.16±0.16	0.48±0.17±0.09
Standard Model	2.7±0.4±1.2	7.6±1.1±1.5	5.3±0.4±1.3
Cosmic rays	$< 10^{-3}$	$< 10^{-3}$	$< 10^{-3}$
Observed	2	8	3

considered by the appropriate error propagation expressions:

$$\Delta\mathcal{S}(\Delta\beta) = \left|\left(-\frac{N(e^{\pm}e^{\mp})}{\beta^2(1-(1-\tau_e)^2)} + \frac{N(\mu^{\pm}\mu^{\mp})}{(1-(1-\tau_\mu)^2)}\right)\cdot\Delta\beta\right| \quad (6.21)$$

$$\Delta\mathcal{S}(\Delta\tau_\mu) = \left|\left(\frac{N(e^{\pm}\mu^{\mp})(1-\tau_\mu)}{(1-(1-\tau_e)\cdot(1-\tau_\mu))^2} - 2\cdot\frac{(1-\tau_e)N(e^{\pm}e^{\mp})}{\beta(1-(1-\tau_e)^2)^2}\right)\cdot\Delta\tau_e\right| \quad (6.22)$$

$$\Delta\mathcal{S}(\Delta\tau_\mu) = \left|\left(\frac{N(e^{\pm}\mu^{\mp})(1-\tau_e)}{(1-(1-\tau_e)\cdot(1-\tau_\mu))^2} - 2\cdot\frac{\beta(1-\tau_\mu)N(\mu^{\pm}\mu^{\mp})}{(1-(1-\tau_\mu)^2)^2}\right)\cdot\Delta\tau_\mu\right| \quad (6.23)$$

The systematics on $\mathcal{S}$ after the flavour subtraction are listed in Tab. 6.18 - Tab. 6.20 for the three signal regions. A general description of systematics effects is given in Sec. 6.6 and specific systematics due to flavour subtraction are derived as reported in [151].

Table 6.18: FS-SR1: Number of events and systematics due to scale uncertainties and flavour subtraction.

process	$\mathcal{S}$	$\text{JES}_{\uparrow}$	$\text{JES}_{\downarrow}$	JER	$\text{E}_{e,\uparrow}$	$\text{E}_{e,\downarrow}$	$\mu_{MS,\uparrow}$	$\mu_{MS,\downarrow}$	$\mu_{ID,\uparrow}$	$\mu_{ID,\downarrow}$	scale
TTbar	-0.652	4.298	9.005	3.286	0.371	0.494	1.788	1.300	0.425	2.025	9.971
Z	88.111	0.979	3.805	6.517	2.621	0.055	0.745	0.774	0.319	0.086	6.633
diBoson	8.845	0.137	1.488	0.772	0.109	0.123	0.093	0.421	0.316	0.284	0.846
singleTop	3.699	0.802	0.768	0.069	0.012	0.123	0.342	0.259	0.210	0.332	0.840
DrellYan	1.206	0.065	0.103	0.583	0.000	0.000	0.000	0.000	0.000	0.000	0.586

process	$\mathcal{S}$	$\mathcal{L}_{sys.}$	pdf_{sys}	σ_{sys}	β_{sys}	$\tau_{e,sys}$	$\tau_{\mu,sys}$	scale	tot. sys.	stats.
TTbar	-0.652	-0.024	-0.033	-0.046	0.069	0.002	0.066	9.971	9.972	19.948
Z	88.111	3.260	4.406	4.406	0.098	0.000	0.006	6.633	9.667	9.455
diBoson	8.845	0.327	0.442	0.442	0.006	0.000	0.005	0.846	1.102	4.100
singleTop	3.699	0.137	0.185	0.185	0.015	0.000	0.006	0.840	0.891	2.342
DrellYan	1.206	0.045	0.060	0.060	0.000	0.000	0.000	0.586	0.594	0.546

Table 6.19: FS-SR2: Number of events and systematics due to scale uncertainties and flavour subtraction.

process	$\mathcal{S}$	$\text{JES}_{\uparrow}$	$\text{JES}_{\downarrow}$	JER	$\text{E}_{e,\uparrow}$	$\text{E}_{e,\downarrow}$	$\mu_{MS,\uparrow}$	$\mu_{MS,\downarrow}$	$\mu_{ID,\uparrow}$	$\mu_{ID,\downarrow}$	scale
TTbar	0.823	6.797	2.509	2.105	1.195	1.129	0.302	0.238	0.530	0.550	7.238
Z	70.742	31.139	6.221	7.868	0.800	1.397	0.538	1.291	0.154	0.170	10.078
diBoson	10.533	2.798	2.395	1.765	0.112	0.341	0.297	0.090	0.113	0.028	2.979
singleTop	2.392	0.302	0.390	0.049	0.009	0.222	0.402	0.303	0.165	0.345	0.461
DrellYan	1.206	0.065	0.124	0.604	0.000	0.000	0.000	0.000	0.000	0.000	0.607

process	$\mathcal{S}$	$\mathcal{L}_{sys.}$	pdf_{sys}	σ_{sys}	β_{sys}	$\tau_{e,sys}$	$\tau_{\mu,sys}$	scale	tot. sys.	stats.
TTbar	0.823	0.030	0.041	0.058	0.048	0.002	0.069	7.238	7.239	20.692
Z	70.742	2.617	3.537	3.537	0.048	0.000	0.007	10.078	11.552	7.856
diBoson	10.533	0.390	0.527	0.527	0.001	0.000	0.002	2.979	3.095	2.393
singleTop	2.392	0.088	0.120	0.120	0.010	0.000	0.004	0.461	0.499	2.072
DrellYan	1.206	0.045	0.060	0.060	0.000	0.000	0.000	0.607	0.615	0.546

Table 6.20: FS-SR3: Number of events and systematics due to scale uncertainties and flavour subtraction.

process	$\mathcal{S}$	$\text{JES}_{\uparrow}$	$\text{JES}_{\downarrow}$	JER	$\text{E}_{e,\uparrow}$	$\text{E}_{e,\downarrow}$	$\mu_{MS,\uparrow}$	$\mu_{MS,\downarrow}$	$\mu_{ID,\uparrow}$	$\mu_{ID,\downarrow}$	scale
TTbar	0.267	1.433	0.273	0.008	0.000	0.772	0.265	0.268	0.268	0.237	1.666
Z	-0.448	0.807	0.017	0.017	0.000	0.000	0.000	0.000	0.000	0.000	0.807
diBoson	1.190	0.052	0.220	0.049	0.000	0.011	0.005	0.001	0.001	0.005	0.071
singleTop	0.037	0.148	0.055	0.060	0.000	0.000	0.000	0.036	0.036	0.000	0.159
DrellYan	0.000	0.000	0.000	0.000	0.000	0.000	0.000	0.000	0.000	0.000	0.000

process	$\mathcal{S}$	$\mathcal{L}_{sys.}$	pdf_{sys}	σ_{sys}	β_{sys}	$\tau_{e,sys}$	$\tau_{\mu,sys}$	scale	tot. sys.	stats.
TTbar	0.267	0.010	0.013	0.019	0.001	0.000	0.000	1.666	1.666	2.014
Z	-0.448	-0.017	-0.022	-0.022	0.001	0.000	0.000	0.807	0.808	0.738
diBoson	1.190	0.044	0.060	0.060	0.000	0.000	0.000	0.071	0.119	0.431
singleTop	0.037	0.001	0.002	0.002	0.000	0.000	0.000	0.159	0.159	0.257
DrellYan	0.000	0.000	0.000	0.000	0.000	0.000	0.000	0.000	0.000	0.000

Table 6.21: Number of measured and estimated events per channel and Signal Region and calculated $\mathcal{S}$. The quoted errors are systematic and statistics for Monte Carlo predictions and systematic due to β and $\tau_{e,\mu}$ for $\mathcal{S}$ calculated from data.

SR	measured	$N(e^{\pm}e^{\mp})$	$N(e^{\pm}\mu^{\mp})$	$N(\mu^{\pm}\mu^{\mp})$
FS-SR1	Monte-Carlo-Only	300.24 ± 19.33 ± 10.46	696.63 ± 48.58 ± 15.05	523.90 ± 29.88 ± 12.28
	Partially data-driven	316.31 ± 20.24 ± 10.09	726.82 ± 44.69 ± 16.24	549.31 ± 30.94 ± 13.56
	data	344	750	551
FS-SR2	Monte-Carlo-Only	288.95 ± 33.03 ± 10.04	696.03 ± 62.56 ± 15.13	522.60 ± 36.48 ± 12.50
	Partially data-driven	285.62 ± 25.42 ± 9.60	728.33 ± 60.36 ± 16.39	537.34 ± 35.30 ± 13.41
	data	336	741	567
FS-SR3	Monte-Carlo-Only	4.62 ± 1.02 ± 1.17	2.90 ± 1.80 ± 1.10	6.32 ± 1.31 ± 1.38
	Partially data-driven	3.31 ± 1.06 ± 0.44	9.32 ± 2.31 ± 1.21	6.87 ± 1.49 ± 0.50
	data	2	8	3

SR	measured	$\mathcal{S}$
FS-SR1	Monte-Carlo-Only	85.70 ± 14.00 ± 22.37
	Partially data-driven	118.7 ± 13.1 ± 23.6
	data	131.6 ± 2.5 (β) ± 0.4 (τ)
FS-SR2	Monte-Carlo-Only	101.21 ± 13.97± 22.58
	Partially data-driven	67.1 ± 16.7 ± 23.2
	data	142.2 ± 0.9 (β) ± 0.4 (τ)
FS-SR3	Monte-Carlo-Only	1.05 ± 1.86 ± 2.20
	Partially data-driven	0.7 ± 1.1 ± 1.1
	data	-3.1 ± 0.00 (β) ± 0.00 (τ)

Flavour Subtraction Results

The mean values of $\mathcal{S}$ after the flavour subtraction are calculated for data ($\mathcal{S}_{obs}$) and Monte-Carlo and data-driven estimates ($\bar{\mathcal{S}}_b$) by the number of events in each flavour channels for the different signal regions (cf. 6.17). The systematics are derived by taking into account all systematic effects described in the precious section (cf Sec. 6.8).

In the presence of only the standard model, the mean value of $\mathcal{S}$, $\bar{\mathcal{S}}_b$, from selected identical-flavour and different-flavour events will be small, but non-zero. The asymmetry in the two flavour samples arising mainly from the Z/γ^*+jets contribution remaining after the E_T^{miss} cuts.

Observation of $\mathcal{S}$ in Data

The observed number of events in the $e^{\pm}e^{\mp}$, $e^{\pm}\mu^{\mp}$ and $\mu^{\pm}\mu^{\mp}$ channels for the three signal regions are listed in Tab. 6.21, together with the calculated $\mathcal{S}_{obs}$. $\mathcal{S}_{obs}$ is calculated according to Eq. (5.10), considering β and $\tau_{e,\mu}$. The uncertainties on $\mathcal{S}_{obs}$ are quoted separately for β and $\tau_{e,\mu}$.

While $\mathcal{S}_{obs}$ in FS-SR 3 is in agreement with zero, the values of $\mathcal{S}$ in the signal regions FS-SR1 and FS-SR2 have a clear same-flavour excess. This excess is mainly caused by remaining $Z \to \ell\ell$ events, which have not been suppressed completely by the selection cuts in these signal regions. Both, the results measured in data and the MC predictions show the same-flavour excess. In addition, there is a discrepancy between data and MC. The $\mathcal{S}$ value determined in data is larger than the MC and the partially data-driven estimations. Figure. 6.15 shows the $\mathcal{S}_{obs}$ distributions of FS-SR1 and FS-SR2 as function of the invariant mass of the two leptons. The excess is located in the bins around the invariant mass peak of the Z-boson. The distributions in Fig 6.13(a) and (b) point out, that the discrepancy between MC and data is dominated by the di-electron channel.

An additional study found, that the $E_{\mathrm{T}}^{\mathrm{miss}}$ is underestimated in MC in $Z \to ee$ events as described in the appendix D.1. Even though, the $\mathcal{S}_{obs}$ distribution still contains SM background contributions in $m_{\ell\ell} < 120\,\mathrm{GeV}$, $\mathcal{S}_{obs}$ is in good agreement with zero above $m_{\ell\ell} \sim 120\,\mathrm{GeV}$. SUSY models which would predict invariant mass edges above, can be excluded with this study.

Monte-Carlo-Only Estimates of $\bar{\mathcal{S}}_b$

The number of $N(e^{\pm}e^{\mp})$, $N(e^{\pm}\mu^{\mp})$, and $N(\mu^{\pm}\mu^{\mp})$ events predicted by Monte Carlo simulation only are summarised in Tab. 6.21. The number of events with electrons in the final states in FS-SR1 and FS-SR2 are slightly underestimated according to the underestimation of $E_{\mathrm{T}}^{\mathrm{miss}}$ as explained in Sec. 6.4.2. The $\mathcal{S}_b$ values in FS-SR1 and FS-SR2 determined by Monte Carlo predictions only are below the measured values $\mathcal{S}_{obs}$, but the discrepancies are still within the systematic and statistical uncertainties. $\mathcal{S}_{obs}$ in FS-SR3 is below the expected value, but in agreement considering the systematic and statistical uncertainties.

Partially Data-Driven Estimate of $\bar{\mathcal{S}}_b$

As described in Sec. 6.5 depending on the signal region, some SM backgrounds cannot be estimated by data-driven techniques. The SM estimations from $t\bar{t}$, di-bosons, and single top rely on MC in FS-SR1 and FS-SR2. For FS-SR3 a data-driven $t\bar{t}$ estimation is available, therefore FS-SR3 only relies on MC expectations for di-bosons and single top backgrounds.

The estimated values of $N(e^{\pm}e^{\mp})$, $N(e^{\pm}\mu^{\mp})$, and $N(\mu^{\pm}\mu^{\mp})$ and the determined values of $\mathcal{S}_b$ are given in Tab. 6.21 for the three signal regions. However the contributions from Z+jets are determined in a CR in data, the transfer factor used to estimated the number of events in the signal region is also affected by the Monte Carlo $E_{\mathrm{T}}^{\mathrm{miss}}$ underestimation, leading to a underestimation of $N(e^{\pm}e^{\mp})$, $N(e^{\pm}\mu^{\mp})$ in FS-SR1 and FS-SR2.

The results from the partially data-driven estimate of $\mathcal{S}_b$ are used as input (mean) values for the toy experiments performed in order to model the shape of $\mathcal{S}$ and to extract exclusion limits for SUSY events with same-flavour excess, described in Ch. 7.

Flavour Subtraction Distributions

The invariant mass distributions from data in $e^{\pm}e^{\mp}$, $e{\pm}\mu^{\mp}$ and $\mu{\pm}\mu^{\mp}$ channels are in good agreement with the distributions generated by Monte Carlo generators (Fig. 6.13(a-f)). The tight $E_{\mathrm{T}}^{\mathrm{miss}}$ cut in FS-SR3 reduces the number of events significantly. A detailed event list of the SUSY candidates found in FS-SR3 is given in the appendix in Tab. D.1. Event displays of a subset of the FS-SR3 SUSY candidates are shown in Fig. D.2 and Fig. D.3 in the appendix.

Due to the very low statistics in this signal region only distributions from FS-SR1 and FS-SR2 are shown in the following. Both signal regions still contain Standard Model processes. $t\bar{t}$ is expected to give the main contribution due to the higher missing transverse energy of the undetected neutrinos. The flavour subtraction analysis is designed to suppress $t\bar{t}$ by subtracting the opposite-sign different-flavour contribution from opposite-sign same-flavour contribution. Other backgrounds like Z are irreducible by flavour subtraction.

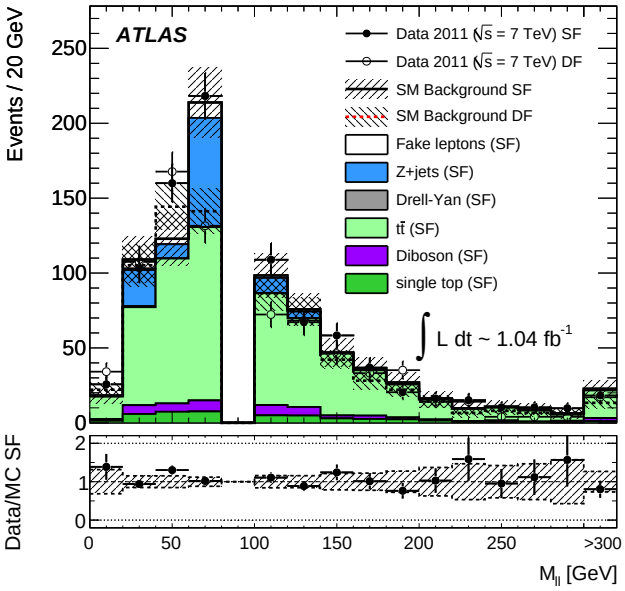

(a)

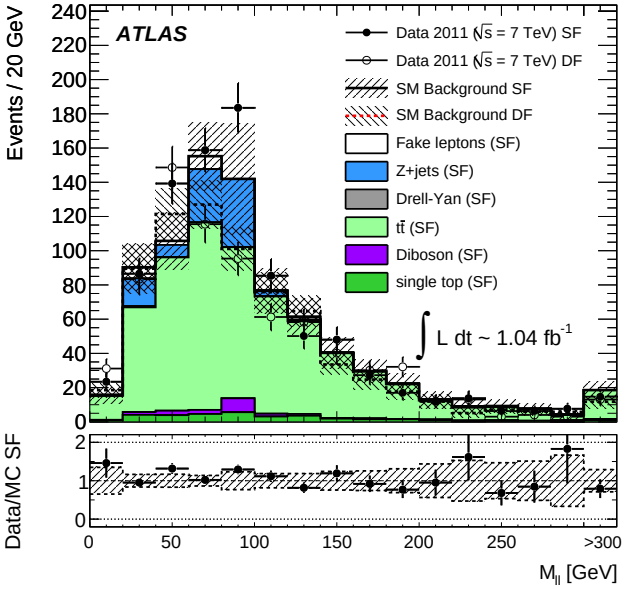

(b)

Figure 6.14: Distributions of the invariant mass in data and the SM for same-flavour (SF) dilepton events with $E_{\mathrm{T}}^{\mathrm{miss}} > 80\,\mathrm{GeV}$ after a Z-veto (FS-SR1) (a) and 2-jet requirement (FS-SR2) (b). The different-flavour (DF) dilepton data events are illustrated as open cirles (data) the SM contribution is summed over DF dashed red line with systematic and statical error (shaded area with lines from top left to bottom right). Errors on data points are statistical, while the error bands on the SM predictions represent the statistical, cross section and luminosity uncertainties, and jet energy scale and resolution uncertainties.

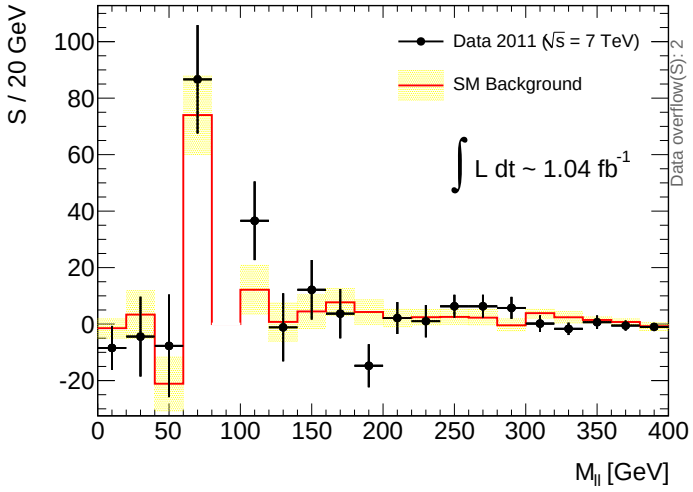

(a)

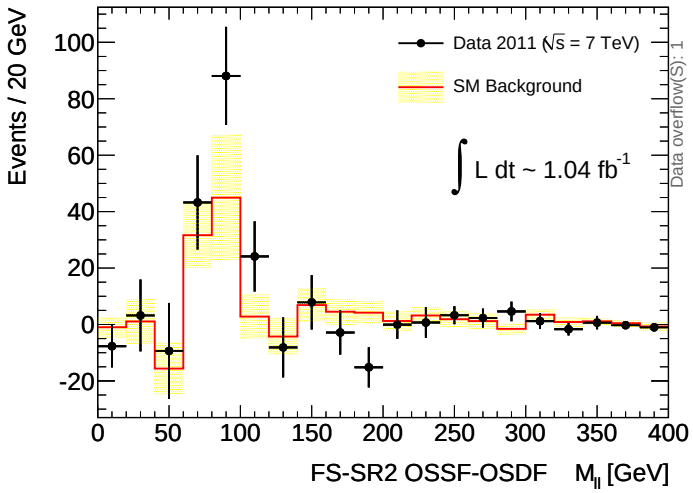

(b)

Figure 6.15: Data and Monte Carlo distributions after flavour subtraction for signal regions FS-SR1 (a) FS-SR2 (b). Both signal regions show good agreement between Monte Carlo-only expectation and data if $m_{\ell\ell} > 120\,\text{GeV}$. The deviation in $m_{\ell\ell} = 190\,\text{GeV}$ is due to a small underestimation of OF and a small overestimation of SF, which leads to a bigger discrepancy after subtraction. Around the Z-boson mass ($60\,\text{GeV} < m_{\ell\ell} < 120\,\text{GeV}$) two effects can be seen. The distributions for both SM prediction and data, are not zero after the subtraction. The contribution in SM prediction originates in $Z \to \ell\ell$ decays, which are not completely suppressed after flavour subtraction. In addition, a deviation between SM and data, can be seen in the same $m_{\ell\ell}$-range.

Figure 6.14 shows the weighted different-flavour (DF) and same-flavour(SF) components of the simplified flavour subtraction formula (5.10), considering all correction factors and systematics of the flavour subtraction procedure:

$$\mathcal{S} = \underbrace{\frac{N(e^{\pm}e^{\mp})}{\beta(1-(1-\tau_e)^2)} + \frac{\beta N(\mu^{\pm}\mu^{\mp})}{(1-(1-\tau_\mu)^2)}}_{same\ flavour\ (SF)} - \underbrace{\frac{N(e^{\pm}\mu^{\mp})}{1-(1-\tau_e)(1-\tau_\mu)}}_{different\ flavour\ (DF)} \tag{6.24}$$

$$\mathcal{S} = SF - DF. \tag{6.25}$$

Histogram (a) shows the $m_{\ell\ell}$distributions for SF and DF selections in FS-SR 1 and histogram (b) for FS-SR2. Both plots show the data distributions of SF (filled black circles) and DF (open cirles) and the Standard Model background contributions from Monte-Carlo and the data estimated *Fakes* summed over SF black line with systematic and statical error (shaded area with lines from bottom left to top right) and summed over DF dashed red line with systematic and statical error (shaded area with lines from top left to bottom right). In addition, the SF distribution is shown in different colours for each background contribution. The ratio plots below the distributions show the ratio of SF data over SF Monte-Carlo.

Apart from the deviations around the $m_{\ell\ell}$value of the Z peak, the data and Monte-Carlo distributions are in good agreement. Especially in the regions dominated by $t\bar{t}$-events. There the flavour subtraction suppresses the background, as expected. The Z contribution is slightly underestimated in the $Z \to ee$ Monte-Carlo samples. The FS-SR1 and FS-SR2 signal regions are defined in order to evaluate the same-flavour excess bin by bin. Therefore, the remaining asymmetric $Z \to ee$ events have to be suppressed more efficiently in the next analysis.

After applying all weights, as simplified in Eq. (6.25), the DF distribution can be subtracted from the SF distribution. The resulting histograms are plotted in Fig. 6.15. The data points are shown in black, the SM background is shown as red line, while the systematic and statistical error are illustrated as yellow uncertainty band. The irreducible $Z \to \ell\ell$ background is not completely suppressed in the bins near the Z-peak. No flavour excess in higher $m_{\ell\ell}$regions have been found.

The analysis set-up described in Ch. 5 has been designed for the measurement and fitting of invariant mass edges if a $m_{\ell\ell}$-excess would have been found. In the following, this exclusive event selection is used for the interpretation and limit setting, in order to extract maximum information from these results.

7 Interpretation

The flavour subtraction (FS) method has several advantageous features: it suppresses flavour symmetric backgrounds like $t\bar{t}$, reduces systematics, and suppresses combinatorial background from possible SUSY background events, allowing precise mass measurements. Nevertheless, the subtraction procedure also introduces some disadvantages: subtracting possible SUSY contributions reduces the sensitivity to new physics, such that the FS is not optimal for limit setting techniques. The distribution of $\mathcal{S}$ after the FS is centred around zero in the case that no flavour excess is present - as expected for example in fully leptonic $t\bar{t}$ decays. It is not possible to construct a test statistic suitable for a profile likelihood method allowing the computation of a p-value for distributions with negative entries. Therefore, the p-value determined from $\mathcal{S}$ after FS is extracted by means of toy experiments.

The toys are created for each process by taking either Monte Carlo or data-driven predictions, depending on the (background) process and the signal region. An uncertainty in the mean value for each process/channel ($e^{\pm}e^{\mp}$, $e^{\pm}\mu^{\mp}$ and $\mu^{\pm}\mu^{\mp}$) is considered, taking into account statistical and systematic uncertainties. Correlations of the systematics in the different di-lepton channels are respected by sharing the same random numbers. The processes with the smeared uncertainties are combined per channel. Toy experiments are produced for each channel following Poisson distributions. The pseudo-data ($e^{\pm}e^{\mp}$, $e^{\pm}\mu^{\mp}$ and $\mu^{\pm}\mu^{\mp}$) distributions are flavour subtracted, as described in Sec. 5.1 considering the uncertainties on β and the trigger efficiencies. This gives the toy distribution of $\mathcal{S}$ which is compared to the results measured in data $\mathcal{S}_{obs}$.

The consistency of the observation, $\mathcal{S}_{obs}$, with the toy result can be computed as the percentage of the distribution of the pseudo-experiments $\mathcal{S}$ exceeding the observed value $\mathcal{S}_{obs}$ (cf. Fig. 7.1). Pseudo-experiments are also used to set a limit on the contribution to $\mathcal{S}$ from new physics, $\bar{\mathcal{S}}_s$ and exclude regions of the parameter spaces of different supersymmetric frameworks.

7.1 Standard Model - Toy Experiments

The toy experiments are based on the data-driven estimates where available; otherwise, Monte-Carlo predictions are used. As discussed in Sec. 6.8, all backgrounds are determined by data-driven methods except $t\bar{t}$, single top, and di-bosons for FS-SR1 and FS-SR2 and single top and di-bosons for FS-SR3. The toy experiments are performed for each of the three flavour channels separately. The predicted mean value of the MC and data-driven background estimation $\bar{\mathcal{S}}_b$ is obtained from the FS (cf. Sec 6.8). The shape is modelled by the toy experiments.

For each toy experiment the number of observed standard model events in the $e^{\pm}e^{\mp}$, $e^{\pm}\mu^{\mp}$ and $\mu^{\pm}\mu^{\mp}$ channels are taken as three random numbers drawn from three Poisson distributions. The means of these three Poisson distributions are denoted as: $\lambda_{b,e^{\pm}e^{\mp}}$, $\lambda_{b,e^{\pm}\mu^{\mp}}$ and $\lambda_{b,\mu^{\pm}\mu^{\mp}}$. These λ_b are not trivially set to equal the respective N_b (the predicted number of background events in each channel). They are instead set to equal the

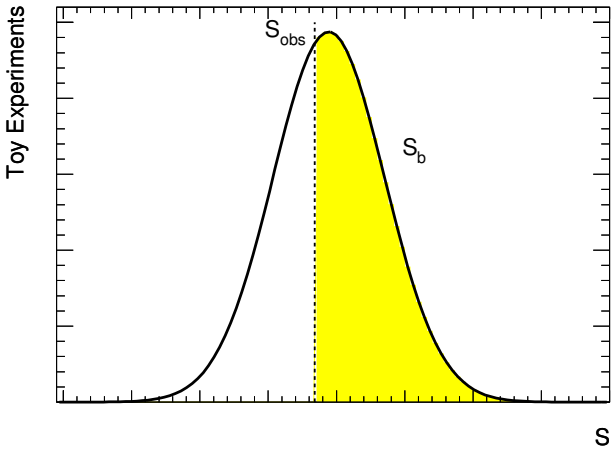

Figure 7.1: A Consistency check of the observation with the SM can be computed as the percentage of Standard Model background only pseudo-experiments recording values of $\mathcal{S}$ greater than the observation, $\mathcal{S}_{obs}$ (yellow filled area).

N_b modified by the application of successive Gaussian random numbers to account for each systematic uncertainty. The statistical uncertainty is considered by drawing the toy experiments using Poisson distributions. The λ_b and N_b are decomposed into the various background contributions, $\lambda_{b,j}$ and $N_{b,j}$ for each background j. The appropriate $\lambda_{b,j}$ for each background are obtained by multiplying each $N_{b,j}$ by a series of random numbers drawn from various Gaussian distributions. For each systematic and statistical uncertainty, one random number is drawn. In the case of correlated systematics between different backgrounds or channels, a single random number is drawn which is then appropriately scaled before application to each individual channel or background estimate. The $\lambda_{b,j}$ are then summed to provide λ_b in each channel. The correction factors β, τ_e, and τ_μ are considered when subtracting the $N_{e\mu}$ toys from the N_{ee} and $N_{\mu\mu}$ toys as described in Eq.(5.10).

The distributions of expected $\mathcal{S}$ from one-million signal-free pseudo-experiments for each signal region are given in Fig. 7.2. The RMS of the pseudo-experiments and the compatibility of the $\mathcal{S}$ distribution from the pseudo-experiments with SM-only hypothesis are given for the three signal regions in Tab. 7.1. The observed $\mathcal{S}$ in data, $\mathcal{S}_{obs}$, is calculated using the measured values of τ_e, τ_μ and β. The Monte Carlo predictions for the number of events in each channel in each FS signal region, and the data-driven estimates, are used separately to determine the expected mean value of $\mathcal{S}$ from standard model events alone ($\bar{\mathcal{S}}_b$). The systematic and statistical uncertainties on the mean $\bar{\mathcal{S}}_b$ are considerably smaller than the width of the distribution of $\mathcal{S}$ values from the standard model alone. The number of pseudo-experiments with $\mathcal{S} > \mathcal{S}_{obs}$ are 39%, 6.8% and 79% for FS-SR1, FS-SR2 and FS-SR3 respectively (cf. Tab. 7.1 right column).

In both signal regions with low $E_{\mathrm{T}}^{\mathrm{miss}}$ cut (FS-SR1 and FS-SR2) the expected value of $\mathcal{S}$ is not centred around zero (cf. Fig. 7.2). The shift to larger values for $\mathcal{S}_b$ is caused by the remaining Z+jets and di-bosons contribution (cf. total number of $\mathcal{S}$ per process in the first column of Tab. 6.18 and Tab. 6.19) which is not completely suppressed by the selection cuts. The nature of the flavour asymmetry of Z+jets and di-bosons processes leads to a shift of $\mathcal{S}_b$ towards positive values. The small discrepancy between

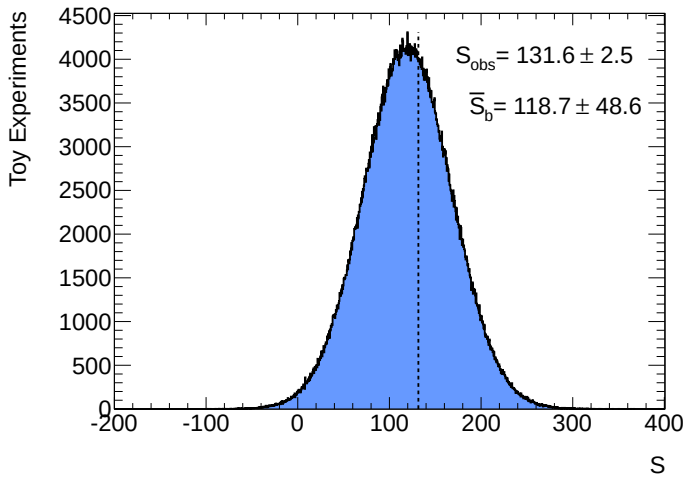

(a)

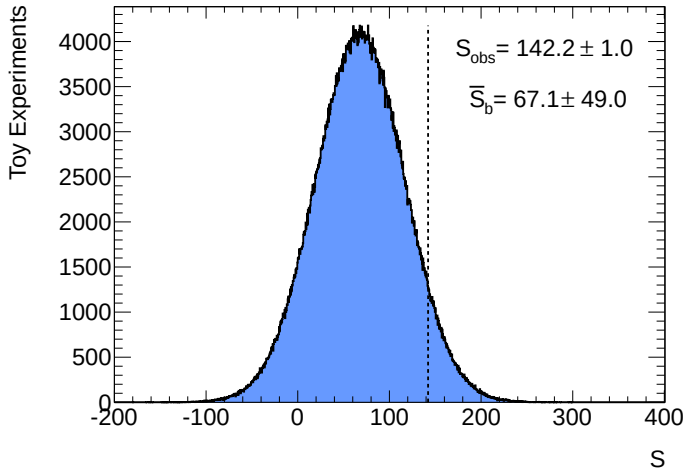

(b)

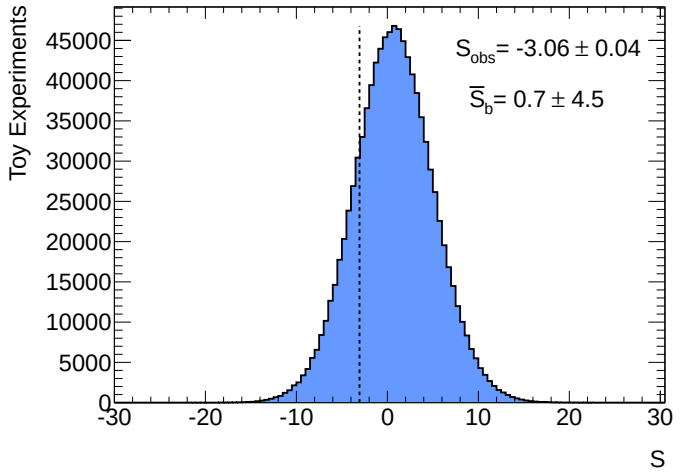

(c)

Figure 7.2: $\mathcal{S}$ distribution of the toy experiments for the signal regions FS-SR1 (a), FS-SR2 (b), and FS-SR3 (c), respectively. $\mathcal{S}_{obs}$ the flavour excess determined from data is marked as dashed black line in the plot. $\bar{\mathcal{S}}_b$ is the mean value of the toy distribution with error given by the root-mean-squared.

Table 7.1: The observed values of $\mathcal{S}$ ($\mathcal{S}_{obs}$), background-only mean and root-mean-squared (RMS) of the distributions of the expected $\mathcal{S}_b$ from one million hypothetical signal-free pseudo-experiments. The quoted errors on $\bar{\mathcal{S}}_b$ are the statistical (from limited MC statistics) and systematic error, respectively. Consistency of the observation with the SM (right column), computed as the fraction of signal-free pseudo-experiments with values of $\mathcal{S}$ larger than the observation, $\mathcal{S}_{obs}$. The systematic error on $\mathcal{S}_{obs}$ in FS-SR3, arising from uncertainties in the trigger and reconstruction efficiencies, is negligible.

	$\mathcal{S}_{obs}$	$\bar{\mathcal{S}}_b$	RMS	$\mathcal{S} > \mathcal{S}_{obs}$ (%)
FS-SR1	131.6±2.5(sys)	118.7±23.6±13.1	48.6	39
FS-SR2	142.2±1.0(sys)	67.1±23.2±16.7	49.0	6.8
FS-SR3	-3.06±0.04(sys)	0.7±1.1±1.1	4.5	79

the observed ($\mathcal{S}_{obs}$) and the expected ($\mathcal{S}_b$) mean value of the $\mathcal{S}$ distributions (numbers are given in Tab. 7.1) is caused by the underestimation of the medium $E_{\mathrm{T}}^{\mathrm{miss}}$-region ($60\,\mathrm{GeV} < E_{\mathrm{T}}^{\mathrm{miss}} < 110\,\mathrm{GeV}$) in $Z \to ee$ events in Monte Carlo.

The MC predictions underestimate the number of $Z \to ee$ events in FS-SR1 in the $\mathrm{m}_{\ell\ell}$ bin [40-60] GeVand in FS-SR2 in the $\mathrm{m}_{\ell\ell}$ bins [40-60] GeV and $\mathrm{m}_{\ell\ell}$ bins [80-100] GeV (cf. Fig 6.13(a) and (b)). The study of a sources of additional $E_{\mathrm{T}}^{\mathrm{miss}}$ contributions summarised in appendix D.1, shows that the $E_{\mathrm{T}}^{\mathrm{miss}}$ in 5% of the events with medium $E_{\mathrm{T}}^{\mathrm{miss}}$ are underestimated due to radiated photons which are not reconstructed because they are pointing to the LAr hole (cf. Sec. 6.4.1). This contributes to the discrepancy discussed above. The invariant mass cut in FS-SR1 suppresses the $Z \to \ell\ell$ contribution slightly more effective than the requirement of having at least 2 jets in the event. Therefore, the discrepancy is bigger in FS-SR2 ($\sim 1.5\sigma$).

The expected number of events in FS-SR3, $\mathcal{S}_b = 0.7 \pm 1.1(stat) \pm 1.1(syst)$, is in good agreement with $\mathcal{S} = 0$ (no same-flavour excess). The tight $E_{\mathrm{T}}^{\mathrm{miss}}$ cut completely suppresses the $Z \to \ell\ell$ contribution. The negative observed value $\mathcal{S}_b = -3.06 \pm 0.04\,(syst)$ is in reasonable agreement with the expectation considering the statistic and systematic uncertainty. This suggests that the observed $\mathcal{S}_{obs}$ in data is consistent with the SM. Exclusion limits can thus be set on $\bar{\mathcal{S}}_s$ in FS-SR3 and regions of the parameter spaces of several supersymmetric models can be analysed.

7.2 Model-Independent Limits

The model-independent limits are calculated based on the p-values extracted from the $\mathcal{S}$-variable of toy distributions. The results are published in [152].

The pseudo-experiments can be modified to include new physics processes as follows. In addition to the λ_b, λ_s can be introduced to give the mean contributions to each flavour channel from new physics. λ_s can be sampled from the N_s predicted by Monte Carlo, to exclude regions of a particular physics scenario. The N_s are subjected to uncertainties on luminosity, parton distribution function and scale uncertainties, jet-energy-scale and statistical uncertainties arising from limited Monte Carlo statistics. Correlations between the N_b and N_s are taken into account using the shared single random number approach described for the signal-free experiment case. The total numbers of events in each channel are therefore drawn from three Poisson distributions for the background, and three

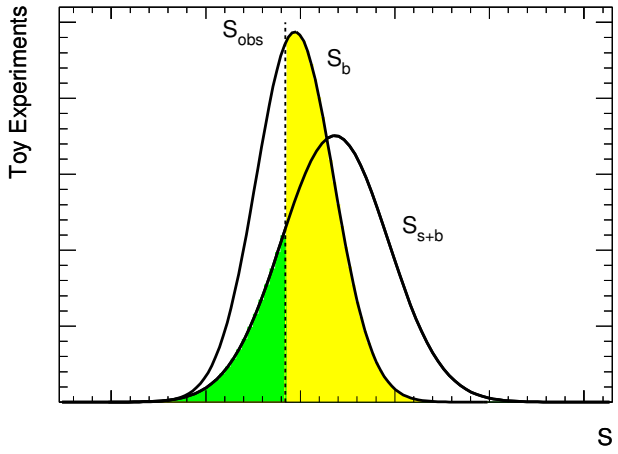

Figure 7.3: If the fraction of $\mathcal{S}_{s+b}$ of the probability to find a value smaller than the observed $\mathcal{S}_{obs}$ is smaller than 5%, the point with the tested hypotheses is excluded at 95% CL (green filled area).

Poisson distributions for the signal. The expected numbers of events are combined per channel and $\mathcal{S}_{s+b}$ is calculated by using the FS considering β, τ_e, and τ_μ.

In order to determine model-independent limits, $\bar{\mathcal{S}}_s$ is found by increasing the λ_s value iteratively, until only 5% of pseudo-experiments predict $\mathcal{S}_{s+b} < \mathcal{S}_{obs}$ (cf. Fig. 7.3). In a new physics scenario for which the N_s are used to give the λ_s, the percentage of experiments with $\mathcal{S}_{s+b} < \mathcal{S}_{obs}$ gives the probability of the signal and background hypothesis (the signal hypothesis) being falsely rejected. If this probability is $< 5\%$, the scenario is excluded at 95% confidence level (CL).

Limits on Scenarios without Combinatorial SUSY Background Events

Table 7.2 shows the minimum number of same-flavour (excess) events from any SUSY scenario $\bar{\mathcal{S}}_s$ which would be excluded at 95% confidence with data-driven and Monte Carlo SM background estimation, respectively. The analysis based on the data-driven SM background estimation excludes SUSY scenarios at 95% CL which would expect a same-flavour excess $\bar{\mathcal{S}}_s$ of at last 102.0, 138.0 or 4.5 events in the signal regions FS-SR1, FS-SR2 and FS-SR3, respectively. These limits are calculated under the assumption that a given SUSY scenario does not have any contribution from SUSY events with di-lepton final states, originating in the different decay chain (cf. Fig. 5.4(b)).

Limits on SUSY Scenarios Considering Combinatorial SUSY Background

The strength of the limit setting procedure depends not just on the same-flavour excess, but also on the number of events in each of the three channels. The greater the number of events in each channel, the wider the $\mathcal{S}$ distribution, and hence the weaker the limit. The best limit on supersymmmetry is found for scenarios which produce no combinatorial SUSY background from different decay chains ($\ell\ell'$ where ℓ' marks that the second lepton flavour is not correlated with the flavour of the first lepton).

This calculation assumes that SUSY events only contribute to the same-flavour di-lepton distributions from decay chains like $\tilde{\chi}_2^0 \to \ell^\pm\ell^\mp\tilde{\chi}_1^0$ ($\ell\ell$). The possibility of having

Table 7.2: The observed model-independent limits are given on the SUSY same-flavour excess $\bar{\mathcal{S}}_s$. The limits are determined considering the data-driven and the purely MC based background estimations, separately. The excess of same-flavour events is multiplied by detector acceptances and efficiencies in each signal region.

	Limit $\bar{\mathcal{S}}_s$ (95% CL)	
	partially Data-Driven	Monte Carlo only
FS-SR1	94	102.0
FS-SR2	158	138.0
FS-SR3	4.5	2.6

uncorrelated same-flavour and opposite-flavour is considered by varying the relative fraction of same-flavour and opposite-flavour contribution to the SUSY mean values, $\mathcal{S}_s$. The FS-SR3 is used for this study, since it provides the most stringent limits. The resulting values for $\bar{\mathcal{S}}_s$ are listed in Tab. 7.3. As shown in Fig. 7.4 the increasing contribution from combinatorial SUSY di-lepton background (0%, 50%, and 100%) yield a broader $\mathcal{S}_s$ distribution. Therefore, models with increasing combinatorial SUSY background require larger values of $\bar{\mathcal{S}}_s$ for an exclusion at 95% CL.

Considering combinatorial SUSY background contributions, models with a ratio of di-leptons from different decay chains over di-leptons from same decay chains of $BR(\ell\ell')/BR(\ell\ell) = 50\%$ ($BR(\ell\ell')/BR(\ell\ell) = 100\%$) can be excluded at 95% CL if $\mathcal{S}_s$ is expected to be 5.5 (6.7) or larger in FS-SR3.

Table 7.3: Observed limits on $\mathcal{S}_s$ obtained for FS-SR3, with different fractions of uncorrelated supersymmetry contributions to the same and different-flavour channels, using both the data-driven and the purely Monte Carlo estimates of the contributions in each channel from SM background.

$BR(\ell\ell')/BR(\ell\ell)$ (%)	partially Data-Driven	Monte Carlo only
0	4.5	2.6
50	5.5	3.5
100	6.7	3.9

7.3 Model-Dependent Limits

In addition to the model-independent limits, studies in a 2-dimensional plane of the SUSY parameter space (grid) of different SUSY models (cf. Sec. 7.3.3 - 5.2.2) have been performed. The $\mathcal{S}_{s+b}$ value is calculated for each point of a given grid, considering the expected SUSY and the SM background contributions. If the integral of $\mathcal{S}_{s+b}$ below the observed value $\mathcal{S}_{obs}$ is smaller than 5%, the model point is excluded at 95% CL (cf. Fig. 7.3).

Monte Carlo samples are generated for each point in the given SUSY grid. The SUSY samples are reconstructed and the complete analysis described in Ch. 6 is applied. The number of SUSY events in each channel N_s extracted from the SUSY samples are con-

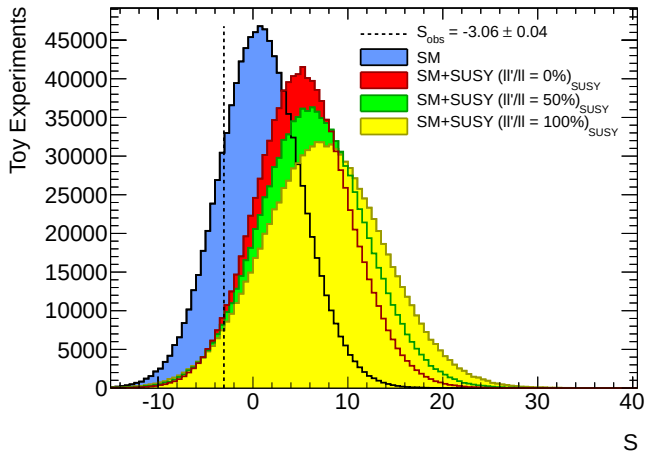

Figure 7.4: $\mathcal{S}$ Distributions with different amount of combinatorial SUSY background contributions are shown for FS-SR3. The blue distribution is the result of the toy experiments with SM only hypothesis, the red distribution includes SUSY contributions from lepton pairs originating in the same decay chains ($\ell\ell$) only, and the green and yellow distributions consider combinatorial background from leptons pairs originating in different decays ($\ell\ell'$) with a ratio of $BR(\ell\ell')/BR(\ell\ell) = 50\%$ and $BR(\ell\ell')/BR(\ell\ell) = 100\%$ respectively. The mean values of the SUSY same-flavour excess $\mathcal{S}_s = 4.5$, 5.5, and 6.7 with (0%, 50%, and 100%) combinatorial SUSY background represent the minimum $\mathcal{S}_s$, which can be exclude at 95% CL with the measured $\mathcal{S}_{obs}$. The width of the $\mathcal{S}_s$ distribution increases with increasing combinatorial SUSY background contribution. Therefore, the exclusion limits becomes weaker and the value of $\mathcal{S}_s$ necessary for an exclusion increases.

sidered in the toy experiments in λ_s. Then, the $\mathcal{S}_{s+b}$ is evaluated as described above.

Figure 7.5 and Fig. 7.6 show two examples of the distributions for two different points in the GMSB and the *PG11 LN* grids. Each figure shows a distribution of the number of N_{ee} (a), $N_{\mu\mu}$ (b), and $N_{e\mu}$ (c) events from the toy experiments for the $s+b$ hypothesis. In addition, the distributions of $\mathcal{S}_{s+b}$ and $\mathcal{S}_b$, as well as the value $\mathcal{S}_{obs}$ measured in data are given in the figures (d).

Figure 7.5 shows two well-separated distributions; the same-flavour excess of the SUSY events shifts the $\mathcal{S}_{s+b}$ distribution to high values, and the point can be excluded. This example also shows that the Gaussian distributions are truncated at low values for N_{ee}, $N_{\mu\mu}$ and $N_{e\mu}$. Due to the fact that no negative number of events are allowed in the toy experiments, the Gaussian random numbers are redrawn if the value is smaller than zero. The blue dashed lines mark the nominal mean value before truncating the distributions and the green lines show the mean value after drawing the toy experiments considering the truncation. Although the individual distributions are slightly shifted due to the truncation, the effect is negligible in comparison to the width of the $\mathcal{S}_{s+b}$ distribution and the truncated Gaussian distributions can be used in the toy experiments. Even though the shift of the mean due to the truncation is a rather small effect, other implementations using Gamma and log-likelihood distributions for drawing the toy experiments have been implemented and tested. The implementations of correlated distributions of

non-Gaussian form require at least one order of magnitude more computing time which effectively prohibits their use for large grids.

Nevertheless, one has to take care that the p-value (in case of the FS, $\mathcal{S}$) based on truncated distributions is not shifted artificially towards higher values and the exclusion is overly optimistic, otherwise it is possible that the analysis will exclude grid points to which it does not have sufficient sensitivity. Usually, the CL_s method [168] (cf. 7.3.1) prevents the exclusion of being overly optimistic in case of low sensitivity by penalizing the p-value of the *signal+background hypothesis* by the *background hypothesis*. The test statistics foreseen for this method should form a likelihood distribution. As described above, the negative yields of the $\mathcal{S}$ distribution prohibits the use of such a test statistic. However using a CL_s inspired method based on the $\mathcal{S}$ variable can prevent the exclusion of parameter points to which the analysis does not have sufficient sensitivity, as discussed in Sec. 7.3.1.

Another example, showing a SUSY point which cannot be excluded with the given measurement, is displayed in Fig. 7.6. The production cross section of this point is not high enough, therefore the expected number of same-flavour SUSY events is not sufficiently large for an exclusion.

7.3.1 CLs Method

The limit calculation for the FS analysis introduced in [52] was based on p-values derived from toy experiments for $\mathcal{S}$, as described in Sec 7.2 and used for the model-independent limits.

The problem with this procedure is that it is possible to exclude a signal hypothesis to which there is no sensitivity. This can happen if the data shows an undershoot with respect to the background estimate at the 5 % CL or below. Therefore, the common ATLAS recommendation is to use the CL_s method, introduced in [168]. In the CL_s method, the p-value is penalized by dividing the p-value of the signal+background hypothesis by one minus the p-value of the background-only hypothesis (cf. Eq.(7.3)). If the signal+background and the background-only hypothesis are well separated, the penalty by dividing those values is rather low. If the distributions are close together, $1-p_b$ becomes small and p_{s+b} is more strongly penalized, such that CL_s increases, which prevents from excluding a model in case of low sensitivity.

However, the proposed test statistics for this technique is a profile likelihood ratio, which cannot express the distribution of $\mathcal{S}$ due to the negative contributions. Therefore, a CL_s-inspired technique is applied in the following. The p-values used to determine the model-independent limits in Sec. 7.2 are based on the hypothesis of having signal and background contributions in the final selection $(s+b)$. The probability of finding events from the signal+background hypothesis with values of $\mathcal{S}_{s+b}$ below the observed value $\mathcal{S}_{obs}$ in data is calculated as:

$$p_{s+b} = P(\mathcal{S} \leq \mathcal{S}_{obs}|s+b) = \int_{-\infty}^{\mathcal{S}_{obs}} f(\mathcal{S}|s+b) \tag{7.1}$$

(cf. Fig. 7.3, green area). The probability of finding events according to the background-only hypothesis with same-flavour excess ($\mathcal{S} > 0$), a value of $\mathcal{S}_b$ larger than the measured $\mathcal{S}_{obs}$ value in data is determined by:

$$p_b = P(\mathcal{S} \geq \mathcal{S}_{obs}|b) = \int_{\mathcal{S}_{obs}}^{\infty} f(\mathcal{S}|b) \tag{7.2}$$

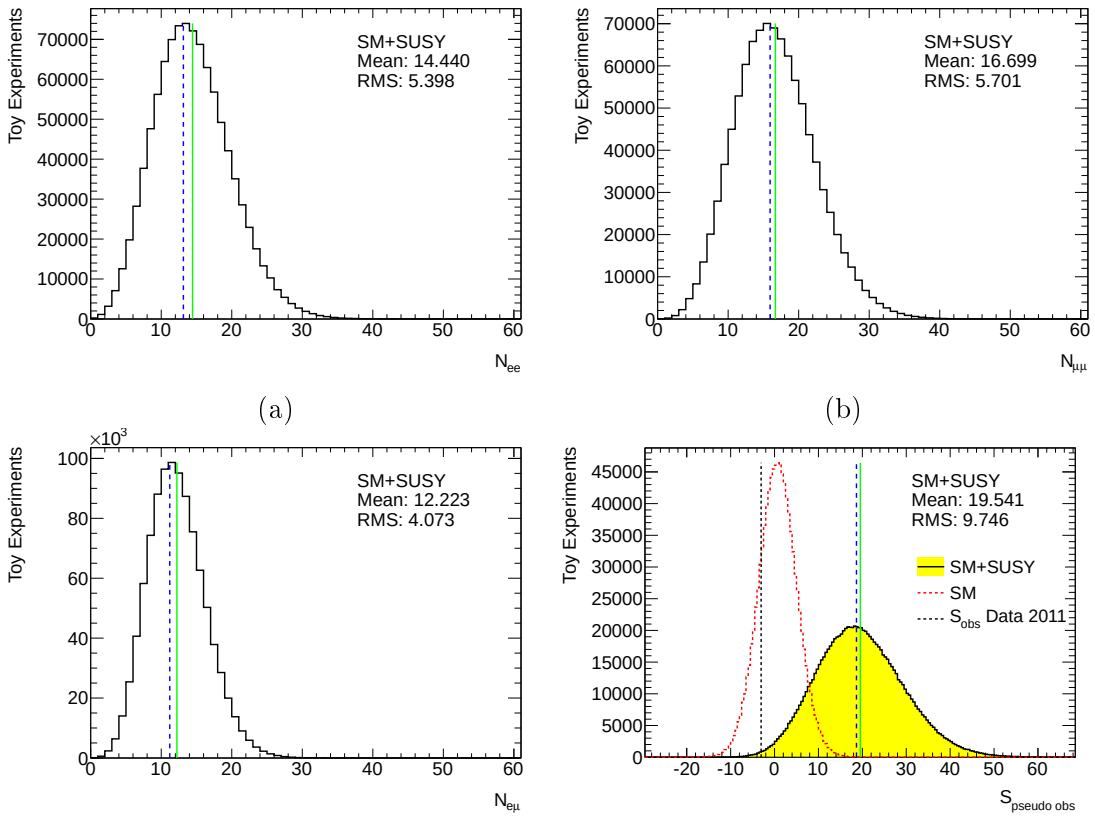

Figure 7.5: Example of an excluded SUSY scenario with truncated Gaussian distributions. This example is taken from the GMSB grid with fixed values for $M_{mes} = 250\,\text{TeV}$, $N_5 = 3$, $sgn(\mu) = +$, and $C_{grav} = 1$, this point is simulated at $\tan\beta = 10$ and $\Lambda = 40\,\text{TeV}$. The distribution are shown for the number of N_{ee} (a), $N_{\mu\mu}$ (b), and $N_{e\mu}$ (c) of one million toy experiments with the SM+SUSY hypothesis in FS-SR3. The distributions $\mathcal{S}_{s+b}$ of the signal+background hypothesis and $\mathcal{S}_b$ of the background only hypothesis are shown in (d). The blue dashed lines mark the nominal mean value before truncating the distributions and the green lines the mean value after truncation. This point is chosen, because the truncation of the mean value has the largest effect observed in this analysis. Although the individual distributions are shifted due to the truncation, the effect is negligible in comparison to the width of the $\mathcal{S}_{s+b}$ distribution.

(cf. Fig. 7.3, yellow area). Given these, the CL_s can be calculated as follows:

$$CL_s \equiv \frac{p_{s+b}}{1 - p_b} < \alpha \tag{7.3}$$

7.3.2 Model-Dependent Limit Setting Procedure

The limits setting applied on the different SUSY grids described below follows a common procedure. For a better overview the procedure is summarised generally, referring to the specific sections or tables where more detailed information can be found:

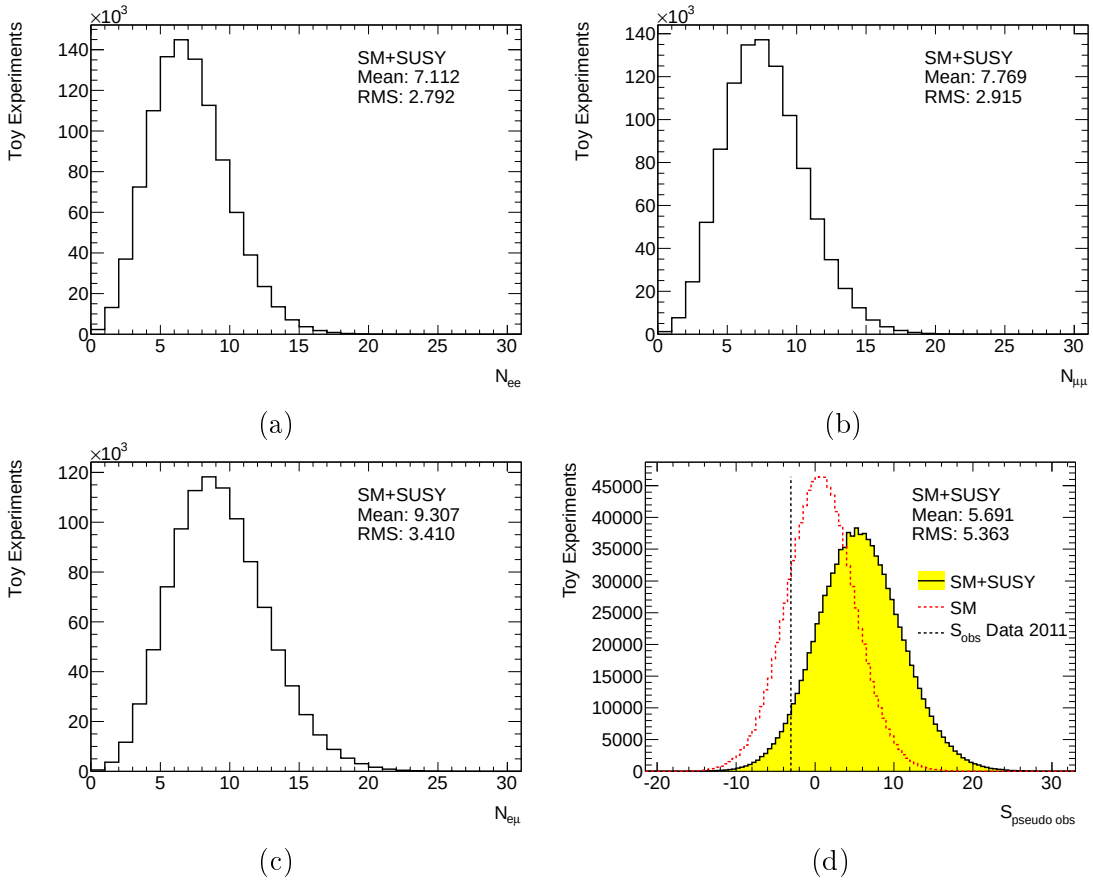

Figure 7.6: Example of an SUSY scenario in the *PG11 LN* with $m_{\tilde{g}} = 1000\,\text{GeV}$ and $m_{\tilde{q}} = 1010\,\text{GeV}$ which cannot be excluded with the given statistics. The distributions are shown for the number of N_{ee} (a), $N_{\mu\mu}$ (b), and $N_{e\mu}$ (c) of one million toy experiments with the SM+SUSY hypothesis in FS-SR3. The distributions $\mathcal{S}_{s+b}$ of the signal+background hypothesis and $\mathcal{S}_b$ of the background hypothesis only are shown in (d). Adding the SUSY contribution to the N_{ll} distributions and performing the FS leads to a shift of $\mathcal{S}_{s+b}$ in comparison to $\mathcal{S}_b$. The number of SUSY events with flavour excess is not sufficient for excluding this point at 95% CL.

1. Determine $\mathcal{S}_{obs}$ in data (calculated by Eq. (5.10))

2. Determine $N_{e^\pm e^\mp}$, $N_{e^\pm \mu^\mp}$, $N_{\mu^\pm \mu^\mp}$ from SM estimations (results are given in Tab. 6.21)

3. Perform toy experiments for SM (background hypothesis) based on the mean value $N_{e^\pm e^\mp}$, $N_{e^\pm \mu^\mp}$, $N_{\mu^\pm \mu^\mp}$ and the systematics summarised in Tab. 6.18 - Tab 6.20

4. Simulate SUSY events for each grid point and evaluate the analysis (cf. Sec. 6.4.1)

5. Determine $N_{e^\pm e^\mp}$, $N_{e^\pm \mu^\mp}$, $N_{\mu^\pm \mu^\mp}$ from SUSY MC for each point

6. Perform toy experiments for SM+SUSY (signal+background hypothesis) considering the systematics as above and additional SUSY theory uncertainties

7. Determine CL_s for each grid point as described in Sec 7.3.1

8. If the CL_s-value is smaller than 5%, the analysed grid point is excluded at 95% CL.

7.3.3 Limits on Phenomenological Grids

Two different phenomenological grids are analysed in this thesis; the light neutralino (*PG11 LN*) with $m_{\tilde{\chi}_1^0} = 100\,\text{GeV}$ and the compressed spectrum (*PG11 CS*). Both have been introduced previously in Sec. 1.2.3 and Sec. 5.2.2. In total, 108 grid points with 5000 events each have been simulated for both grids, separately. One million toy experiments have been evaluated for the signal+background hypothesis per grid point and compared via the CL_s method with $\mathcal{S}_{obs}$ measured in data. The best exclusion limits have been determined for FS-SR3, which are shown in Fig 7.7(a) for *PG LN* and Fig. 7.7(b) for *PG CS*. The blue dashed line marks the expected CL_s limits at 95% CL, the black dashed lines the expected limits $\pm 1\,\sigma$ and the red line the observed limits. The area below the observed curve is excluded.

Both observed limits are slightly better than the expectations. This is a consequence of the downward fluctuation of the observed $\mathcal{S}_{obs}$ in comparison to the expected $\mathcal{S}_b$ (cf. Fig 7.1). The expected limits are calculated with the same equations (Eq. (7.1) - Eq. (7.3)) by replacing the $\mathcal{S}_{obs}$ in the bounds of integration by the mean value $\mathcal{S}_b$ of the SM toy experiments given in Tab. 7.1.

Although both grids have the same production cross section, the area of excluded model points of the compressed spectrum is much smaller than the excluded area in the light neutralino grid. This difference is caused by the difference in the lepton momentum. The small mass differences of the $\tilde{\chi}_2^0$, the $\tilde{\ell}$ and the $\tilde{\chi}_1^0$ in *PG CS* leads to much softer leptons than the lepton momenta predicted in *PG LN*.

The exclusion limits determined in FS-SR1 and FS-SR2 are attached to the appendix D.3 for both grids, respectively (cf. Fig D.4 and Fig D.5). Additional plots of FS-SR3 showing the expected and the observed limits separately with the positions of the simulated grid points are given in Fig. D.6 for both grids. The best limits are determined in FS-SR3. They improve the excluded area in the $m_{\tilde{g}}$-$m_{\tilde{q}}$-plane in comparison to the results from inclusive di-lepton searches published 2010 in [52] (cf. 1.16) for both the light neutralino model and the compressed spectrum model, respectively. Figure 7.8 compares the observed limits of the three signal regions in (a) for the LN model and in (b) for the CS model. In addition to the limits, the production cross sections are marked as grey lines in both plots and the masses of the corresponding LSP in black in Fig. 7.8(b). In the light neutralino scenarios, gluino masses up to $m_{\tilde{g}} \sim 560\,\text{GeV}$ and squark masses up to $m_{\tilde{g}} \sim 800\,\text{GeV}$ are excluded at 95% CL in FS-SR3, and in the compressed spectrum, gluinos with a mass up to $m_{\tilde{g}} \sim 560\,\text{GeV}$, squark masses up to $m_{\tilde{q}} \sim 475\,\text{GeV}$ and light neutralino masses up to $m_{\tilde{g}} \sim 325\,\text{GeV}$ are excluded.

7.3.4 Limits on GMSB

The GMSB model has been evaluated for 80 grid points with 20 k events each, in the Λ-$\tan\beta$ plane of the the SUSY parameter space with fixed values for $M_{mes} = 250\,\text{TeV}$, $N_5 = 3$, $sgn(\mu) = +$, and $C_{grav} = 1$. The best exclusion limits are determined with FS-SR3 ($E_{\text{T}}^{\text{miss}} > 250\,\text{GeV}$) shown in Fig. 7.9. The CoNLSP and the $\tilde{\ell}_{\text{R}}$-NLSP regions have been excluded at 95% CL up to $\Lambda = 40\,\text{TeV}$ based on the same-flavour excess

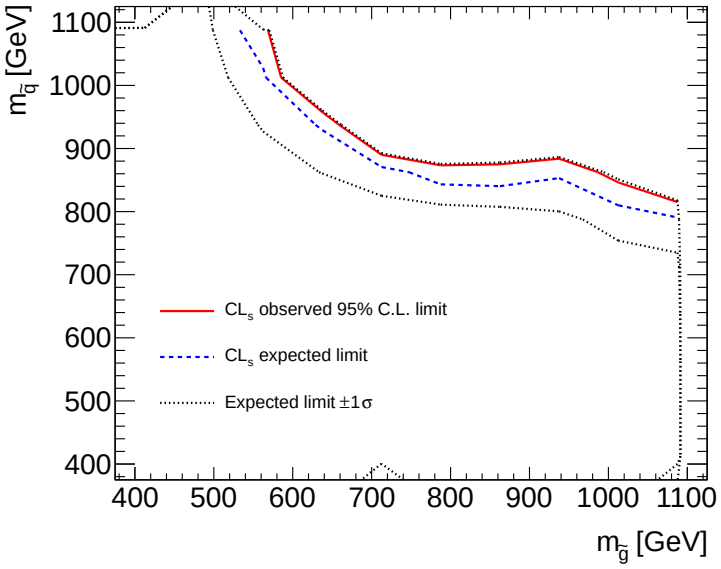

(a)

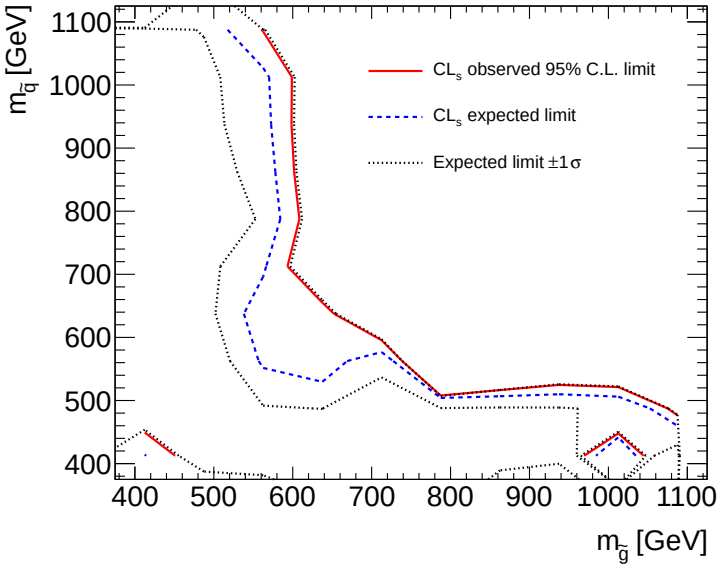

(b)

Figure 7.7: The limits on light LSP (a) and compressed spectrum (b) phenomenological grids are determined for 108 grid points in each grid. For each grid point one million toy experiments are evaluated using the CL_s method. If the CL_s value of a given grid point is $< 5\%$, the point is excluded at 95% CL. The limits are calculated for the FS-SR3 ($E_T^{miss} > 250\,GeV$). The solid red lines mark the observed limits, the blue dashed line the expected limits and the black dotted lines show the expected limit $\pm 1\sigma$.

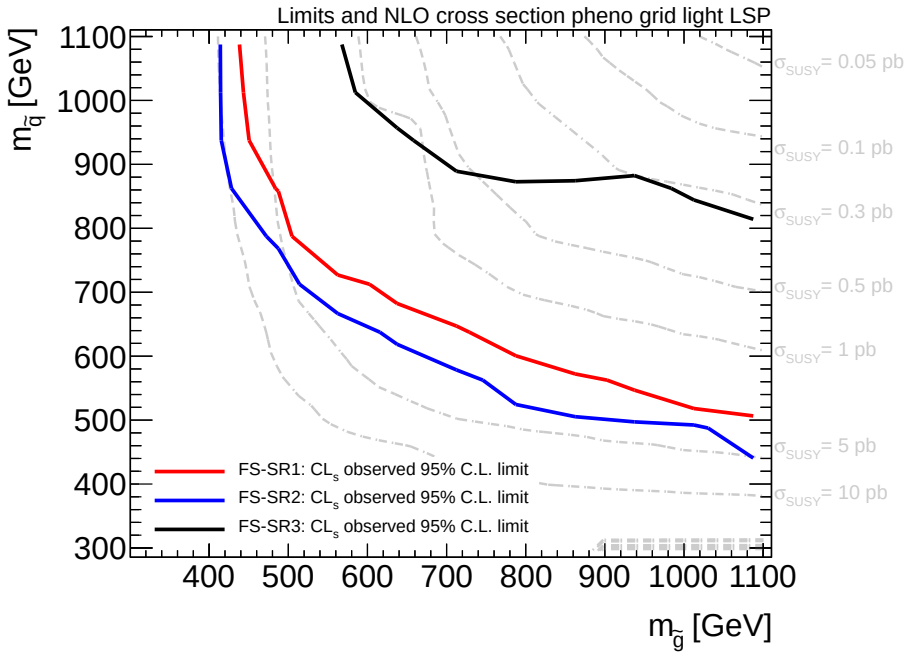

(a)

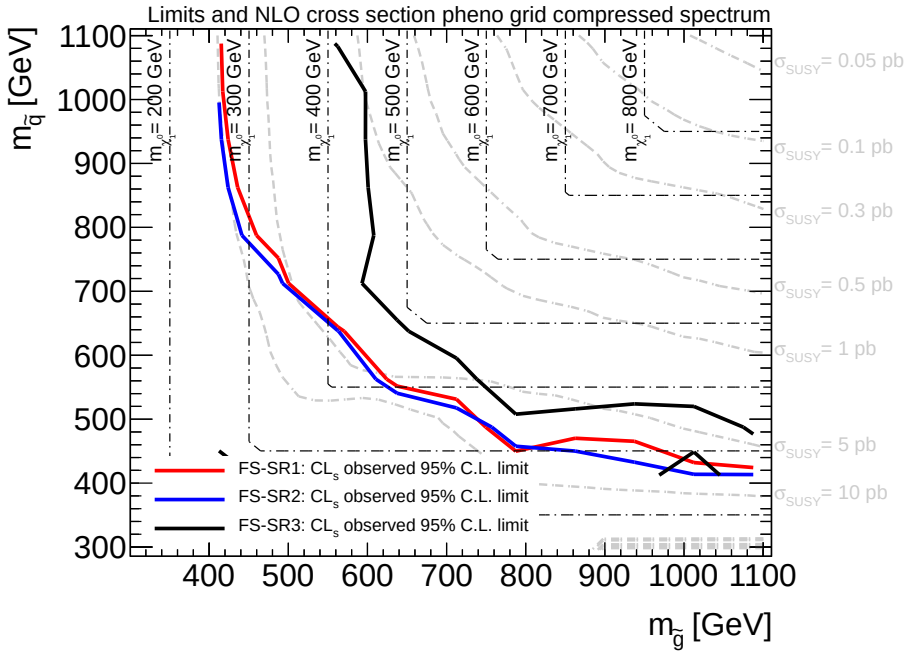

(b)

Figure 7.8: Comparison of PG limits for all FS-SRs with NLO production cross section (a) for the LN grid and (b) for the CS grid. The tightest limits are determined with FS-SR3. The red line marks the exclusion limit at 95% CL in FS-SR1, the blue line in FS-SR2 and the black line in FS-SR3. The production cross sections are shown in light grey. In case of the compressed spectrum, $m_{\tilde{\chi}_1^0}$ is calculated as function of $m_{\tilde{q}}$ and $m_{\tilde{g}}$, the corresponding masses are added as black dash-dotted lines.

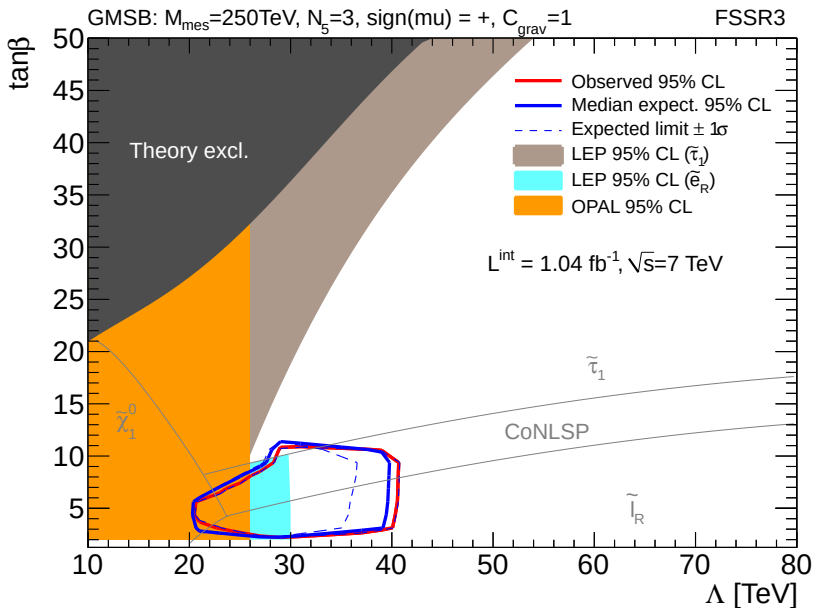

Figure 7.9: The limits on the GMSB model with the following fixed SUSY parameters: $M_{mes} = 250\,\text{TeV}$, $N_5 = 3$, $C_{grav} = 1$, and $sgn(\mu) = +$ are determined for 60 grid points. For each grid point one million toy experiments are evaluated using the CL_s method. If the CL_s value of a given grid point is $< 5\%$, the point is excluded at 95% CL. The limits are calculated for the FS-SR3 ($E_\text{T}^\text{miss} > 250\,\text{GeV}$).The solid red lines mark the observed limits, the blue dashed line the expected limits and the black dotted lines show the expected limit $\pm 1\sigma$.

variable $\mathcal{S}$ and the CL_s-method described in Sec. 7.3.1. Additional plots can be found in appendix D.3.

As explained in Sec. 5.2.2, the largest region of the GMSB grid is the $\tilde{\tau}_1$-NLSP region which is dominated by τ-lepton production. If both τ-leptons from one chain decay leptonically, the electrons and muons are considered in the FS analysis. But there is no constraint on the lepton family between the first and the second lepton produced in the τ-lepton decay, such that the FS analysis treats those leptons as combinatorial background. Therefore, even if a lepton excess is measured in the $\tilde{\tau}_1$-NLSP region, it is observed in all channels and after the subtraction $\mathcal{S}_{s+b}$ is symmetrically distributed around zero.

The di-lepton events reconstructed in the CoNLSP and the $\tilde{\ell}_\text{R}$-NLSP regions originate mainly from $\tilde{\chi}_1^0 \to \tilde{\ell}_\text{R}^\pm \ell^\mp \to \ell^\pm \ell^\mp \tilde{\chi}$ decays. In these events the lepton flavour is constrained by lepton flavour conservation and the FS analysis can determine a flavour excess.

The boundaries of the excluded area in the GMSB model are constrained in $\tan\beta$ by the dominated decay processes and in Λ by the steeply falling production cross section (cf. Fig. 5.10). Figure 7.10 shows, in addition to the FS-SR3 limit, the results from the FS-SR1 and FS-SR2 limit determination, and the NLO production cross section in grey.

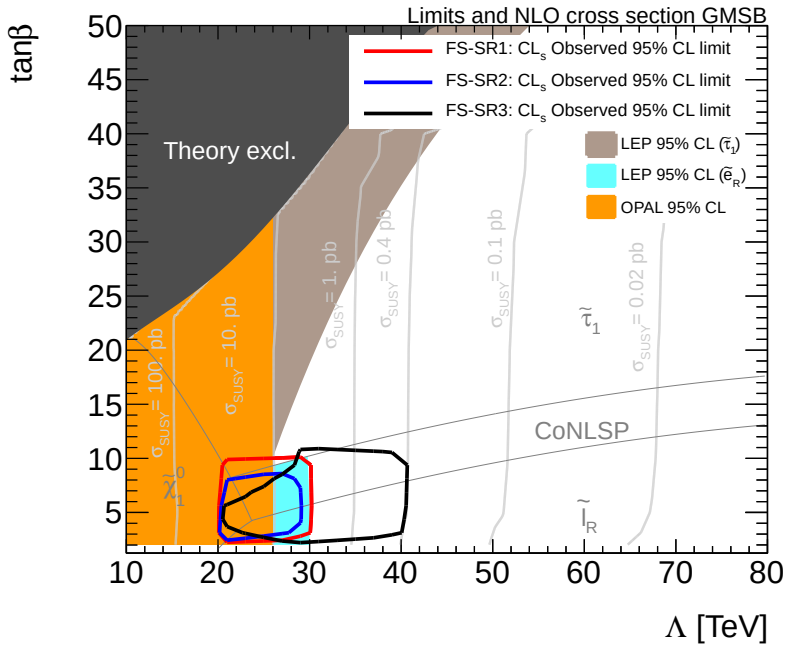

Figure 7.10: Comparison of GMSB limits for all FS-SRs with NLO production cross section. The tightest limits are determined with FS-SR3. The excluded are is limited in $\tan\beta$ by the decay processes, because the FS method is mainly sensitive to $\tilde{\ell}$ decays. The excluded area in the x-axis, is mainly limited by statistics, due to the steep decrease of the production cross section with increasing Λ.

7.4 Comparison to Results of other SUSY Searches in ATLAS

The FS analysis described in this thesis has been published in [155] together with a same-sign and an opposite-sign di-lepton inclusive analysis. The three analyses share the same object definition and event selection. Three signal regions are defined for the opposite-sign search: OS-SR1 requires a tight missing transverse energy cut only[1] ($E_{\mathrm{T}}^{\mathrm{miss}} > 250\,\mathrm{GeV}$), OS-SR2 requires $E_{\mathrm{T}}^{\mathrm{miss}} > 220\,\mathrm{GeV}$ and at least three jets with jet $p_{\mathrm{T}} > 80, 40, 40\,\mathrm{GeV}$ and OS-SR3 requires a softer $E_{\mathrm{T}}^{\mathrm{miss}}$ cut ($E_{\mathrm{T}}^{\mathrm{miss}} > 100\,\mathrm{GeV}$) but at least four jets with larger transverse momentum jet $p_{\mathrm{T}} > 100, 70, 70, 70\,\mathrm{GeV}$. The same-sign search defines two signal regions, SS-SR1 requires $E_{\mathrm{T}}^{\mathrm{miss}} > 100\,\mathrm{GeV}$ and SS-SR2 requires $E_{\mathrm{T}}^{\mathrm{miss}} > 80\,\mathrm{GeV}$ and at least two jets with $p_{\mathrm{T}} > 50, 50\,\mathrm{GeV}$. The observation in data and the estimated background events are listed in Tab. 7.4 together with the extracted limits given as the cross section times the efficiency times the acceptance ($\sigma \times \epsilon \times A$) for each signal region. The exclusion limits are combinations of CLs [168] limits derived from profile-likelihood ratios [169].

Direct comparisons between the FS limits and the limits set by inclusive searches are not trivial because the FS is an exclusive method designed for precision measurements. By subtracting the different-flavour contribution, the sensitivity in terms of discovery is reduced intrinsically. The negative entries in the test statistics of $\mathcal{S}$ does not allow the use

[1] this SR is identical to the FS-SR3

Table 7.4: Predicted background events, the observed number of events and the corresponding 95% CL upper limit on A$\times\epsilon\times\sigma$, calculated using the CL_s technique, for each opposite-sign and same-sign signal region [155].

	Background	Obs.	95% CL
OS-SR1	$15.5 \pm 1.2 \pm 3.8$	13	9.9 fb
OS-SR2	$13.0 \pm 1.8 \pm 3.6$	17	14.4 fb
OS-SR3	$5.7 \pm 1.1 \pm 3.4$	2	6.4 fb
SS-SR1	$32.6 \pm 4.4 \pm 6.0$	25	14.8 fb
SS-SR2	$24.9 \pm 4.1 \pm 4.2$	28	17.7 fb

of a profile likelihood distribution. Instead, toy experiments have been performed and the CL_s method has been applied. The limits of both the light neutralino and the compressed spectrum phenomenological grids (cf. Fig 7.7) could be improved in comparison to the limits found in the previous di-lepton analysis performed in [52] (cf. Fig 1.16).

The FS analysis interpreted in the GMSB model with $M_{mes} = 250\,\text{TeV}, N_5 = 3, sgn(\mu) = +$ and $C_{grav} = 1$ as described in Sec 7.3.4, excludes the CoNLSP and the $\tilde{\ell}_R$-NLSP regions up to $\Lambda \sim 40\,\text{TeV}$. In the CoNLSP and the $\tilde{\ell}_R$-NLSP regions the limits are comparable with the OS inclusive di-lepton analysis published in [170], whereas the inclusive search shows a better sensitivity in the $\tilde{\tau}_1$-NLSP region. The observed exclusion region is shown as red curve in Fig. 7.11(a).

The best limits for the MSUGRA/CMSSM model could be achieved in the combined 0-lepton searches published in [171], as shown in Fig. 7.11(b). As discussed in Sec. 1.2.1, the 0-lepton analyses are extremely sensitive for searches in the MSUGRA scenario due to the enhanced strong coupling.

Figure 7.12 gives an overview of the model-dependent searches in the ATLAS experiment showing the analysed integrated luminosity, the excluded mass scale, and the corresponding publication. The limit on the $\tilde{g}$ mass in the GMSB model is determined by the inclusive same-flavour di-lepton analysis. The FS analysis shows comparable sensitivity in the CoNSLP and the $\tilde{\ell}$-NLSP regions and no sensitivity at all in the $\tilde{\tau}$-NLSP region due the subtraction method. The results of the mass limits in the phenomenological models extracted from the FS analysis are added to the same plot, marked in red.

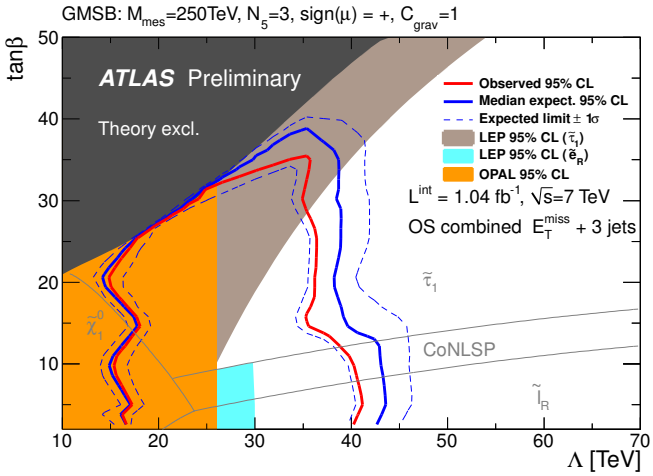

(a)

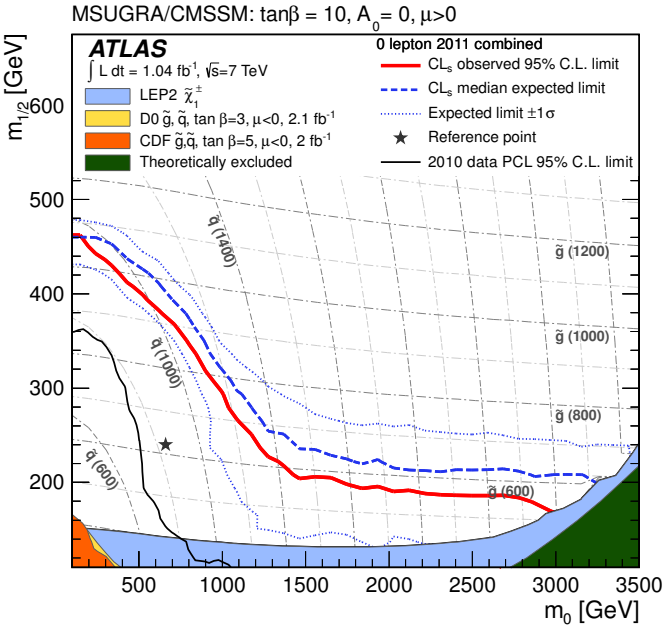

(b)

Figure 7.11: (a) Observed (red) and expected (blue) 95% CL exclusion limits as function of Λ and $\tan\beta$ for the combination of all three channels ($e^{\pm}e^{\mp}$, $e^{\pm}\mu^{\mp}$ and $\mu^{\pm}\mu^{\mp}$). The expected limit $\pm 1\sigma$ is shown as (dashed) lines. The different NLSP regions as well as the region excluded by theory and LEP experiments indicated in different colours.[170]. (b) Combined exclusion limits for MSUGRA/CMSSM models with $tan\beta = 10$, $A_0 = 0$ and $\mu > 0$ [171]. The combined limits are obtained by using the signal region which generates the best expected limit at each point in the parameter plane. The dashed blue line corresponds to the median expected 95% CL limit and the red line corresponds to the observed limit at 95% CL The dotted blue lines correspond to the $\pm 1\sigma$ variation in the expected limits. The limits from the Tevatron and LEP experiments are plotted as filled areas, previous published ATLAS limits are also shown.

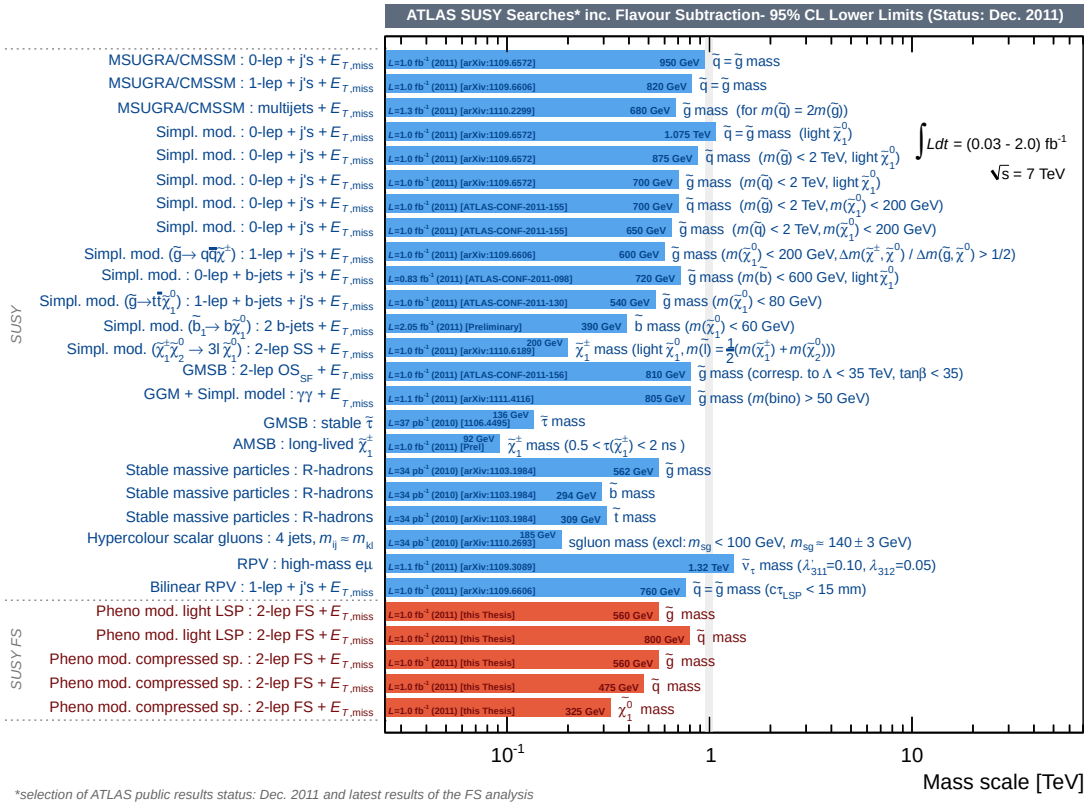

Figure 7.12: Overview of the model-dependent ATLAS SUSY searches. A selection of ATLAS public results is shown with the analysed integrated luminosity, the excluded mass scale, and the corresponding publication [150]. The limits determined with the FS analysis in the phenomenological models are added in red.

8 Summary and Outlook

8.1 Summary

The LHC and its experiments were constructed for two main tasks, finding the Higgs boson and searching for signatures of physics beyond the SM. Despite the tremendous and unprecedented success of the SM, there are several theoretical and experimental shortcomings of the SM: Most notably the hierarchy problem, the non-unification of the three distinct gauge forces, and the missing explanation for cosmological dark matter. These shortcomings are solved by introducing a supersymmetric extension of the SM (SUSY).

SUSY introduces a new symmetry between fermions and boson by adding a bosonic superpartner to each SM fermion and a fermionic superpartner to each SM boson. An additional quantum number, R-parity, is required to prevent baryon and lepton number violating processes. If this number is conserved, SUSY particles are produced in pairs and decay to the lightest supersymmetric particle (LSP), which is only weakly interacting and therefore a very good candidate for dark matter. Various SUSY searches are performed at the different LHC experiments at CERN. SUSY must be broken at electroweak scale, otherwise SUSY particles would have been found before, since their masses would be the same as their SM partners. Different breaking mechanisms have been proposed in the literature. Two different models have been studied in this thesis: gauge mediated supersymmetry breaking (GMSB) and phenomenological models. If a non-SM signal compatible with SUSY expectations is found, precision measurements are necessary in order to assign the observation to a given breaking scenario with specific SUSY parameters. The invariant mass distribution of the leptons from explicit SUSY decay chains such as $\tilde{\chi}_2^0 \to \ell^{\pm}\ell^{\mp}\tilde{\chi}_1^0$ have a sharp endpoint. This endpoint can be fitted and used to extracted SUSY mass differences.

In this thesis the flavour subtraction method (FS) is used to suppress flavour symmetric SM background and to isolate SUSY di-lepton decays in order to measure the invariant mass distribution and to determine the end endpoint. The FS method is very powerful for suppressing fully leptonic $t\bar{t}$ decays, which form the main background in many SUSY searches. By subtracting the opposite-sign different-flavour lepton pairs ($e^{\pm}\mu^{\mp}$) from the opposite-sign same-flavour lepton pairs ($e^{\pm}e^{\mp}$, $\mu^{\pm}\mu^{\mp}$), combinatorial SUSY background from other decays producing di-leptons final states can be rejected and explicit decays with same-flavour excess can be selected.

The data set recorded from 13th March to June 28th 2011, corresponding to an integrated luminosity of $1.04\,\mathrm{fb}^{-1}$, is analysed with the FS method. Three different FS signal regions have been defined: two signal regions with a low $E_{\mathrm{T}}^{\mathrm{miss}}$ cut ($E_{\mathrm{T}}^{\mathrm{miss}} > 80\,\mathrm{GeV}$), FS-SR1 and FS-SR2, and one signal region with a tight $E_{\mathrm{T}}^{\mathrm{miss}}$cut ($E_{\mathrm{T}}^{\mathrm{miss}} > 250\,\mathrm{GeV}$), FS-SR3. The soft $E_{\mathrm{T}}^{\mathrm{miss}}$ signal regions require additional cuts in order to suppress flavour asymmetric di-lepton backgrounds, dominated by single Z-boson and di-boson events. Therefore, events in FS-SR1 are rejected if they have an invariant mass compatible with the Z-boson mass peak (veto for event with $80\,\mathrm{GeV} < \mathrm{m}_{\ell\ell} < 100\,\mathrm{GeV}$), and FS-SR2

requires a jet multiplicity larger than one. Both signal regions, FS-SR1 and FS-SR2, allow the study of phase space regions which are not covered by inclusive analyses. The enhanced statistics can be used for fitting mass edges or to determine multi-bin or shape-based exclusion limits. FS-SR3 was chosen for a one-bin counting limit setting approach.

In order to be as independent as possible from MC simulation, the SM background processes are estimated with data-driven methods if possible. Cosmic muon background, fake lepton contribution and Z-boson decays are determined with data-driven estimates for all signal regions. The contributions from single-top and di-boson are estimated from pure Monte Carlo predictions for all signal regions. The only difference between the low $E_{\mathrm{T}}^{\mathrm{miss}}$ signal regions and the tight $E_{\mathrm{T}}^{\mathrm{miss}}$ signal region is the estimation of fully leptonic $t\bar{t}$ events. Whereas the estimate for FS-SR1 and FS-SR2 have to rely on the MC predictions, the estimates for FS-SR3 are determined from data.

Since the measured kinematic distributions are in good agreement with the SM predictions, no sign of a signal from physics beyond the SM is visible. The size of the excess of same-flavour di-lepton pairs is defined as $\mathcal{S}$. The distribution of $\mathcal{S}$ is centred around zero in the case that no flavour excess is present - as expected for example in fully leptonic $t\bar{t}$ decays. Such a distribution might have negative entries, which is a rather complicated feature for constructing a suitable test statistic. The p-value determined from $\mathcal{S}$ after FS is extracted by means of toy experiments. The statistical and systematic uncertainties are modelled as Gaussian distributions per uncertainty, di-lepton channel, and SM background process. The constraint of having no negative number of events is taken into account by using truncated Gaussian distributions. For the model dependent limits the $\mathrm{CL_s}$ method was applied in order to account for a deficit of the data with respect to the background in limit settings.

Based on the variable $\mathcal{S}$, model-independent and model-dependent exclusion limits have been determined. The model-independent limits are $\mathcal{S}_s \geq 102.0$ (138.0) in the low $E_{\mathrm{T}}^{\mathrm{miss}}$regions FS-SR1 (FS-SR2) and $\mathcal{S}_s \geq 4.5$ in the tight $E_{\mathrm{T}}^{\mathrm{miss}}$ region (FS-SR3), assuming no contribution from combinatorial SUSY background events. Considering background events from uncorrelated lepton pairs ($\ell\ell'$) of different SUSY decay chains yields a broader $\mathcal{S}_s$ distribution and therefore weakens the determined limit. The effect of SUSY background is studied in the FS-SR3 by considering different ratios of combinatorial background to SUSY signal ($\ell\ell$) contributions (0%, 50% and 100%). Models with a ratio of $BR(\ell\ell')/BR(\ell\ell) = 0\%$, 50% and 100% could be excluded at 95% CL if $\mathcal{S}_s$ is expected to be larger than 4.5, 5.5 and 6.7, respectively. Model-dependent limits have been determined for two phenomenological models with compressed spectrum and light neutralino scenarios, and for the GMSB model with fixed values for $M_{mes} = 250\,\mathrm{TeV}$, $N_5 = 3$, $sgn(\mu) = +$, and $C_{grav} = 1$. The tightest limits have been determined in FS-SR3 for all scenarios. Both limits in the phenomenological models is improved in comparison to the limits determined in the ATLAS analysis with the data set recorded in 2010. The light neutralino (compressed spectrum) model is excluded up to $m_{\tilde{g}} \sim 560\,\mathrm{GeV}$ and $m_{\tilde{q}} \sim 800\,\mathrm{GeV}$ ($m_{\tilde{g}} \sim 560\,\mathrm{GeV}$, $m_{\tilde{q}} \sim 475\,\mathrm{GeV}$ and $m_{ninoone} \sim 325\,\mathrm{GeV}$) with the current analysis. The GMSB scenario is excluded in the CoNLSP and $\tilde{\ell}$-NLSP regions up to $\Lambda \sim 40\,\mathrm{TeV}$.

8.2 Outlook

In terms of future developments of the analysis presented here, one can expect better limits in near future, when the complete 2011 data set, corresponding to an integrated

luminosity of $5\,\mathrm{fb}^{-1}$, is analysed.A first estimation can be done by extrapolating the observed limits by a factor of five as function of the production cross section. This is a rough estimate, because not only the production cross section, but also the mass hierarchy and the BR change from model point to model point.Increasing statistics by a factor of five would yield an improvement of the excluded area in the phenomenological model for *PG11 LN* as maximum to $m_{\tilde{g}} = m_{\tilde{q}} \sim 1000\,\mathrm{GeV}$ and for the *PG11 CS* up to $m_{\tilde{g}} = 800\,\mathrm{GeV} = m_{\tilde{q}} \sim 800\,\mathrm{GeV}$ corresponding to a light neutralino mass of about $650\,\mathrm{GeV}$, and for the GMSB grid excluding the area in the CoNLSP and the $\tilde{\ell}$-NLSP region up to $\Lambda \sim 50\,\mathrm{TeV}$.

Since the soft $E_{\mathrm{T}}^{\mathrm{miss}}$ signal regions have been designed for measuring the endpoint of the invariant mass distribution of the di-leptons, the limit setting can consider the shape of a given scenario and determine either multi-bin exclusion limits or exclusions based on the invariant mass shape directly. For now truncated Gaussian distributions have been used for modelling the number of the expected events in the three different channels, which yields a small shift of the mean value towards higher values. The negligible impact in comparison to the broad distributions and the application of the $\mathrm{CL_s}$ method takes account for this effect. Another solution could be to use other distributions, for example Gamma or log-likelihood distributions, for drawing the toy experiments. Several SUSY scenarios predict small mass differences between the neutralino and the slepton yielding low transverse momenta for the leptons. An improvement of the low momentum reconstruction, and much more importantly, a decrease in the trigger threshold, for example by applying di-lepton triggers, could improve the FS analysis significantly.Despite being aimed at precision measurements, this analysis provides complementary and relevant limits to several SUSY scenarios. The improvement of the analysis, by taking advantage of the shape information will furthermore increase it's sensitivity.

The search for new physics beyond the SM Higgs boson remain a major task despite the current non-observation of new physics. The discovery of a SM-like Higgs boson would be a tremendous achievement, but solving the experimental and theoretical shortcomings of the SM would still remain an equally important task for future experimens at LHC end elsewhere. Truly explaining the mystery of electroweak symmetry breaking requires the understanding of physics beyond the SM - and SUSY could be such an explanation, if properly understood with analyses like the one presented here.

Appendix A

Data and Monte Carlo Samples

A.1 Data

Table A.1: Overview of the analysed data taking periods used in this analysis and integrated luminosities before (corresponding to the ATLAS ready configuration) and after GRL selection.

Period	Run Number	Date	$\int \mathcal{L}dt$ [pb] before GRL	$\int \mathcal{L}dt$ [pb] after GRL
B2	178044 – 178109	2011-Mar-22 – 2011-Mar-24	12.7	11.3
D1	179710 – 179739	2011-Apr-14 – 2011-Apr-16	11.6	9.3
D2	179771 – 179804	2011-Apr-16 – 2011-Apr-17	10.8	8.6
D3	179938 – 180144	2011-Apr-18 – 2011-Apr-22	34.6	29.4
D4	180149 – 180212	2011-Apr-22 – 2011-Apr-24	36.0	31.5
D5	180225 – 180242	2011-Apr-24 – 2011-Apr-26	30.2	27.1
D6	180309 – 180448	2011-Apr-26 – 2011-Apr-28	30.4	25.2
D7	180481	2011-Apr-28 – 2011-Apr-29	23.2	21.1
E1	180614 – 180776	2011-Apr-30 – 2011-May-03	49.2	41.7
F2	182161 – 182486	2011-May-17 – 2011-May-24	132.0	108.7
F3	182516 – 182519	2011-May-24 – 2011-May-25	18.2	15.7
G1	182726	2011-May-27	5.8	4.3
G2	182747 – 182886	2011-May-28 – 2011-May-31	112.9	97.2
G3	182997 – 183021	2011-Jun-01 – 2011-Jun-03	75.3	63.1
G4	183038 – 183130	2011-Jun-03 – 2011-Jun-07	111.5	105.2
G5	183216 – 183347	2011-Jun-07 – 2011-Jun-11	105.2	92.3
G6	183391 – 183462	2011-Jun-11 – 2011-Jun-14	141.0	100.2
H1	183544 – 183602	2011-Jun-16 – 2011-Jun-18	52.5	48.5
H2	183780	2011-Jun-20 – 2011-Jun-21	47.4	43.3
H3	183963 – 184072	2011-Jun-24 – 2011-Jun-26	66.2	53.5
H4	184074 – 184169	2011-Jun-26 – 2011-Jun-28	112.3	95.1
Total	177531 – 184169	2011-Mar-13 – 2011-Jun-28	1237.6	1035.4

A.2 Monte Carlo Samples

Table A.2: Overview of W-boson, $t\bar{t}$, and single top Monte Carlo samples with sample ID, generator, cross section, and NLO k-factors. For some samples the k-factors are included in the total cross section and not given explicitly in the table.

Sample ID	Name	Generator	σxBR [pb]	k–factor
107680	WenuNp0_pt20	AlpgenJimmy	$6.9{\cdot}10^{3}$	1.20
107681	WenuNp1_pt20	AlpgenJimmy	$1.3{\cdot}10^{3}$	1.20
107682	WenuNp2_pt20	AlpgenJimmy	$3.8{\cdot}10^{2}$	1.20
107683	WenuNp3_pt20	AlpgenJimmy	$1.0{\cdot}10^{2}$	1.20
107684	WenuNp4_pt20	AlpgenJimmy	$2.5{\cdot}10^{1}$	1.20
107685	WenuNp5_pt20	AlpgenJimmy	6.9	1.20
107690	WmunuNp0_pt20	AlpgenJimmy	$6.9{\cdot}10^{3}$	1.20
107691	WmunuNp1_pt20	AlpgenJimmy	$1.3{\cdot}10^{3}$	1.20
107692	WmunuNp2_pt20	AlpgenJimmy	$3.8{\cdot}10^{2}$	1.20
107693	WmunuNp3_pt20	AlpgenJimmy	$1.0{\cdot}10^{2}$	1.20
107694	WmunuNp4_pt20	AlpgenJimmy	$2.5{\cdot}10^{1}$	1.20
107695	WmunuNp5_pt20	AlpgenJimmy	6.9	1.20
107700	WtaunuNp0_pt20	AlpgenJimmy	$6.9{\cdot}10^{3}$	1.20
107701	WtaunuNp1_pt20	AlpgenJimmy	$1.3{\cdot}10^{3}$	1.20
107702	WtaunuNp2_pt20	AlpgenJimmy	$3.8{\cdot}10^{2}$	1.20
107703	WtaunuNp3_pt20	AlpgenJimmy	$1.0{\cdot}10^{2}$	1.20
107704	WtaunuNp4_pt20	AlpgenJimmy	$2.5{\cdot}10^{1}$	1.20
107705	WtaunuNp5_pt20	AlpgenJimmy	6.9	1.20
106280	WbbNp0_pt20	AlpgenJimmy	3.2	1.20
106281	WbbNp1_pt20	AlpgenJimmy	2.6	1.20
106282	WbbNp2_pt20	AlpgenJimmy	1.4	1.20
106283	WbbNp3_pt20	AlpgenJimmy	0.6	1.20
107280	WbbFullNp0_pt20	AlpgenJimmy	$4.6{\cdot}10^{1}$	-
107281	WbbFullNp1_pt20	AlpgenJimmy	$3.4{\cdot}10^{1}$	-
107282	WbbFullNp2_pt20	AlpgenJimmy	$1.7{\cdot}10^{1}$	-
107283	WbbFullNp3_pt20	AlpgenJimmy	6.3	-
105200	T1	MC@NLO Jimmy	$8.9{\cdot}10^{1}$	-
105860	$t\bar{t}$	PowHeg Jimmy	$7.9{\cdot}10^{1}$	-
105861	$t\bar{t}$	PowHeg Pythia	$7.9{\cdot}10^{1}$	-
108340	st_tchan_enu	MC@NLO Jimmy	7.0	-
108341	st_tchan_munu	MC@NLO Jimmy	7.0	-
108342	st_tchan_taunu	MC@NLO Jimmy	7.0	-
108343	st_schan_enu	MC@NLO Jimmy	$4.7{\cdot}10^{-1}$	-
108344	st_schan_munu	MC@NLO Jimmy	$4.7{\cdot}10^{-1}$	-
108345	st_schan_taunu	MC@NLO Jimmy	$4.7{\cdot}10^{-1}$	-
108346	st_Wt	MC@NLO Jimmy	$1.3{\cdot}10^{1}$	-

Table A.3: Overview of the Z and Drell-Yan Monte Carlo samples with sample ID, generator, cross section, k-factors. For some samples k-factors are included in the total cross section and not given explicitly in the table.

Sample ID	Name	Generator	σxBR [pb]	k–factor
107650	ZeeNp0_pt20	AlpgenJimmy	$6.6{\cdot}10^{2}$	1.25
107651	ZeeNp1_pt20	AlpgenJimmy	$1.3{\cdot}10^{2}$	1.25
107652	ZeeNp2_pt20	AlpgenJimmy	$4.0{\cdot}10^{1}$	1.25
107653	ZeeNp3_pt20	AlpgenJimmy	$1.1{\cdot}10^{1}$	1.25
107654	ZeeNp4_pt20	AlpgenJimmy	2.9	1.25
107655	ZeeNp5_pt20	AlpgenJimmy	$7.5{\cdot}10^{-1}$	1.25
107660	ZmumuNp0_pt20	AlpgenJimmy	$6.6{\cdot}10^{2}$	1.25
107661	ZmumuNp1_pt20	AlpgenJimmy	$1.3{\cdot}10^{2}$	1.25
107662	ZmumuNp2_pt20	AlpgenJimmy	$4.0{\cdot}10^{1}$	1.25
107663	ZmumuNp3_pt20	AlpgenJimmy	$1.1{\cdot}10^{1}$	1.25
107664	ZmumuNp4_pt20	AlpgenJimmy	2.9	1.25
107665	ZmumuNp5_pt20	AlpgenJimmy	$7.5{\cdot}10^{-1}$	1.25
107670	ZtautauNp0_pt20	AlpgenJimmy	$6.6{\cdot}10^{2}$	1.25
107671	ZtautauNp1_pt20	AlpgenJimmy	$1.3{\cdot}10^{2}$	1.25
107672	ZtautauNp2_pt20	AlpgenJimmy	$4.0{\cdot}10^{1}$	1.25
107673	ZtautauNp3_pt20	AlpgenJimmy	$1.1{\cdot}10^{1}$	1.25
107674	ZtautauNp4_pt20	AlpgenJimmy	2.9	1.25
107675	ZtautauNp5_pt20	AlpgenJimmy	$7.5{\cdot}10^{-1}$	1.25
116250	ZeeNp0_Mll10to40	AlpgenJimmy	$3.0{\cdot}10^{3}$	-
116251	ZeeNp1_Mll10to40	AlpgenJimmy	84.91	-
116252	ZeeNp2_Mll10to40	AlpgenJimmy	41.19	-
116253	ZeeNp3_Mll10to40	AlpgenJimmy	8.35	-
116254	ZeeNp4_Mll10to40	AlpgenJimmy	1.85	-
116255	ZeeNp5_Mll10to40	AlpgenJimmy	0.46	-
116260	Z$\mu\mu$Np0_Mll10to40	AlpgenJimmy	$3.0{\cdot}10^{3}$	-
116261	Z$\mu\mu$Np1_Mll10to40	AlpgenJimmy	84.78	-
116262	Z$\mu\mu$Np2_Mll10to40	AlpgenJimmy	41.13	-
116263	Z$\mu\mu$Np3_Mll10to40	AlpgenJimmy	8.34	-
116264	Z$\mu\mu$Np4_Mll10to40	AlpgenJimmy	1.87	-
116265	Z$\mu\mu$Np5_Mll10to40	AlpgenJimmy	0.46	-
116270	Z$\tau\tau$Np0_Mll10to40	AlpgenJimmy	$3.0{\cdot}10^{3}$	-
116271	Z$\tau\tau$Np1_Mll10to40	AlpgenJimmy	84.88	-
116272	Z$\tau\tau$Np2_Mll10to40	AlpgenJimmy	41.28	-
116273	Z$\tau\tau$Np3_Mll10to40	AlpgenJimmy	8.35	-
116274	Z$\tau\tau$Np4_Mll10to40	AlpgenJimmy	1.83	-
116275	Z$\tau\tau$Np5_Mll10to40	AlpgenJimmy	0.46	-

Table A.4: Overview of Di-boson Monte Carlo samples with sample ID, generator, cross section numbers.

Sample ID	Name	Generator	σxBR [pb]
105985	WW	Herwig	$1.7{\cdot}10^{1}$
105986	ZZ	Herwig	$1.3{\cdot}10^{1}$
105987	WZ	Herwig	$5.5{\cdot}10^{1}$
107100	WWlnulnuNp0	Alpgen	2.6
107101	WWlnulnuNp1	Alpgen	1.3
107102	WWlnulnuNp2	Alpgen	$5.7{\cdot}10^{-1}$
107103	WWlnulnuNp3	Alpgen	$2.2{\cdot}10^{-1}$
107104	WZincllNp0	Alpgen	$8.6{\cdot}10^{-1}$
107105	WZincllNp1	Alpgen	$5.3{\cdot}10^{-1}$
107106	WZincllNp2	Alpgen	$2.9{\cdot}10^{-1}$
107107	WZincllNp3	Alpgen	$1.2{\cdot}10^{-1}$
107108	ZZincllNp0	Alpgen	$6.6{\cdot}10^{-1}$
107109	ZZincllNp1	Alpgen	$3.0{\cdot}10^{-1}$
107110	ZZincllNp2	Alpgen	$1.1{\cdot}10^{-1}$
107111	ZZincllNp3	Alpgen	$4.1{\cdot}10^{-2}$
119357	W^+W^+_jj	MadGraph	$2.2{\cdot}10^{-1}$
105921	W^+W^-_eνeν	MC@NLO Jimmy	$5.7\cdot10^{-1}$
105922	W^+W^-_e$\nu\mu\nu$	MC@NLO Jimmy	$5.7\cdot10^{-1}$
105923	W^+W^-_e$\nu\tau\nu$	MC@NLO Jimmy	$5.7\cdot10^{-1}$
105924	W^+W^-_$\mu\nu\mu\nu$	MC@NLO Jimmy	$5.7\cdot10^{-1}$
105925	W^+W^-_$\mu\nu$eν	MC@NLO Jimmy	$5.7\cdot10^{-1}$
105926	W^+W^-_$\mu\nu\tau\nu$	MC@NLO Jimmy	$5.7\cdot10^{-1}$
105927	W^+W^-_$\tau\nu\tau\nu$	MC@NLO Jimmy	$5.7\cdot10^{-1}$
105928	W^+W^-_$\tau\nu$eν	MC@NLO Jimmy	$5.7\cdot10^{-1}$
105929	W^+W^-_$\tau\nu\mu\nu$	MC@NLO Jimmy	$5.7\cdot10^{-1}$
105930	ZZ_llqq	MC@NLO Jimmy	$5.3\cdot10^{-1}$
105931	ZZ_llll	MC@NLO Jimmy	$2.5\cdot10^{-2}$
105932	ZZ_ll$\nu\nu$	MC@NLO Jimmy	$1.5\cdot10^{-1}$
105940	W^+Z_lνqq	MC@NLO Jimmy	1.7
105941	W^+Z_lνll	MC@NLO Jimmy	$1.6\cdot10^{-1}$
105942	W^+Z_qqlli	MC@NLO Jimmy	$5.0\cdot10^{-1}$
105970	W^-Z_lνqq	MC@NLO Jimmy	$9.8\cdot10^{-1}$
105971	W^-Z_lνll	MC@NLO Jimmy	$8.0\cdot10^{-2}$
105972	W^-Z_qqlli	MC@NLO Jimmy	$2.7\cdot10^{-1}$
108323	Z_ee_γ	MadGraph	$1.0{\cdot}10^{1}$
108324	Z_$\mu\mu$_γ	MadGraph	$1.0{\cdot}10^{1}$
108325	Z_$\tau\tau$_γ	MadGraph	1.6
108388	W^-_$e\nu$_γ	MadGraph	$1.9{\cdot}10^{1}$
106001	W^-_$\mu\nu$_γ	MadGraph	$1.9{\cdot}10^{1}$
108388	W^-_$e\nu$_γ	MadGraph	2.9
106001	W^+_$e\nu$_γ	MadGraph	$2.8{\cdot}10^{1}$
106002	W^+_$\mu\nu$_γ	MadGraph	$2.8{\cdot}10^{1}$
106003	W^+_$\tau\nu$_γ	MadGraph	4.0

Appendix B

Flavour Subtraction for different Monte Carlo Samples

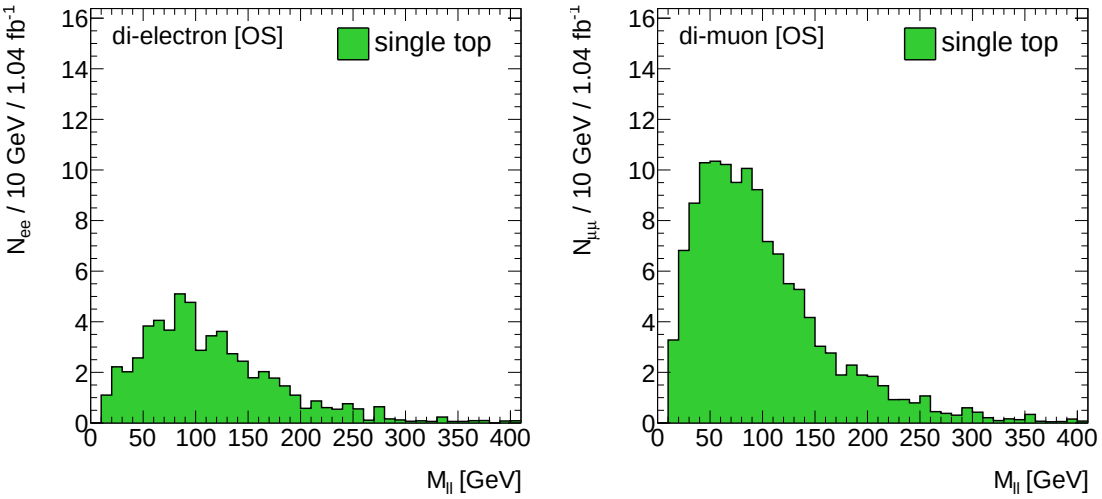

Figure B.1: FS applied to the event selection directly after the *exactly 2 opposite-sign leptons* cut on the $t\bar{t}$ sample only. The invariant mass distributions of N_{ee}(a) is added to the $N_{\mu\mu}$(b) distribution then, the different-flavour sample $N_{e\mu}$(c) is subtracted. The trigger, reconsruction and identification efficiencies are considered as explained above. The distribution of $\mathcal{S}$ after the subtraction is shown in (d).

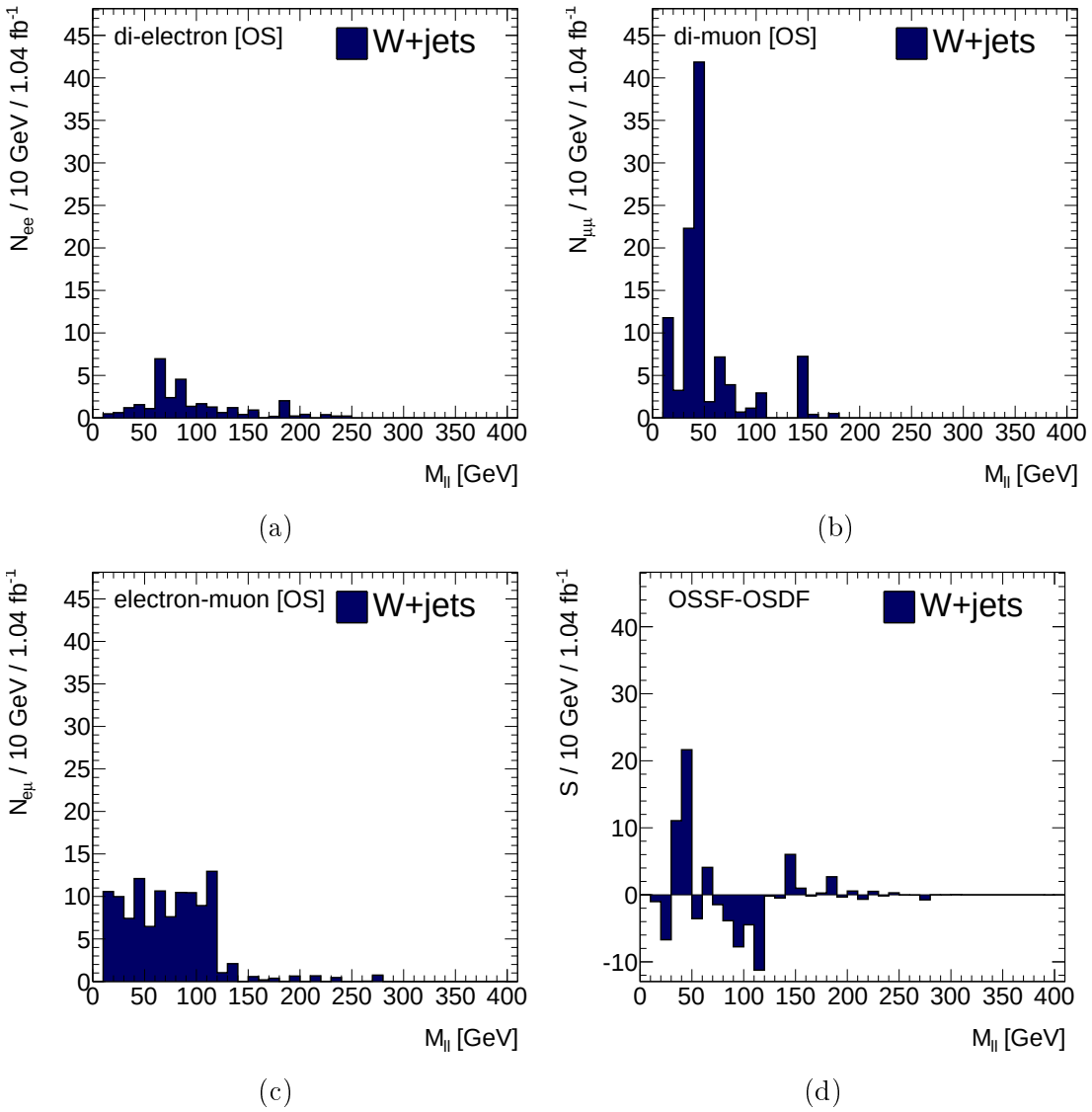

Figure B.2: FS applied to the event selection directly after the *exactly 2 opposite-sign leptons* cut on the W sample only. The invariant mass distributions of N_{ee}(a) is added to the $N_{\mu\mu}$(b) distribution then, the different-flavour sample $N_{e\mu}$(c) is subtracted. The trigger, reconsruction and identification efficiencies are considered as explained above. The distribution of $\mathcal{S}$ after the subtraction is shown in (d).

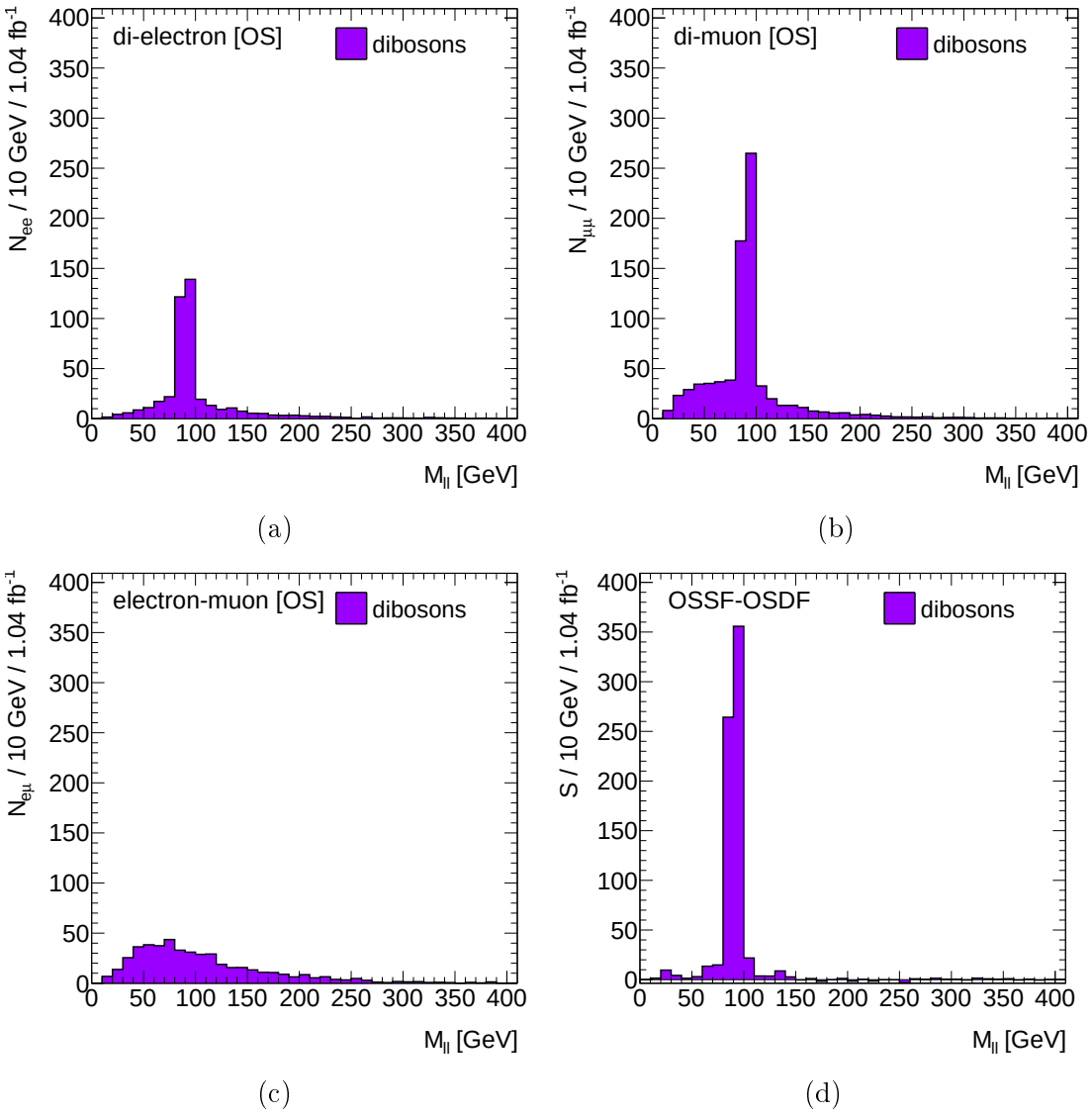

Figure B.3: FS applied to the event selection directly after the *exactly 2 opposite-sign leptons* cut on the di-boson sample only. The invariant mass distributions of N_{ee}(a) is added to the $N_{\mu\mu}$(b) distribution then, the different-flavour sample $N_{e\mu}$(c) is subtracted. The trigger, reconsruction and identification efficiencies are considered as explained above. The distribution of $\mathcal{S}$ after the subtraction is shown in (d).

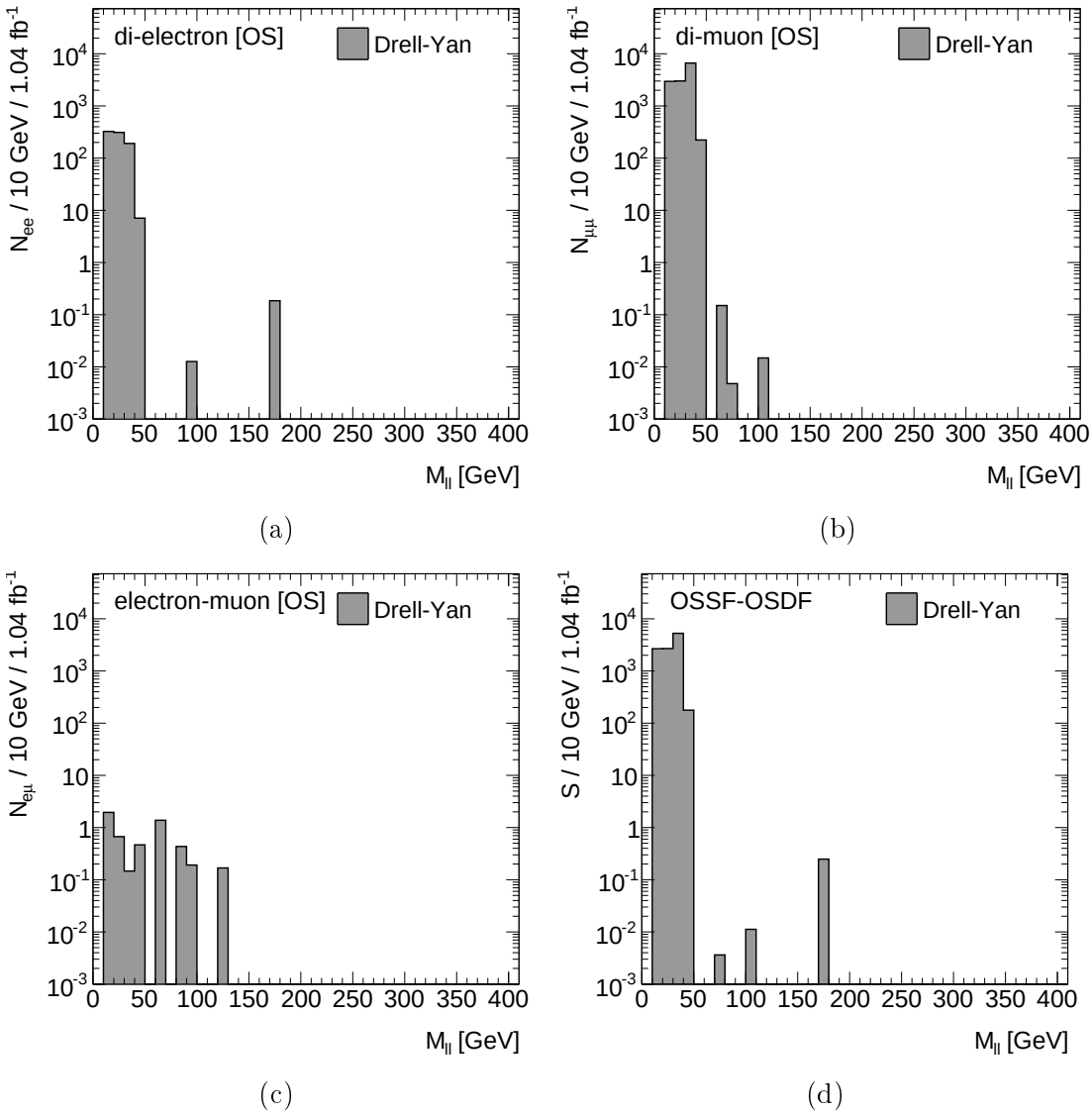

Figure B.4: FS applied to the event selection directly after the *exactly 2 opposite-sign leptons* cut on the Drell-Yan sample only. The invariant mass distributions of N_{ee}(a) is added to the $N_{\mu\mu}$(b) distribution then, the different-flavour sample $N_{e\mu}$(c) is subtracted. The trigger, reconsruction and identification efficiencies are considered as explained above. The distribution of $\mathcal{S}$ after the subtraction is shown in (d).

Appendix C

Tables of Background Estimation

C.1 Fake Background Estimation

Table C.1: A selection of one lepton QCD control regions for the electron channel. The number of events in the control regions is shown in parentheses as (T/(T+l)). All ratios are shown in percent.

	Electrons			
	Fake-rates	**T/(T + l)**	**Purity (l , T, comb)**	**Cuts**
R1	11.20 ± 0.01	(1732406/15470558)	98.93 , 69.67 , 95.65	$E_{\mathrm{T}}^{\mathrm{miss}} < 20$
R2	10.50 ± 0.01	(1277942/12167258)	99.18 , 73.41 , 96.48	$E_{\mathrm{T}}^{\mathrm{miss}} < 20$, $N_j \geq 1$
R3	10.67 ± 0.02	(269289/2523150)	98.96 , 68.23 , 95.68	$E_{\mathrm{T}}^{\mathrm{miss}} < 20$, $\Delta\phi_{E_{\mathrm{T}}^{\mathrm{miss}},l} < 0.5$
R4	10.03 ± 0.02	(199487/1989537)	99.21 , 72.31 , 96.52	$E_{\mathrm{T}}^{\mathrm{miss}} < 20$, $\Delta\phi_{E_{\mathrm{T}}^{\mathrm{miss}},l} < 0.5$, $N_j \geq 1$,
R5	11.27 ± 0.01	(560939/4979407)	98.94 , 69.90 , 95.67	$E_{\mathrm{T}}^{\mathrm{miss}} < 20$, $\Delta\phi_{E_{\mathrm{T}}^{\mathrm{miss}},l} < 1.0$
R6	10.62 ± 0.02	(415657/3913077)	99.19 , 73.84 , 96.50	$E_{\mathrm{T}}^{\mathrm{miss}} < 20$, $\Delta\phi_{E_{\mathrm{T}}^{\mathrm{miss}},l} < 1.0$, $N_j \geq 1$
R7	14.56 ± 0.01	(3126052/21464546)	97.79 , 53.85 , 91.39	$E_{\mathrm{T}}^{\mathrm{miss}} < 30$
R9	14.03 ± 0.02	(488777/3484878)	97.83 , 52.09 , 91.42	$E_{\mathrm{T}}^{\mathrm{miss}} < 30$, $\Delta\phi_{E_{\mathrm{T}}^{\mathrm{miss}},l} < 0.5$
R10	10.96 ± 0.02	(293423/2676088)	98.85 , 63.20 , 94.94	$E_{\mathrm{T}}^{\mathrm{miss}} < 30$, $\Delta\phi_{E_{\mathrm{T}}^{\mathrm{miss}},l} < 0.5$, $N_j \geq 1$,
R15	13.41 ± 0.02	(440585/3284471)	97.82 , 44.97 , 90.73	$M_T < 40$, $\Delta\phi_{E_{\mathrm{T}}^{\mathrm{miss}},l} < 0.5$, $N_j \geq 1$,
R20	13.41 ± 0.02	(440585/3284471)	97.82 , 44.97 , 90.73	$M_T < 60$, $\Delta\phi_{E_{\mathrm{T}}^{\mathrm{miss}},l} < 0.5$, $N_j \geq 1$,
R24	10.80 ± 0.03	(92587/857005)	98.80 , 60.05 , 94.62	$N_j \geq 2$, $\Delta\phi_{E_{\mathrm{T}}^{\mathrm{miss}},l} < 0.5$, $E_{\mathrm{T}}^{\mathrm{miss}} < 30$
R28	11.44 ± 0.02	(194103/1697330)	98.78 , 62.29 , 94.61	$N_j \geq 2$, $\Delta\phi_{E_{\mathrm{T}}^{\mathrm{miss}},l} < 1.0$, $E_{\mathrm{T}}^{\mathrm{miss}} < 30$
R32	10.69 ± 0.08	(16576/155000)	98.85 , 60.73 , 94.77	$N_j \geq 3$, $\Delta\phi_{E_{\mathrm{T}}^{\mathrm{miss}},l} < 0.5$, $E_{\mathrm{T}}^{\mathrm{miss}} < 20$

Table C.2: A selection of two lepton same-sign QCD control regions for the muon channel. The number of events in the control regions is shown in parentheses as (lT/(lT + ll)). Equation 6.3 must be applied to the ratio Tl/(Tl + ll) in order to reproduce the single lepton fake-rate in this table.

	Muons			
	Rake-rates	**Tl/(Tl+ll)**	**Purity (ll , lT,comb)**	**Cuts**
R1	47.20 ± 2.05	(413/ 644)	100.00 , 98.79 , 99.22	$E_{\mathrm{T}}^{\mathrm{miss}} < 10$
R2	47.15 ± 1.39	(901/ 1406)	100.00 , 98.21 , 98.85	$E_{\mathrm{T}}^{\mathrm{miss}} < 20$
R3	47.63 ± 1.26	(1097/ 1700)	99.98 , 97.74 , 98.54	$E_{\mathrm{T}}^{\mathrm{miss}} < 30$
R4	49.06 ± 1.21	(1256/ 1908)	99.89 , 93.03 , 95.38	$E_{\mathrm{T}}^{\mathrm{miss}} < 60$
R5	48.20 ± 2.11	(402/ 618)	100.00 , 98.70 , 99.15	$E_{\mathrm{T}}^{\mathrm{miss}} < 10, /Z$
R6	47.73 ± 1.42	(871/ 1348)	100.00 , 98.31 , 98.91	$E_{\mathrm{T}}^{\mathrm{miss}} < 20, /Z$
R7	47.95 ± 1.30	(1054/ 1626)	100.00 , 97.91 , 98.65	$E_{\mathrm{T}}^{\mathrm{miss}} < 30, /Z$
R8	49.30 ± 1.24	(1204/ 1823)	99.92 , 93.33 , 95.56	$E_{\mathrm{T}}^{\mathrm{miss}} < 60, /Z$
R9	53.85 ± 1.86	(595/ 850)	99.22 , 86.82 , 90.54	$N_j \geq 1$
R10	50.83 ± 2.49	(308/ 457)	100.00 , 96.50 , 97.64	$N_j \geq 1$, $E_{\mathrm{T}}^{\mathrm{miss}} < 20$
R14	50.34 ± 2.55	(292/ 436)	100.00 , 96.79 , 97.85	$N_j \geq 1, /Z$, $E_{\mathrm{T}}^{\mathrm{miss}} < 20$
R18	51.83 ± 4.45	(99/ 145)	100.00 , 97.56 , 98.33	$N_j \geq 2$, $E_{\mathrm{T}}^{\mathrm{miss}} < 20$
R19	51.50 ± 3.55	(155/ 228)	99.86 , 95.52 , 96.91	$N_j \geq 2$, $E_{\mathrm{T}}^{\mathrm{miss}} < 30$
R22	51.38 ± 4.57	(93/ 137)	100.00 , 98.55 , 99.01	$N_j \geq 2, /Z$, $E_{\mathrm{T}}^{\mathrm{miss}} < 20$
R23	50.69 ± 3.62	(146/ 217)	100.00 , 96.15 , 97.41	$N_j \geq 2, /Z$, $E_{\mathrm{T}}^{\mathrm{miss}} < 30$

Table C.3: Nominal estimates and each contribution of the differences in estimates (region, pt, MC subtraction from left to right), together with the combined difference obtained by summing each contribution in quadrature. The positive or negative numbers show whether the systematic error contributes upward or downward compared to the nominal value. The asymmetric systematic difference is shown in the second column from the right ($\Delta(\mathrm{est})^{comb}_{asym}$), while the maximum of these values is shown in last column ($\Delta(\mathrm{est})^{comb}_{sym}$).

Region	Channel	est(nom)	$\Delta(est)$ $^{reg}_{sym}$	$^{p_{\mathrm{T}}}_{asym}$	$^{MC}_{asym}$	$\Delta(\mathrm{est})^{comb}_{asym}$	$\Delta(\mathrm{est})^{comb}_{sym}$
FS-SR1	EE	5.270± 1.697	+1.131	-1.092	-1.805	+ 1.131 - 2.393	± 2.393
FS-SR2	EE	1.503± 1.515	+0.305	+0.587	-0.493	+ 0.662 - 0.580	± 0.662
FS-SR3	EE	0.175± 0.186	+0.044	-0.027	-0.065	+ 0.044 - 0.083	± 0.083
FS-SR1	EM	30.224± 6.190	+4.846	+1.740	-2.776	+ 5.149 - 5.585	± 5.585
FS-SR2	EM	32.261± 6.375	+5.234	+5.646	-2.543	+ 7.699 - 5.819	± 7.699
FS-SR3	EM	0.925± 0.963	+0.156	+0.048	-0.060	+ 0.164 - 0.167	± 0.167
FS-SR1	MM	21.760± 6.165	+3.244	-3.653	-0.499	+ 3.244 - 4.911	± 4.911
FS-SR2	MM	19.379± 5.766	+3.036	+4.928	-0.462	+ 5.788 - 3.071	± 5.788
FS-SR3	MM	-0.080± 0.033	+0.012	+0.009	0.002	+ 0.015 - 0.012	± 0.015

Table C.4: Fake estimates per bin in $m_{\ell\ell}$ for di-electron opposite-sign final-state in FS-SR1 . The first column gives the measured number of tight-tight, tight-loose, loose-tight and loose-loose di-lepton pairs, the second and third the estimates calculated by the matrix (cf. Eq. 6.1).

Bin [GeV]	N(TT)	N(Tl)	N(lT)	N(ll)	est(rf)	est(fr)	est(ff)	est(rf+fr+ff)
0 - 20	9	2	2	3	0.03 ±0.19	0.03 ±0.19	0.04 ±0.03	0.10 ±0.28
20 - 40	17	10	8	3	0.90 ±0.42	0.65 ±0.37	0.01 ±0.03	1.57 ±0.56
40 - 60	51	15	9	6	0.80 ±0.52	0.05 ±0.41	0.05 ±0.04	0.90 ±0.67
60 - 80	91	29	22	7	1.79 ±0.72	0.91 ±0.63	0.02 ±0.05	2.71 ±0.96
80 - 100	0	0	0	0	0.00 ±0.00	0.00 ±0.00	0.00 ±0.00	0.00 ±0.00
100 - 120	49	12	8	5	0.47 ±0.47	-0.03 ±0.39	0.05 ±0.04	0.49 ±0.61
120 - 140	32	11	4	4	0.70 ±0.44	-0.18 ±0.28	0.04 ±0.03	0.55 ±0.53
140 - 160	26	5	1	7	-0.00 ±0.31	-0.51 ±0.17	0.11 ±0.04	-0.40 ±0.35
160 - 180	19	4	2	4	0.06 ±0.27	-0.19 ±0.20	0.06 ±0.03	-0.07 ±0.34
180 - 200	9	2	1	2	0.04 ±0.19	-0.08 ±0.14	0.03 ±0.02	-0.01 ±0.24
200 - 220	7	0	0	1	-0.16 ±0.06	-0.16 ±0.06	0.02 ±0.02	-0.30 ±0.08
220 - 240	9	0	2	2	-0.21 ±0.07	0.04 ±0.19	0.03 ±0.02	-0.14 ±0.20
240 - 260	6	1	0	3	-0.04 ±0.14	-0.17 ±0.06	0.05 ±0.03	-0.16 ±0.15
260 - 280	6	0	1	1	-0.14 ±0.05	-0.01 ±0.14	0.02 ±0.02	-0.13 ±0.15
280 - 300	5	0	1	1	-0.12 ±0.05	0.01 ±0.14	0.02 ±0.02	-0.09 ±0.15
300 - 320	2	0	0	0	-0.04 ±0.03	-0.04 ±0.03	0.00 ±0.00	-0.08 ±0.04
320 - 340	1	0	0	0	-0.02 ±0.02	-0.02 ±0.02	0.00 ±0.00	-0.04 ±0.03
340 - 360	2	1	0	0	0.09 ±0.13	-0.04 ±0.03	-0.00 ±0.00	0.05 ±0.13
Overflow	3	1	3	3	0.03 ±0.02	0.28 ±0.18	0.04 ±0.02	0.34 ±0.19
Sum	344	93	64	52	4.17 ±1.30	0.53 ±1.10	0.56 ±0.12	5.27 ±1.71

Table C.5: Fake estimates per bin in $m_{\ell\ell}$ for electron-muon opposite-sign final-state in FS-SR1. The first column gives the measured number of tight-tight, tight-loose, loose-tight and loose-loose di-lepton pairs, the second and third the estimates calculated by the matrix (cf. Eq. 6.1).

Bin [GeV]	N(TT)	N(Tl)	N(lT)	N(ll)	est(rf)	est(fr)	est(ff)	est(rf+fr+ff)
0 - 20	34	4	9	5	2.74 ±1.91	-0.05 ±0.48	0.50 ±0.26	3.18 ±1.98
20 - 40	107	14	27	1	5.07 ±2.51	2.15 ±0.78	-0.04 ±0.13	7.18 ±2.63
40 - 60	167	16	23	5	2.85 ±2.33	0.32 ±0.82	0.46 ±0.26	3.63 ±2.49
60 - 80	131	22	29	5	9.93 ±3.44	1.82 ±0.86	0.31 ±0.27	12.06 ±3.56
80 - 100	0	0	0	0	0.00 ±0.00	0.00 ±0.00	0.00 ±0.00	0.00 ±0.00
100 - 120	72	6	17	2	2.58 ±1.90	0.79 ±0.61	0.14 ±0.17	3.52 ±2.00
120 - 140	68	7	7	1	-1.01 ±0.17	0.27 ±0.52	0.11 ±0.12	-0.63 ±0.56
140 - 160	46	6	6	0	-0.60 ±0.10	0.59 ±0.46	-0.01 ±0.01	-0.03 ±0.47
160 - 180	33	8	1	2	-0.66 ±0.18	0.24 ±0.43	0.23 ±0.16	-0.20 ±0.50
180 - 200	35	3	1	0	0.47 ±0.94	-0.32 ±0.25	-0.01 ±0.02	0.14 ±0.98
200 - 220	14	1	2	0	-0.18 ±0.05	0.10 ±0.23	-0.00 ±0.00	-0.09 ±0.24
220 - 240	14	0	0	0	-0.19 ±0.05	-0.29 ±0.08	0.00 ±0.00	-0.47 ±0.09
240 - 260	4	0	4	1	1.71 ±1.34	0.09 ±0.22	0.08 ±0.12	1.88 ±1.36
260 - 280	4	1	1	0	-0.05 ±0.03	0.17 ±0.18	-0.00 ±0.00	0.12 ±0.19
280 - 300	4	0	0	0	-0.05 ±0.03	-0.08 ±0.04	0.00 ±0.00	-0.14 ±0.05
300 - 320	4	1	0	0	-0.05 ±0.03	0.05 ±0.13	-0.00 ±0.00	-0.01 ±0.14
320 - 340	3	0	1	0	-0.04 ±0.02	0.07 ±0.13	-0.00 ±0.00	0.03 ±0.13
340 - 360	2	0	0	0	-0.03 ±0.02	-0.04 ±0.03	0.00 ±0.00	-0.07 ±0.03
360 - 380	2	0	0	0	-0.03 ±0.02	-0.04 ±0.03	0.00 ±0.00	-0.07 ±0.03
380 - 400	1	0	2	0	-0.01 ±0.01	0.23 ±0.18	-0.00 ±0.00	0.22 ±0.18
Overflow	5	1	0	0	-0.07 ±0.00	0.02 ±0.00	-0.00 ±0.00	-0.04 ±0.00
Sum	750	90	130	22	22.38 ±5.80	6.09 ±1.89	1.75 ±0.56	30.22 ±6.12

Table C.6: Fake estimates per bin in $m_{\ell\ell}$ for di-muon opposite-sign final-state in FS-SR1. The first column gives the measured number of tight-tight, tight-loose, loose-tight and loose-loose di-lepton pairs, the second and third the estimates calculated by the matrix (cf. Eq. 6.1).

Bin [GeV]	N(TT)	N(Tl)	N(lT)	N(ll)	est(rf)	est(fr)	est(ff)	est(rf+fr+ff)
0 - 20	18	0	0	0	-0.24 ±0.06	-0.24 ±0.06	0.00 ±0.00	-0.48 ±0.08
20 - 40	106	5	5	0	3.30 ±2.10	3.30 ±2.10	-0.10 ±0.04	6.50 ±2.97
40 - 60	121	5	2	0	3.06 ±2.10	0.30 ±1.33	-0.06 ±0.03	3.30 ±2.49
60 - 80	127	10	4	1	6.83 ±3.09	1.30 ±2.06	0.70 ±0.85	8.83 ±3.81
80 - 100	0	0	0	0	0.00 ±0.00	0.00 ±0.00	0.00 ±0.00	0.00 ±0.00
100 - 120	57	2	1	0	1.11 ±1.33	0.19 ±0.94	-0.03 ±0.02	1.28 ±1.63
120 - 140	32	0	2	0	-0.41 ±0.08	1.44 ±1.33	-0.02 ±0.02	1.01 ±1.33
140 - 160	31	0	2	0	-0.39 ±0.08	1.45 ±1.33	-0.02 ±0.02	1.04 ±1.33
160 - 180	15	1	0	0	0.73 ±0.94	-0.19 ±0.05	-0.01 ±0.01	0.53 ±0.94
180 - 200	11	0	0	0	-0.15 ±0.05	-0.15 ±0.05	0.00 ±0.00	-0.29 ±0.06
200 - 220	9	0	0	0	-0.12 ±0.04	-0.12 ±0.04	0.00 ±0.00	-0.24 ±0.06
220 - 240	4	0	0	0	-0.05 ±0.03	-0.05 ±0.03	0.00 ±0.00	-0.11 ±0.04
240 - 260	3	0	1	0	-0.03 ±0.03	0.89 ±0.94	-0.01 ±0.01	0.85 ±0.94
260 - 280	3	0	0	0	-0.04 ±0.02	-0.04 ±0.02	0.00 ±0.00	-0.08 ±0.03
280 - 300	4	0	0	0	-0.05 ±0.03	-0.05 ±0.03	0.00 ±0.00	-0.11 ±0.04
300 - 320	2	0	0	0	-0.03 ±0.02	-0.03 ±0.02	0.00 ±0.00	-0.05 ±0.03
320 - 340	0	0	0	0	0.00 ±0.00	0.00 ±0.00	0.00 ±0.00	0.00 ±0.00
340 - 360	0	0	0	0	0.00 ±0.00	0.00 ±0.00	0.00 ±0.00	0.00 ±0.00
360 - 380	2	0	0	0	-0.03 ±0.02	-0.03 ±0.02	0.00 ±0.00	-0.05 ±0.03
380 - 400	0	0	0	0	0.00 ±0.00	0.00 ±0.00	0.00 ±0.00	0.00 ±0.00
Overflow	6	0	0	0	-0.08 ±0.00	-0.08 ±0.00	0.00 ±0.00	-0.16 ±0.00
Sum	551	23	17	1	13.42 ±4.59	7.89 ±3.96	0.46 ±0.86	21.76 ±6.12

Table C.7: Fake estimates per bin in $m_{\ell\ell}$ for di-electron opposite-sign final-state in FS-SR2. The first column gives the measured number of tight-tight, tight-loose, loose-tight and loose-loose di-lepton pairs, the second and third the estimates calculated by the matrix (cf. Eq. 6.1).

Bin [GeV]	N(TT)	N(Tl)	N(lT)	N(ll)	est(rf)	est(fr)	est(ff)	est(rf+fr+ff)
0 - 20	9	1	2	2	-0.08 ±0.14	0.04 ±0.19	0.03 ±0.02	-0.01 ±0.24
20 - 40	16	7	5	2	0.55 ±0.35	0.30 ±0.30	0.01 ±0.02	0.85 ±0.46
40 - 60	44	9	7	3	0.22 ±0.41	-0.03 ±0.37	0.02 ±0.03	0.21 ±0.55
60 - 80	54	16	10	4	0.90 ±0.54	0.15 ±0.43	0.02 ±0.03	1.07 ±0.69
80 - 100	86	19	7	2	0.65 ±0.59	-0.86 ±0.39	0.00 ±0.03	-0.21 ±0.71
100 - 120	36	8	4	3	0.25 ±0.38	-0.26 ±0.29	0.03 ±0.03	0.02 ±0.48
120 - 140	21	10	2	1	0.84 ±0.42	-0.17 ±0.21	-0.01 ±0.02	0.67 ±0.46
140 - 160	20	5	0	3	0.18 ±0.30	-0.45 ±0.10	0.04 ±0.03	-0.22 ±0.32
160 - 180	13	3	1	1	0.10 ±0.23	-0.15 ±0.15	0.01 ±0.02	-0.03 ±0.28
180 - 200	7	1	1	1	-0.03 ±0.14	-0.03 ±0.14	0.01 ±0.02	-0.05 ±0.20
200 - 220	5	0	0	0	-0.10 ±0.05	-0.10 ±0.05	0.00 ±0.00	-0.20 ±0.07
220 - 240	8	0	0	0	-0.16 ±0.06	-0.16 ±0.06	0.00 ±0.00	-0.33 ±0.08
240 - 260	3	0	0	1	-0.08 ±0.04	-0.08 ±0.04	0.02 ±0.02	-0.14 ±0.06
260 - 280	3	0	0	1	-0.08 ±0.04	-0.08 ±0.04	0.02 ±0.02	-0.14 ±0.06
280 - 300	4	0	1	1	-0.10 ±0.04	0.03 ±0.14	0.01 ±0.02	-0.05 ±0.14
300 - 320	2	0	0	0	-0.04 ±0.03	-0.04 ±0.03	0.00 ±0.00	-0.08 ±0.04
320 - 340	1	0	0	0	-0.02 ±0.02	-0.02 ±0.02	0.00 ±0.00	-0.04 ±0.03
340 - 360	2	0	0	0	-0.04 ±0.03	-0.04 ±0.03	0.00 ±0.00	-0.08 ±0.04
Overflow	2	0	3	2	-0.07 ±0.02	0.31 ±0.18	0.02 ±0.02	0.27 ±0.18
Sum	336	79	43	27	2.89 ±1.20	-1.64 ±0.93	0.25 ±0.09	1.50 ±1.52

[FS-SR2 Electron-Muon Fake Estimates per $m_{\ell\ell}$-Bin]Fake estimates per bin in $m_{\ell\ell}$ for electron-muon opposite-sign final-state in FS-SR2.The first column gives the measured number of tight-tight, tight-loose, loose-tight and loose-loose di-lepton pairs, the second and third the estimates calculated by the matrix (cf. Eq. 6.1).

Bin [GeV]	N(TT)	N(Tl)	N(lT)	N(ll)	est(rf)	est(fr)	est(ff)	est(rf+fr+ff)
0 - 20	31	3	9	3	2.07 ±1.65	0.22 ±0.45	0.28 ±0.20	2.57 ±1.72
20 - 40	83	12	20	1	5.38 ±2.51	1.50 ±0.68	-0.03 ±0.13	6.85 ±2.60
40 - 60	148	13	14	4	1.33 ±1.90	-0.49 ±0.70	0.39 ±0.24	1.23 ±2.04
60 - 80	115	21	20	4	10.25 ±3.44	0.99 ±0.75	0.21 ±0.24	11.44 ±3.53
80 - 100	95	15	19	2	4.17 ±2.32	1.50 ±0.72	0.10 ±0.17	5.77 ±2.44
100 - 120	61	4	13	0	2.96 ±1.89	0.48 ±0.49	-0.08 ±0.04	3.36 ±1.95
120 - 140	58	7	6	1	-0.88 ±0.16	0.35 ±0.50	0.11 ±0.12	-0.42 ±0.54
140 - 160	40	5	5	0	-0.53 ±0.09	0.45 ±0.42	-0.01 ±0.01	-0.08 ±0.43
160 - 180	30	7	1	1	-0.51 ±0.14	0.29 ±0.39	0.11 ±0.12	-0.11 ±0.43
180 - 200	32	2	1	0	0.51 ±0.94	-0.38 ±0.21	-0.01 ±0.02	0.11 ±0.97
200 - 220	12	1	2	0	-0.16 ±0.05	0.14 ±0.23	-0.00 ±0.00	-0.02 ±0.24
220 - 240	13	0	0	0	-0.18 ±0.05	-0.27 ±0.07	0.00 ±0.00	-0.44 ±0.09
240 - 260	3	0	4	0	1.84 ±1.33	0.23 ±0.19	-0.04 ±0.03	2.03 ±1.35
260 - 280	4	1	1	0	-0.05 ±0.03	0.17 ±0.18	-0.00 ±0.00	0.12 ±0.19
280 - 300	3	0	0	0	-0.04 ±0.02	-0.06 ±0.04	0.00 ±0.00	-0.10 ±0.04
300 - 320	3	0	0	0	-0.04 ±0.02	-0.06 ±0.04	0.00 ±0.00	-0.10 ±0.04
320 - 340	3	0	1	0	-0.04 ±0.02	0.07 ±0.13	-0.00 ±0.00	0.03 ±0.13
340 - 360	2	0	0	0	-0.03 ±0.02	-0.04 ±0.03	0.00 ±0.00	-0.07 ±0.03
360 - 380	1	0	0	0	-0.01 ±0.01	-0.02 ±0.02	0.00 ±0.00	-0.03 ±0.02
380 - 400	1	0	1	0	-0.01 ±0.01	0.11 ±0.13	-0.00 ±0.00	0.09 ±0.13
Overflow	3	1	0	0	-0.04 ±0.00	0.07 ±0.00	-0.00 ±0.00	0.03 ±0.00
Sum	741	92	117	16	25.99 ±6.02	5.24 ±1.81	1.02 ±0.48	32.26 ±6.30

Table C.8: Fake estimates per bin in $m_{\ell\ell}$ for di-muon opposite-sign final-state in FS-SR2 . The first column gives the measured number of tight-tight, tight-loose, loose-tight and loose-loose di-lepton pairs, the second and third the estimates calculated by the matrix (cf. Eq. 6.1).

Bin [GeV]	N(TT)	N(Tl)	N(lT)	N(ll)	est(rf)	est(fr)	est(ff)	est(rf+fr+ff)
0 - 20	15	0	0	0	-0.20 ±0.05	-0.20 ±0.05	0.00 ±0.00	-0.40 ±0.07
20 - 40	86	5	5	0	3.57 ±2.10	3.57 ±2.10	-0.11 ±0.04	7.04 ±2.97
40 - 60	106	4	2	0	2.33 ±1.88	0.49 ±1.33	-0.05 ±0.03	2.77 ±2.30
60 - 80	114	8	4	0	5.98 ±2.67	2.30 ±1.88	-0.13 ±0.04	8.16 ±3.26
80 - 100	90	3	0	0	1.59 ±1.63	-1.18 ±0.14	-0.02 ±0.02	0.39 ±1.63
100 - 120	49	0	1	0	-0.65 ±0.10	0.27 ±0.94	-0.00 ±0.01	-0.38 ±0.94
120 - 140	29	0	2	0	-0.37 ±0.08	1.48 ±1.33	-0.02 ±0.02	1.09 ±1.33
140 - 160	28	0	1	0	-0.36 ±0.07	0.56 ±0.94	-0.01 ±0.01	0.18 ±0.94
160 - 180	13	1	0	0	0.76 ±0.94	-0.16 ±0.05	-0.01 ±0.01	0.59 ±0.94
180 - 200	10	0	0	0	-0.13 ±0.04	-0.13 ±0.04	0.00 ±0.00	-0.27 ±0.06
200 - 220	7	0	0	0	-0.09 ±0.04	-0.09 ±0.04	0.00 ±0.00	-0.19 ±0.05
220 - 240	4	0	0	0	-0.05 ±0.03	-0.05 ±0.03	0.00 ±0.00	-0.11 ±0.04
240 - 260	3	0	1	0	-0.03 ±0.03	0.89 ±0.94	-0.01 ±0.01	0.85 ±0.94
260 - 280	3	0	0	0	-0.04 ±0.02	-0.04 ±0.02	0.00 ±0.00	-0.08 ±0.03
280 - 300	3	0	0	0	-0.04 ±0.02	-0.04 ±0.02	0.00 ±0.00	-0.08 ±0.03
300 - 320	2	0	0	0	-0.03 ±0.02	-0.03 ±0.02	0.00 ±0.00	-0.05 ±0.03
320 - 340	0	0	0	0	0.00 ±0.00	0.00 ±0.00	0.00 ±0.00	0.00 ±0.00
340 - 360	0	0	0	0	0.00 ±0.00	0.00 ±0.00	0.00 ±0.00	0.00 ±0.00
360 - 380	1	0	0	0	-0.01 ±0.01	-0.01 ±0.01	0.00 ±0.00	-0.03 ±0.02
380 - 400	0	0	0	0	0.00 ±0.00	0.00 ±0.00	0.00 ±0.00	0.00 ±0.00
Overflow	4	0	0	0	-0.05 ±0.00	-0.05 ±0.00	0.00 ±0.00	-0.11 ±0.00
Sum	567	21	16	0	12.17 ±4.31	7.56 ±3.76	-0.35 ±0.08	19.38 ±5.72

Table C.9: Fake estimates per bin in $m_{\ell\ell}$ for di-electron opposite-sign final-state in FS-SR3 ($E_{\mathrm{T}}^{\mathrm{miss}} > 250\,\mathrm{GeV}$). First column shows the measured number of tight-tight, tight-loose, loose-tight and loose-loose di-lepton pairs. The second and third columns list the number of estimated events calculated by the matrix (cf. Eq. 6.1) for real-fake, fake-real, fake-fake and their combination, respectively.

Bin [GeV]	N(TT)	N(Tl)	N(lT)	N(ll)	est(rf)	est(fr)	est(ff)	est(rf+fr+ff)
0 - 50	235934	48012	36418	12770	1183.48 ±39.43	-272.93 ±35.07	83.57 ±1.99	994.11 ±52.81
50 - 100	2079	594	436	418	27.81 ±3.29	7.96 ±2.86	4.83 ±0.33	40.60 ±4.37
100 - 150	183	50	32	23	2.36 ±0.95	0.09 ±0.78	0.23 ±0.08	2.68 ±1.23
150 - 200	31	5	9	3	-0.02 ±0.31	0.48 ±0.40	0.02 ±0.03	0.48 ±0.51
200 - 250	12	2	0	3	-0.04 ±0.20	-0.29 ±0.08	0.05 ±0.03	-0.28 ±0.21
250 - 300	1	0	1	0	-0.02 ±0.02	0.11 ±0.13	-0.00 ±0.00	0.09 ±0.13
300 - 350	1	0	1	0	-0.02 ±0.02	0.11 ±0.13	-0.00 ±0.00	0.09 ±0.13
Overflow	0	0	0	0	0.00 ±0.00	0.00 ±0.00	0.00 ±0.00	0.00 ±0.00
Sum	238241	48663	36897	13217	1213.55 ±39.58	-264.47 ±35.20	88.70 ±2.02	1037.77 ±53.00
Sum > 250	2	0	2	0	-0.04 ±0.03	0.22 ±0.18	-0.00 ±0.00	0.17 ±0.19

Table C.10: Fake estimates per bin in $m_{\ell\ell}$ for electron-muon opposite-sign final-state in FS-SR3 ($E_{\mathrm{T}}^{\mathrm{miss}} > 250\,\mathrm{GeV}$). First column shows the measured number of tight-tight, tight-loose, loose-tight and loose-loose di-lepton pairs. The second and third columns list the number of estimated events calculated by the matrix (cf. Eq. 6.1) for real-fake, fake-real, fake-fake and their combination, respectively.

Bin [GeV]	N(TT)	N(Tl)	N(lT)	N(ll)	est(rf)	est(fr)	est(ff)	est(rf+fr+ff)
0 - 50	4027	1944	4166	3916	452.03 ±38.30	131.96 ±24.40	427.20 ±24.00	1011.20 ±51.36
50 - 100	1383	326	364	157	57.14 ±9.97	30.60 ±3.56	15.72 ±1.69	103.46 ±10.72
100 - 150	405	43	66	9	11.48 ±4.17	2.48 ±1.32	0.65 ±0.36	14.61 ±4.39
150 - 200	72	5	15	0	1.87 ±1.64	0.75 ±0.55	-0.06 ±0.03	2.55 ±1.73
200 - 250	12	3	3	0	1.72 ±1.33	0.30 ±0.27	-0.04 ±0.03	1.98 ±1.36
250 - 300	7	1	1	0	0.85 ±0.94	0.00 ±0.14	-0.02 ±0.02	0.83 ±0.95
Overflow	1	0	1	0	-0.01 ±0.00	0.11 ±0.13	-0.00 ±0.00	0.09 ±0.13
Sum	5907	2322	4616	4082	525.08 ±39.86	166.20 ±24.71	443.44 ±24.07	1134.73 ±52.71
Sum > 250	8	1	2	0	0.84 ±0.94	0.11 ±0.19	-0.02 ±0.02	0.92 ±0.96

Table C.11: Fake estimates per bin in $m_{\ell\ell}$ for di-muon opposite-sign final-state in FS-SR3 ($E_{\mathrm{T}}^{\mathrm{miss}} > 250\,\mathrm{GeV}$). First column shows the measured number of tight-tight, tight-loose, loose-tight and loose-loose di-lepton pairs. The second and third columns list the number of estimated events calculated by the matrix (cf. Eq. 6.1) for real-fake, fake-real, fake-fake and their combination, respectively.

Bin [GeV]	N(TT)	N(Tl)	N(lT)	N(ll)	est(rf)	est(fr)	est(ff)	est(rf+fr+ff)
0 - 50	443481	9600	7613	2034	1356.28 ±111.90	-475.14 ±100.15	1595.46 ±168.75	2476.61 ±225.90
50 - 100	1527	109	43	14	69.86 ±10.77	9.03 ±6.92	10.30 ±3.36	89.19 ±13.24
100 - 150	308	8	10	0	3.44 ±2.66	5.29 ±2.98	-0.17 ±0.05	8.57 ±4.00
150 - 200	42	1	1	0	0.38 ±0.94	0.38 ±0.94	-0.02 ±0.02	0.74 ±1.33
200 - 250	11	0	1	0	-0.14 ±0.05	0.79 ±0.94	-0.01 ±0.01	0.64 ±0.94
250 - 300	1	0	0	0	-0.01 ±0.01	-0.01 ±0.01	0.00 ±0.00	-0.03 ±0.02
300 - 350	1	0	0	0	-0.01 ±0.01	-0.01 ±0.01	0.00 ±0.00	-0.03 ±0.02
Overflow	1	0	0	0	-0.01 ±0.01	-0.01 ±0.01	0.00 ±0.00	-0.03 ±0.02
Sum	445372	9718	7668	2048	1429.79 ±112.45	-459.70 ±100.44	1605.57 ±168.79	2575.67 ±226.33
Sum > 250	3	0	0	0	-0.04 ±0.02	-0.04 ±0.02	0.00 ±0.00	-0.08 ±0.03

C.2 Z/γ^* Background Estimation

Table C.12: The scale factors and predictions for the Z/γ^* contribution for OS di-leptons in the different-flavour subtraction signal regions with for the ee, $\mu\mu$, and $e\mu$ channels (syst) and stats. (only one error, than its stats). Due to suffering statistics, $e\mu$ results are computed using MC.

	FS SR1	FS SR2	FS SR3
	ee		
β	$4.98 \times 10^{-4} \pm 0.30 \times 10^{-4}$	$3.76 \times 10^{-3} \pm 0.27 \times 10^{-3}$	$7.57 \times 10^{-8} \pm 4.37 \times 10^{-8}$
$N_{Z/\gamma^*}^{\text{est,SR}}$	$85.944 \pm 4.580 \pm 5.096$	$45.62 \pm 11.76 \pm 3.31$	$0.012 \pm 0.672(\text{sys.}) \pm 0.007$
$N_{Z/\gamma^*}^{\text{MC,SR}}$	80.952 ± 4.795	50.95 ± 3.66	0.012 ± 0.007
	$\mu\mu$		
β	$1.33 \times 10^{-4} \pm .09 \times 10^{-4}$	$1.75 \times 10^{-3} \pm 0.1 \times 10^{-3}$	$2.62 \times 10^{-6} \pm 0.83 \times 10^{-6}$
$N_{Z/\gamma^*}^{\text{est,SR}}$	$40.924 \pm 10.458 \pm 2.866$	$37.95 \pm 4.89 \pm 2.60$	$0.81 \pm 0.06 \pm 0.26$
$N_{Z/\gamma^*}^{\text{MC,SR}}$	37.647 ± 2.636	42.77 ± 2.92	0.75 ± 0.24
	$e\mu$		
$N_{Z/\gamma^*}^{\text{MC,SR}}$	$40.814 \pm 5.713 \pm 3.207$	$29.09 \pm 5.64 \pm 2.68$	$1.028 \pm 0.023 \pm 0.420$

C.3 $t\bar{t}$ Background Estimation

Table C.13: Jet energy scale, jet energy resolution, ISR/FSR, and generator systematics on the signal region and control region expected $t\bar{t}$, and on their ratio. The rates for MC@NLO, Powheg+Pythia, Powheg+Jimmy, and Alpgen are reported (unweighted for pile-up).

Region	nominal	up	down	systematics
jet energy scale systematics				
CR	848.2	852.1	837.9	0.008
SR	10.4	12.2	9.8	0.114
SR/CR	0.0123	0.0143	0.0117	0.106
jet energy resolution systematics				
CR	848.2	844.8	842.1	0.003
SR	10.4	11.0	10.9	0.008
SR/CR	0.0123	0.0130	0.0129	0.0055
ISR/FSR systematics				
CR	848.2	781.0	824.1	0.0254
SR	10.43	6.94	10.74	0.1822
SR/CR	0.0123	0.0086	0.0135	0.200

region	MC@NLO	Powheg+Pythia	Powheg+Jimmy	Alpgen	systematics
CR	844.8	805.0	820.4	822.3	0.035
SR	11.00	12.03	13.07	10.29	0.126
SR/CR	0.0130	0.0149	0.0159	0.0125	0.156

Appendix D

Analysis and Limits

D.1 $E_{\mathrm{T}}^{\mathrm{miss}}$ Discrepancy in $Z \to ee$ Decays Between Data and MC

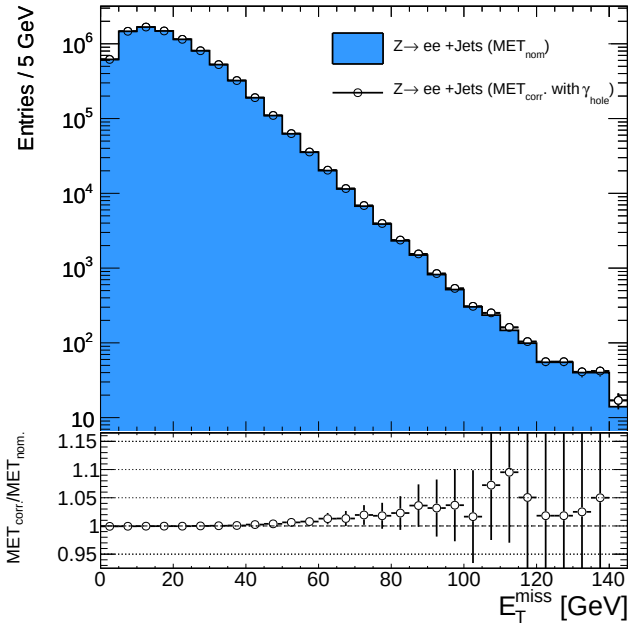

Figure D.1: Comparison of the nominal $E_{\mathrm{T}}^{\mathrm{miss}}$ and a $E_{\mathrm{T}}^{\mathrm{miss}}$ distribution considering the momentum of radiated photons pointing to the LAr hole. Therefore, the true γ momentum is used to correct the reconstructed $E_{\mathrm{T}}^{\mathrm{miss}}$.

The comparisons of data and MC distributions in Sec. 6.4.2 and the evaluation of the toy experiments discussed in Sec. 7.1 show some differences between data and MC. The most significant discrepancy is found in the $E_{\mathrm{T}}^{\mathrm{miss}}$ distribution in the ee-channel around the Z-boson peak (cf. Fig. 6.7).

A source of additional $E_{\mathrm{T}}^{\mathrm{miss}}$ in data in comparison to MC is the loss of transverse momentum caused by photons pointing into the LAr hole. As explained in Sec. 6.4.1 dead Front-End-Board (FEB) electronics in the LAr calorimeter (from period-E onwards) induce a $\eta - \phi$-region ($-0.1 < \eta < 1.5$ and $-0.9 < \phi < -0.5$) which cannot be used in the analysis. Events with electrons or jets pointing into that region are rejected. As the di-lepton analysis does not reconstruct photons explicitly, neither additional cuts for vetoing events which might contain unreconstructed photons have been defined nor the $E_{\mathrm{T}}^{\mathrm{miss}}$ of the MC samples has been corrected for these losses. The $E_{\mathrm{T}}^{\mathrm{miss}}$ in MC is hence

underestimated and therefore the number of simulated events in MC in the medium $E_{\mathrm{T}}^{\mathrm{miss}}$ region is lower than the number of events measured in data. This explains why the number of events are underestimated with both, the data-driven estimates and the Monte Carlo only predictions.

Figure D.1 gives a rough estimate of the effect of undetected radiated photons on the $E_{\mathrm{T}}^{\mathrm{miss}}$ distribution of $Z \to ee$ events. The reconstructed $E_{\mathrm{T}}^{\mathrm{miss}}$ is corrected by the momentum of the true (on MC generator level) photons pointing to the LAr hole. In total a 5% effect has to be considered above 80 GeV.

D.2 Events and Event Displays in FS-SR3

Table D.1: Complete events list for signal candidates measured in the flavour subtraction signal region 3 with $E_{\mathrm{T}}^{\mathrm{miss}} > 250\,\mathrm{GeV}$ in data. The table lists the run and event number, the measured missing transverse momentum, invariant mass, signal leading and next-to-leading lepton transverse momentum and the jet multiplicity for jets with $|\eta| < 2.8$ and $p_{\mathrm{T}} > 20\,\mathrm{GeV}$.

Run No.	Event No.	$E_{\mathrm{T}}^{\mathrm{miss}}$[GeV]	$m_{\ell\ell}$[GeV]	$p_{\mathrm{T}\ lep_1}$ [GeV]	$p_{\mathrm{T}\ lep_2}$ [GeV]	N jets
ee						
180122	8295683	261.855	92.6174	147.213	105.607	0
182787	12895389	300.673	93.4532	54.1738	28.1605	6
$e\mu$						
180144	1395055	282.836	43.6477	11.9333	66.1253	6
180400	115341046	277.24	13.1634	11.3718	33.2494	4
182516	10854629	252.145	363.638	27.8232	314.433	1
183003	41337610	260.354	220.454	148.064	81.9169	4
182886	1100476	250.532	150.203	13.4892	65.0855	8
183780	103984901	261.877	16.891	32.0025	24.564	7
182787	21047345	281.411	175.166	65.8499	112.487	3
183003	85014655	418.986	54.7563	108.773	34.3677	5
$\mu\mu$						
182284	15150909	350.612	62.2081	54.9322	40.7305	6
183021	102318024	265.81	144.48	405.57	35.5816	3
182787	64797947	332.421	95.663	45.9433	34.1826	3

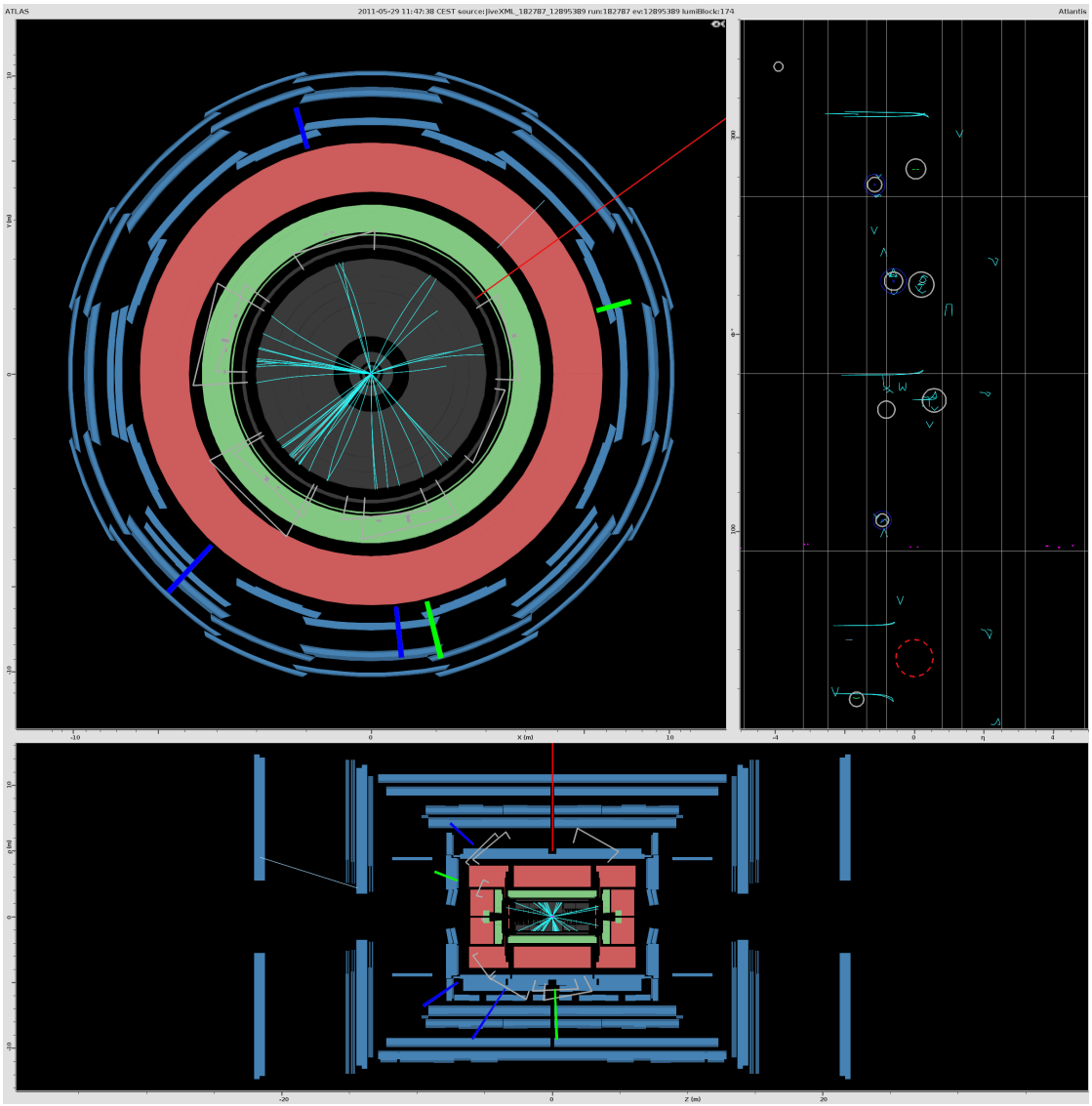

Figure D.2: Event Display of Event 12895389 from run 182787 which was found in FS-SR3. Top left plot shows the $X-Y$-plane, the top right plot the $\eta-\phi$-plane and the bottom plot the $Z-\rho$-plane. The green bars mark the direction of the selected electrons and the long narrow red bar marks the missing transverse momentum. The cone of the reconstructed jets are highlighted by light grey markers in the calorimeter regions (drawn in green and red). The b-tagged jets are marked with additional blue bars. The detailed event information is given in Tab. D.1 (second line).

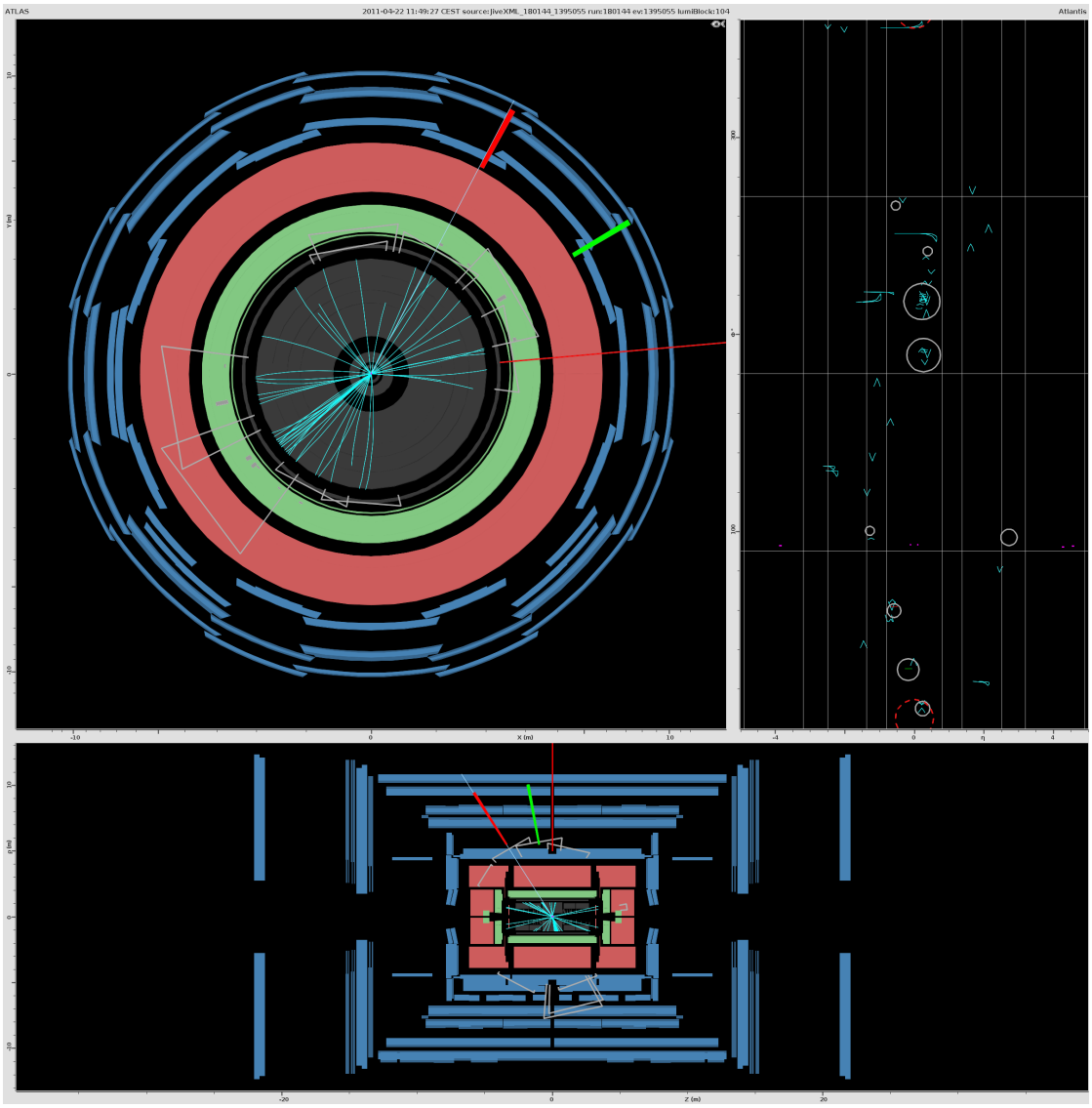

Figure D.3: Event Display of Event 1395055 from run 180144 which was found in FS-SR3. Top left plot shows the $X-Y$-plane, the top right plot the $\eta-\phi$-plane and the bottom plot the $Z-\rho$-plane. The red bar marks the direction of the selected muon, the green bar the direction of the selected electron and the long narrow red bar marks the missing transverse momentum. The cone of the reconstructed jets are highlighted by light grey markers in the calorimeter regions (drawn in green and red). The detailed event information is given in Tab. D.1 (third line).

Table D.2: FS-SR1 ($E_{\mathrm{T}}^{\mathrm{miss}} > 80\,\mathrm{GeV}$ and Z veto): Number of predicted events and systematic and statistical uncertainties considered in the FS analysis. The first column shows the total number of events predicted by MC per SM process and final state. The columns JES$_\uparrow$, JES$_\downarrow$, JER, E$_{e,\uparrow}$, E$_{e,\downarrow}$, $\mu_{MS,\uparrow}$, $\mu_{MS,\downarrow}$, $\mu_{ID,\uparrow}$,$\mu_{ID,\downarrow}$ list the relative number of events after smearing the individual scale or resolution as explained in Sec. 6.6 in order to estimate the corresponding systematic uncertainty. The scale and resolution systematics (the larger value per uncertainty) are added in quadrature given in column tot$_{scale}$. The last columns show the uncertainties for the luminosity, cross section, pdf and due to MC statistics.

$N_{e^\pm e^\mp}$

process	Events	JES$_\uparrow$	JES$_\downarrow$	JER	E$_{e,\uparrow}$	E$_{e,\downarrow}$	$\mu_{MS,\uparrow}$	$\mu_{MS,\downarrow}$	$\mu_{ID,\uparrow}$	$\mu_{ID,\downarrow}$	tot$_{scale}$	lumi	σ	pdf	stat.
$t\bar{t}$	197.76	16.718	-13.745	2.980	0.048	-0.512	-0.305	0.012	-0.305	0.012	16.99	7.32	13.84	9.89	8.30
Z	75.14	0.651	0.271	-3.856	-1.956	0.706	0.000	0.000	0.000	0.000	4.37	2.78	3.76	3.76	6.02
diBoson	14.32	1.364	-0.439	0.599	0.011	0.341	-0.000	0.000	0.000	-0.000	1.53	0.53	0.72	0.72	1.79
singleTop	12.45	1.042	-1.343	0.249	0.073	0.067	0.000	-0.000	-0.000	-0.000	1.37	0.46	0.87	0.62	0.89
DrellYan	0.57	0.014	0.064	0.064	0.000	0.000	0.000	0.000	0.000	0.000	0.09	0.02	0.03	0.03	0.37

$N_{e^\pm \mu^\mp}$

process	Events	JES$_\uparrow$	JES$_\downarrow$	JER	E$_{e,\uparrow}$	E$_{e,\downarrow}$	$\mu_{MS,\uparrow}$	$\mu_{MS,\downarrow}$	$\mu_{ID,\uparrow}$	$\mu_{ID,\downarrow}$	tot$_{scale}$	lumi	σ	pdf	stat.
$t\bar{t}$	580.83	40.183	-21.337	11.420	0.435	-0.191	-6.726	-5.859	-7.905	-4.608	43.05	21.49	40.66	29.04	14.12
Z	40.72	5.382	-5.458	-0.790	-0.000	-0.890	-0.643	-0.643	-0.643	-0.643	5.66	1.51	2.04	2.04	4.08
diBoson	34.23	3.304	-0.678	0.298	0.123	0.580	-0.323	-0.323	-0.323	0.023	3.40	1.27	1.71	1.71	2.76
singleTop	40.80	2.537	-1.881	0.451	-0.086	-0.213	-0.276	-0.268	-0.192	-0.376	2.63	1.51	2.86	2.04	1.65
DrellYan	0.04	0.000	0.000	0.000	0.000	0.000	0.000	0.000	0.000	0.000	0.00	0.00	0.00	0.00	0.03

$N_{\mu^\pm \mu^\mp}$

process	Events	JES$_\uparrow$	JES$_\downarrow$	JER	E$_{e,\uparrow}$	E$_{e,\downarrow}$	$\mu_{MS,\uparrow}$	$\mu_{MS,\downarrow}$	$\mu_{ID,\uparrow}$	$\mu_{ID,\downarrow}$	tot$_{scale}$	lumi	σ	pdf	stat.
$t\bar{t}$	417.52	17.891	-15.792	5.492	-0.000	-0.000	-10.721	-9.450	-10.481	-8.752	23.98	15.45	29.23	20.88	11.38
Z	37.26	7.263	-1.715	2.828	0.000	-0.000	1.835	-1.873	0.429	-0.737	8.05	1.38	1.86	1.86	3.63
diBoson	31.63	2.137	-2.085	0.353	-0.000	-0.000	-0.305	-0.984	-0.845	-0.405	2.53	1.17	1.58	1.58	2.43
singleTop	36.83	0.454	-1.125	0.248	-0.000	-0.000	-0.817	-0.697	-0.531	-0.936	1.69	1.36	2.58	1.84	1.53
DrellYan	0.63	0.060	0.024	0.657	0.000	0.000	0.000	0.000	0.000	0.000	0.66	0.02	0.03	0.03	0.28

Table D.3: FS-SR2 ($E_{\mathrm{T}}^{\mathrm{miss}} > 80\,\mathrm{GeV}$ and 2 jets(20,20)): Number of predicted events and systematic and statistical uncertainties considered in the FS analysis. The first column shows the total number of events predicted by MC per SM process and final state. The columns JES$_\uparrow$, JES$_\downarrow$, JER, E$_{e,\uparrow}$, E$_{e,\downarrow}$, $\mu_{MS,\uparrow}$, $\mu_{MS,\downarrow}$, $\mu_{ID,\uparrow}$,$\mu_{ID,\downarrow}$ list the relative number of events after smearing the individual scale or resolution as explained in Sec. 6.6 in order to estimate the corresponding systematic uncertainty. The scale and resolution systematics (the larger value per uncertainty) are added in quadrature given in column tot$_{scale}$. The last columns show the uncertainties for the luminosity, cross section, pdf and due to MC statistics.

$N_{e^\pm e^\mp}$

process	Events	JES$_\uparrow$	JES$_\downarrow$	JER	E$_{e,\uparrow}$	E$_{e,\downarrow}$	$\mu_{MS,\uparrow}$	$\mu_{MS,\downarrow}$	$\mu_{ID,\uparrow}$	$\mu_{ID,\downarrow}$	tot$_{scale}$	lumi	σ	pdf	stat.
$t\bar{t}$	220.35	21.225	-19.668	-0.720	-0.089	-0.175	-0.305	0.012	-0.305	0.012	21.24	8.15	15.42	11.02	8.72
Z	50.45	23.288	-6.268	3.906	0.597	1.063	0.000	0.000	0.000	-0.000	23.64	1.87	2.52	2.52	4.76
diBoson	7.69	2.802	-1.308	-1.241	-0.026	0.004	0.000	0.000	0.000	0.000	3.06	0.28	0.38	0.38	1.13
singleTop	9.89	1.328	-1.584	0.325	-0.034	-0.042	-0.000	-0.000	-0.000	-0.000	1.62	0.37	0.69	0.49	0.81
DrellYan	0.57	0.014	-0.079	-0.079	0.000	0.000	0.000	0.000	0.000	0.000	0.11	0.02	0.03	0.03	0.37

$N_{e^\pm \mu^\mp}$

process	Events	JES$_\uparrow$	JES$_\downarrow$	JER	E$_{e,\uparrow}$	E$_{e,\downarrow}$	$\mu_{MS,\uparrow}$	$\mu_{MS,\downarrow}$	$\mu_{ID,\uparrow}$	$\mu_{ID,\downarrow}$	tot$_{scale}$	lumi	σ	pdf	stat.
$t\bar{t}$	624.32	56.450	-42.860	4.714	1.313	-1.361	-6.938	-6.301	-7.637	-5.807	57.59	23.10	43.70	31.22	14.59
Z	29.06	5.633	-4.730	-0.685	0.000	-0.028	-0.157	-0.157	-0.157	-0.157	5.68	1.08	1.45	1.45	3.43
diBoson	11.09	4.657	-1.580	-0.414	0.000	0.346	-0.335	-0.335	-0.335	0.012	4.71	0.41	0.55	0.55	1.51
singleTop	31.52	3.308	-3.415	-0.632	0.055	-0.278	-0.142	-0.115	-0.172	-0.199	3.49	1.17	2.21	1.58	1.45
DrellYan	0.04	0.000	0.000	0.000	0.000	0.000	0.000	0.000	0.000	0.000	0.00	0.00	0.00	0.00	0.03

$N_{\mu^\pm \mu^\mp}$

process	Events	JES$_\uparrow$	JES$_\downarrow$	JER	E$_{e,\uparrow}$	E$_{e,\downarrow}$	$\mu_{MS,\uparrow}$	$\mu_{MS,\downarrow}$	$\mu_{ID,\uparrow}$	$\mu_{ID,\downarrow}$	tot$_{scale}$	lumi	σ	pdf	stat.
$t\bar{t}$	437.02	28.132	-25.202	2.181	-0.000	-0.000	-9.039	-8.631	-8.865	-8.389	30.93	16.17	30.59	21.85	11.68
Z	42.59	7.362	-3.380	4.386	0.000	-0.000	0.920	-1.913	-0.005	-0.433	8.79	1.58	2.13	2.13	4.02
diBoson	14.98	4.897	-2.939	-0.683	-0.102	0.000	-0.051	-0.324	-0.294	-0.052	4.96	0.55	0.75	0.75	1.42
singleTop	27.36	2.424	-2.229	-0.327	-0.000	-0.000	-0.719	-0.552	-0.446	-0.718	2.65	1.01	1.92	1.37	1.31
DrellYan	0.63	0.060	0.024	0.657	0.000	0.000	0.000	0.000	0.000	0.000	0.66	0.02	0.03	0.03	0.28

Table D.4: FS-SR3 ($E_{\mathrm{T}}^{\mathrm{miss}} > 250\,\mathrm{GeV}$): Number of predicted events and systematic and statistical uncertainties considered in the FS analysis. The first column shows the total number of events predicted by MC per SM process and final state. The columns JES$_\uparrow$, JES$_\downarrow$, JER, E$_{e,\uparrow}$, E$_{e,\downarrow}$, $\mu_{MS,\uparrow}$, $\mu_{MS,\downarrow}$, $\mu_{ID,\uparrow}$,$\mu_{ID,\downarrow}$ list the relative number of events after smearing the individual scale or resolution as explained in Sec. 6.6 in order to estimate the corresponding systematic uncertainty. The scale and resolution systematics (the larger value per uncertainty) are added in quadrature given in column tot$_{scale}$. The last columns show the uncertainties for the luminosity, cross section, pdf and due to MC statistics.

$N_{e^\pm e^\mp}$

process	Events	JES$_\uparrow$	JES$_\downarrow$	JER	E$_{e,\uparrow}$	E$_{e,\downarrow}$	$\mu_{MS,\uparrow}$	$\mu_{MS,\downarrow}$	$\mu_{ID,\uparrow}$	$\mu_{ID,\downarrow}$	tot$_{scale}$	lumi	σ	pdf	stat.
$t\bar{t}$	2.23	1.555	-0.621	0.052	-0.000	0.576	-0.000	-0.000	0.000	0.000	1.66	0.08	0.16	0.11	1.05
Z	0.01	0.614	0.000	0.000	0.000	0.000	0.000	0.000	0.000	0.000	0.61	0.00	0.00	0.00	0.01
diBoson	0.54	0.043	0.000	0.015	0.000	0.008	0.000	0.000	0.000	0.000	0.05	0.02	0.03	0.03	0.29
singleTop	0.11	0.000	0.000	0.047	0.000	0.000	0.000	0.000	0.000	0.000	0.05	0.00	0.01	0.01	0.11
DrellYan	0.00	0.000	0.000	0.000	0.000	0.000	0.000	0.000	0.000	0.000	0.00	0.00	0.00	0.00	0.00

$N_{e^\pm \mu^\mp}$

process	Events	JES$_\uparrow$	JES$_\downarrow$	JER	E$_{e,\uparrow}$	E$_{e,\downarrow}$	$\mu_{MS,\uparrow}$	$\mu_{MS,\downarrow}$	$\mu_{ID,\uparrow}$	$\mu_{ID,\downarrow}$	tot$_{scale}$	lumi	σ	pdf	stat.
$t\bar{t}$	4.78	1.261	-1.183	0.252	-0.000	-0.000	-0.000	-0.000	-0.000	-0.000	1.29	0.18	0.33	0.24	1.23
Z	1.03	-0.017	-0.017	-0.017	0.000	0.000	0.000	0.000	0.000	0.000	0.02	0.04	0.05	0.05	0.62
diBoson	0.04	0.030	-0.017	0.000	0.000	0.000	0.000	0.000	0.000	0.000	0.03	0.00	0.00	0.00	0.03
singleTop	0.47	0.163	-0.087	-0.003	-0.000	0.000	-0.000	0.000	0.000	0.000	0.16	0.02	0.03	0.02	0.16
DrellYan	0.00	0.000	0.000	0.000	0.000	0.000	0.000	0.000	0.000	0.000	0.00	0.00	0.00	0.00	0.00

$N_{\mu^\pm \mu^\mp}$

process	Events	JES$_\uparrow$	JES$_\downarrow$	JER	E$_{e,\uparrow}$	E$_{e,\downarrow}$	$\mu_{MS,\uparrow}$	$\mu_{MS,\downarrow}$	$\mu_{ID,\uparrow}$	$\mu_{ID,\downarrow}$	tot$_{scale}$	lumi	σ	pdf	stat.
$t\bar{t}$	2.73	0.809	-0.106	0.252	0.000	0.000	-0.350	-0.354	-0.354	-0.313	0.98	0.10	0.19	0.14	0.99
Z	0.74	0.000	0.000	0.000	0.000	0.000	0.000	0.000	0.000	0.000	0.00	0.03	0.04	0.04	0.53
diBoson	0.67	-0.031	0.312	-0.038	-0.000	-0.000	0.006	-0.001	-0.001	0.006	0.31	0.02	0.03	0.03	0.25
singleTop	0.48	0.021	-0.042	-0.000	-0.000	-0.000	0.000	-0.048	-0.048	0.000	0.08	0.02	0.03	0.02	0.17
DrellYan	0.00	0.000	0.000	0.000	0.000	0.000	0.000	0.000	0.000	0.000	0.00	0.00	0.00	0.00	0.00

D.3 Model Dependent Limits

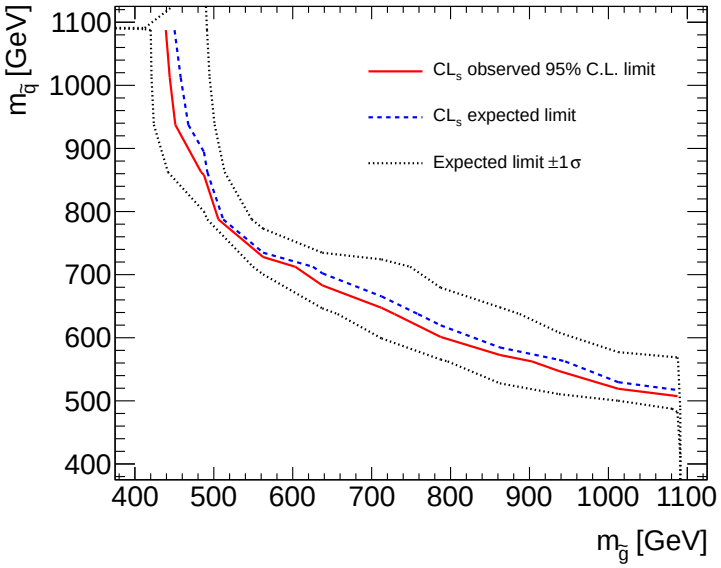

(a)

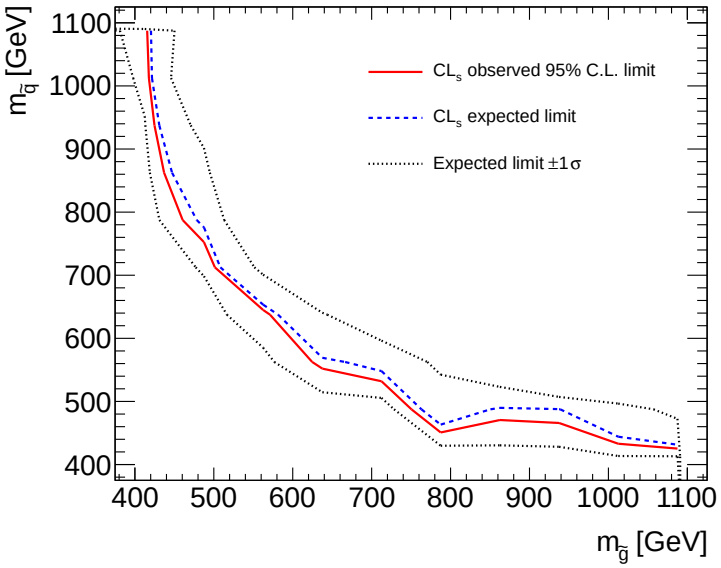

(b)

Figure D.4: The limits on light LSP (a) and compressed spectrum (b) phenomenological grids are determined for N grid points in each grid. For each grid point one million toy experiments are evaluated by the CL$_s$ method. If the CL$_s$ value of a given grid point is $< 5\%$, the point is excluded at 95% confidence. The limits are calculated for the FS-SR1 ($E_{\mathrm{T}}^{\mathrm{miss}} > 80\,\mathrm{GeV}$ and Z-veto).

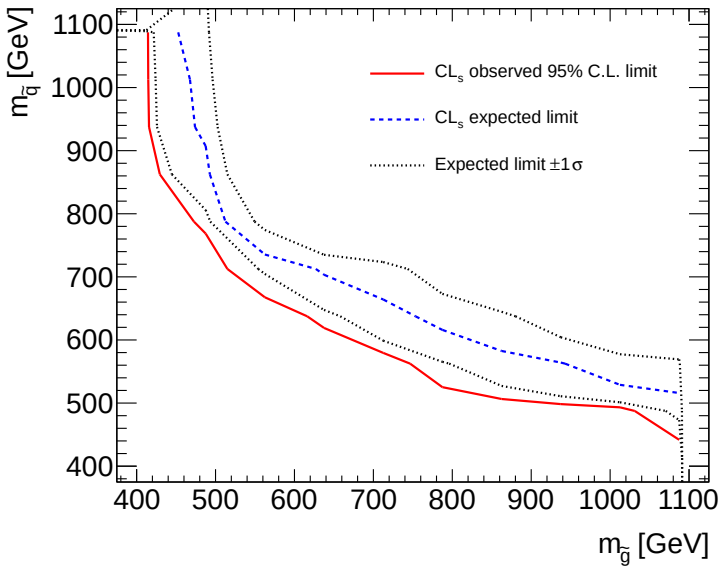

(a)

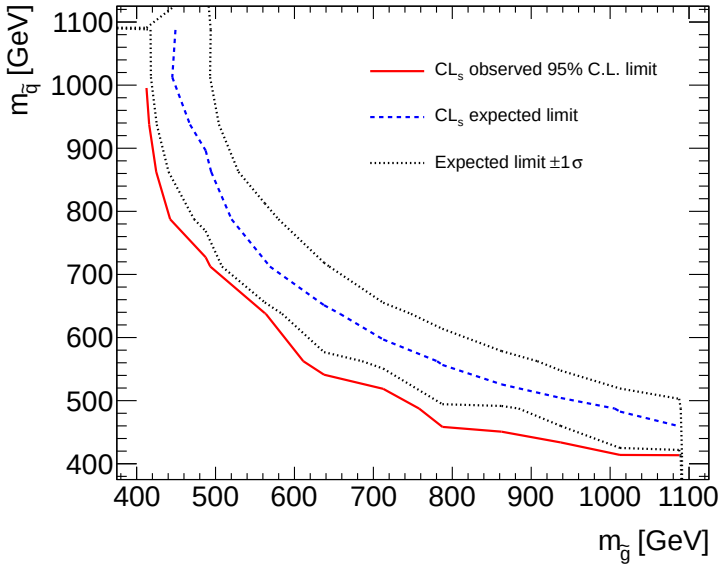

(b)

Figure D.5: The limits on light LSP (a) and compressed spectrum (b) phenomenological grids are determined for N grid points in each grid. For each grid point one million toy experiments are evaluated by the CL_s method. If the CL_s value of a given grid point is $< 5\%$, the point is excluded at 95% confidence. The limits are calculated for the FS-SR2 ($E_{\mathrm{T}}^{\mathrm{miss}} > 80\,\mathrm{GeV}$ and n-jets ≥ 2).

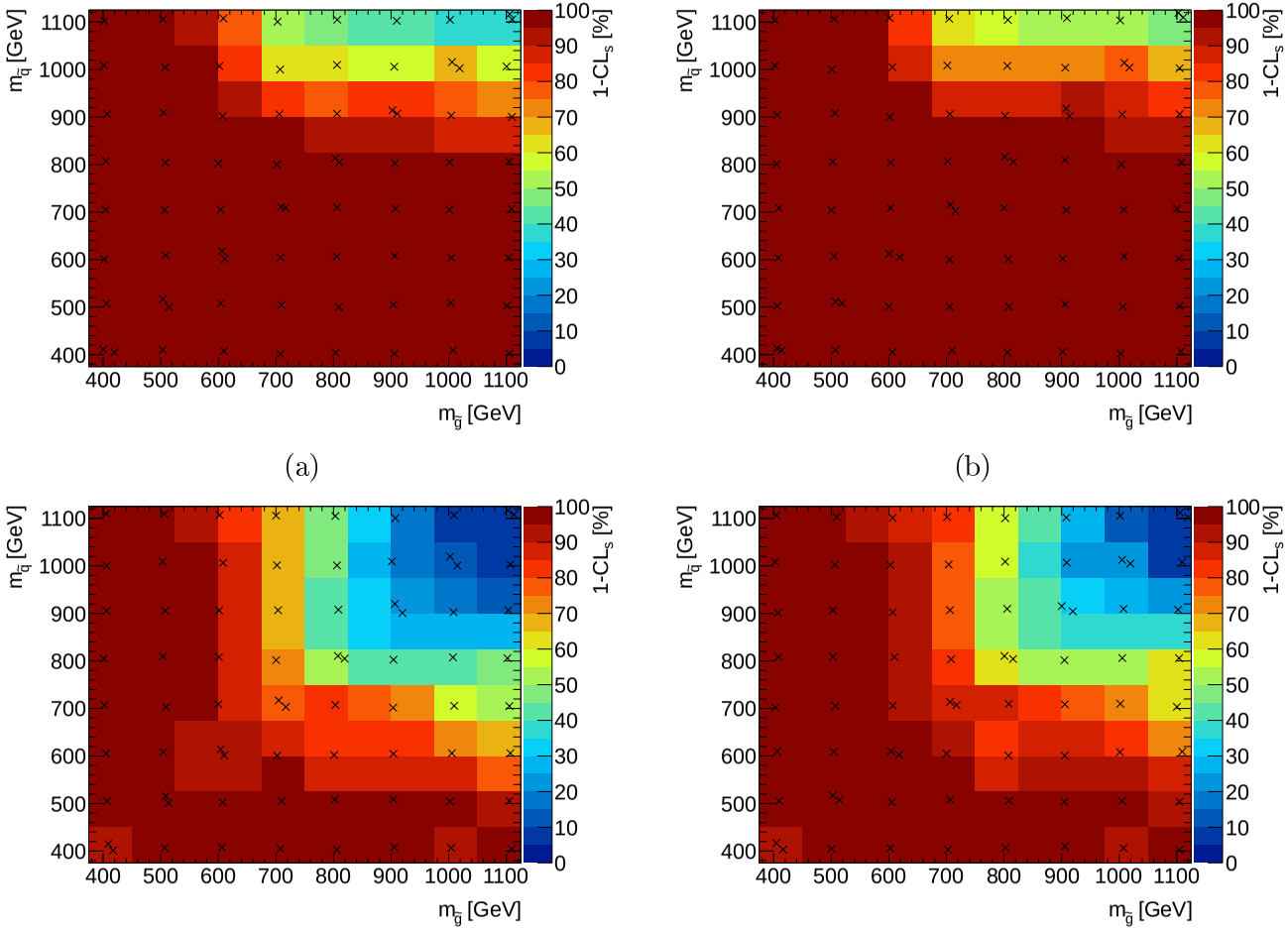

Figure D.6: The expected (a) and observed (b) $1 - \mathrm{CL_s}$ values and the position of the generated grid points are shown for light LSP phenomenological grid and expected (c) and observed (d) for compressed spectrum phenomenological grid. If the $\mathrm{CL_s}$ value of a given grid point is $< 5\%$, the point is excluded at 95% confidence. The limits are calculated for the FS-SR3 ($E_{\mathrm{T}}^{\mathrm{miss}} > 250\,\mathrm{GeV}$).

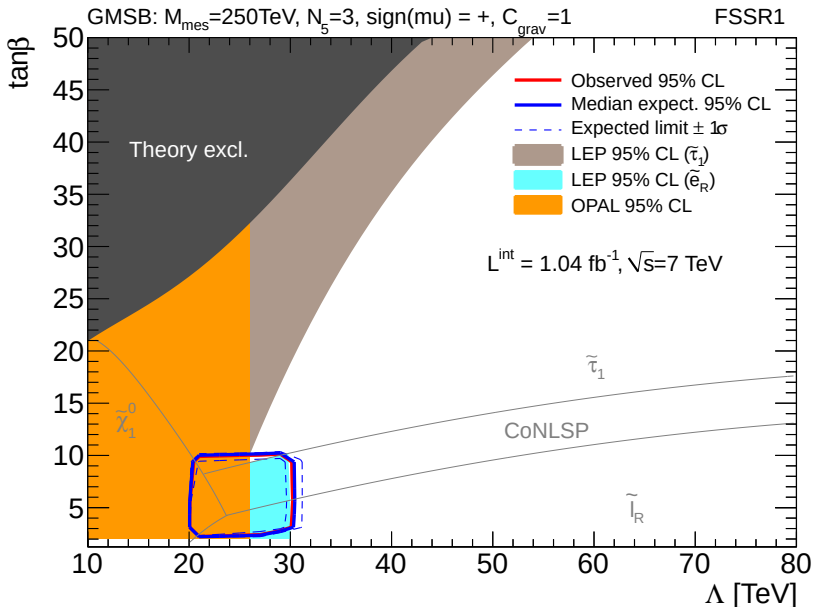

(a)

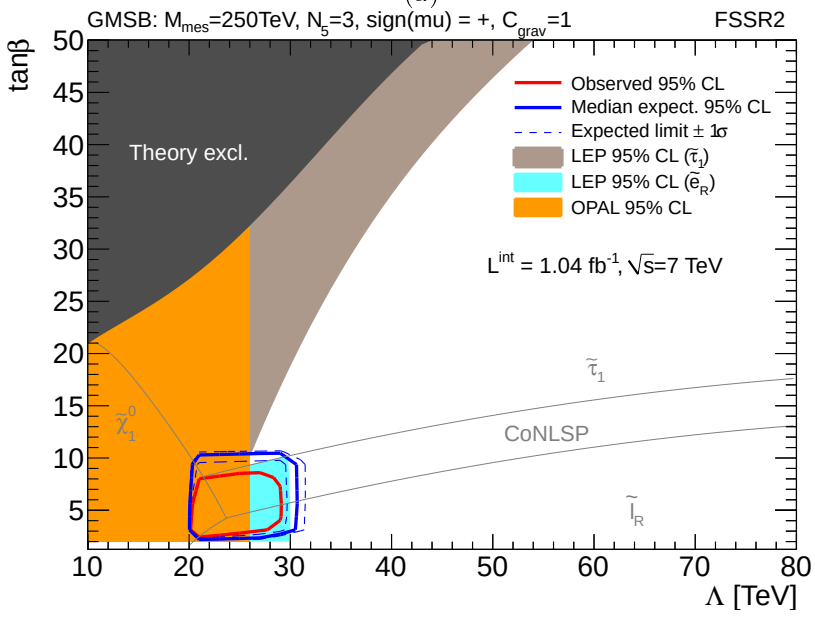

(b)

Figure D.7: The limits on GMSB with the following fixed SUSY parameters: $M_{mes} = 250\,\text{TeV}$, $N_5 = 3$, $C_{grav} = 1$, and $\mu = 1$ are determined for 60 grid points. For each grid point one million toy experiments are evaluated by the CL_s method. If the CL_s value of a given grid point is $< 5\%$, the point is excluded at 95% confidence. The limits are calculated for the FS-SR1 (a) and FS-SR2 (b), respectively.

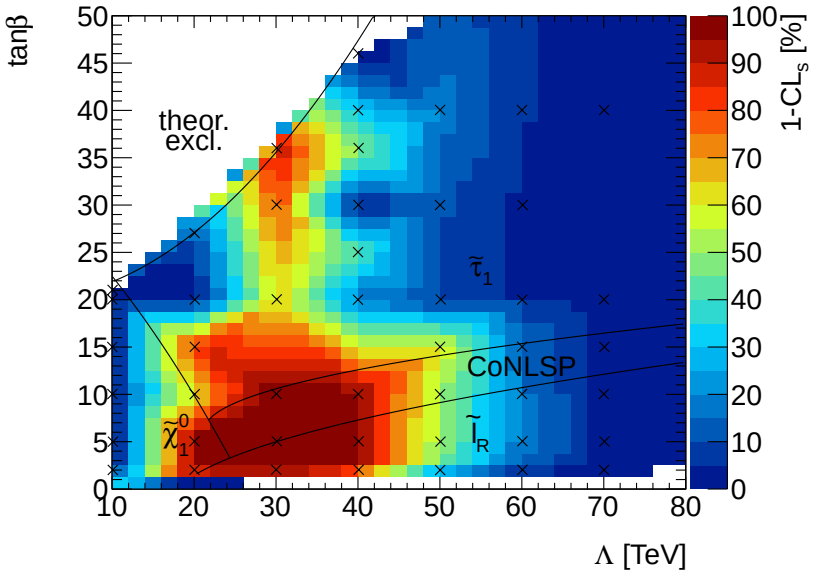

(a)

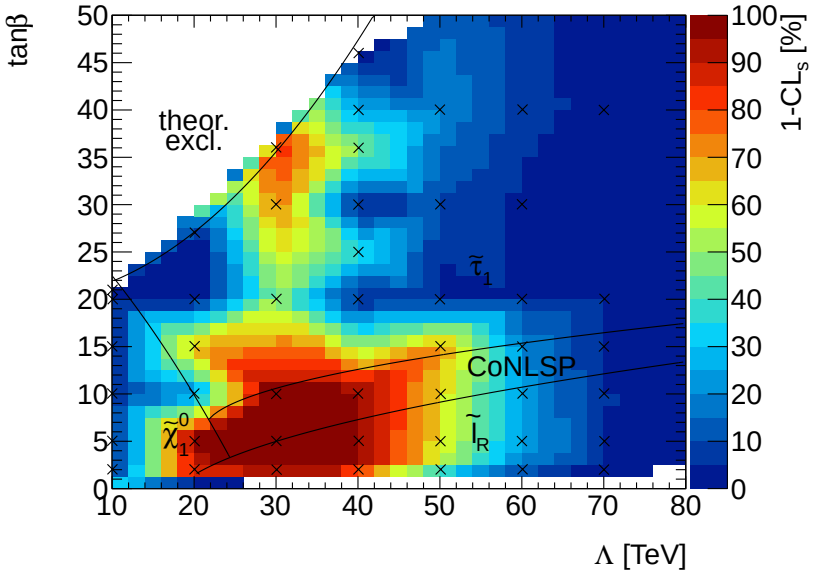

(b)

Figure D.8: The expected (a) and observed (b) $1 - \mathrm{CL_s}$ values and the position of the generated grid points are shown for GMSB grid. If the $\mathrm{CL_s}$ value of a given grid point is $< 5\%$, the point is excluded at 95% confidence. The limits are calculated for the FS-SR3 ($E_{\mathrm{T}}^{\mathrm{miss}} > 250\,\mathrm{GeV}$).

List of Figures

List of Tables

Bibliography

[1] S. L. Glashow. Partial-symmetries of weak interactions. *Nuclear Physics*, 22(4):579 – 588, 1961.

[2] S. Weinberg. Elementary particle theory of composite particles. *Phys. Rev.*, 130:776–783, Apr 1963.

[3] S. Weinberg. A model of leptons. *Phys. Rev. Lett.*, 19:1264–1266, Nov 1967.

[4] P. W. Higgs. Broken symmetries, massless particles and gauge fields. *Phys. Lett.*, 12:132–133, 1964.

[5] P. W. Higgs. Broken symmetries and the masses of gauge bosons. *Phys. Rev. Lett.*, 13:508–509, Oct 1964.

[6] F. Englert and R. Brout. Broken symmetry and the mass of gauge vector mesons. *Phys. Rev. Lett.*, 13:321–323, Aug 1964.

[7] G. S. Guralnik, C. R. Hagen, and T. W. B. Kibble. Global conservation laws and massless particles. *Phys. Rev. Lett.*, 13:585–587, Nov 1964.

[8] K. Nakamura and Particle Data Group. Review of particle physics. *Journal of Physics G: Nuclear and Particle Physics*, 37(7A):075021, 2010.

[9] Tevatron Electroweak Working Group, CDF, and D0 Collaborations. Combination of CDF and D0 results on the mass of the top quark using up to 5.8 fb-1 of data, 2011.

[10] K. Adel and F. J. Ynduráin. Production of heavy quarks close to threshold. *Phys. Rev. D*, 52:6577–6594, Dec 1995.

[11] J. Schwinger. On Quantum-Electrodynamics and the Magnetic Moment of the Electron. *Phys. Rev., 73, 416*, 1948.

[12] R. P. Feynman. Mathematical Formulation of the Quantum Theory of Electromagnetic Interaction. *Phys. Rev., 80, 440*, 1950.

[13] S. L. Glashow. Partial Symmetries of Weak Interactions. *Nucl. Phys.*, 22:579–588, 1961.

[14] A. Salam and J. Ward. Weak and electromagnetic interactions. *Il Nuovo Cimento (1955-1965)*, 11:568–577, 1959. 10.1007/BF02726525.

[15] H. Fritzsch, M. Gell-Mann, and H Leutwyler. Advantages of the color octet gluon picture. *Phys. Lett. B*, 47(4):365–368, 1973.

[16] N. Cabibbo. Unitary symmetry and leptonic decays. *Phys. Rev. Lett.*, 10:531–533, Jun 1963.

[17] M. Kobayashi and T. Maskawa. *cp*-violation in the renormalizable theory of weak interaction. *Progress of Theoretical Physics*, 49(2):652–657, 1973.

[18] Z. Maki, M. Nakagawa, and S. Sakata. Remarks on the unified model of elementary particles. *Progress of Theoretical Physics*, 28(5):870–880, 1962.

[19] SNO Collaboration. Direct evidence for neutrino flavor transformation from neutral-current interactions in the Sudbury neutrino observatory. Phys.Rev.Lett.89:011301,2002, 2002.

[20] D. J. Gross and F. Wilczek. Ultraviolet behavior of non-abelian gauge theories. *Phys. Rev. Lett.*, 30:1343–1346, Jun 1973.

[21] H. D. Politzer. Reliable perturbative results for strong interactions? *Phys. Rev. Lett.*, 30:1346–1349, Jun 1973.

[22] I. Abt, T. Ahmed, and V. Andreev et al. Measurement of the proton structure function F2 (x, Q2) in the low-x region at HERA. *Nuclear Physics B*, 407(3):515 – 535, 1993.

[23] M. Derrick, D. Krakauer, and S. Magill et al. Measurement of the proton structure function F2 in ep scattering at HERA. *Physics Letters B*, 316(2-3):412 – 426, 1993.

[24] H1 and ZEUS Collaboration. QCD analysis and determination of $\alpha_s(m_z)$ using the combined H1 and ZEUS inclusive cross sections together with the jet production cross section measured by the H1 and ZEUS experiments. *H1prelim-11-034,ZEUS-prel-11-001*, 2011.

[25] S. Bethke. The 2009 world average of α_s. Eur.Phys.J.C64:689-703,2009, 2009.

[26] H. Flaecher, M. Goebel, and J. Haller et al. Revisiting the global electroweak fit of the standard model and beyond with Gfitter. Eur.Phys.J.C60:543-583,2009; Erratum-ibid.C71:1718,2011, 2008.

[27] M. Baak, M. Goebel, and J. Haller et al. Updated status of the global electroweak fit and constraints on new physics, 2011.

[28] G. Abbiendi et al. Search for the standard model higgs boson at LEP. Phys.Lett.B565:61-75,2003, 2003.

[29] The CDF, D0 Collaborations, the Tevatron New Phenomena, and Higgs Working Group. Combined CDF and D0 upper limits on standard model higgs boson production with up to 8.6 fb-1 of data, 2011.

[30] ATLAS Collaboration. Combination of higgs boson searches with up to 4.9 fb-1 of pp collisions data taken at a center-of-mass energy of 7 TeV with the ATLAS experiment at the LHC. Technical Report ATLAS-CONF-2011-163, CERN, Geneva, Dec 2011.

[31] G. 't Hooft and M. Veltman. Regularization and renormalization of gauge fields. *Nuclear Physics B*, 44(1):189 – 213, 1972.

[32] S. P. Martin. A supersymmetry primer, 1997.

[33] C. L. Bennett et al. First Year Wilkinson Microwave Anisotropy Probe (WMAP) Observations: Preliminary Maps and Basic Results. *Astrophys. J. Suppl.*, 148:1, 2003.

[34] E. W. Kolb and M. S. Turner. *The Early Universe*. Addison-Wesley, Redwood City, USA, 1990. Frontiers in physics, 69.

[35] D. N. Spergel, L. Verde, and H. V. Peiris et al. First year wilkinson microwave anisotropy probe (wmap) observations: Determination of cosmological parameters. Astrophys.J.Suppl.148:175-194,2003, 2003.

[36] C. Bambi and A. D. Dolgov. Antimatter in the milky way. Nucl.Phys.B784:132-150,2007, 2007.

[37] Yu.A. Golfand and E.P. Likhtman, JETP Lett. 13 (1971) 323; A. Neveu and J.H. Schwartz, Nucl. Phys. B31 (1971) 86; A. Neveu and J.H. Schwartz, Phys. Rev. D4 (1971) 1109; P. Ramond, Phys. Rev. D3 (1971) 2415; D.V. Volkov and V.P. Akulov, Phys. Lett. B46 (1973) 109; J. Wess and B. Zumino, Phys. Lett. B49 (1974) 52; J. Wess and B. Zumino, Nucl. Phys. B70 (1974) 39.

[38] P. Fayet and J. Iliopoulos. Spontaneously broken supergauge symmetries and goldstone spinors. *Physics Letters B*, 51(5):461 – 464, 1974.

[39] L. O'Raifeartaigh. Spontaneous symmetry breaking for chirals scalar superfields. *Nuclear Physics B*, 96(2):331 – 352, 1975.

[40] P. Nath and R. Arnowitt. Generalized super-gauge symmetry as a new framework for unified gauge theories. *Physics Letters B*, 56(2):177 – 180, 1975.

[41] R. Arnowitt, P. Nath, and B. Zumino. Superfield densities and action principle in curved superspace. *Physics Letters B*, 56(1):81 – 84, 1975.

[42] E. Cremmer, S. Ferrara, L. Girardello, and A. Van Proeyen. Yang-mills theories with local supersymmetry: Lagrangian, transformation laws and super-higgs effect. *Nuclear Physics B*, 212(3):413 – 442, 1983.

[43] A.H. Chamseddine, R.L. Arnowitt and P. Nath, Phys. Rev. Lett. 49 (1982) 970; R. Barbieri, S. Ferrara and C.A. Savoy, Phys. Lett. B 119 (1982) 343; L.E. Ibanez, Phys. Lett. B 118 (1982) 73; L.J. Hall, J.D. Lykken and S. Weinberg, Phys. Rev. D 27 (1983) 2359; N. Ohta, Prog. Theor. Phys. 70 (1983) 542.

[44] https://twiki.cern.ch/twiki/bin/view/AtlasProtected/PhenoGrid2.

[45] I. Hinchliffe, F. E. Paige, M. D. Shapiro, J. Söderqvist, and W. Yao. Precision SUSY measurements at cern LHC. *Phys. Rev. D*, 55:5520–5540, May 1997.

[46] D. Costanzo and D. R. Tovey. Supersymmetric particle mass measurement with invariant mass correlations. *Journal of High Energy Physics*, 2009(04):084, 2009.

[47] B. C. Allanach, C. G. Lester, M. A. Parker, and B. R. Webber. Measuring sparticle masses in non-universal string inspired models at the LHC. *Journal of High Energy Physics*, 2000(09):004, 2000.

[48] P. Langacker and M. Luo. Implications of precision electroweak experiments for m_t, ρ_0, $\sin^2\theta_w$ and grand unification. *Phys. Rev. D*, 44:817–822, Aug 1991.

[49] P. Bechtle, K. Desch, and P. Wienemann. Fittino, a program for determining MSSM parameters from collider observables using an iterative method. Comput.Phys.Commun. 174 (2006) 47-70, 2004.

[50] P. Bechtle, K. Desch, and H. Dreiner et al. Present and possible future implications for mSUGRA of the non-discovery of SUSY at the LHC, 2011.

[51] ATLAS Collaboration. Combined exclusion reach of searches for squarks and gluinos using final states with jets, missing transverse momentum, and zero or one lepton, with the ATLAS detector in $\sqrt{s} = 7\,\text{TeV}$ proton-proton collisions. Technical Report ATLAS-CONF-2011-064, CERN, Geneva, Apr 2011.

[52] ATLAS Collaboration, G. Aad, B. Abbott, M. Boehler, et al. Search for an excess of events with an identical flavour lepton pair and significant missing transverse momentum in $\sqrt{s} = 7\,\text{TeV}$ proton-proton collisions with the ATLAS detector. *The European Physical Journal C - Particles and Fields*, 71:1–18, 2011. 10.1140/epjc/s10052-011-1647-9.

[53] LEP SUSY Working Group (ALEPH, DELPHI, L3, OPAL), Notes LEPSUSYWG/01-03.1 and 04-01.1, http://lepsusy.web.cern.ch/lepsusy/Welcome.html.

[54] T. Aaltonen and for the CDF Collaboration. Inclusive search for squark and gluino production in ppbar collisions at $\sqrt{s} = 1.96\,\text{TeV}$. Phys.Rev.Lett.102:121801,2009, 2008.

[55] D0 Collaboration and V. Abazov. Search for squarks and gluinos in events with jets and missing transverse energy using 2.1 fb-1 of ppbar collision data at $\sqrt{s} = 1.96\,\text{TeV}$. Phys.Lett.B660:449-457,2008, 2007.

[56] D0 Collaboration and V. Abazov. Search for associated production of charginos and neutralinos in the trilepton final state using 2.3 fb-1 of data. Phys.Lett.B680:34-43,2009, 2009.

[57] R. Barate et al. Single- and multi-photon production in e^+e^- collisions at $\sqrt{s}$ up to 209 GeV. *Eur. Phys. J*, C28:1, 2003.

[58] J. Abdallah et al. Photon events with missing energy in e^+e^- collisions at $\sqrt{s} = 130$ to 209 GeV. *Eur. Phys. J*, C38:394–411, 2005.

[59] G. Abbiendi et al. Multi-photon events with large missing energy in e^+e^- collisions at $\sqrt{s} = 192 - 209\,\text{GeV}$. *Phys. Lett.*, B602:167–179, 2004.

[60] P. Achard et al. Single- and multi-photon events with missing energy in e^+e^- collisions at LEP. *Phys. Lett.*, B587:16, 2004.

[61] V. Abazov et al. Search for diphoton events with large missing transverse energy in 6.3 fb^{-1} of $p\bar{p}$ collisions at $\sqrt{s} = 1.96\,\text{TeV}$. *Phys. Rev. Lett.*, 105:221802, 2010.

[62] T. Aaltonen et al. Search for supersymmetry with gauge-mediated breaking in diphoton events with missing transverse energy at CDF ii. *Phys. Rev. Lett.*, 105:011801, 2010.

[63] The OPAL Collaboration. Searches for gauge-mediated SUSY breaking topologies in e^+e^- collisions at $\sqrt{s} = 189 - 209\,\text{GeV}$. oai:cds.cern.ch:837821. Technical Report CERN-OPAL-PN-504. OPAL-PN-504, CERN, Geneva, Jul 2002.

[64] L. Evans and P. Bryant. LHC machine. *Journal of Instrumentation*, 3(08):S08001, 2008.

[65] G. Aad et al. ATLAS experiment at the cern large hadron collider. *Journal of Instrumentation*, 3(08):S08003, 2008.

[66] M. Benedikt, P. Collier, V. Mertens, et al. *LHC Design Report*. CERN, Geneva, 2004.

[67] J. M. Campbell, J. W. Huston, and W. J. Stirling. Hard interactions of quarks and gluons: a primer for LHC physics. Rept.Prog.Phys.70:89,2007, 2006.

[68] S. Chatrchyan et al. The CMS experiment at the cern LHC. *Journal of Instrumentation*, 3(08):S08004, 2008.

[69] A. Augusto Alves Jr. and et al. The LHCb detector at the LHC. *Journal of Instrumentation*, 3(08):S08005, 2008.

[70] K. Aamodt et al. The ALICE experiment at the cern LHC. *Journal of Instrumentation*, 3(08):S08002, 2008.

[71] Design report Tevatron 1 Project, 1982.

[72] J. L. Augneres et al. HERA - A Proposal for a Large Electron Proton Colliding Beam Facility at DESY, 1981.

[73] G. Anelli et al. The TOTEM experiment at the cern large hadron collider. *Journal of Instrumentation*, 3(08):S08007, 2008.

[74] O. Adriani et al. The LHCf detector at the cern large hadron collider. *Journal of Instrumentation*, 3(08):S08006, 2008.

[75] The LEP Electroweak Working Group. The LEP Electroweak Working Group (LEP EWWG) Combines the Measurements of the four LEP Experiments ALEPH, DELPHI, L3 and OPAL. `http://lepewwg.web.cern.ch/LEPEWWG/`, date 27 Sept 2008.

[76] ATLAS Collaboration. *ATLAS magnet system: Technical Design Report, 1.* Technical Design Report ATLAS. CERN, Geneva, 1997.

[77] ATLAS Collaboration. *ATLAS central solenoid: Technical Design Report.* Technical Design Report ATLAS. CERN, Geneva, 1997. Electronic version not available.

[78] J. P. Badiou, J. Beltramelli, J. M. Maze, and J Belorgey. *ATLAS barrel toroid: Technical Design Report.* Technical Design Report ATLAS. CERN, Geneva, 1997. Electronic version not available.

[79] ATLAS Collaboration. *ATLAS end-cap toroids: Technical Design Report.* Technical Design Report ATLAS. CERN, Geneva, 1997. Electronic version not available.

[80] ATLAS Collaboration. *ATLAS inner detector: Technical Design Report, 1.* Technical Design Report ATLAS. CERN, Geneva, 1997.

[81] N. Wermes and G Hallewel. *ATLAS pixel detector: Technical Design Report.* Technical Design Report ATLAS. CERN, Geneva, 1998.

[82] A. Ahmad and Z. Albrechtskirchinger et al. The silicon microstrip sensors of the ATLAS semiconductor tracker. *Nuclear Instruments and Methods in Physics Research Section A: Accelerators, Spectrometers, Detectors and Associated Equipment*, 578(1):98 – 118, 2007.

[83] ATLAS TRT Collaboration, E. Abat, and T. N. Add et al. ATLAS transition radiation tracker (trt) proportional drift tube: design and performance. *Journal of Instrumentation*, 3(02):P02013, 2008.

[84] ATLAS Collaboration. Alignment performance of the ATLAS inner detector tracking system in 7 TeV proton-proton collisions at the LHC. Technical Report ATLAS-CONF-2010-067, CERN, Geneva, Jul 2010.

[85] ATLAS Collaboration. Alignment of the ATLAS inner detector tracking system with 2010 LHC proton-proton collisions at $\sqrt{s} = 7$ TeV. Technical Report ATLAS-CONF-2011-012, CERN, Geneva, Mar 2011.

[86] ATLAS Collaboration. *ATLAS liquid-argon calorimeter: Technical Design Report.* Technical Design Report ATLAS. CERN, Geneva, 1996.

[87] ATLAS Collaboration. *ATLAS tile calorimeter: Technical Design Report.* Technical Design Report ATLAS. CERN, Geneva, 1996.

[88] ATLAS Collaboration. The ATLAS Experiment at the CERN Large Hadron Collider. *Journal of Instrumentation*, 3(08):S08003, 2008.

[89] M. Aharrouche and J. Colas et al. Energy linearity and resolution of the ATLAS electromagnetic barrel calorimeter in an electron test-beam. *Nuclear Instruments and Methods in Physics Research Section A: Accelerators, Spectrometers, Detectors and Associated Equipment*, 568(2):601 – 623, 2006.

[90] ATLAS Collaboration. Electron performance measurements with the ATLAS detector using the 2010 LHC proton-proton collision data, 2011.

[91] P. Adragna, C. Alexa, K. Anderson, et al. Testbeam studies of production modules of the ATLAS tile calorimeter. *Nucl. Instrum. Methods Phys. Res., A*, 606(ATL-TILECAL-PUB-2009-002 .ATL-COM-TILECAL-2009-004. 3):362–394. 73 p, Feb 2009. revised version, includes new author lists.

[92] ATLAS Collaboration. *ATLAS muon spectrometer: Technical Design Report.* Technical Design Report ATLAS. CERN, Geneva, 1997. distribution.

[93] ATLAS Collaboration. Studies of the performance of the ATLAS detector using cosmic-ray muons. Eur.Phys.J. C71 (2011) 1593, 2010.

[94] ATLAS Collaboration. Muon reconstruction efficiency in reprocessed 2010 LHC proton-proton collision data recorded with the ATLAS detector. Technical Report ATLAS-CONF-2011-063, CERN, Geneva, Apr 2011.

[95] ATLAS Collaboration. Muon momentum resolution in first pass reconstruction of pp collision data recorded by ATLAS in 2010. Technical Report ATLAS-CONF-2011-046, CERN, Geneva, Mar 2011.

[96] ATLAS Collaboration. *ATLAS Level-1 Trigger: Technical Design Report.* Technical Design Report ATLAS. CERN, Geneva, 1998.

[97] P. Jenni, M. Nessi, M. Nordberg, and K. Smith. *ATLAS high-level trigger, data-acquisition and controls: Technical Design Report.* Technical Design Report ATLAS. CERN, Geneva, 2003.

[98] ATLAS Collaboration. Performance of the ATLAS trigger system in 2010, 2011.

[99] ATLAS Collaboration. Luminosity public results. `https://twiki.cern.ch/twiki/bin/view/AtlasPublic/LuminosityPublicResults#Luminosity_versus_day`, date 25 Sept 2011.

[100] J. A. Frost. Commissioning of ATLAS data quality infrastructure with first collision data. Technical Report ATL-COM-SOFT-2010-101, CERN, Geneva, Dec 2010. 15/01/2011.

[101] ATLAS Collaboration. Data quality information for 2010 and 2011 data. `https://twiki.cern.ch/twiki/bin/view/AtlasPublic/RunStatsPublicResults2010?redirectedfrom=Atlas.RunStatsPublicResults2010#2011`, date 25 Sept 2011.

[102] ATLAS Collaboration. *ATLAS Computing: Technical Design Report*. Technical Design Report ATLAS. CERN, Geneva, 2005. revised version submitted on 2005-06-20 16:33:46.

[103] M. Boehler and the ATLAS Collaboration. Processing, calibration and reprocessing of ATLAS data from LHC collisions at 7 TeV. *Proceedings of Science (ICHEP 2010)*, 500, 2011.

[104] ATLAS Collaboration. Luminosity determination in pp collisions at $\sqrt{s} = 7\,\text{TeV}$ using the ATLAS detector at the LHC. Eur.Phys.J.C71:1630,2011, 2011.

[105] S. van der Meer. Calibration of the effective beam height in the isr. oai:cds.cern.ch:296752. Technical Report CERN-ISR-PO-68-31. ISR-PO-68-31, CERN, Geneva, 1968.

[106] M. Boehler and the ATLAS Collaboration. Data-driven auto-configuration of the ATLAS reconstruction software. *Journal of Physics: Conference Series*, 331(3):032037, 2011.

[107] A. Valassi, R. Basset, M. Clemencic, et al. Cool, lcg conditions database for the LHC experiments: Development and deployment status. oai:cds.cern.ch:1142723. LHC: Large Hadron Collider. Technical Report CERN-IT-Note-2008-019, CERN, Geneva, Nov 2008. The NSS 2008 proceedings are being published by IEEE under their copyright policy.

[108] S. Albrand, J. Collot, and J. Fulachier. The ami database project: Atlas data challenge bookkeeping, and the tag collector, a new tool for release management, 2003.

[109] C. Arnault et al. The Atlas Computing Workbook, 2007.

[110] M. A. Dobbs, S. Frixione, and E. Laenen et al. Les houches guidebook to monte carlo generators for hadron collider physics, 2004.

[111] B. Andersson, G. Gustafson, G. Ingelman, and T. Sjöstrand. Parton fragmentation and string dynamics. Technical Report LUTP-83-10, Lunds Univ. Dept. Theor. Phys., Lund, Apr 1983.

[112] T. Sjöstrand. Monte Carlo Generators for the LHC (1/4), 2008.

[113] T. Sjöstrand, S. Mrenna, and P. Skands. Pythia 6.4 physics and manual. JHEP 0605:026,2006, 2006.

[114] G. Corcella, I. G. Knowles, and G. Marchesini et al. Herwig 6.5: an event generator for hadron emission reactions with interfering gluons (including supersymmetric processes). JHEP 0101:010,2001, 2000.

[115] H. Baer, F. E. Paige, S. D. Protopescu, and X. Tata. Isajet 7.69: A monte carlo event generator for pp, $\bar{p}p$, and $e^{=}e^{-}$ reactions, 2003.

[116] S. Moretti, K. Odagiri, and P. Richardson et al. Implementation of supersymmetric processes in the herwig event generator. JHEP 0204:028,2002, 2002.

[117] M. L. Mangano, M. Moretti, and F. Piccinini et al. ALPGEN, a generator for hard multiparton processes in hadronic collisions. JHEP 0307 (2003) 001, 2002.

[118] S. Frixione, F. Stoeckli, and P. Torrielli et al. The mc@nlo 4.0 event generator, 2010.

[119] S. Agostinelli and J. Allison et al. Geant4-a simulation toolkit. *Nuclear Instruments and Methods in Physics Research Section A: Accelerators, Spectrometers, Detectors and Associated Equipment*, 506(3):250 – 303, 2003.

[120] O. Arnaez and C Goy. *Préparation de la mesure de la section efficace inclusive du $Z \to e^+e^-$ dans ATLAS. Etude des premières données avec le calorimètre électromagnétique.. oai:cds.cern.ch:1309894.* PhD thesis, Chambéry, France, Université de Savoie, Annecy-le-Vieux, France, 2010. Presented on 05 Jul 2010.

[121] The ALEPH Collaboration, the DELPHI Collaboration, the L3 Collaboration, the OPAL Collaboration, the SLD Collaboration, the LEP Electroweak Working Group, the SLD electroweak, and heavy flavour groups. Precision electroweak measurements on the z resonance. Phys.Rept.427:257-454,2006, 2005.

[122] W. Lampl, S. Laplace, D. Lelas, and et al. Calorimeter clustering algorithms: Description and performance. Technical Report ATL-LARG-PUB-2008-002. ATL-COM-LARG-2008-003, CERN, Geneva, Apr 2008.

[123] M. Cacciari, G. P. Salam, and G. Soyez. The anti-kt jet clustering algorithm. JHEP 0804:063,2008, 2008.

[124] ATLAS Collaboration, G. Aad, E. Abat, and B. Abbott et al. Expected performance of the ATLAS experiment - detector, trigger and physics, 2008.

[125] ATLAS Collaboration. Data-quality requirements and event cleaning for jets and missing transverse energy reconstruction with the atlas detector in proton-proton collisions at a center-of-mass energy of $\sqrt{s} = 7\,\text{TeV}$. Technical Report ATLAS-CONF-2010-038, CERN, Geneva, Jul 2010.

[126] ATLAS Collaboration. Measurement of inclusive jet and dijet cross sections in proton-proton collision data at 7 TeV centre-of-mass energy using the ATLAS detector. Technical Report ATLAS-CONF-2011-047, CERN, Geneva, Mar 2011.

[127] P. Adragna, C. Alexa, K. et Anderson, et al. Measurement of pion and proton response and longitudinal shower profiles up to 20 nuclear interaction lengths with the ATLAS tile calorimeter. oai:cds.cern.ch:1214935. Technical Report CERN-PH-EP-2009-019. ATL-TILECAL-PUB-2009-009, CERN, Geneva, Oct 2009.

[128] E. Abat, J. M. Abdallah, T. N. Addy, et al. Response and shower topology of 2 to 180 GeV pions measured with the ATLAS barrel calorimeter at the cern test-beam and comparison to monte carlo simulations. Technical Report ATL-CAL-PUB-2010-001, CERN, Geneva, May 2010.

[129] E. Abat, J. M. Abdallah, T. N. Addy, et al. Study of energy response and resolution of the ATLAS barrel calorimeter to hadrons of energies from 20 GeV to 350 GeV. *Nucl. Instrum. Methods Phys. Res., A*, 621:134–150. 17 p, Oct 2010.

[130] E. Abat, J.M. Abdallah, T.N. Addy, et al. Study of the response of the ATLAS central calorimeter to pions of energies from 3 to 9 GeV. *Nuclear Instruments and Methods in Physics Research Section A: Accelerators, Spectrometers, Detectors and Associated Equipment*, 607(2):372 – 386, 2009.

[131] C. Cojocaru, J. L. Pinfold, J. Soukup, et al. Hadronic calibration of the ATLAS liquid argon endcap calorimeter in the pseudorapidity region 1.6 |eta| 1.8 in beam tests. oai:cds.cern.ch:909043. *Nucl. Instrum. Methods Phys. Res., A*, 531(physics/0407009. MPP-2004-81. 3):481–514. 66 p, Jul 2004.

[132] ATLAS Collaboration. Jet energy scale and its systematic uncertainty in proton-proton collisions at $\sqrt{s} = 7\,\text{TeV}$ in ATLAS 2010 data. Technical Report ATLAS-CONF-2011-032, CERN, Geneva, Mar 2011.

[133] E. Khramov, N. Rusakovich, T. Carli, et al. Study of the response of the hadronic barrel calorimeter in the ATLAS combined test-beam to pions of energies from 20 to 350 GeV for beam impact points from 0.2 to 0.65. Technical Report ATL-TILECAL-PUB-2009-007. ATL-COM-TILECAL-2009-006, CERN, Geneva, Apr 2009.

[134] ATLAS Collaboration. Electron and photon reconstruction and identification in atlas: expected performance at high energy and results at 900 GeV. Technical Report ATLAS-CONF-2010-005, CERN, Geneva, Jun 2010.

[135] ATLAS Collaboration. Tau reconstruction and identification performance in atlas. Technical Report ATLAS-CONF-2010-086, CERN, Geneva, Oct 2010.

[136] T Barillari, E. Bergeaas Kuutmann, T. Carli, et al. Local hadronic calibration. Technical Report ATL-LARG-PUB-2009-001-2, CERN, Geneva, Jun 2008. Due to a report-number conflict with another document, the report-number ATL-LARG-PUB-2009-001-2 has been assigned.

[137] ATLAS Collaboration. Performance of missing transverse momentum reconstruction in proton-proton collisions at 7 TeV with atlas, 2011.

[138] P. Bechtle, K. Desch, M. Uhlenbrock, and P. Wienemann. Constraining SUSY models with fittino using measurements before, with and beyond the LHC, 2009.

[139] ATLAS Collaboration. Measurement of the inclusive W+- and Z/gamma cross sections in the electron and muon decay channels in pp collisions at $\sqrt{s} = 7$ TeV with the ATLAS detector, 2011.

[140] ATLAS Collaboration. Measurement of the W+W- production cross section in proton-proton collisions at $\sqrt{s} = 7$ TeV with the atlas detector. Technical Report ATLAS-CONF-2011-110, CERN, Geneva, Aug 2011.

[141] ATLAS Collaboration. Measurement of the WZ production cross-section in proton-proton collisions at $\sqrt{s} = 7$ TeV with the atlas detector. Technical Report ATLAS-CONF-2011-099, CERN, Geneva, Jul 2011.

[142] ATLAS Collaboration. Measurement of the ZZ production cross section and limits on anomalous neutral triple gauge couplings in proton-proton collisions at $\sqrt{s} = 7$ TeV with the ATLAS detector, 2011.

[143] ATLAS Collaboration. Measurement of the top quark pair production cross-section based on a statistical combination of measurements of dilepton and single-lepton final states at $\sqrt{s} = 7$ TeV with the ATLAS detector. Technical Report ATLAS-CONF-2011-108, CERN, Geneva, Aug 2011.

[144] N. Kidonakis. Next-to-next-to-leading-order collinear and soft gluon corrections for t-channel single top quark production. Phys.Rev.D83:091503,2011, 2011.

[145] N. Kidonakis. Two-loop soft anomalous dimensions for single top quark associated production with a w- or h-. Phys.Rev.D82:054018,2010, 2010.

[146] N. Kidonakis. Nnll resummation for s-channel single top quark production. Phys.Rev.D81:054028,2010, 2010.

[147] ATLAS Collaboration. Measurement of the t-channel single top-quark production cross section in 0.70fb^{-1} of pp collisions at $\sqrt{s} = 7$ TeV with the ATLAS detector. Technical Report ATLAS-CONF-2011-101, CERN, Geneva, Jul 2011.

[148] ATLAS Collaboration. Reconstruction, energy calibration, and identification of hadronically decaying tau leptons. Technical Report ATLAS-CONF-2011-077, CERN, Geneva, May 2011.

[149] ATLAS Collaboration. Expected performance of the ATLAS detector in gmsb models with tau final states. Technical Report ATL-PHYS-PUB-2009-089, CERN, Geneva, Nov 2009.

[150] A. Hoecker, private communication.

[151] A. Alonso, S. Brazzale, M. Boehler, et al. Searching for supersymmetry with two leptons and missing transverse momentum at $\sqrt{s} = 7$ TeV. Technical Report ATL-COM-PHYS-2011-649, CERN, Geneva, Jun 2011.

[152] ATLAS Collaboration. Searches for supersymmetry with the ATLAS detector using final states with two leptons and missing transverse momentum in $\sqrt{s} = 7$ TeV proton-proton collisions, 2011. Accepted by Phys. Lett. B.

[153] R. Brun and F. Rademakers. ROOT: An Object Oriented Data Analysis Framework. *Nucl. Instrum. Meth.*, A389:81–86, 1997.

[154] M. Hamer, C. Hensel, F. Kohn, and A. Quadt. Measurement of trigger efficiencies from data and their application in physics analyses. Technical Report ATL-COM-DAQ-2011-083, CERN, Geneva, Sep 2011.

[155] ATLAS Collaboration. Search for supersymmetry in final states with jets, missing transverse momentum and one isolated lepton in $\sqrt{s} = 7\,\text{TeV}$ pp collisions using 1 fb-1 of ATLAS data, 2011.

[156] https://twiki.cern.ch/twiki/bin/viewauth/Atlas/CoolLumiCalcTutorial.

[157] https://twiki.cern.ch/twiki/bin/view/AtlasProtected/EnergyRescaler.

[158] S. Hassani, L. Chevalier, and E. Lançon et al. A muon identification and combined reconstruction procedure for the ATLAS detector at the LHC using the (MUONBOY, STACO, MuTag) reconstruction packages. *Nuclear Instruments and Methods in Physics Research Section A: Accelerators, Spectrometers, Detectors and Associated Equipment*, 572(1):77 – 79, 2007.

[159] D. R. Tovey. On measuring the masses of pair-produced semi-invisibly decaying particles at hadron colliders. JHEP0804:034,2008, 2008.

[160] G. Polesello and D. R. Tovey. Supersymmetric particle mass measurement with the boost-corrected contransverse mass. JHEP 1003:030,2010, 2009.

[161] ATLAS Collaboration. Luminosity determination in pp collisions at $\sqrt{s} = 7\,\text{TeV}$ using the ATLAS detector in 2011. Technical Report ATLAS-CONF-2011-116, CERN, Geneva, Aug 2011.

[162] S. Moch and P. Uwer. Theoretical status and prospects for top-quark pair production at hadron colliders. *Phys. Rev.*, D78:034003, 2008.

[163] U. Langenfeld, S. Moch, and P. Uwer. New results for $t\bar{t}$ production at hadron colliders, 2009.

[164] ATLAS Collaboration. Jet energy scale and its systematic uncertainty in ATLAS for jets produced in proton-proton collisions at $\sqrt{s} = 7\,\text{TeV}$. Technical Report ATLAS-COM-CONF-2010-056, CERN, Geneva, Jul 2010.

[165] https://twiki.cern.ch/twiki/bin/view/AtlasProtected/JESUncertaintyProvider.

[166] ATLAS Collaboration. Jet energy resolution and selection efficiency relative to track jets from in-situ techniques with the ATLAS detector using proton-proton collisions at a center of mass energy $\sqrt{s} = 7\,\text{TeV}$. Technical Report ATLAS-CONF-2010-054, CERN, Geneva, Jul 2010.

[167] https://twiki.cern.ch/twiki/bin/view/AtlasProtected/MCPAnalysisGuidelinesPLHC2011.

[168] A. L. Read. Presentation of search results: The CL(s) technique. *J.Phys.G*, G28:2693–2704, 2002.

[169] G. Cowan, K. Cranmer, Ei. Gross, and O. Vitells. Asymptotic formulae for likelihood-based tests of new physics. *Eur.Phys.J.*, C71:1554, 2011.

[170] ATLAS Collaboration. Constraining the gauge-mediated supersymmetry breaking model in final states with two leptons, jets and missing transverse momentum with the ATLAS experiment at $\sqrt{s} = 7\,\text{TeV}$. Technical Report ATLAS-CONF-2011-156, CERN, Geneva, Nov 2011.

[171] ATLAS Collaboration. Search for squarks and gluinos using final states with jets and missing transverse momentum with the ATLAS detector in $\sqrt{s} = 7\,\text{TeV}$ proton-proton collisions, 2011.

Acknowledgement

At this point, I would like to thank many people, whose help was indispensable in order to accomplish this thesis. First of all, many thanks to my supervisor Dr. Philip Bechtle who gave me the possibility to work in the ATLAS collaboration on my analysis, for his suggestions, advices and his creative ideas. I would like to thank Prof. Dr. Johannes Haller, Prof. Dr. Peter Schleper, and Dr. Georg Steinbrück who agreed to be the referees for the dissertation, the thesis defence, and the chair of the thesis committee.

I am thankful to Dr. David Coté who was offering me a smooth start at CERN, gave me the possibility for an interesting service task, introduced me to the ATLAS software as well as to (all) the people involved, and gave me the opportunity to gain first experiences in teaching. I would like to thank Dr. João Firmino da Costa for joining the group exactly at the right moment and supporting me in the analysis day and night. Thanks for your patience, the endless discussions at DESY, CERN, and skype about physics and toys, and for the coffee.

More coffee and a lot of technical support I got from Dr. Wolfgang Ehrenfeld - thanks for fruitful discussions and lectures about everything (from TGB couplings to GMSB), and thanks for taking care that I did not overstress any NAF resources.

I would like to thank all the ATLAS and (not ATLAS) fellows from Hamburg who were there for discussion, support, and thesis reading and re-reading (Dr. Nicholas Styles, Dr. Mark Terwort, Jörgen Samson, Dörthe Kennedy, Milan Zvolský, Almut Pingel) and all the colleagues and friends I met during this work - many thanks for a great time.

Special thanks to Claudia Giuliani for demonstrating that Goethe's sentence is not only true for art and physics.

An dieser Stelle möchte ich mich auch noch ganz herzlich bei meinen Eltern bedanken, die mich immer unterstützt habe, wo auch immer ich gerade war - Vielen Dank.